Resolvent analysis for compressible wall turbulence

Beverley Mckeon
CALIFORNIA INSTITUTE OF TECHNOLOGY

08/16/2019
Final Report

			Form Approved
REPORT DOCUMENTATION PAGE			*Form Approved* *OMB No. 0704-0188*

The public reporting burden for this collection of information is estimated to average 1 hour per response, including the time for reviewing instructions, searching existing data sources, gathering and maintaining the data needed, and completing and reviewing the collection of information. Send comments regarding this burden estimate or any other aspect of this collection of information, including suggestions for reducing the burden, to Department of Defense, Washington Headquarters Services, Directorate for Information Operations and Reports (0704-0188), 1215 Jefferson Davis Highway, Suite 1204, Arlington, VA 22202-4302. Respondents should be aware that notwithstanding any other provision of law, no person shall be subject to any penalty for failing to comply with a collection of information if it does not display a currently valid OMB control number.
PLEASE DO NOT RETURN YOUR FORM TO THE ABOVE ADDRESS.

1. REPORT DATE *(DD-MM-YYYY)*	2. REPORT TYPE	3. DATES COVERED *(From - To)*
08/13/2019	FINAL	05-15-2016 - 05-14-2019

4. TITLE AND SUBTITLE	5a. CONTRACT NUMBER
RESOLVENT ANALYSIS FOR COMPRESSIBLE WALL TURBULENCE	FA9550-16-1-0232
	5b. GRANT NUMBER
	FA9550-16-1-0232
	5c. PROGRAM ELEMENT NUMBER

6. AUTHOR(S)	5d. PROJECT NUMBER
BEVERLEY J MCKEON	
	5e. TASK NUMBER
	5f. WORK UNIT NUMBER

7. PERFORMING ORGANIZATION NAME(S) AND ADDRESS(ES)	8. PERFORMING ORGANIZATION REPORT NUMBER
CALIFORNIA INSTITUTE OF TECHNOLOGY 1200 E CALIFORNIA BLVD PASADENA, CA 91125-0001	

9. SPONSORING/MONITORING AGENCY NAME(S) AND ADDRESS(ES)	10. SPONSOR/MONITOR'S ACRONYM(S)
AIR FORCE OFFICE OF SCIENTIFIC RESEARCH 875 NORTH RANDOLPH STREET ARLINGTON, VA 22203-1954	AFOSR
	11. SPONSOR/MONITOR'S REPORT NUMBER(S)

12. DISTRIBUTION/AVAILABILITY STATEMENT
Distribution A - Approved for Public Release

13. SUPPLEMENTARY NOTES

14. ABSTRACT
Obtaining data from high-speed boundary layers requires either rare flight tests, large-scale, expensive experimental facilities or massive, challenging numerical simulations. This work sought to lay the foundation for predictive tools which exploit recent developments in incompressible turbulent flows related to resolvent analysis, or the identification of the natural amplification and nonlinear interaction mechanisms of the equations of motion. The key conclusion is that the equations of motion support Morkovin's hypothesis over a broad range of conditions as Mach number increases, with the important implication that developments in incompressible flows may be exploited for the compressible regime.

15. SUBJECT TERMS

16. SECURITY CLASSIFICATION OF:			17. LIMITATION OF ABSTRACT	18. NUMBER OF PAGES	19a. NAME OF RESPONSIBLE PERSON
a. REPORT	**b. ABSTRACT**	**c. THIS PAGE**			BEVERLEY MCKEON
					19b. TELEPHONE NUMBER *(Include area code)*
U	U	U	UU		626 395 4460

Standard Form 298 (Rev. 8/98)
Prescribed by ANSI Std. Z39.18

FINAL REPORT

Grant # FA9550-16-1-0232

Resolvent analysis for compressible wall turbulence

Beverley J. McKeon
Graduate Aerospace Laboratories
California Institute of Technology
Pasadena, CA 91125

Executive Summary

Obtaining data from high-speed boundary layers requires either rare flight tests, large-scale, expensive experimental facilities or massive, challenging numerical simulations. The former two approaches provide challenges due to short run times, limited diagnostic accessibility, sensitivity of the flow to intrusive measurement techniques and stringent resolution requirements (spatial and temporal).

This work sought to lay the foundation for predictive tools which exploit recent developments in incompressible turbulent flows related to resolvent analysis, or the identification of the natural amplification and nonlinear interaction mechanisms of the equations of motion.

The modeling advances developed under this grant offer the potential to lead to significant savings in the prediction of energetic turbulent structures in compressible turbulent boundary layers (relative to full simulations). A full predictive capability would require learning the relative weights (magnitudes and phases) of these structures (mode shapes), which is determined by nonlinear interactions. The focus of this work was on the linear dynamics of compressible flows; study of the nonlinear forcing is reserved for future work. The key conclusion is that the equations of motion support Morkovin's hypothesis over a broad range of conditions as Mach number increases, with the important implication that developments in incompressible flows may be exploited for the compressible regime.

This research resulted in one manuscript to be published in the Journal of Fluid Mechanics [1], one currently under review [2], one in preparation [3] and two AIAA conference papers [4], [5].

Contents

1   Introduction and Objectives

The work performed under this grant pertained to the extension of the resolvent analysis developed by McKeon & Sharma (2010)[6] for incompressible wall turbulence to compressible boundary layer flows. The over-arching goal was to exploit recent developments in order reduction, sparsity and structure in the Navier-Stokes equations to provide the Air Force with a suite of tools of increasing complexity (laptop to HPC) and fidelity to model high-speed turbulent boundary layers (canonical and practical).

Obtaining data from high-speed boundary layers requires either rare flight tests, large-scale, expensive experimental facilities or massive, challenging numerical simulations. The former two approaches provide challenges due to short run times, limited diagnostic accessibility, sensitivity of the flow to intrusive measurement techniques and stringent resolution requirements (spatial and temporal). In addition, the flow state can be sensitive to facility conditions, such as freestream noise and tripping configuration. Typically point measurements, wall-normal line profiles and/or surface information may be obtained, usually of a limited number of variables. Direct Numerical Simulations, which would provide full-field information on the complete state, exist, but are numerically challenging due to algorithmic demands nd the enormous resolution requirement. Further, detailed characterization of flow inlet and boundary conditions is required to obtain agreement with experiments. Impressive calculations can be performed, e.g. [7, 8], but remain out of reach for complex geometries. Large Eddy Simulations (LES) and Reynolds-Averaged Navier-Stokes calculations (RANS) of compressible boundary layers require insight specific to compressible flows to implement appropriate wall, sub-grid scale and/or eddy viscosity type models.

Thus, there is an opportunity to lay the foundation for predictive tools which exploit recent developments in incompressible turbulent flows related to resolvent analysis, or the identification of the natural amplification and nonlinear interaction mechanisms of the equations of motion.

The specific objectives of the research, as listed in the original proposal, were as follows.

Develop and validate compressible resolvent analysis for the modeling of compressible wall turbulence, and (secondary) advance the capability to incorporate coupling between turbulence and a wall with generalized properties.

1. Develop resolvent analysis for wall turbulence with non-zero Mach number. The essence of this development will be the identification of a suitable norm for decomposition of the resolvent in the wall-normal direction, the choice of which and implications thereof - is less obvious than in incompressible flow. Identify and exploit mathematical simplifications analogous to those identified above for incompressible flow (if any but there is reason to believe that the low rank nature of wall turbulence is not an exclusively incompressible phenomenon).

2. Validate compressible resolvent analysis against experimental and numerical observations in the literature. Investigate and document different mechanisms underlying compressible and incompressible wall turbulence, as illuminated by the resolvent analysis. Identify origins of structure, reasons for similarities and differences, and Reynolds number and wall-normal scalings for the compressible case.

A secondary objective was also proposed:

3. Advance the modeling of turbulence-wall interaction via the incorporation of general linearized wall boundary conditions into the compressible resolvent analysis. Consider the coupled interaction of wall turbulence with surface of various properties corresponding to compliant, vibrating and morphing (actively driven) walls.

It was anticipated that progress on this secondary objective would be limited given the proposed scope and duration of the main project.

The proposed timeline is outlined in Figure 1. The project essentially ran to this schedule, with the exceptions that only a small portion of the final year was devoted to considering wall boundary conditions, and that the availability of personnel and the difficulty of the project ultimately led to staffing by postdoctoral scholars rather than GRAs. Dr. Scott Dawson and Dr. Jane Bae performed this role.

DISTRIBUTION A: Distribution approved for public release

	YEAR 1	YEAR 2	YEAR 3
PI	Project management and advising		
	Identification of (1) mathematical simplifications for the compressible case, (2) differences and similarities with the incompressible flow results, (3) limitations in the compressible analysis		
GRA	Resolvent training; review of resolvent and transient growth approaches to transition	Completion of compressible resolvent code; Validation against experiments and simulation in the literature	Exploit compressible resolvent analysis: origins of structure, limitations, etc; Consideration of wall boundary condition

Figure 1: Timeline from original proposal (essentially reflective of actual schedule).

2   Background

The analysis employed in this work is a logical development of the resolvent analysis laid out by McKeon & Sharma [6] for incompressible turbulent flows. The essence of that approach is described in Figure 2. The resolvent is the transfer function between the nonlinear terms in the Navier-Stokes equations, which are treated as a forcing of the linear dynamics, and the linear state response (here indicated in terms of the velocity fluctuations, i.e. for a divergence-free basis, relative to the turbulent mean). The analysis accounts for the amplification of forcing input due to the non-normality of the resolvent [9], which is similar to the linearized Navier-Stokes operator familiar from hydrodynamic stability theory although without the restrictions on the magnitude of the perturbation from the equilibrium (laminar) state. Analysis of the resolvent using a singular value decomposition (SVD) subject to an energy norm at each spatio-temporal scale reveals that it can be approximated in an extremely low-order fashion when there is a physical mechanism extracting energy from the mean flow [10]. Equivalently, the spatio-temporal basis used in the analysis efficiently identifies forcing structure which is preferentially amplified by the resolvent, giving rise to the "most likely observable" response mode shapes at each scale. The analysis can be considered to be the equation-driven equivalent of data analysis techniques such as Proper Orthogonal Decomposition, which require full-field information rather than simply the governing equations [11]. Full details of the analysis will be laid out in the context of compressible turbulent boundary layers in Section 3 below.

Notably, the cost of resolvent analysis is significantly less than high performance computations, since it rests on linear algebra techniques which have been the subject of intensive development in other fields in recent years. For a one-dimensional turbulent mean profile, i.e. a quasi-parallel assumption for a turbulent boundary or a periodic domain for an internal flow, the cost of performing the SVD is so low that analysis can proceed on a laptop computer. More computing power is required for two-dimensional mean flows - with associated data storage limitations which have limited the size of the domain which can be considered - but still at the local core rather than national HPC facility level.

A recent review of resolvent analysis for incompressible wall turbulence and an overview of what can be learned about turbulence structure and self-sustaining mechanisms is given in [12]. The approach has now been used to analyze a wide range of turbulent flow configurations. The focus of our current work in incompressible wall turbulence now pertains to "closing the loop", or determining the characteristics of the *nonlinear* forcing that lead to self-sustaining turbulence and consistency with the turbulent mean profile used in forming the resolvent. As will be discussed below, these efforts can be said to have direct relevance to compressible turbulent boundary layers as a result of the work performed under this grant.
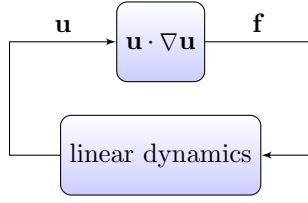
Figure 2: A high-level description of the turbulence process in resolvent analysis. The lower block contains the linear dynamics of the fluctuations interacting with the mean velocity profile. After [6].
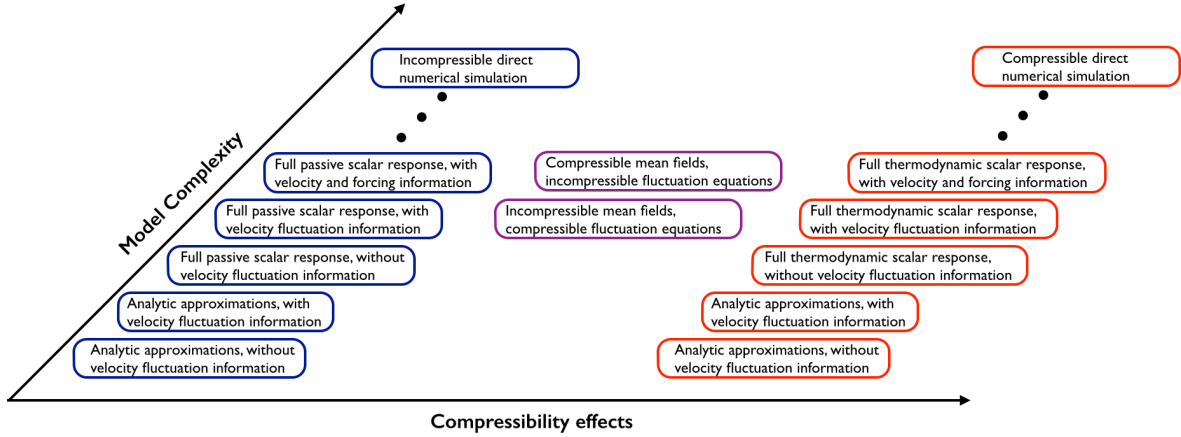

Figure 3: Complexity hierarchies.

3 Approach

The approach taken was to develop a suite of tools to address increasing importance of the effects of compressibility and model complexity, ranging from analytical approximations of reoslvent mode shapes in an incompressible turbulent boundary layer with a passive scalar to detailed information about the relative magnitudes of thermodynamic and velocity fluctuations for Mach number $M > 1$. A schematic of the steps in this approach is shown in Figure 3.

Resolvent analysis for a passive scalar in a turbulent boundary layer was developed first, during which period a method for semi-analytic approximation of the most amplified resolvent modes was also developed and used to reconstruct scalar variance and velocity-covariance statistics, demonstrating the efficacy of the analysis for such flows.

Our efforts then focused on compressible turbulent boundary layers, i.e. coupled velocity and thermodynamic variables at non-zero Mach number. Considerable effort was invested in determining the signature of compressibility in resolvent analysis, the differences between compressible and incompressible mean flows, and the norm to be used in the SVD.

Finally, an assessment of the differences between the results of resolvent analysis for incompressible and compressible turbulent boundary layers was made with a view to assessing Morkovin's hypothesis in the context of resolvent analysis, and (related) to determining which, if any, elements of the progress made in the linear and nonlinear analysis of incompressible wall turbulence were also relevant for Mach numbers greater than one.

6

4 Summary of Results

An outline of key results and outcomes from the grant is given in this section. The archival manuscripts which give full information are identified (and appended to this report).

4.1 Resolvent formulation for compressible turbulent boundary layers

For a fully developed, locally parallel, compressible flow with the directions x_1, x_2 and x_3 signifying the streamwise, wall-normal, and spanwise directions, respectively, the state variable becomes $\boldsymbol{q} = [q_1, q_2, q_3, q_4, q_5]^\dagger = [u_1, u_2, u_3, \rho, T]^\dagger$. As in the incompressible analysis, it is decomposed using the Fourier transform in homogeneous directions and time,

$$\boldsymbol{q}(x_1, x_2, x_3, t) = \iiint_{-\infty}^{\infty} \hat{\boldsymbol{q}}(x_2; \kappa_1, \kappa_3, \omega) e^{i(\kappa_1 x_1 + \kappa_3 x_3 - \omega t)} \mathrm{d}\kappa_1 \mathrm{d}\kappa_3 \mathrm{d}\omega, \tag{1}$$

where $(\hat{\cdot})$ denotes variables in the transformed domain, and the triplet $(\kappa_1, \kappa_3, \omega)$ identifies the streamwise and spanwise wavenumbers and the temporal frequency, respectively. Here, the superscript $\dagger$ denotes the transpose for real variables (vectors) and the conjugate transpose for complex values.

The mean turbulent state, $\bar{\boldsymbol{q}}(x_2) = [\bar{u}_1(x_2), 0, 0, \bar{\rho}(x_2), \bar{T}(x_2)]^\dagger$, corresponds to $(\kappa_1, \kappa_3, \omega) = (0, 0, 0)$ and is assumed to be known. In our work, this was obtained from publicly available DNS databases, in particular the adiabatic wall studies of Bernadini & Pirozzoli [13, 14]. The parallel-flow assumption, which is reasonable as the base flow variations depend on the viscous time scale compared to the much faster convective times scale for fluctuations, leads to a significantly more straightforward interpretation of underlying physical mechanisms than for two-dimensional mean flows, which are reserved for future work.

The governing equations for the compressible turbulent boundary layer can be rewritten in the Fourier domain for each $(\kappa_1, \kappa_3, \omega) \neq (0, 0, 0)$ in the form

$$\hat{\boldsymbol{q}}(x_2; \kappa_1, \kappa_3, \omega) = \left[-i\omega \mathbf{I} + \mathbf{L}(\kappa_1, \kappa_3, \omega)\right]^{-1} \hat{\boldsymbol{f}}(x_2; \kappa_1, \kappa_3, \omega) = \mathbf{H}\hat{\boldsymbol{f}}(x_2; \kappa_1, \kappa_3, \omega), \tag{2}$$

where $\mathbf{L}$ is the linearised operator of the governing equations around the supersonic turbulent mean profile [15] and $\hat{\boldsymbol{f}}$ contains the nonlinear terms. The operator $\mathbf{H} = \left[-i\omega \mathbf{I} + \mathbf{L}(\kappa_1, \kappa_3, \omega)\right]^{-1}$ is called the resolvent operator and exists if there are no eigenvalues of $\mathbf{L}$ with zero real part.

For the compressible boundary layer, the boundary conditions at the wall are given by

$$u_i(x_2 = 0) = 0, \quad T(x_2 = 0) = \bar{T}(x_2 = 0). \tag{3}$$

The boundary conditions on the velocity fluctuations are the usual no-slip conditions, and the boundary condition on the temperature fluctuation is consistent for a gas flowing over a solid wall.

The boundary conditions at the freestream are given by

$$u_i(x_2 \to \infty), \rho(x_2 \to \infty), T(x_2 \to \infty) < \infty, \tag{4}$$

which are less restrictive than requiring all fluctuations to be zero at infinity. However, in supersonic flow, waves may propagate to infinity and this boundary condition allows the waves with constant amplitude to be included.

Note that some of the norm and mean profile studies were performed for compressible planar Couette flow rather than boundary layer because the simplicity of the mean profile in the laminar case led to some simpler analytical developments with regards to the sensitivity of the eigenspectrum and modeling of resolvent mode shapes.

In what follows, superscript + denotes wall units defined in terms of $\bar{\rho}$ and μ at the wall and the friction velocity u_τ.
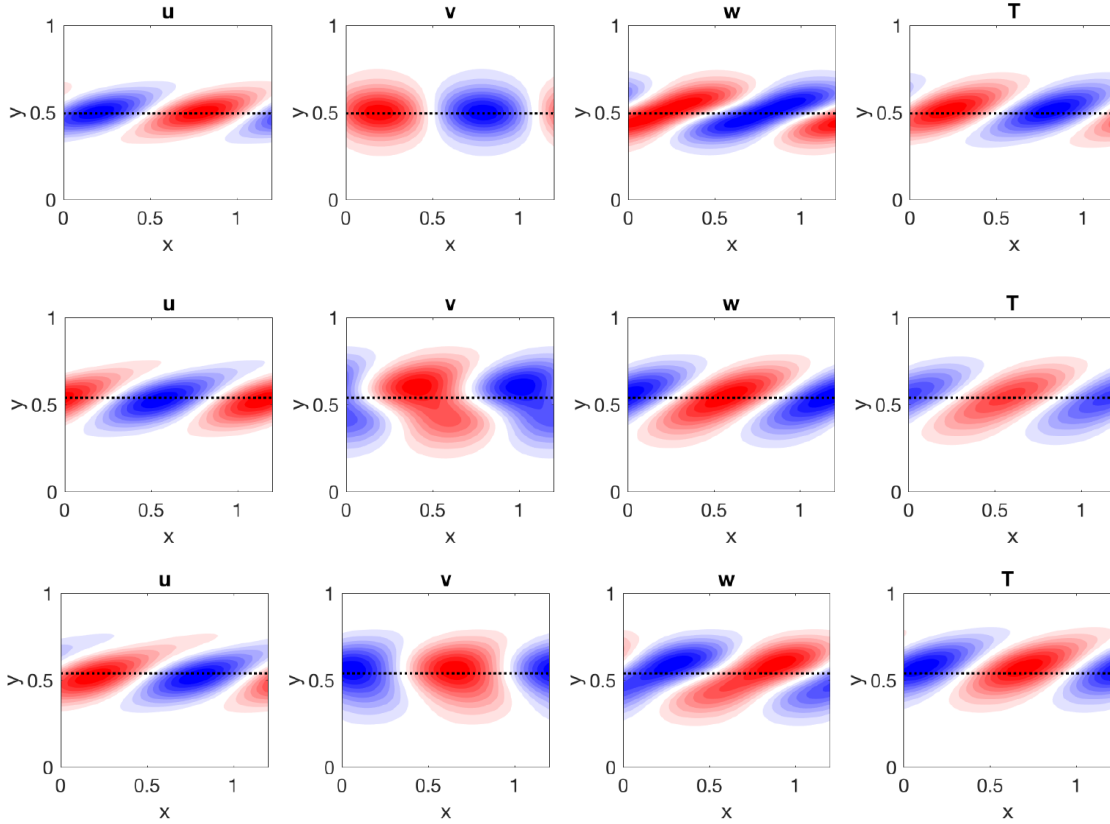
Figure 4: Leading resolvent modes for laminar planar Couette flow (a) $M = 0$, $Re = 1000$, $(\kappa_1, \kappa_3) = (5\pi/3, 10\pi/3)$, $c = 0.5$; (b) $M = 2$, $Re = 2000$, $(\kappa_1, \kappa_3) = (5\pi/3, 10\pi/3)$, $c = 0.5$, Chu norm; (c) $M = 2$, $Re = 2000$, $(\kappa_1, \kappa_3) = (5\pi/3, 10\pi/3)$, $c = 0.5$, kinetic energy pseudonorm. Red and blue represent positive and negative fluctuations about the mean.

4.2 Effect of norm and mean velocity profile

The identification of a suitable norm (inner product) is required to perform an SVD of the resolvent. This is most naturally simply the 2-norm, i.e. the kinetic energy norm, for incompressible flows, but this becomes a semi-norm for the compressible case, and other definitions can be constructed here. Chu [16] introduced a norm that is familiar from compressible stability studies and which eliminates pressure-induced (compression) work:

$$2E = (\boldsymbol{q}, \boldsymbol{q})_E = \|\boldsymbol{q}\|_E^2 = \int_0^\infty \left(\bar{\rho} u_i^\dagger u_i + \frac{\bar{T}}{\gamma \bar{\rho} M^2} \rho^\dagger \rho + \frac{\bar{\rho}}{\gamma(\gamma - 1)\bar{T}M^2} T^\dagger T \right) \mathrm{d}x_2 \tag{5}$$

This norm was adopted and found to give interpretable results for compressible resolvent analysis.

Comparisons between the leading response modes (first singular functions) using the kinetic energy semi-norm for incompressible and compressible Couette flow, and the Chu norm for $M = 2$ are shown in Figure 4. Compressibility has a noticeable effect on the mode shapes shown, but it is clear that some of this can be attributed to the difference in norm applied.

The mean profile used (compressible or incompressible) also has an effect, as shown in Figure 5. The velocity mode amplitude obtained for this flow from the compressible analysis using an incompressible mean profile and semi-norm are almost indistinguishable from their incompressible counterparts [5].
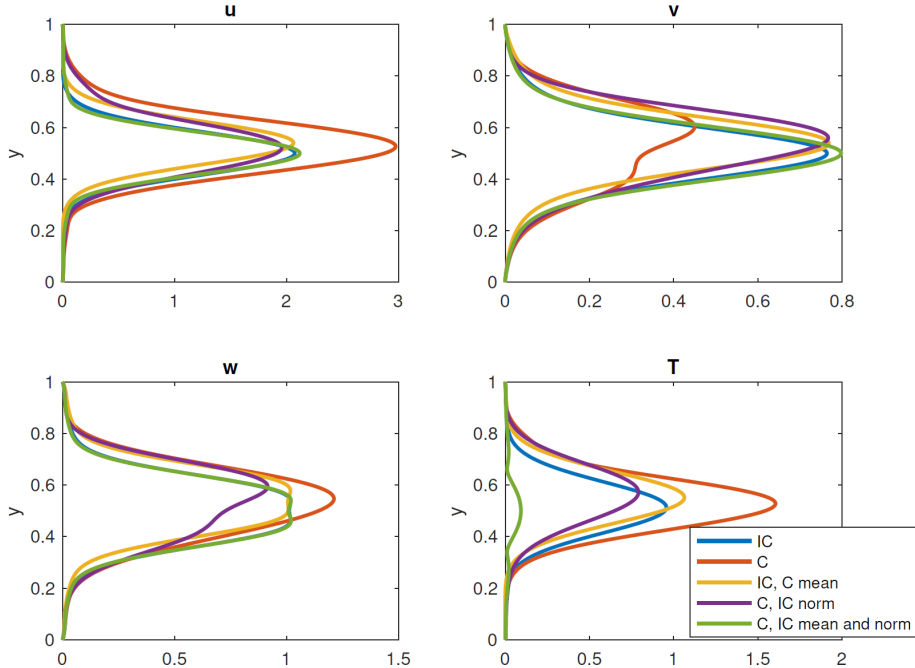
8

Figure 5: Leading resolvent modes amplitudes in planar Couette flow for incompressible (IC in the figure legend), compressible (C, with M=2), incompressible with a compressible mean, compressible with an incompressible (kinetic energy pseudo-norm, and compressible with an incompressible mean and pseud-norm, with $Re = 1000$, $k_x = 5\pi/3$, $k_z = 10\pi/3$, and $c = \omega/k_x = 0.5$.

4.3   Passive scalar modeling

The incompressible resolvent analysis was first extended to account for a passive scalar, i.e. adding a scalar equation which is driven by, but uncoupled from, the momentum and continuity equations. The analysis then provides a scalar mode shape additional to the other state variables, corresponding to the most amplified full state input forcing. The mode shapes were found to be relatively insensitive to the inclusion or weighting of the magnitude of the temperature response in the norm, meaning that the kinetic energy dominates the resolvent in the presence of this kind of scalar and a kinetic energy semi-norm can be used. The passive scalar modeling results are described in [4]; a description of two key results follows.

Examination of the scalar equation led to the identification of self-similar scaling for the scalar response. The scalar equation becomes self-similar for any two conditions and wavenumber triplets which obey

$$\omega_1 Pr_1 = \omega_0 Pr_0, \quad k_{x1} Pr_1 = k_{x0} Pr_0, \quad k_{x1}^2 + k_{z1}^2 = k_{x0}^2 + k_{z0}^2. \tag{6}$$

These results are complementary to the self-similar scalings of the velocity modes that were established by [10].

The resolvent framework can also be used to model single point statistics. In [10], the resolvent framework was used to model energy spectra and densities of streamwise velocity in turbulent channel flow; this approach was extended to model passive scalar statistics in a turbulent boundary layer.

The DNS velocity and temperature profiles were obtained from the zero-pressure-gradient turbulent boundary layer simulations of [17]. The mean profiles and turbulent statistics are computed from data collected at a constant streamwise location, corresponding to a friction Reynolds number of approximately 900. The scalar field has unit Prandtl number, and the dimensionless scalar field has a value of unit at the wall, and zero in the far field. In contrast to the experimental data, here we keep the mean scalar field with an opposite gradient to the mean streamwise velocity.

Following [10], the premulitiplied streamwise energy density of the resolvent model is given by

$$E_{uu}(y; k_x, k_z, c) = k_x^2 k_z \left[\sigma_1(k_x, k_z, c) |u_1(y; k_x, k_z, c)| \right]^2, \tag{7}$$

where σ_1 is the leading singular value, and u_1 is the streamwise component of the leading response mode, and the associated integrated energy density as a function of wall-normal location:

$$E_{uu}(y) = \iiint_{k_x, k_z, c} E_{uu}(y; k_x, k_z, c) d\log(k_x) d\log(k_z) dc. \tag{8}$$

We may similarly define the equivalent quantities for the fluctuating temperature field:

$$E_{TT}(y; k_x, k_z, c) = k_x^2 k_z \left[\sigma_1(k_x, k_z, c) |T_1(y; k_x, k_z, c)| \right]^2 \tag{9}$$

$$E_{TT}(y) = \iiint_{k_x, k_z, c} E_{TT}(y; k_x, k_z, c) d\log(k_x) d\log(k_z) dc, \tag{10}$$

where T_1 is the temperature component of the leading resolvent response mode. We can further consider the cross-correlation between streamwise velocity and temperature:

$$E_{uT}(y; k_x, k_z, c) = k_x^2 k_z \sigma_1(k_x, k_z, c) u_1^*(y; k_x, k_z, c) T_1(y; k_x, k_z, c) \tag{11}$$

$$E_{uT}(y) = \iiint_{k_x, k_z, c} E_{UT}(y; k_x, k_z, c) d\log(k_x) d\log(k_z) dc. \tag{12}$$

It was demonstrated in [10] that introducing an empirical weighting function into the integral in equation 8 can give a quantitatively accurate fit to the equivalent directly measured quantities in numerical simulations. For example, we may introduce a weight function W_{uu} into the integral in equation 8 to give the weighted energy intensity

$$E_{uu,W}(y) = \iiint_{k_x, k_z, c} W_{uu}(c) E_{uu}(y; k_x, k_z, c) d\log(k_x) d\log(k_z) dc. \tag{13}$$

W_{uu} may be computed using a regularized least-squares optimization.

The same methods may be applied to predict the scalar fluctuation energy, as well as the covariance between u and T. The latter is shown in Figure 6. Not only can an accurate prediction be made when directly fitting the corresponding (and similarly defined) weight functions W_{TT} and W_{uT}, but it is further observed that using only W_{uu} also gives estimated statistics that match the main features of the scalar statistics of the DNS data. The fact that the streamwise velocity is typically the dominant component in leading resolvent response modes seems to be part of the underlying reason as to why statistics in this component are easiest to predict using resolvent analysis [10]. The similarity between the streamwise velocity and scalar components of response modes, along with the strong statistical correlation between these fluctuating quantities in turbulent shear flows (e.g. [18]), suggests the utility of the resolvent framework for modeling scalar fluctuations. The results from this grant appear to indicate that this inference is well-founded.

4.4 Semi-analytical mode shope predictions

A methodology for approximating leading resolvent (i.e., pseudospectral) modes for quasi-parallel shear-driven flows using prescribed analytic functions was developed [1]. These functions arise from the consideration of wavepacket pseudoeigenmodes of simplified linear operators [19], and give an accurate approximation of the class of nominally wall-detached modes that are centred about the critical layer.

In essence, the method reduces the space of possible mode shapes from an infinite-dimensional space (which in practice is approximated by a high dimensional space defined by the numerical discretisation) to a two-dimensional family of functions. Once this template function is identified, the optimal shape parameters (which govern the width and phase variation of the mode) may be found as the minimisers of a cost function, which is directly related to the resolvent norm of the underlying operator. In practice, this amounts to finding the roots of a pair of coupled equations, which may be arranged to be polynomials in the shape parameters. In addition, it is possible to derive differential equations in parameter space that govern the evolution of
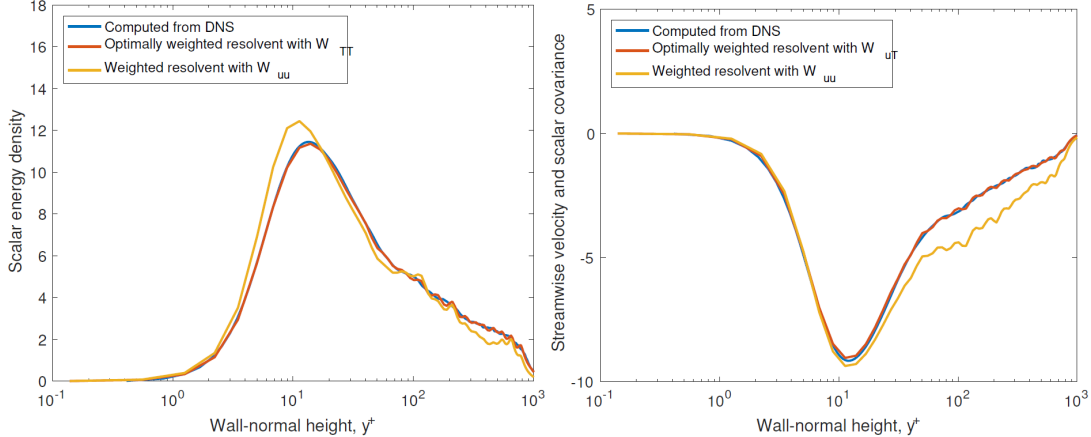
10

Figure 6: Measured and predicted/fitted scalar energy density (left) and and streamwise velocity-scalar covariance (right).

these optimal shape parameters. Using this method, optimal mode shapes may be found by finding the appropriate root of a polynomial. In addition, the variation in mode shape as a function of wavenumber and Reynolds number may be captured by evolving a low dimensional differential equation in parameter space.

This characterisation provides a theoretical framework for understanding the origin of structures observed in turbulent boundary layers, and allows for rapid estimation of dominant resolvent mode characteristics without the need for operator discretisation or large numerical computations. The method remains accurate even when the modes have some amount of "attachment" to the wall, and in particular large-scale and very-large-scale motions, and sheds some additional light onto the classical lift-up and Orr amplification mechanisms in shear-driven flows.

Figure 7 shows the comparison between results for the Squire operator and the full Navier–Stokes system for laminar planar Couette flow. The latter analysis relies on additional simplifications to arrive at a scalar differential operator which has a leading response mode (left singular vector) which approximates the wall-normal vorticity component of the response mode of the Navier–Stokes resolvent operator.

Importantly, this method precludes the need for the formulation and decomposition of discretised linear operators, leading to substantial reduction in computational cost. The extent of the reduction in computational cost is dependent on the size of the discretisation, and on the extent and resolution of the parameter space (e.g., wavenumbers and temporal frequencies) that one wishes to study.

4.5 Compressible turbulent boundary layer

The major portion of the research was devoted to analyzing compressible turbulent boundary layers [2]. Since the properties of the resolvent mode are determine by the mean profiles (for this study of velocity, density and temperature), different transformations were studied to determine whether the self-similarity associated with the incompressible mean velocity could be recovered. The generalized semi-local transformation of Trettel & Larsson [20] was found to give good collapse of the mean velocity profile in the inner (and logarithmic) region over a range of Mach numbers. This transformation is given by

$$x_2^* = \frac{\bar{\rho} \left(\tau_w / \bar{\rho} \right)^{1/2} x_2}{\bar{\mu}}, \tag{14}$$

$$\bar{u}_1^* = \int_0^{\bar{u}_1^+} \left(\frac{\bar{\rho}}{\bar{\rho}_w} \right)^{1/2} \left(1 + \frac{1}{2\bar{\rho}} \frac{\mathrm{d}\bar{\rho}}{\mathrm{d}x_2} x_2 - \frac{1}{\bar{\mu}} \frac{\mathrm{d}\bar{\mu}}{\mathrm{d}x_2} x_2 \right) \mathrm{d}\bar{u}_1^+. \tag{15}$$

Here, the subscript w indicates quantities evaluated at the wall and τ_w is the wall shear stress. The results of this transformation are illustrated in figure 8(a) and (b), and an improved collapse of the mean velocity
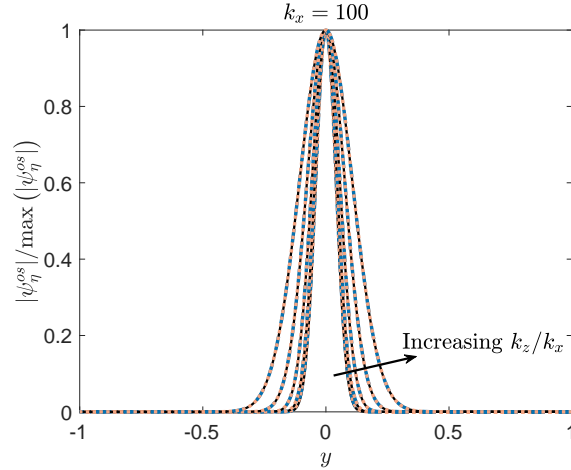
11

Figure 7: Comparison between true (numerically computed, ——) and predicted (·····) mode amplitudes for laminar Couette flow with $Re = 1000$ and $k_x = 100$ and aspect ratios $k_z/k_x \in \{0.5, 1, 2, 4, 8\}$.

profile in the inner and logarithmic region for the various Mach numbers is achieved. This scaling gives rise to a local Reynolds number at each wall-normal location

$$Re_\tau^*(x_2) = \frac{\bar{\rho}(\tau_w/\bar{\rho})^{1/2}\delta}{\bar{\mu}} \tag{16}$$

such that $x_2^* = (x_2/\delta)Re_\tau^*$. While this transformation works well for the inner and logarithmic region, the collapse is not as good for the outer region. We find that best collapse is achieved with the transformation

$$\bar{u}_1^\star = \bar{u}_1^+ \left(\frac{\bar{\rho}}{\bar{\rho}_w}\right)^{1/2}, \tag{17}$$

which is equivalent to scaling the velocity with the semi-local $u_\tau^* = \sqrt{\tau_w/\bar{\rho}}$ instead of $u_\tau = \sqrt{\tau_w/\bar{\rho}_w}$, and the results are given in figure 8(c) and (d). A different transformation for the outer layer is expected, since the transformation given in (15) is based on the idea that the momentum conservation is equivalent to the stress balance condition, which only holds in the inner layer of nearly parallel shear flow at reasonable turbulence Mach numbers. Note that despite the better scaling in the outer region, the collapse is not perfect, which is a known issue for low Reynolds number boundary layer flows. Still, the inner, logarithmic and outer layer all utilise the semi-local scaling to achieve a universal mean velocity profile.

The importance of this transformation to collapse the mean profile to the incompressible result lies in the validity of the scaling results for resolvent mode shapes obtained in our earlier incompressible work, which is explored in detail in [2].

We find that the resolvent operator is low-rank for the supersonic turbulent boundary layer as well as the subsonic one. The energy contribution of $\boldsymbol{\psi}_k$ to the total response subject to broadband forcing in the wall-normal direction can be quantified by $\sigma_k^2/(\sum_j \sigma_j)$. A three-dimensional depiction of the principal energy contribution from the leading response mode $\boldsymbol{\psi}_1$ for the incompressible case and the $M_\infty = 4$ as a function of streamwise and spanwise wavenumbers and wave speeds is given in figure 9.

The results from the incompressible and compressible turbulent boundary layer show similarities in region where the principal energy contribution of the incompressible boundary layer is concentrated and thus low-rank approximation is valid for the incompressible regime. This region coincides with the most energetic wavenumbers from DNS of incompressible channel flows [2]. The most notable difference between the incompressible and compressible results is in the triangular region where the freestream relative Mach number, $\overline{M}_\infty$, is greater than unity. The relative Mach number, defined as

$$\overline{M}(x_2) = \frac{(\kappa_1 \bar{u}_1(x_2) - \omega)M_\infty}{\left(\kappa_1^2 + \kappa_3^2\right)^{1/2} \bar{T}(x_2)^{1/2}}, \tag{18}$$
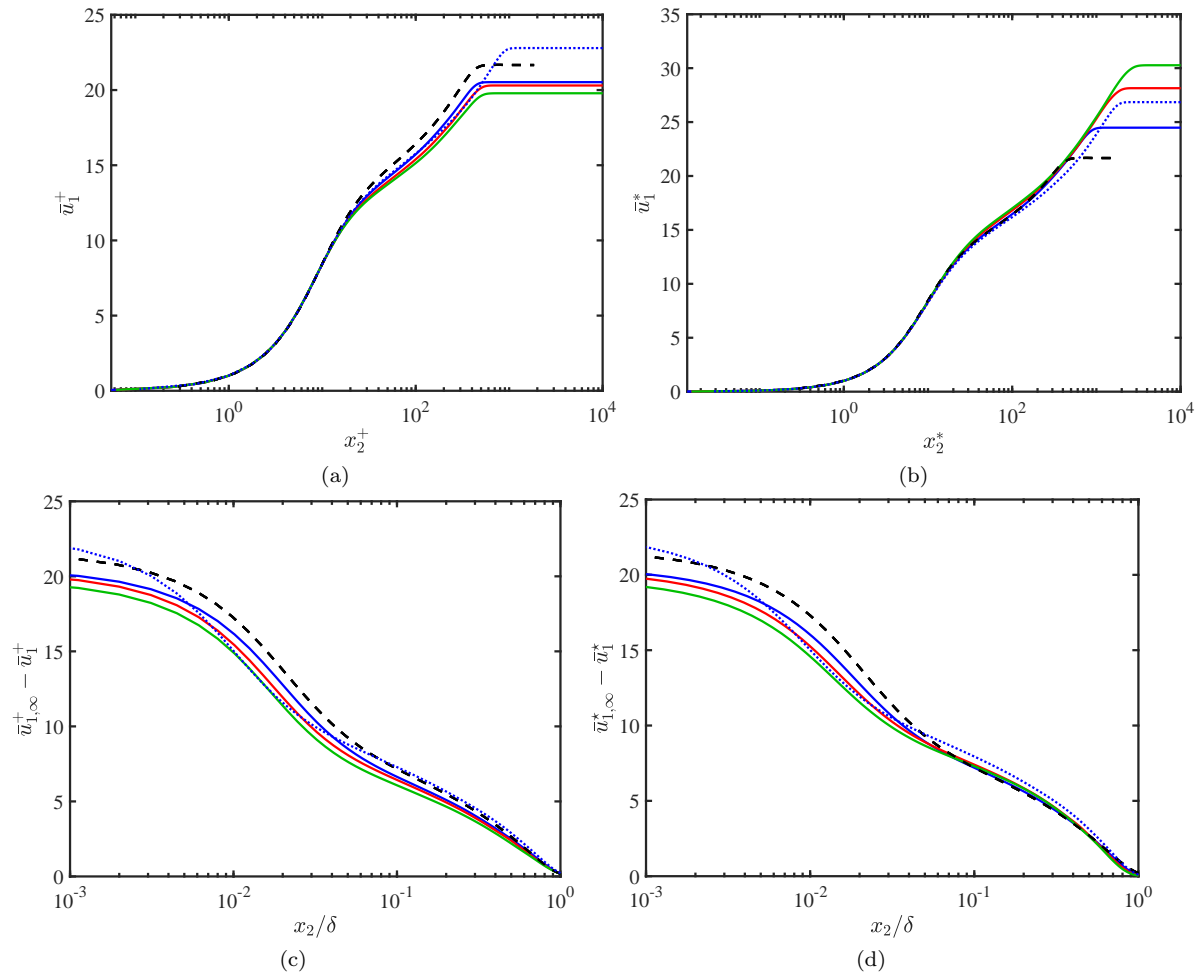
12

Figure 8: (a) Turbulent mean streamwise velocity profile $\bar{u}_1^+(x_2^+)$, (b) the transformed velocity profile $\bar{u}_1^\star(x_2^\star)$ under the Trettel & Larsson scaling [20], (c) the defect velocity $\bar{u}_{1,\infty}^+ - \bar{u}_1^+(x_2/\delta)$ with respect to the freestream, and (d) the transformed defect velocity $\bar{u}_{1,\infty}^\star - \bar{u}_1^\star(x_2/\delta)$. Lines indicate $M_\infty = 0$ (- - -), $M_\infty = 2, Re_\tau = 450$ (——), $M_\infty = 2, Re_\tau = 900$ (·······), $M_\infty = 3$ (——), and $M_\infty = 4$ (——).
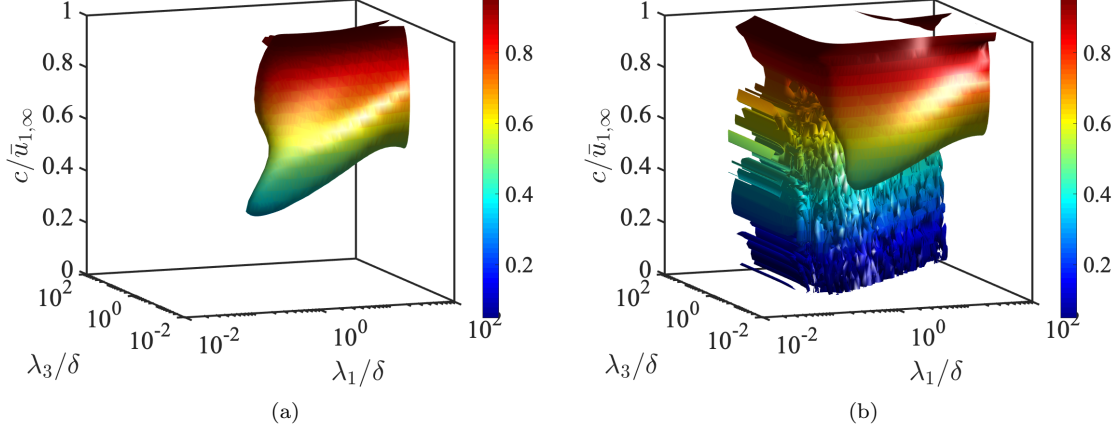
13

Figure 9: Energy contained in the principal response mode relative to the total response, $\sigma_1^2/(\sum_j \sigma_j^2)$, for different streamwise and spanwise wavelengths and wall-normal distance for the (a) incompressible and (b) $M_\infty = 4$ cases. The contour surface is $\sigma_1^2/(\sum_j \sigma_j^2) = 0.75$ coloured by wall-normal distance from the wall.

can be understood as the local Mach number of the mean flow in the direction of the wavenumber vector, $[\kappa_1, \kappa_3]^\dagger$, relative to the wave speed at a given wall-normal location x_2.

The region with $\overline{M}_\infty > 1$, i.e. the relatively supersonic region, increases with Mach number (not shown) and grows from the wall towards the freestream. In linear stability theory, $\overline{M}$ has been used to classify disturbances as subsonic, sonic, or supersonic depending on its value at the boundary layer [15, 9]. Moreover, it has been shown that if $\overline{M} > 1$, a compressible boundary layer is unstable to inviscid waves regardless of any other feature of the velocity and temperature profiles [15]. Considering that the family of modes with $\overline{M} > 1$ does not have any counterpart in incompressible boundary layers, it is expected that the most deviation between the behaviour of the compressible and incompressible boundary layers occurs in this regime. In particular, the irregular low-rank behaviour present in the relatively supersonic region in figure 9(b) is due to the discrete acoustic eigenmodes of the system approaching the wave speed c, thus giving resonant amplification of the resolvent operator [5]. Representative response mode shapes (Figure 10) also reflect the emergence of the acoustic modes.

Due to the orthonormality constraint of the resolvent modes, the comparisons between the compressible and incompressible resolvent modes above are made for for normalised response modes $\widetilde{(q_i)}_1$. However, the distribution of energy among the kinetic and thermodynamic variables for the supersonic cases can also be examined. The ratio of turbulent kinetic energy to the sum of the mean-square density and temperature fluctuations obtained from DNS [13, 14] as a function of x_2 is shown in Figure 11. In particular, we plot

$$\left(\frac{E_T}{E_K}\right)^{\text{DNS}} = \gamma M_\infty^2 \frac{\bar{\rho} u_{i,rms} u_{i,rms}}{\rho_{rms}^2/\bar{\rho}^2 + T_{rms}^2/\bar{T}^2}, \tag{19}$$

where rms denotes the root-mean-squared fluctuations from DNS. For all wall-normal locations, the the ratio increases with Mach number. Moreover, the ratio increases as a function of x_2 for a fixed Mach number. In order to compare the results from the resolvent modes to DNS, we define the energy ratio of the most energetic mode as

$$\left(\frac{E_T}{E_K}\right)^{\text{res}} = \frac{E_T}{E_K}\left(\arg\max_{\kappa_1,\kappa_3} \Phi_{u_1 u_1}(\kappa_1, \kappa_3)\right), \tag{20}$$

where $\Phi_{u_1 u_1}$ is the premultiplied streamwise energy spectra for the channel flow at $Re_\tau = 550$ obtained *a priori* from [21]. The agreement between the ratio of kinetic and thermodynamic energy given by the most energetic principal response mode of the resolvent analysis and the DNS is excellent in the logarithmic region. The discrepancy in the outer region, especially for the higher Mach numbers, may be due to the larger value of Re_τ^* compared to the Re_τ of the premultiplied spectra used to choose the wave parameters for the most energetic modes. In the inner region, the estimated energy ratio plateaus, deviating from the DNS profile.
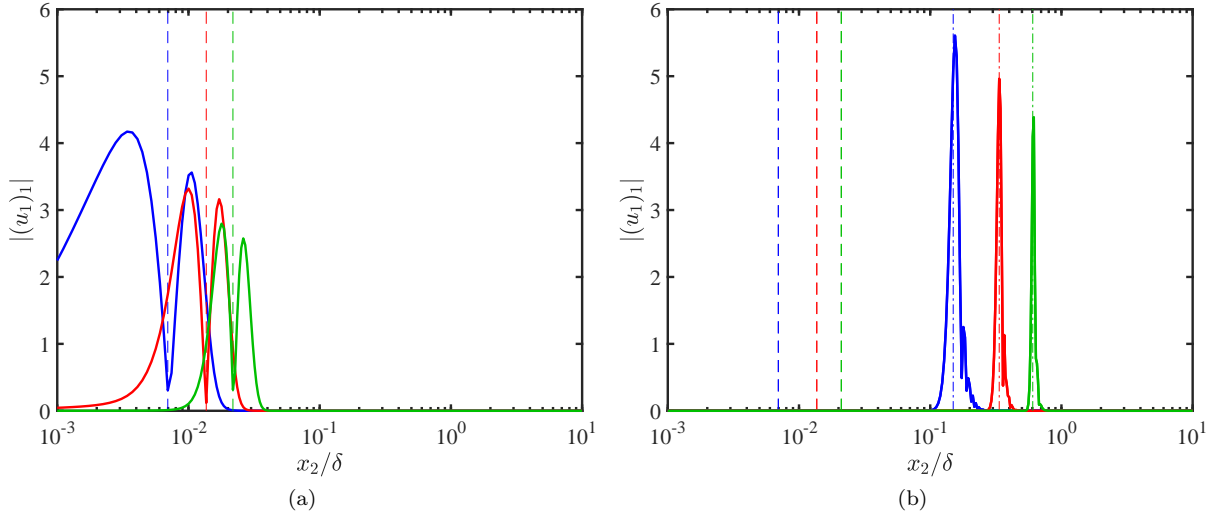
14

Figure 10: The response modes $(u_1)_1$ for the (a) incompressible and (b) supersonic ($M_\infty = 2$, $Re_\tau = 450$) turbulent boundary layer with $\lambda_1/\delta = 0.01$, $\lambda_3/\delta = 10$, and $c = 0.14$ (blue), 0.26 (red), 0.38 (green). Reference lines are $x_2 = x_2^c$ (- - -) and $x_2 = x_2^s$ (-·-·).

This could be due to the increased contributions from relatively supersonic region, which is more prevalent in the near-wall region. Additionally, it has been shown in [22] that the energetic contribution of structures with convection velocities less than $10u_\tau$ is negligible in real turbulent flows, which corresponds to the region where the mismatch is pronounced.

The observation that the correct energy distribution between E_T and E_K can be obtained by considering the most energetic principal response modes in a wide range of wall normal locations is a useful tool in terms of modelling and flow prediction.

4.6 Wall compliance

Our previous work has incorporated a compliant wall boundary condition into the incompressible resolvent analysis [23, 24]. Development of the compressible equivalent was not achieved during the grant period; however experiments were performed in a water tunnel to examine the response of a compliant surface to a forced turbulent boundary layer under AFOSR (FA 9550-16-1-0361) and ONR (N00014-17-1-2960) funding during the same period. The positive comparison between the observed response and the resolvent predictions is sufficient to give confidence in the modeling capability for incompressible flows. However a dedicated analysis for the compressible resolvent analysis with wall parameters that will be relevant for compressible flows in air (which will differ significantly due to the mass ratio between air and most walls) is required to make progress on this topic.
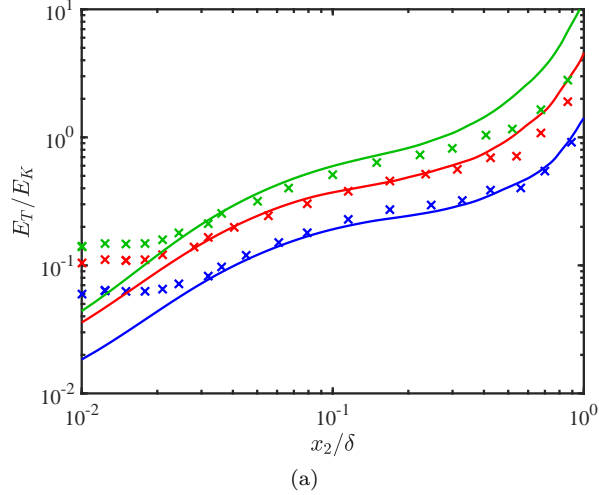
Figure 11: The values of E_T/E_K at the most energetic wave parameters as defined in Equation (20) for the principal resolvent modes ($\times$) and DNS (solid line) for $M_\infty = 2$, $Re_\tau = 450$ (blue), $M_\infty = 3$ (red), and $M_\infty = 4$ (green).

5 Conclusions and Outlook

Resolvent analysis has been used to study the most amplified structures and associated gain characteristics in compressible turbulent boundary layers under a quasi-parallel assumption and with adiabatic walls. Under a semi-local scaling which collapses incompressible and compressible mean velocity profiles, the resolvent reveals the same characteristics across Mach number close to the wall, giving support to Morkovin's hypothesis. For an increasing wall-normal range, which grows from the wall outwards with increasing Mach number and which is determined by the local Mach number of the flow, the presence of acoustic eigenmodes changes the response, leading to localization in the wall-normal direction around the relative sonic line instead of the critical layer. The balance between thermodynamic and kinetic energy in the leading resolvent modes has promising agreement with DNS results.

A semi-analytical approach for predicting mode shapes has been proposed and validated for wall detached modes using pseudo-wavepacket theory. This enables the determination of mode structure without performing an SVD.

Resolvent analysis for an incompressible turbulent boundary layer with passive scalar was also developed and used to predict velocity-temperature covariance statistics using a simple weighting.

The modeling advances developed under this grant offer the potential to lead to significant savings in the prediction of energetic turbulent structures in compressible turbulent boundary layers (relative to full simulations). A full predictive capability would require learning the relative weights (magnitudes and phases) of these structures (mode shapes), which is determined by nonlinear interactions. The focus of this work was on the linear dynamics of compressible flows; study of the nonlinear forcing is reserved for future work. The key conclusion is that the equations of motion support Morkovin's hypothesis over a broad range of conditions as Mach number increases, with the important implication that developments in incompressible flows may be exploited for the compressible regime.

6 References

[1] S. T. M. Dawson and B. J. McKeon. On the shape of resolvent modes in wall-bounded turbulence. *J. Fluid Mech. (to appear)*, 2019.

[2] H. J. Bae, S. T. M. Dawson, and B. J. McKeon. Resolvent-based study of the effects of compressibility on wall turbulence. *(submitted)*, 2019.

[3] T. Saxton-Fox, S. T. M. Dawson, and B. J. McKeon. Modeling passive scalar dynamics and aero-optic distortion in wall-bounded turbulence using resolvent analysis. *(in preparation)*, 2019.

[4] S. T. M. Dawson, T. Saxton-Fox, and B. J. McKeon. Modeling passive scalar dynamics in wall-bounded turbulence using resolvent analysis. *AIAA*, (2018-4042), 2018.

[5] S. T. M. Dawson and B. J. McKeon. Studying the effects of compressibility in planar couette flow using resolvent analysis. *AIAA*, (2019-2139), 2019.

[6] B. J. McKeon and A. S. Sharma. A critical layer model for turbulent pipe flow. *J. Fluid Mech.*, 658:336–382, 2010.

[7] M. P. Martín. Direct numerical simulation of hypersonic turbulent boundary layers. Part 1. Initialization and comparison with experiments. *J. Fluid Mech.*, 570:347–364, 2007.

[8] C. Zhang, L. Duan, and M. M. Choudhari. Direct numerical simulation database for supersonic and hypersonic turbulent boundary layers. *AIAA J.*, 56(11):4297–4311, 2018.

[9] P J Schmid and D S Henningson. *Stability and Transition in Shear Flows*. Springer-Verlag, New York, 2001.

[10] R. Moarref, A. S. Sharma, J. A. Tropp, and B. J. McKeon. Model-based scaling and prediction of the streamwise energy intensity in high-Reynolds number turbulent channels. *J. Fluid Mech.*, 734:275–316, 2013.

[11] K. Taira, S. L. Brunton, S. T. M. Dawson, C. W. Rowley, T. Colonius, B. J. McKeon, O. T. Schmidt, S. Gordeyev, V. Theofilis, and L. S. Ukeiley. Modal analysis of fluid flows: An overview. *AIAA J.*, 55 (12):4013–4041, 2017.

[12] B. J. McKeon. The engine behind (wall) turbulence: Perspectives on scale interactions. *J. Fluid Mech.*, 817:P1, 2017.

[13] M. Bernardini and S. Pirozzoli. Wall pressure fluctuations beneath supersonic turbulent boundary layers. *Phys. Fluids*, 23(8):085102, 2011.

[14] S. Pirozzoli and M. Bernardini. Turbulence in supersonic boundary layers at moderate Reynolds number. *J. Fluid Mech.*, 688:120–168, 2011.

[15] L. M. Mack. Boundary-layer linear stability theory. AGARD Report No. 709, Part 3, NASA Jet Propulsion Laboratory, 1984.

[16] B.-T. Chu. On the energy transfer to small disturbances in fluid flow (Part I). *Acta Mech.*, 1(3):215–234, 1965.

[17] Xiaohua Wu, Parviz Moin, and Jean-Pierre Hickey. Boundary layer bypass transition. *Physics of Fluids*, 26(9):091104, 2014.

[18] John Kim and Parviz Moin. Transport of passive scalars in a turbulent channel flow. In *Turbulent Shear Flows 6*, pages 85–96. Springer, 1989.

[19] L. N. Trefethen. Wave packet pseudomodes of variable coefficient differential operators. In *Proceedings of the Royal Society of London A: Mathematical, Physical and Engineering Sciences*, volume 461, pages 3099–3122. The Royal Society, 2005.

[20] A. Trettel and J. Larsson. Mean velocity scaling for compressible wall turbulence with heat transfer. *Phys. Fluids*, 28(2):026102, 2016.

[21] J. C. del Álamo, J. Jiménez, P. Zandonade, and R. D. Moser. Scaling of the energy spectra of turbulent channels. *J. Fluid Mech.*, 500:135–144, 2004.

[22] J. LeHew, M. Guala, and B. J. McKeon. A study of the three-dimensional spectral energy distribution in a zero pressure gradient turbulent boundary layer. *Expts. in Fluids*, 51(4):997–1012, 2011.

[23] M. Luhar, A. S. Sharma, and B. J. McKeon. A framework for studying the effect of compliant surfaces on wall turbulence. *J. Fluid Mech.*, 768:415–441, 2015.

[24] M. Luhar, A. S. Sharma, and B. J. McKeon. On the design of optimal compliant walls for turbulence control. *J. Turb.*, 17(8):787–806, 2016.

7   Appendices

1. Dawson, S. T. M. & McKeon, B. J. On the shape of resolvent modes in wall-bounded turbulence J. Fluid Mech. (to appear) [1]

2. Bae, H. J., Dawson, S. T. M. & McKeon, B. J. Resolvent-based study of the effects of compressibility on wall turbulence (Under review) [2]

3. Dawson, S. T. M., Saxton-Fox, T. & McKeon, B. J. Modeling passive scalar dynamics in wall-bounded turbulence using resolvent analysis AIAA paper 2018-4042 [4]

4. Dawson, S. T. M. & McKeon, B. J. Studying the effects of compressibility in planar Couette flow using resolvent analysis AIAA paper 2019-2139 [5]

On the shape of resolvent modes in wall-bounded turbulence

Scott T. M. Dawson[1]†, Beverley J. McKeon[1]

[1]Graduate Aerospace Laboratories, California Institute of Technology, Pasadena, CA 91125, USA

The resolvent formulation of the Navier–Stokes equations gives a means for the characterisation and prediction of features of turbulent flows—such as statistics, structures and their nonlinear interactions—using the singular value decomposition of the resolvent operator based on the appropriate turbulent mean, following the framework developed by McKeon & Sharma (2010). This work will describe a methodology for approximating leading resolvent (i.e., pseudospectral) modes for shear-driven turbulent flows using prescribed analytic functions. We will demonstrate that these functions, which arise from the consideration of wavepacket pseudoeigenmodes of simplified linear operators (Trefethen 2005), in particular give an accurate approximation of the class of nominally wall-detached modes that are centred about the critical layer. Focussing in particular on modelling wall-normal vorticity modes, we present a series of simplifications to the governing equations that result in scalar differential operators that are amenable to such analysis. We validate our method on a model operator related to the Squire equation, and show for this simplified case how wavepacket pseudomodes relate to truncated asymptotic expansions of Airy functions. We demonstrate that the leading wall-normal vorticity response mode for the full Navier–Stokes equations may be accurately approximated by considering a second order scalar operator, equipped with a non-standard scalar inner product. Using this method, optimal mode shapes may be found by finding the appropriate root of a polynomial. In addition, the variation in mode shape as a function of wavenumber and Reynolds number may be captured by evolving a low dimensional differential equation in parameter space. This characterisation provides a theoretical framework for understanding the origin of observed structures, and allows for rapid estimation of dominant resolvent mode characteristics without the need for operator discretisation or large numerical computations. We explore regions of validity for this method, and in particular find that it remains accurate even when the modes have some amount of "attachment" to the wall. In particular, we demonstrate that the region of validity contains the regions in parameter space where large-scale and very-large-scale motions typically reside. We relate these findings to classical lift-up and Orr amplification mechanisms in shear-driven flows.

1. Introduction

The identification of pertinent structures that arise in the transition towards, and as coherent features within, turbulent wall-bounded flows has been the focus of much research over the past several decades. Qualitatively, such analysis includes identification and classification of empirically-observed structures, such as near-wall streaks (Kline *et al.*

† Email address for correspondence: sdawson5@iit.edu

1967), hairpin structures (Theodorsen 1952; Head & Bandyopadhyay 1981) and their grouping in large-scale motions (Zhou *et al.* 1999; Guala *et al.* 2006), and very large-scale motions or superstructures (Kim & Adrian 1999; Guala *et al.* 2006; Hutchins & Marusic 2007). For more details concerning the (sometimes debated) properties, taxonomy and dynamics of such structures, see reviews such as Robinson (1991), Smits *et al.* (2011), and Jiménez (2018), and references within.

On a quantitative level, a starting point for the prediction of coherent structure comes from consideration of properties of the governing equations, most typically in linearised form. Features emergent in wall-bounded turbulent flows often bear little resemblance to modes identified from classical stability analysis (Drazin & Reid 2004), where two-dimensional modes are predicted to be the least stable by Squire's theorem, and mean-linearised flows often have only stable eigenvalues (Reynolds & Tiederman 1967; Del Alamo & Jimenez 2006; Cossu *et al.* 2009). Perhaps the most important realisation in the study of such linear operators is the fact that their non-normality can result in high amplification (in either the time or frequency domain), which cannot be predicted from their spectra alone (Böberg & Brösa 1988; Butler & Farrell 1992; Reddy & Henningson 1993; Trefethen *et al.* 1993; Schmid & Henningson 1994; McKeon & Sharma 2010; Bamieh & Dahleh 2001; Jovanović & Bamieh 2005; Schmid 2007; Hwang & Cossu 2010; Schmid & Henningson 2012). Operator nonnormality is responsible for both finite-time energy growth of the linear system from a from a given initial condition, and the amplification resulting from continual forcing (be it stochastic or harmonic). Indeed, these two notions are mathematically related via the Kriess constant of the operator (Schmid 2007).

While most initial works considered laminar base flows (with one notable exception being Farrell & Ioannou (1993), who considered mean-linearised equations using stochastic forcing), more recent developments have used similar methods for prediction of turbulent features by linearizing about states computed from turbulent data and/or models (which is most often a mean state). For example, Del Alamo & Jimenez (2006) and Cossu *et al.* (2009) have demonstrated transient growth of near wall-streaks and large scale motions for turbulent channel and zero-pressure-gradient boundary layers respectively, while Schoppa & Hussain (2002) has showed that a turbulent mean with the addition of low-speed streaks can give rise to the growth of structures in the near-wall region of turbulent channel flow.

The characterisation of the nonlinear Navier–Stokes equations in the frequency domain as the linear resolvent operator acting on the nonlinear "forcing" terms, as developed by McKeon & Sharma (2010) has been particularly fruitful for elucidating operator-based predictions of structure in wall-bounded turbulence, including very large scale motions and their scaling (McKeon & Sharma 2010), and hairpin structures (Sharma & McKeon 2013). McKeon (2017) summarizes further developments in this area. Note that this approach has also been applied in other contexts, such as in the study of cavity (Gómez *et al.* 2016; Qadri & Schmid 2017), airfoil (Yeh & Taira 2018), and jet (Garnaud *et al.* 2013; Jeun *et al.* 2016; Towne *et al.* 2018; Schmidt *et al.* 2018) flows.

While such developments are recent and ongoing, many of the underlying physical mechanisms in shear flows have been understood for at least several decades. These include the Orr mechanism (Orr 1907; Jiménez 2013), which amplifies upstream-leaning disturbances while tilting them towards the downstream direction, and the lift-up mechanism (Landahl 1980, 1975), in which wall-normal disturbances lead to large streamwise responses. Streamwise inhomogeneity provides an additional mechanism for amplification of disturbances (Chomaz 2005; Hack & Moin 2017), which, as with the Orr and lift-up

mechanisms, arises through different aspects of non normality of the underlying linear operator (Symon *et al.* 2018).

Recent results concerning the pseudospectral properties of certain matrices (Trefethen & Chapman 2004) and linear differential operators by (Trefethen 2005) have revealed criteria by which pseudomodes exist that are localised in both space and spatial frequency, and are highly amplified by the associated resolvent operator. This method of analysis has been used, for example, in the analysis of swept wing flow by Obrist & Schmid (2010, 2011).

An alternative route to quantitatively define coherent structure in turbulent flows is to consider data collected from simulations or experiments. The proper orthogonal decomposition (Lumley 1967), which computes spatial modes of highest energy in a dataset, is perhaps the most ubiquitous such method. The original formulation computes a set of energetically optimal modes for each temporal frequency. This method was recently shown by Towne *et al.* (2018) to give modes equivalent to resolvent response modes, under the assumption that the true forcing to the system, arising from the nonlinear term in the Navier–Stokes equations, results in uncorrelated resolvent response mode expansion coefficients. Note that quantitatively correct prediction of characteristics of wall-bounded turbulence using resolvent-based approaches can be improved by considering the properties of the nonlinear forcing terms, which are dependent on second order turbulence statistics (Zare *et al.* 2017). Connections may also be made between resolvent analysis and the dynamic mode decomposition (Schmid & Sesterhenn 2008; Schmid 2010; Rowley *et al.* 2009), which computes spatial modes from the eigendecomposition of an linear operator that best matches the evolution of the data between adjacent snapshots, as described in Sharma *et al.* (2016) and Towne *et al.* (2018). A widely used POD variant computes modes without filtering into temporal frequencies, which gives a basis that can be used to project the Navier–Stokes equations onto to obtain a reduced-order model (Berkooz *et al.* 1993; Holmes *et al.* 2012). Note in particular that this has been used to describe the dynamics of coherent structures in wall-bounded turbulent flows, such as those associated with the near-wall cycle (Aubry *et al.* 1988). Reviews of modal decomposition techniques, and their use in reduced-order modelling, may be found respectively in Taira *et al.* (2017) and Rowley & Dawson (2017).

With the exception of very simple systems, the identification of mode shapes typically requires resorting to numerical methods, applied either to the discretised (and most-often linearised) governing equations, or to data collected from experiments or numerical simulations of their evolution. In this work, we describe methods to approximate mode shapes and amplification mechanisms without requiring the formation of discretised operators, for shear flows with arbitrary mean velocity profiles. In section 2, we provide a review of the mathematical concepts that underpin our analysis. Section 3 presents the formulation and sample results for resolvent analysis of a turbulent boundary layer, and presents a sequence of simplifications to the governing equations that retain the correct features of the leading resolvent response mode. In Section 4, we detail a procedure for estimating mode shapes by solving an optimisation problem using a prescribed template function, which may be derived either from approximations to exact solutions of the given operator, or from the wavepacket pseudomode theory introduced in section 2.

2. Mathematical preliminaries: The resolvent and pseudospectra of a linearised operator

This section presents material on the pseudospectral analysis of a mean-linearised system, which will provide background for the analysis in later sections. Section 2.1 intro-

duces the resolvent formulation of a nonlinear system. The singular value decomposition of the resolvent and its connection with pseudospectra is discussed in Section 2.2. Section 2.3 discusses the underlying theory behind the existence of wavepacket pseudospectral modes, which will be related to our subsequent analysis.

2.1. *The resolvent form of a nonlinear dynamical system*

We begin by considering a nonlinear dynamical system

$$\dot{\boldsymbol{u}} = \mathbf{g}(\boldsymbol{u}). \tag{2.1}$$

Let $\boldsymbol{u}_0$ denote the temporal mean of the state of the system, where we are assuming that the dynamics are statistically stationary. Expressing the system state as $\boldsymbol{u}(t) = \boldsymbol{u}_0 + \boldsymbol{u}'(t)$, we may rewrite equation 2.1 as

$$\dot{\boldsymbol{u}}' = \mathbf{g}(\boldsymbol{u}_0 + \boldsymbol{u}') = \left.\frac{\partial \mathbf{g}}{\partial \boldsymbol{u}}\right|_{\boldsymbol{u}_0} \boldsymbol{u}' + \boldsymbol{f}(\boldsymbol{u}), \tag{2.2}$$

where we have linearised about the mean state, but retained the full dynamics of the system with the remaining nonlinear dynamics $\boldsymbol{f}(\boldsymbol{u})$. Taking a Fourier transform in time, equation 2.2 may be expressed as

$$\left(-i\omega - \left.\frac{\partial \mathbf{g}}{\partial \boldsymbol{u}}\right|_{\boldsymbol{u}_0}\right)\hat{\boldsymbol{u}}' = \widehat{\boldsymbol{f}(\boldsymbol{u})},$$

where $\hat{\cdot}$ denotes a Fourier-transformed function. The mean-subtracted state of the system may then be expressed by

$$\hat{\boldsymbol{u}}' = \left(-i\omega - \left.\frac{\partial \mathbf{g}}{\partial \boldsymbol{u}}\right|_{\boldsymbol{u}_0}\right)^{-1} \widehat{\boldsymbol{f}(\boldsymbol{u}')} = \mathcal{H}_\omega \widehat{\boldsymbol{f}(\boldsymbol{u}')}, \tag{2.3}$$

where we refer to $\mathcal{H}_\omega$ as the associated resolvent operator for this system for a given frequency ω, where we are assuming here that this inverse exists (i.e., that $i\omega$ is not an eigenvalue of $\left.\frac{\partial \mathbf{g}}{\partial \boldsymbol{u}}\right|_{\boldsymbol{u}_0}$). It is important to note that we have not made any approximations to the nonlinear system at this point, and have only made the assumption that the system is statistically stationary in time with a well-defined mean.

2.2. *The singular value decomposition of the resolvent operator*

From equation 2.3, the properties of the mean-subtracted state $\boldsymbol{u}'$ will depend both on the nature of the nonlinear term $\hat{\boldsymbol{f}}$, and the properties of the linear operator $\mathcal{H}_\omega = (-i\omega + \mathcal{L})^{-1}$, where following on from section 2.1, we let $\mathcal{L} = -\left.\frac{\partial \mathbf{g}}{\partial \boldsymbol{u}}\right|_{\boldsymbol{u}_0}$. In particular, if $\mathcal{H}_\omega$ amplifies a small number of directions, or "modes" to a much larger degree than all others, then so long as these directions are excited to some extent by $\hat{\boldsymbol{f}}$, this can allow prediction of the dominant features of $\boldsymbol{u}'$ by studying only $\mathcal{H}_\omega$.

More precisely, we consider the singular value decomposition of the resolvent operator

$$\mathcal{H}_\omega = \sum_{j=1}^\infty \sigma_j \psi_j \phi_j^*, \tag{2.4}$$

with $\sigma_k > \sigma_{k+1}$ for all k. For the remainder of this work, we will consider $\mathcal{H}_\omega$ to be a discretised operator, with a corresponding singular value decomposition (SVD) defined in the same manner as 2.4, but with a finite sum of modes. The SVD of a linear operator

requires the definition of an inner product (or more precisely, inner products on both the input and output spaces), which prescribes how the adjoint is prescribed and computed (and also induces the norms used in defining various properties of the SVD). For discrete operators, we may characterise an inner product by a positive definite weighting matrix $\boldsymbol{M}$ for which

$$\langle \boldsymbol{x}_1, \boldsymbol{x}_2 \rangle = \boldsymbol{x}_1^{\bar{T}} \boldsymbol{M} \boldsymbol{x}_2, \tag{2.5}$$

where $\cdot^{\bar{T}}$ denotes the conjugate transpose. If $\boldsymbol{M}$ characterises the inner product on the spaces containing both the forcing and response functions of a finite-dimensional linear operator $\boldsymbol{L}$ (which we consider the discretisation of a linear operator $\mathcal{L}$), the adjoint $\boldsymbol{L}^*$ satisfies $\langle \boldsymbol{L} \boldsymbol{x}_1, \boldsymbol{x}_2 \rangle = \langle \boldsymbol{x}_1, \boldsymbol{L}^* \boldsymbol{x}_2 \rangle$, from which one may show that $\boldsymbol{L}^* = \boldsymbol{M}^{-1} \boldsymbol{L}^T \boldsymbol{M}$. Throughout this paper we will largely work with (infinite-dimensional) operators acting on a continuous domain, with the understanding that numerical computation of the SVD is performed on a finite-dimensional discrete approximation.

For some aspects of this work, it will be convenient to think of the leading singular values and vectors of $\mathcal{H}_\omega$ as defined in the following manner:

$$\sigma_1 = \max_{\|\phi\|=1} \|\mathcal{H}_\omega \phi\| := \|\mathcal{H}_\omega\|, \tag{2.6}$$

$$\psi_1 = \operatorname*{argmax}_{\psi:\ \|\psi\|=1} \|\mathcal{H}_\omega^* \psi\|, \tag{2.7}$$

$$\phi_1 = \operatorname*{argmax}_{\phi:\ \|\phi\|=1} \|\mathcal{H}_\omega \phi\|, \tag{2.8}$$

where here and throughout we use the spectral norm when taking the norm of an operator. Note that we also have the relationship $\psi_1 = \sigma_1^{-1} \mathcal{H}_\omega \phi_1$, which may also be rearranged as $\phi_1 = \sigma_1 \mathcal{H}_\omega^{-1} \psi_1$. In other words, ϕ_1 gives the shape of the forcing which gives rise to the largest amplification (a factor of σ_1) upon the application of the operator $\mathcal{H}_\omega$, the result of which is the (scaled by σ_1) response mode ψ_1. It will also be useful to recognise that these singular values and vectors are related to the smallest singular values and vectors of $\mathcal{H}_\omega^{-1} = (-i\omega + \mathcal{L})$, by

$$\sigma_1 = \left(\min_{\|\psi\|=1} \|\mathcal{H}_\omega^{-1} \psi\| \right)^{-1}, \tag{2.9}$$

$$\psi_1 = \operatorname*{argmin}_{\psi:\ \|\psi\|=1} \|\mathcal{H}_\omega^{-1} \psi\|, \tag{2.10}$$

$$\phi_1 = \operatorname*{argmin}_{\phi:\ \|\phi\|=1} \|\left(\mathcal{H}_\omega^{-1}\right)^* \phi\|. \tag{2.11}$$

In this work, we will make use of these definitions, that allow us to define leading singular values and vectors as solutions to an optimisation problem. Roughly speaking, we will search for analytic functions that become as small as possible upon the action of $(-i\omega + \mathcal{L}) = \mathcal{H}_\omega^{-1}$, and reason from equation 2.10 they will be close approximations to leading resolvent response modes.

These ideas may be formalised as follows. For a linear operator $\mathcal{L}$ and some $\epsilon > 0$, define the ϵ-pseudospectrum as a set $\Lambda_\epsilon(\mathcal{L}) \subset \mathbb{C}$ satisfying

$$\Lambda_\epsilon(\mathcal{L}) = \{z : (\mathcal{L} + \mathcal{E})\boldsymbol{u} = z\boldsymbol{u}, \text{ for some } \boldsymbol{u} \text{ and } \mathcal{E}, \text{ with } \|\mathcal{E}\| \leqslant \epsilon\}. \tag{2.12}$$

Here $\mathcal{E}$ is an operator mapping between the same spaces as $\mathcal{L}$. Note in particular that we have the equivalent definition of pseudospectra based on the norm of the resolvent:

$$z \in \Lambda_\epsilon(\mathcal{L}) \backslash \Lambda(\mathcal{L}) \iff \|(-z + \mathcal{L})^{-1}\| \geqslant \epsilon^{-1},$$

where here the $\backslash$ operator refers to set exclusion. In particular, for any $z \in \mathbb{C}$, $\epsilon_z =$

$\min\{\epsilon : z \in \Lambda_\epsilon(\mathcal{L})\} = \sigma_1^{-1}(z)$, where $\sigma_1(z)$ is the largest singular value of $(-z + \mathcal{L})^{-1}$. Furthermore, the corresponding pseudoeigenvector $\boldsymbol{u}$ satisfying $(\mathcal{L} + \mathcal{E})\boldsymbol{u} = z\boldsymbol{u}$, for some $\mathcal{E}$ with $\|\mathcal{E}\| = \epsilon_z$ is the left singular vector of $(-z + \mathcal{L})^{-1}$ corresponding to $\sigma_1(z)$. Note that the presence of the operator norm in the definition means that, unlike when looking at the spectrum, the definition of pseudospectra requires that we work in a vector space equipped with a norm, which the ϵ-pseudospectrum associated with an operator is dependent upon.

2.3. *Conditions for the existence of wavepacket resolvent modes*

Here we briefly describe the conditions under which a linear differential operator permits wavepacket pseudomodes corresponding to small ϵ (or equivalently, large resolvent norm). More complete description of this phenomenon, as well as the related proofs, may be found in Trefethen & Embree (2005) and Trefethen (2005). For some (small) parameter $h > 0$, we may define a family of scaled differential operators

$$\mathcal{D}_h^j = (ih)^j \frac{d^j}{(dy)^j}, \tag{2.13}$$

which we assume to act on a closed finite interval. We may then assemble any arbitrary n-th order differential operator $\mathcal{L}_h$ acting on a scalar variable $u(y)$ by

$$(\mathcal{L}_h u)(y) = \sum_{j=0}^{n} c_j(y) \mathcal{D}_h^j u(y). \tag{2.14}$$

Defining a test function $v_h(y) = \exp(-iky/h)$ for a complex scalar k, we have

$$(\mathcal{L}_h v_h)(y) = \sum_{j=0}^{n} c_j(y) k^j v_h(y) = f(y, k) v_h(y), \tag{2.15}$$

where we refer to $f(y, k)$ as the symbol corresponding to the family of differential operators $\mathcal{L}_h$. We will consider potential pseudoeigenvalues $\lambda = f(y_*, k_*)$. The symbol $f(y, k)$ is said to satisfy the twist condition for real k if we have

$$\text{Im}\left(\frac{\partial_y f}{\partial_k f}\right) > 0. \tag{2.16}$$

When the twist condition is satisfied for some (y_*, k_*), one it can be a pseudomode $\psi(y; y_*, k_*)$ (of unit norm) that has phase variation matching v_h close to y_*, satisfying both

$$\|(-\lambda + \mathcal{L}_h)\psi(y; y_*, k_*)\| \leqslant M^{-1/h} \tag{2.17}$$

for some $M > 1$, and also that

$$\frac{|\psi(y; y_*, k_*)|}{\max |\psi(y; y_*, k_*)|} \leqslant C \exp\left(-b(y - y_*)^2/h\right), \tag{2.18}$$

for some $b, C > 0$. In other words, we have modes that are spatially localised near y_*, have localised spatial frequency k_*, and are "asymptotically good" pseudoeigenfuctions. Note that the region of $\mathbb{C}$ where the twist condition is satisfied is independent of the choice of norm. Note also that this theory developed in Trefethen (2005) builds upon earlier observations of certain classes of equations by Davies (1999a,b). More generally, these ideas are closely related to classical WKBJ expansions, which have also been utilised recently by Leonard (2016) in the context of studying approximate inviscid solutions for channel flow.

In this work, using these ideas as justification and inspiration, for a given temporal frequency (where $\lambda = i\omega$), we will assume that the leading resolvent response mode may be closely approximated by a function that is localised in the wall-normal direction, both spatially (as for functions satisfying equation 2.18) and in the frequency domain (as is the case for the test functions v_h). When this assumption is justified, it allows for a reformulation of resolvent analysis in terms of finding the spatial width and frequency of a template function ψ that minimises $\|(-\lambda + \mathcal{L})\psi\|$, and thus are close to the true leading resolvent response mode (from equation 2.10).

3. The behaviour of leading resolvent modes in wall-bounded turbulence

This section will apply the concepts introduced in section 2 to explore methods by which the shape of resolvent modes may be approximated. In this section and elsewhere, we will largely focus on a boundary layer configuration, which is assumed to be approximately homogeneous in the streamwise direction (as well as being homogeneous in the spanwise direction), though the analysis holds for any (approximately) parallel shear-driven turbulent flow.

In section 3.1 we introduce a resolvent formulation of the Navier–Stokes equations. The setup is similar to that developed in McKeon & Sharma (2010), though following more closely the formulation used in Rosenberg & McKeon (2018). Following this, in section 3.2 we will present a sequence of simplifications to the governing equations, that will render them amenable to application of wavepacket pseudomode theory. We will additionally present some sample results to motivate these developments, as well as those later presented in section 4.

3.1. *A resolvent formulation of the Navier–Stokes equations*

We will restrict attention to flows which are (approximately) homogenous in the streamwise (x) and spanwise (z) directions, with a mean streamwise velocity $(u, v, w) = (U, 0, 0)$ that varies in the wall normal (y) direction. We will consider the incompressible Navier–Stokes equations in (wall-normal) velocity-vorticity form, and will take Fourier transforms in the streamwise and spanwise directions, with wavenumbers given by k_x and k_z. Applying the procedure detailed in section 2.1 gives

$$\begin{pmatrix} \hat{v} \\ \hat{\eta} \end{pmatrix} = \underbrace{\begin{pmatrix} -i\omega + \Delta^{-1}\mathcal{L}_{os} & 0 \\ ik_z U_y & -i\omega + \mathcal{L}_{sq} \end{pmatrix}^{-1}}_{\mathcal{H}_{\boldsymbol{k}}} \begin{pmatrix} \hat{f}_v \\ \hat{f}_\eta \end{pmatrix}. \tag{3.1}$$

where $\hat{v}$ and $\hat{\eta} = ik_z\hat{u} - ik_x\hat{w}$ are the Fourier-transformed wall-normal velocity and vorticity fields, U_y is the wall-normal gradient of the streamwise velocity, and the Laplacian $\Delta = \partial_{yy} - k_\perp^2$, with $k_\perp^2 = k_x^2 + k_z^2$. The Orr-Sommerfeld (OS) and Squire (SQ) operators are given respectively by

$$\mathcal{L}_{os} = ik_x U\Delta - ik_x U_{yy} - \frac{1}{Re}\Delta^2, \tag{3.2}$$

$$\mathcal{L}_{sq} = ik_x U - \frac{1}{Re}\Delta. \tag{3.3}$$

Further details concerning the equivalence of this formulation to one using primitive variables (in particular the implicit restriction of the forcing to the solenoidal component) is given in Rosenberg & McKeon (2018). The resolvent operator $\mathcal{H}_{\boldsymbol{k}}$ is now parametrised by the spatiotemporal wavevector $\boldsymbol{k} = (\omega, k_x, k_z)$.

The SVD of the resolvent operator is computed using an inner product that is proportional to kinetic energy for a given set of spatial wavenumbers (Gustavsson 1986; Butler & Farrell 1992), defined by

$$\langle (\hat{v}_1, \hat{\eta}_1), (\hat{v}_2, \hat{\eta}_2) \rangle = \frac{1}{k^2} \int_y \left(-\bar{\hat{v}}_1 \Delta \hat{v}_2 + \bar{\hat{\eta}}_1 \hat{\eta}_2 \right) dy, \tag{3.4}$$

where the overbar denotes complex conjugation.

In later sections, we will consider the following two scalar inner products arising from the components of 3.4:

$$\langle \hat{z}_1, \hat{z}_2 \rangle = \frac{1}{k_\perp^2} \int_y \bar{\hat{z}}_1 \hat{z}_2 dy, \tag{3.5}$$

$$\langle \hat{z}_1, \hat{z}_2 \rangle_\Delta = -\frac{1}{k_\perp^2} \int_y \bar{\hat{z}}_1 \Delta \hat{z}_2 dy. \tag{3.6}$$

That is to say, when considering scalar operators, we will assume that the inner product is the "standard" one unless using a Δ-subscript. We will also refer to $\langle \cdot, \cdot \rangle_\Delta$ as the Laplacian inner product.

We will now present some sample results that will motivate many of the developments in the remainder of this paper. We consider a turbulent boundary layer with friction Reynolds number $Re_\tau = 900$. Mean velocity profiles are obtained from the DNS data of Wu *et al.* (2017), by averaging data at a single streamwise location. Figure 1 shows leading resolvent response mode shapes for this system. The wavenumbers $k_x = \pi/2$, and $k_z = 2\pi$ and wavespeed ($c = 0.8U_\infty$) have been chosen to be consistent with the typical size of large-scale motions in zero-pressure-gradient boundary layers (e.g., Monty *et al.* (2009); Kovasznay *et al.* (1970); Cantwell (1981); Saxton-Fox & McKeon (2017)). Here and throughout, the resolvent operator is discretised using a Chebyshev collocation method, utilising the toolbox of Weideman & Reddy (2000).

We observe that the mode is dominated by the wall-normal vorticity component, which is centred on and localised around the critical layer, and has an approximately linear variation in phase within this region. These observations, which are typical of modes that are "detached" from the wall, suggests that this numerically computed mode resembles a wavepacket mode as described in section 2.3. Here and throughout, we consider a mode to be detached from the wall if its shape is not substantially effected by the wall's presence. In section 4 we will seek to predict the shape of this mode without explicitly computing an SVD (or indeed, without explicitly forming a discretised resolvent operator). Making this procedure tractable, however, will require simplification of the governing equations, which are described in section 3.2.

3.2. *Simplifications to the Navier–Stokes operator for resolvent mode approximation*

Following Rosenberg & McKeon (2018), rather than studying the full system we may start by separating the resolvent modes into those being forced by f_v and f_η separately. In particular, defining scalar resolvent operators

$$\mathcal{H}_{vv} = (-i\omega + \Delta^{-1}\mathcal{L}_{os})^{-1}, \tag{3.7}$$

$$\mathcal{H}_{\eta\eta} = (-i\omega + \mathcal{L}_{sq})^{-1}, \tag{3.8}$$
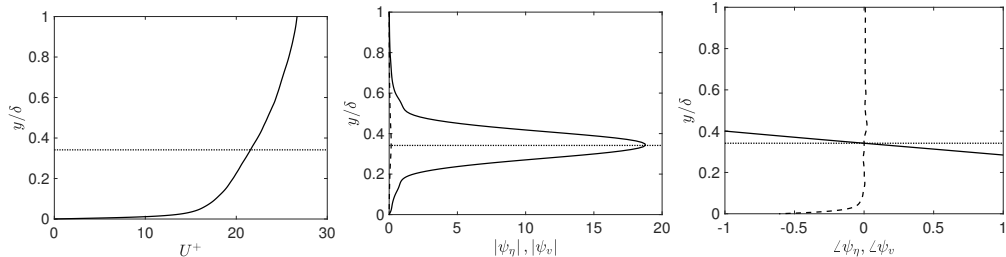
FIGURE 1. (a) Mean velocity profile for a turbulent boundary layer at $Re_\tau = 900$ ($-$) and critical layer location corresponding to a wavespeed $c = 0.8U_\infty$ ($\cdot\cdot$). (b) Amplitude and (c) phase of wall normal velocity ($-\cdot$) and vorticity (-) for leading resolvent response modes with $k_x = \pi/2$, $k_z = 2\pi$ and $c = 0.8U_\infty$.

the Orr-Sommerfeld (OS) and Squire (SQ) modes may be computed by taking SVD's of the reduced resolvent operators given as

$$\begin{pmatrix} \hat{v} \\ \hat{\eta}_{os} \end{pmatrix} = \underbrace{\begin{pmatrix} \mathcal{H}_{vv} & 0 \\ ik_z \mathcal{H}_{\eta\eta} U_y \mathcal{H}_{vv} & 0 \end{pmatrix}}_{\mathcal{H}_{os,\boldsymbol{k}}} \begin{pmatrix} \hat{g}_v \\ 0 \end{pmatrix}, \tag{3.9}$$

$$\begin{pmatrix} 0 \\ \hat{\eta}_{sq} \end{pmatrix} = \underbrace{\begin{pmatrix} 0 & 0 \\ 0 & \mathcal{H}_{\eta\eta} \end{pmatrix}}_{\mathcal{H}_{sq,\boldsymbol{k}}} \begin{pmatrix} 0 \\ \hat{g}_\eta \end{pmatrix}. \tag{3.10}$$

While the modes computed from different subsystems are no longer orthogonal, Rosenberg & McKeon (2018) demonstrated they can provide a basis that better captures dynamical features of the system. Our interest in this decomposition is primarily concerned with using this decomposition to simplify the required analysis. Figure 2 shows the η-component of the response modes of the OS and SQ subsystems for the same parameters considered in figure 1. We observe in particular that the OS operator gives the same mode shape as the full system, with the SQ mode also sharing the same qualitative characteristics. This suggests that the ability to predict and understand the shape of the vorticity response of the full system can be reduced to studying only the OS subsystem.

In order to make the ensuing analysis more tractable, we will require additional simplifications. Note first that the components of the OS and SQ sub-operators may be written in scalar form as

$$\hat{v} = H_{vv}\hat{g}_v \tag{3.11}$$

$$\hat{\eta}_{os} = \mathcal{H}_{\eta v}\hat{g}_v, \tag{3.12}$$

$$\hat{\eta}_{sq} = \mathcal{H}_{\eta\eta}\hat{g}_\eta, \tag{3.13}$$

where $\mathcal{H}_{\eta v} = (ik_z \mathcal{H}_{\eta\eta} U_y \mathcal{H}_{vv})$ is the off-diagonal term in $\mathcal{H}_{os,\boldsymbol{k}}$ in equation 3.9.

When considering the SVD of these subsystems, it is important that we use the appropriate inner product on both the input and output spaces. Since the response is energetically dominated by wall-normal vorticity, it is reasonable that a close approximation to the η response of the full system (which itself is approximated by the OS response) can be obtained just by considering the scalar operator in equation 3.12. Figure 3 shows that this assumption is indeed valid for the sample parameters considered in this section. As well as simplifying the analysis, reducing the full resolvent operator to a scalar operator brings us closer to being able to apply the wavepacket pseudomode theory discussed in
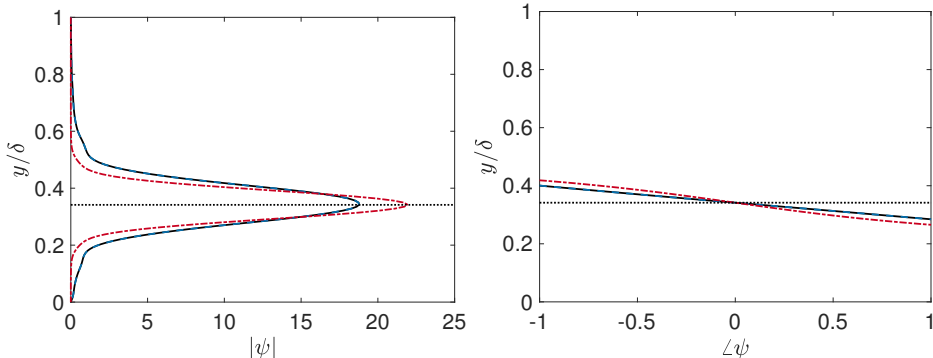
FIGURE 2. (a) Amplitude and (b) phase of wall normal vorticity response mode computed from full system $(-)$, SQ subsystem $(-\cdot)$, and OS subsystem $(--)$, with the same parameters as in figure 1.

section 2.3. An additional requirement for the direct application of this theory is that the operator under consideration be representable as a differential operator in the form of equation 2.14. The operator in equation 3.12 does not satisfy this property, as the OS component contains the inverse Laplacian.

Motivated by this, we now present an approximating simplification to 2.14, which we believe to be novel. This development will take advantage of the similarity between the OS and SQ operators, and will consider variations of the "standard" inner products discussed in section 3.1. We start by taking advantage of the localised nature of the resolvent response modes, and assume that the mean velocity profile may be linearised about the critical layer location, y_c. Under this assumption, we have

$$\mathcal{H}_{vv} = \Delta^{-1}\mathcal{H}_{\eta\eta}\Delta. \tag{3.14}$$

This means that the operator that we are attempting to simplify is

$$\mathcal{H}_{\eta v}^{Lin} = (ik_z U_{y_c})\mathcal{H}_{\eta\eta}\mathcal{H}_{vv} \tag{3.15}$$

$$= (ik_z U_{y_c})\mathcal{H}_{\eta\eta}\Delta^{-1}\mathcal{H}_{\eta\eta}\Delta, \tag{3.16}$$

where U_{y_c} is the wall-normal gradient in the mean velocity profile at the critical layer location, y_c, and the Lin superscript denotes that the mean velocity profile has been linearised about y_c. Figures 2 and 3 show that the resolvent response modes of $\mathcal{H}_{\eta\eta}$ do not quantitatively match those of $\mathcal{H}_{\eta v}$. This is because the leading forcing mode of $\mathcal{H}_{\eta\eta}$ does not coincide with the mode most amplified by $\mathcal{H}_{vv}$. Given that the leading resolvent modes are dependent on the choice of inner product, it is reasonable to ask if a different choice of inner product could be used in the SVD of $\mathcal{H}_{\eta\eta}$, such that the leading forcing mode approximately coincides with the leading response of $\mathcal{H}_{vv}$. Physically, what we are seeking to do is to find an inner product weighting that will most amplify the lift-up mechanism (at the expense of optimising the Orr mechanism in isolation).

Let $\mathcal{H}_{\eta\eta}^*$ denote the adjoint of $\mathcal{H}_{\eta\eta}$ with respect to the standard scalar inner product, equation 3.5. If we instead consider the "Laplacian" inner product, we obtain

$$\mathcal{H}_{\eta\eta}^{*,\Delta} = \Delta^{-1}\mathcal{H}_{\eta\eta}^*\Delta.$$

This has the same form as equation 3.14, except with the (standard) adjoint of $\mathcal{H}_{\eta\eta}$, which amounts to taking the complex conjugate of the critical layer term. Note also that $\mathcal{H}_{\eta\eta}$ with the regular inner product has leading forcing and response modes (i.e., right
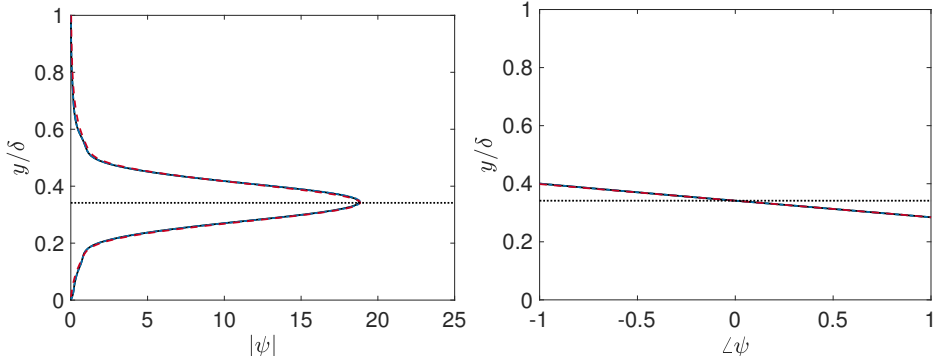
FIGURE 3. (a) Amplitude and (b) phase of wall normal vorticity response mode computed from the OS subsystem $(-)$, the scalar off-diagonal term $\mathcal{H}_{\eta v}$ of OS subsystem $(-\cdot)$, and its simplified scalar approximation computed using $\mathcal{H}_{\eta\eta}$ with a Laplacian inner product $(--)$, all with the same parameters as in figure 1.

and left singular vectors) that differ only in the direction of the phase change. We also then have

$$\left(\mathcal{H}_{\eta\eta}^*\right)^{*,\Delta} = \Delta^{-1}\mathcal{H}_{\eta\eta}\Delta,$$

which is identical to equation 3.14, meaning in particular that both share the same resolvent forcing and response modes. If we are to weight this operator explicitly to compute an SVD in the Laplacian scalar norm, we obtain

$$\mathcal{H}_{vv}^{W,\Delta} = \left[\left(\mathcal{H}_{\eta\eta}^*\right)^{*,\Delta}\right]^{W,\Delta} = \Delta^{-1/2}\mathcal{H}_{\eta\eta}\Delta^{1/2}. \tag{3.17}$$

Therefore, computing this SVD should give a leading forcing mode for $\mathcal{H}_{\eta\eta}$ that coincides with the leading response mode of $\mathcal{H}_{vv}$, thus minimising the "projection loss" of the total amplification. In effect, we are modifying the inner product used for $\mathcal{H}_{\eta\eta}$ such that it's leading forcing mode aligns with the leading response mode of $\mathcal{H}_{vv}$. This analysis therefore relies on the assumption that the total amplification is dominated by the lift-up, rather than the Orr, mechanism. With this assumption, this trick allows us to compute optimal response mode shapes by only considering the Squire operator, which is a differential operator of the general form given in equation 2.13, rather than the full OS operator, which is not. It will be shown later that this assumption holds except for large $k_\perp^2$, in which case the Laplacian approaches a constant, and so $\mathcal{H}_{\eta\eta}$ and $\mathcal{H}_{vv}$ converge to the same operator. Figure 3 shows that this modification to the inner product allows us to closely match the wall-normal vorticity component of the response mode of the full Navier–Stokes system, for the sample parameters chosen. We will discuss reasons for the success of this approximation, and in particular the relative balance between optimising the Orr and lift-up mechanisms, in section 4.

4. Predicting the shape of resolvent modes

This section will present a method that allows for the prediction of resolvent mode shapes, focusing in particular on the wall-normal vorticity component. The main idea will be to assume the existence of a mode that is localised in both wall-normal location, and wall-normal spatial frequency, and then find the parameters which result from maximum amplification of the resolvent operator, or equivalently, minimisation of the action of its inverse, on a given function. We will start by predicting the shape of a model operator (which is closely related to the Squire operator) in sections 4.1, which relates mode shapes

to asymptotic expansions of Airy functions, and 4.2, which approximates mode shapes under the assumption of the existence of wavepacket pseudomodes. This latter approach is then extended to consider the shape of modes for the full incompressible Navier–Stokes system in section 4.3, using the approximations presented in section 3.2. We will validate our method first on laminar Couette flow with a linear velocity profile in section 4.3, before returning to the turbulent boundary layer configuration in section 4.4.

4.1. *Relationship between wavepacket resolvent modes and Airy functions*

Before applying wavepacket pseudomode theory more generally, in this section we focus on a model (Airy) operator that is equivalent to the Squire operator with a linearised mean velocity profile. This analysis will show how numerically computed resolvent response modes relate to exact analytical solutions to simplified governing equations. Linearising the mean velocity profile about the critical layer, the Squire equation reduces to

$$(-i\omega + \mathcal{L}_{sq}^{Lin}) = ik_x U_{y_c}(y - y_c) - Re^{-1}\Delta. \tag{4.1}$$

For clarity, we let $R = k_x U_{y_c} Re$, and consider the closely-related operator

$$\mathcal{T} = (ik_x U_{y_c})^{-1}(-i\omega + \mathcal{L}_{sq}^{Lin}) = -(iR)^{-1}\frac{d^2}{dy^2} + \left(y - y_c + (iR)^{-1}k_\perp^2\right)$$

$$= -(iR)^{-1}\frac{d^2}{dy^2} + (y - y_c - \omega_c i)$$

$$= -(iR)^{-1}\frac{d^2}{dy^2} + (y - \lambda), \tag{4.2}$$

where $\lambda = y_c + \omega_c i$, and $\omega_c = R^{-1}k_\perp^2$, and we are assuming that $k_x \neq 0$. Note that we are generally interested in performing resolvent analysis along the axis of neutral stability (i.e., for real-valued frequencies with no growth or decay), but here we are incorporating the viscous dissipation term ω_c into λ, so in general λ is complex for this analysis. $\mathcal{T}$ is a complex Airy-type operator, and is identical to the operator considered, for example, in Reddy *et al.* (1993) as a model for studying the pseudospectra of the Orr-Sommerfeld operator. The equation $\mathcal{T}u = 0$ has a general solution that can be expressed by two independent Airy functions, such as

$$u(y) = c_1 Ai[z] + c_2 Ai[e^{2\pi i/3}z],$$

with

$$z = (iR)^{1/3}(y - \lambda). \tag{4.3}$$

Note that distinct solutions are obtained through the choice of contour in the complex plane when applying standard Laplace transform methods.

Shown in figure 4 are eigenvalues and selected eigenfuctions of $\mathcal{T}$ with Dirichlet boundary conditions on a finite domain $y \in [-1, 1]$, with $R = 3000$. In figure 5, these numerical eigenfunctions are compared to Ai$[z]$, Ai$[e^{2\pi i/3}z]$, and Ai$[e^{-2\pi i/3}z]$, and it is seen that Ai$[e^{2\pi i/3}z]$ (when appropriately-scaled) closely matches the numerically computed eigenfunctions on the finite domain. Note that if we had chosen eigenvalues on the left branch (i.e., with negative real component), then the Ai$[z]$ solution would have been accurate for all cases. This can be seen more clearly by overlaying the y-domain on the amplitude of the Airy functions in the complex plane, as shown in figure 6.
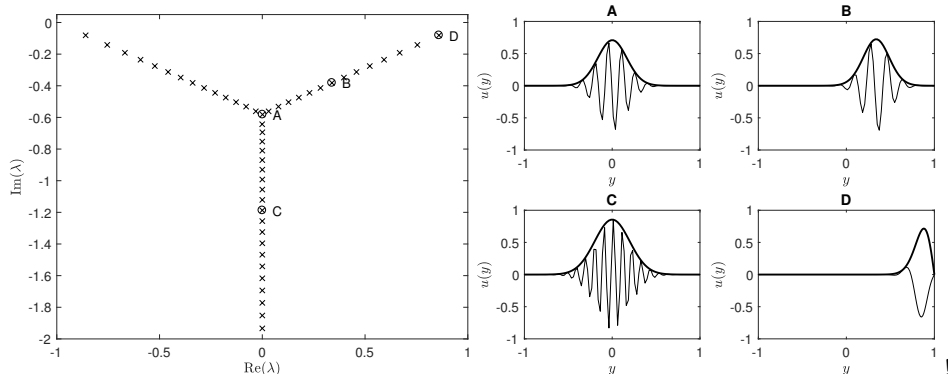
FIGURE 4. Spectrum (left) and selected eigenfunctions (right) of $\mathcal{T}$ with Dirichlet boundary conditions on the domain $y \in [-1, 1]$, with $R = 3000$. Absolute value and real component of eigenfunctions are shown with thick and thin lines, respectively.
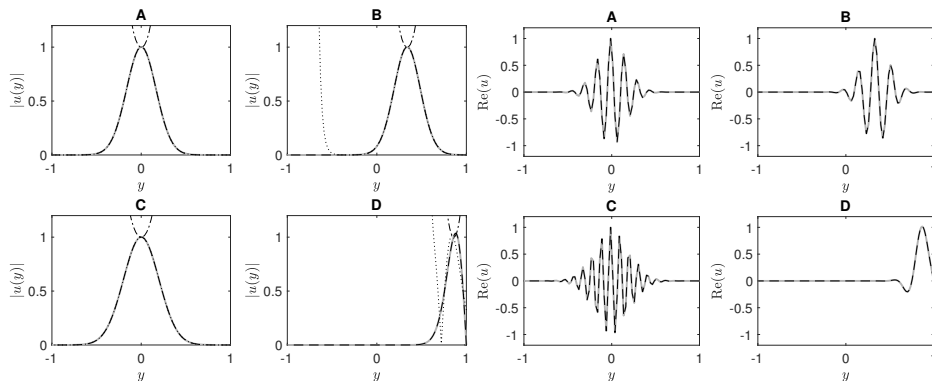

FIGURE 5. Comparison between absolute value (left) and real component (right) of numerically computed eigenfunctions (grey solid lines) of $\mathcal{T}$ with $R = 3000$, and those obtained from analytical solutions of the Airy equation $\text{Ai}[z]$, $\text{Ai}[e^{2\pi i/3}z]$, and $\text{Ai}[e^{-2\pi i/3}z]$. The analytic solution $\text{Ai}[e^{2\pi i/3}z]$ closely matches the numerical solution for all cases, and is the only analytic solution shown in the right subplot.

On an infinite domain (and when acting on square-integrable functions) $\mathcal{T}$ has an empty spectrum, and ϵ-pseudospectra that are independent of location on the real axis (that is, the boundaries of the pseudospectrum for various ϵ are horizontal lines).

As discussed in Reddy *et al.* (1993), a solution to $\mathcal{T}u = 0$ which is within ϵ of a function that satisfies the appropriate boundary conditions will be an ϵ-pseudoeigenfunction. We consider the pseudospectra of $\mathcal{T}$, again for the finite domain $y \in [-1, 1]$. As discussed in section 2.2, this amounts to computing the leading singular values and vectors of the resolvent of $\mathcal{T}$ for each $\lambda \in \mathbb{C}$ of interest. In particular, we may seek analytic approximations of these resolvent (optimal pseudospectral) modes using the same method as for eigenfunctions. In other words, for a given $\lambda \in \mathbb{C}$, we are interested in finding a function which is as close as possible to an eigenmode of $\mathcal{T}$. Noting that the Airy functions are continuous, the fact that there are regions of $\mathbb{C}$ for which they are very close to satisfying the boundary conditions of the finite domain suggest that these regions correspond to very large values of resolvent norm σ_1.

Figure 7 shows ϵ-pseudospectra for $\mathcal{T}$, along with optimal pseudoeigenmodes (i.e.,
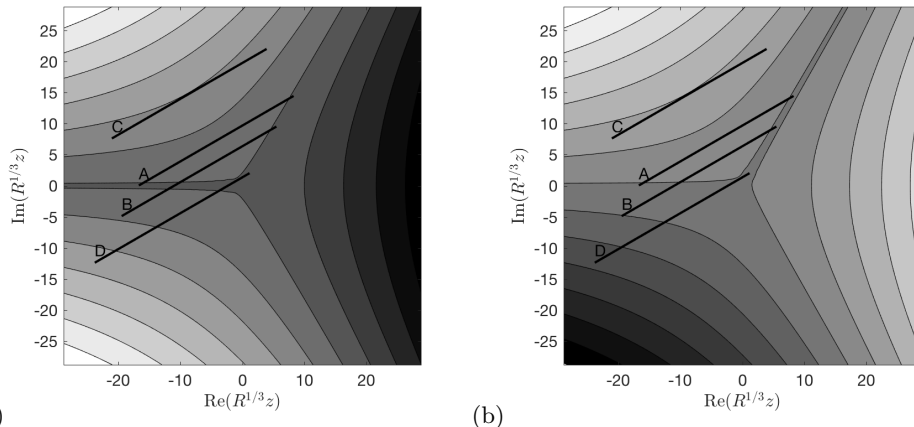
FIGURE 6. Contour plots of the magnitude of solutions Ai[z] (left) and Ai[$e^{2\pi i/3}z$] (right) to the Airy equation, with intervals overlaid representing the domains of the eigenfunctions considered in figures 4 and 5. 14 logarithmically-spaced contours between contours are 10^{-70} (black) and 10^{60} (white) are shown.
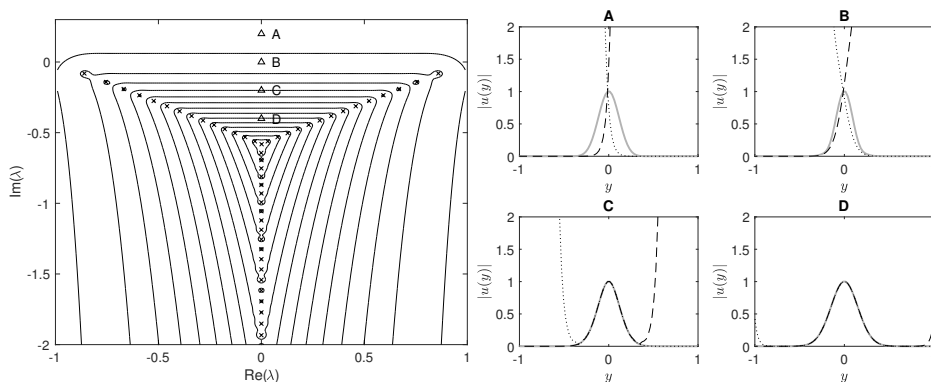

FIGURE 7. (left) ϵ-pseudospectra of $\mathcal{T}$ (with parameters equal to those for figures 4 and 5), with contour levels corresponding to $\epsilon \in \{10^{-15}, 10^{-14}, \cdots, 10^{-1}\}$, and (right) amplitudes of resolvent modes for locations in $\mathbb{C}$ as indicated on the left subplot. The right subplot compares numerically computed modes (grey) with Airy functions Ai[z] ($\cdot\cdot$), and Ai[$e^{2\pi i/3}z$] (—).

resolvent modes) and Airy function approximations thereof, for specified locations in the centre of the domain. In the central region, the pseudospectral properties of $\mathcal{T}$ resemble that of the operator on an infinite domain, where resolvent modes, which are "detached" from the boundary, are invariant to horizontal translation within this region. Moreover, resolvent modes within this region will resemble translated versions of eigenmodes along the inclined branches at the same vertical position. We observe that, as ϵ increases and we approach the real axis, the analytical Airy functions become less accurate, owing to their growth in magnitude occurring closer and closer to the critical layer, eventually saturating the component resembling the numerically computed response mode. As discussed in Reddy *et al.* (1993), these Airy functions can be used to compute constructive lower bounds to the pseudospectrum of $\mathcal{T}$, though these bounds are inaccurate whenever the Airy functions diverge far away from $y = \text{Re}(\lambda)$. The fact that $\omega_c = R^{-1}k_\perp^2$ means that the most physically-relevant region of the complex plane is in the upper half-plane, which

means that the Airy functions themselves are not close approximations of physically-relevant resolvent modes.

Away from the origin, one may approximate Airy functions by simpler expressions that do not involve integrals. The derivation of such asymptotic approximations involves finding a location in the complex that has a dominant contribution to the contour integral. We may derive the approximation (e.g., Olver (2014); Vallée & Soares (2010))

$$\mathrm{Ai}(z) \approx \frac{1}{2}\sqrt{\pi}z^{-1/4}\exp\left(-\frac{2}{3}z^{3/2}\right) \sim \exp\left(-\frac{2}{3}z^{3/2}\right), \qquad (4.4)$$

which is accurate for large $|z|$, where here $z = \gamma(y-\lambda)$, where (with reference to equation 4.3) we have $\gamma = (iR)^{1/3}$, $\lambda = ik_\perp^2/R = \omega_c i$, and we assume for now that $y_c = 0$. Expanding the exponential term gives

$$\exp\left(-\frac{2}{3}z^{3/2}\right) = \exp\left[-\frac{2}{3}(-\lambda\gamma)^{3/2}\left(1 - \frac{3}{2}\frac{y}{\lambda} + \frac{3}{8}\left(\frac{y}{\lambda}\right)^2 - \cdots\right)\right],$$

and thus

$$\mathrm{Ai}(z) \sim C \exp\left[(-\lambda\gamma)^{3/2}\frac{y}{\lambda} - \frac{1}{4}(-\lambda\gamma)^{3/2}\left(\frac{y}{\lambda}\right)^2 - \cdots\right], \qquad (4.5)$$

where we must take care when dealing with multi-valued roots. In particular, for a bounded approximation, we require that

$$\mathrm{Re}\left[(-\lambda\gamma)^{3/2}\lambda^{-1}\right] = 0.$$

If $\lambda = |\lambda|e^{i\theta_\lambda}$, then we find that this condition is only satisfied when $\theta_\lambda = \frac{3\pi}{2}$. Note that this corresponds to the lower half plane region where Airy functions can give close approximations to the numerically-computed solutions. Assuming $y_c = 0$, so that $\lambda = \omega_c i$, for $\omega_c < 0$ we obtain an approximation of the form

$$\psi(y) \sim \exp\left[-i\sqrt{|\omega_c|R}y - \frac{1}{4}\sqrt{\frac{R}{|\omega_c|}}y^2\right]. \qquad (4.6)$$

4.2. *Predicting wavepacket modes for a model operator*

Section 4.1 demonstrated that, in certain regimes, resolvent modes may be approximated by a function of the general form

$$\psi(y) = c\exp\left(aiy - by^2\right), \qquad (4.7)$$

where $a \in \mathbb{R}$ and $b > 0$ are functions of ω_c and R, and

$$c = \left(\frac{2b}{\pi}\right)^{1/4}$$

is a constant that gives ψ unit norm with respect to the regular scalar inner product.

This section will present an alternative analysis with this template function as a starting point. Applying wavepacket pseudomode theory as described in section 2.3, one may show that $\mathcal{T}$ satisfies the twist condition (equation 2.16) is satisfied within the half strip

$$\{\lambda : -1 < \mathrm{Re}(\lambda) < 1, \mathrm{Im}(\lambda) < 0\}. \qquad (4.8)$$

The $\mathrm{Imag}(\lambda) < 0$ condition is consistent with the predicted condition for a spatially localised mode from the truncated asymptotic expansion of an Airy function in equation
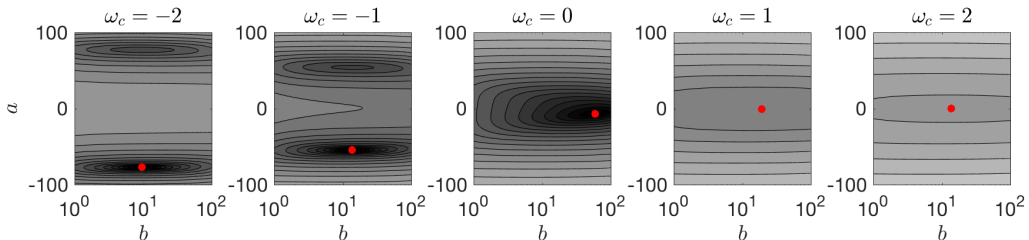
FIGURE 8. Contours of the cost function $J_\mathcal{T}$ as a function of shape parameters (a, b) for $R = 3000$ and several values of ω_c, with global minima identified with filled circles. 25 contour levels spaced logarithmically between 10^{-8} (black) and 10^4 (white) are used.

4.6. Note that the region described in equation 4.8 is outside the region that is most physically relevant for resolvent analysis of the Squire operator, where a positive $k_\perp^2$ and R give a positive imaginary component of ω_c. Despite this, figure 7 shows that even outside this region, the numerically computed pseudomode still maintains the same spatially localised structure. To predict the shape of resolvent modes outside this region, we will seek to directly optimize the shape parameters in the template function, equation 4.7. In particular, we wish to find the values of a and b for which $\|\mathcal{T}\psi\|$ is minimized. That is, we seek the minimum of the cost function

$$J_\mathcal{T}(a, b; R, \omega_c) = \|\mathcal{T}\psi\|^2 = \int_{y=-\infty}^{\infty} (\mathcal{T}\psi)^* \, (\mathcal{T}\psi)dy, \qquad (4.9)$$

where we are assuming that our mode is "detached" and localised, so can integrate over an infinite domain, and are assuming a standard inner product for this model operator (note that including a constant multiplicative factor of $k_\perp^{-2}$ as in equation 3.5 does not affect mode shapes or singular values). For simplicity, we again take $y_c = 0$. Note that the leading resolvent singular value is related to this cost function by

$$\sigma_1(R, \omega_c) = \left[\min_{a,b} J_\mathcal{T}(a, b; R, \omega_c)\right]^{-1/2}.$$

Noting that we have

$$\mathcal{T}^* = (iR)^{-1}D_{yy} + (y + i\omega_c),$$
$$\psi^*(y) = c\exp[-ayi - by^2],$$

it can be shown that

$$\mathcal{T}\psi(y) = -\frac{1}{iR}\left[4b^2y^2 - i(4ab + R)y - a^2 - 2b - R\omega_c\right]\psi(y),$$
$$(\mathcal{T}\psi(y))^* = \frac{1}{iR}\left[4b^2y^2 + i(4ab + R)y - a^2 - 2b - R\omega_c\right]\psi^*(y).$$

From this, we may compute

$$J_\mathcal{T}(a, b; R, \omega_c) = \frac{1}{4b} + \frac{3}{R^2}b^2 + \frac{2(3a^2 + R\omega_c)}{R^2}b + \frac{a^4 + 2aR + 2\omega_c a^2 R + \omega_c^2 R^2}{R^2}. \qquad (4.10)$$

Contours of this cost function for $R = 3000$ and several values of ω_c are shown in figure 8. We may analytically determine the locations of these minima as follows. This

cost function is minimised when

$$\frac{\partial J_{\mathcal{T}}}{\partial a} = \frac{2}{R^2}\left(6ab + 2a^3 + 2R\omega_c a + R\right) = 0 \tag{4.11}$$

$$\frac{\partial J_{\mathcal{T}}}{\partial b} = -\frac{1}{4b^2} + \frac{2}{R^2}\left(3b + 3a^2 + R\omega_c\right) = 0 \tag{4.12}$$

The equations 4.11 and 4.12 may be solved to give the parameters $\{a, b\}$ minimising $J_{\mathcal{T}}$, with care taken to select the correct minimising solution. It is also possible to obtain a parametrised family of solutions as follows. Assuming that R is fixed, suppose that we seek the optimal values $(a(\omega_c), b(\omega_c))$ for a range of values of ω_c. By implicitly differentiating equations 4.11 and 4.12 with respect to ω_c, the following ordinary differential equations governing the evolution of the optimal mode shape parameters may be found:

$$\frac{\partial a}{\partial \omega_c} = \frac{-R^3 a}{\omega_c R^3 + 3(a^2 + b)R^2 + 12\omega_c b^3 R + 36b^3(b - a^2)}, \tag{4.13}$$

$$\frac{\partial b}{\partial \omega_c} = \frac{-4b^3 R(\omega_c R - 3a^2 + 3b)}{\omega_c R^3 + 3(a^2 + b)R^2 + 12\omega_c b^3 R + 36b^3(b - a^2)}. \tag{4.14}$$

Note that this approach assumes that the global minimiser of $J_{\mathcal{T}}$ stays on the same branch, and is smoothly continuous with ω_c. Figure 9 shows that the predicted values of the optimal values of parameters a and b closely match both the asymptotic approximations (for $\omega_c < 0$), and the values obtained from fitting the numerically computed modes. The width parameter for this fit to the numerically-computed mode data is found by fitting a Gaussian function to the amplitude of the computed mode using MATLAB's `fit` command. The phase parameter is found by considering the gradient of the phase in a small region near the critical layer location. The predicted shape parameters are obtained from evolving the equations 4.13 and 4.14 from an initial condition obtained by solving equations 4.11 and 4.12 directly (at $\omega_c = 0$). Here, and in subsequent sections, such solutions (along with the symbolic computation of integrals) are obtained using Mathematica. Note that one could also use the asymptotic approximation 4.6 for initial conditions, where we must start from a sufficiently large negative value of ω_c to ensure that the initial conditions are accurate. It is additionally shown that the value of the cost function $J_{\mathcal{T}}$ for these optimal shape parameters closely matches the value of the cost function that may be computed directly from the numerically computed singular value. In essence, this shows that the optimal mode and amplification across all functions is closely approximated by the optimal over the class of functions of the form given in equation 4.7.

We may also consider the behaviour of the optimal shape parameters as R varies. Keeping ω_c constant, from equations 4.11-4.12 we obtain

$$\frac{\partial a}{\partial R} = \frac{(1 + 2\omega_c a)R^3 + 4a(a^2 + 3b)R^2 + 12b^3 R - 96a^3 b^3}{2R\left(\omega_c R^3 + 3(a^2 + b)R^2 + 12\omega_c b^3 R + 36b^3(b - a^2)\right)} \tag{4.15}$$

$$\frac{\partial b}{\partial R} = \frac{4b^3\left(\omega_c^2 R^2 + 3R(-a + \omega_c a^2 + 9\omega_c b) + 6a^4 + 18b^2\right)}{R\left(\omega_c R^3 + 3(a^2 + b)R^2 + 12\omega_c b^3 R + 36b^3(b - a^2)\right)} \tag{4.16}$$

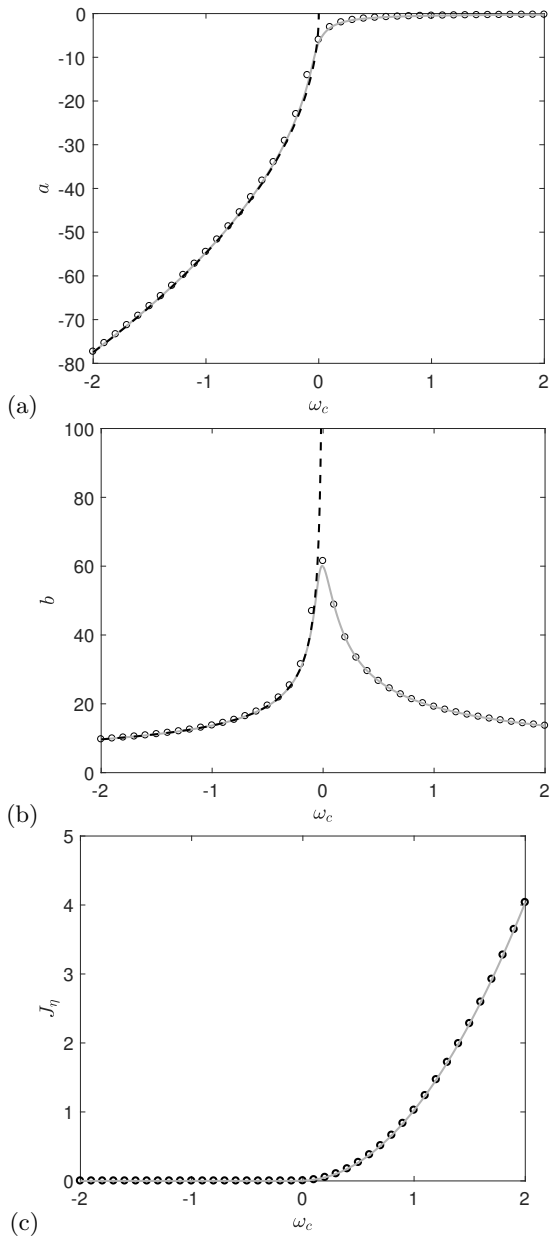In the limit of large R and for $\omega_c \neq 0$, (and assuming restrictions on the growth of a and

FIGURE 9. Prediction of optimal shape parameters a (a) and b (b) as a function of $\omega_c = \text{Imag}(\lambda)$ with $R = 3000$ using both the truncated asymptotic Airy function approximation (equation 4.6, black dashed lines) and minimising the cost function given in equation 4.10 (grey lines), in comparison to values fitted to numerically computed eigenfunctions on a finite domain (circles). (c) compares the cost function value to the true value (σ_1^{-2}) obtained from the resolvent norm.

b with R), we have the approximations

$$\frac{\partial a}{\partial R} \approx \frac{1}{2\omega_c R} \tag{4.17}$$

$$\frac{\partial b}{\partial R} \approx \frac{4b^3 \omega_c}{R^2}, \tag{4.18}$$

from which we may infer the scalings $a \to C$, $b \propto R^{1/2}$. For large R but with $R\omega_c \ll 1$, we instead obtain

$$\frac{\partial a}{\partial R} \approx \frac{1}{3(a^2 + b)} \qquad (4.19)$$

$$\frac{\partial b}{\partial R} \approx -\frac{4ab^3}{R^2(a^2 + b)}, \qquad (4.20)$$

which can be shown to permit a consistent asymptotic solution with $a \propto R^{1/3}$ and $b \propto R^{2/3}$. This scaling of b corresponds to a mode with that scales with $R^{1/3}$, which agrees with the critical layer scaling (Drazin & Reid 2004), and can also be inferred from the transformation described in equation 4.3. Figure 10 shows that these scalings closely match the shape parameter trends obtained from the numerically computed modes. Moreover, these shape parameters are accurately predicted from finding optimal parameters of cost function $J_{\mathcal{T}}$, which can be obtained either from solving equations 4.11 and 4.12 for each ω_c and R, or by evolving the differential equations 4.15 and 4.16 over R. It should be noted that, even for this model system, computing the leading resolvent modes directly can require substantial computational resources for large R, highlighting an advantage of approximations using the methods described in this section. We lastly note that one could seek alternative parameterisations of the two-dimensional space of optimal mode shapes, such as by varying R while keeping $\omega_c R$ ($= k_\perp^2$) constant.

4.3. *Predicting the shape of resolvent modes for laminar Couette flow*

In this section, we will extend the analysis in section 4.2 to consider the Navier–Stokes operator and suboperators considered in sections 3.1 and 3.2. We again will restrict our attention to predicting the vorticity component of the leading response mode of the resolvent operators $\mathcal{H}_{\boldsymbol{k}}$, $\mathcal{H}_{os,\boldsymbol{k}}$ and $\mathcal{H}_{sq,\boldsymbol{k}}$. For the Squire suboperator, the analysis is almost identical to that of the model operator considered in section 4.2. To predict the mode shapes of the full system, we rely on the fact that the response is dominated by the effect of the OS suboperator, which we analyse using the simplifying approximations introduced in section 3.2. In particular, this also results in a methodology similar to that used in section 4.2, but with a modification to use the Laplacian scalar inner product (equation 3.6.

We begin by again assuming mode shapes of the form

$$\psi_{sq}(y) = c_{sq} \exp\left(a_{sq}iy - b_{sq}y^2\right),$$
$$\psi_{os}(y) = c_{os} \exp\left(a_{os}iy - b_{os}y^2\right),$$

but now to satisfy the unit-norm requirements of the relevant inner products (equation 3.5) for the SQ operator, equation 3.6 for the OS) we have

$$c_{os} = \left(\frac{2b_{sq}}{\pi}\right)^{1/4} k_\perp, \qquad c_{sq} = \left(\frac{2b_{os}}{\pi}\right)^{1/4} k_\perp (b_{os} + a_{os}^2 + k_\perp^2),$$

where, with reference to the previous section, we have $k_\perp^2 = \omega_c R$. Using the approximation to the Orr-Sommerfeld operator introduced in section 3.2, and noting that $U_{y_c} = 1$, the relevant cost functions for optimizing the shape of the SQ and OS template functions are
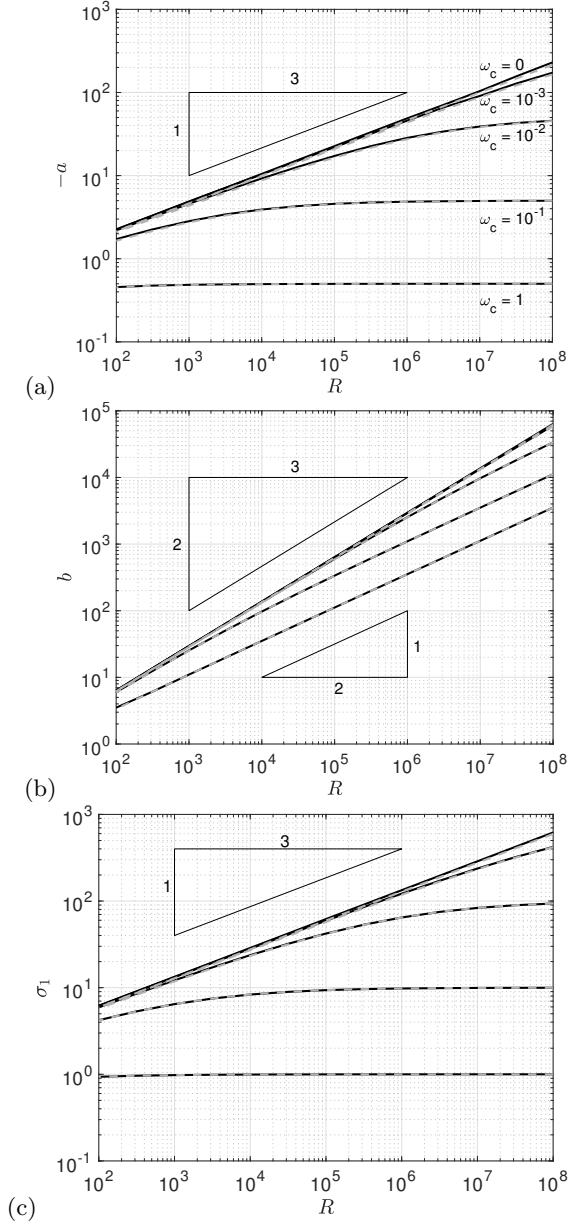
FIGURE 10. Comparison between predicted $(-)$ and fitted $(--)$ parameters a (subplot a) and b (b), and associated singular value (c) as a function R.

$$J_{sq}(a,b;R,\boldsymbol{k}) = \|U_{y_c}k_x\mathcal{T}\psi_{os}\|^2 = \frac{U_{y_c}^2 k_x^2}{k_\perp^2}\int_{y=-\infty}^{\infty}(\mathcal{T}\psi_{os})^*(\mathcal{T}\psi_{os})dy \qquad (4.21)$$

$$J_{os}(a,b;R,\boldsymbol{k}) = \|U_{y_c}k_x\mathcal{T}\psi_{os}\|_\Delta^2 = \frac{U_{y_c}^2 k_x^2}{k_\perp^2}\int_{y=-\infty}^{\infty}(\mathcal{T}\psi_{os})^{*,\Delta}(\mathcal{T}\psi_{os})dy$$

$$= -\frac{U_{y_c}^2 k_x^2}{k_\perp^2}\int_{y=-\infty}^{\infty}(\mathcal{T}\psi_{os})^*\,\Delta(\mathcal{T}\psi_{os})dy \qquad (4.22)$$

For laminar Couette flow we have $U_{y_c} = 1$ for all y_c in the domain, but we keep this term so that the equations are directly applicable for arbitrary mean velocity profiles. Also note that while the cost function for the Squire modes is "exact" given the assumed template function and a linear mean velocity profile, the OS modes are relying on the accuracy of a simplified operator (being the scalar Squire operator with a Laplacian inner product) capturing the correct behavior of the response mode.

Substituting in the mode template functions (and dropping the subscripts on a and b parameters for brevity), explicit expressions for the cost functions are

$$J_{sq}(a, b; R, \boldsymbol{k}) = \frac{U_{y_c}^2 k_x^2}{k_\perp^2} \left[\frac{1}{4b} + \frac{3}{R^2} b^2 + \frac{2(3a^2 + k_\perp^2)}{R^2} b + \frac{a^4 + 2aR + 2k_\perp^2 a^2 + k_\perp^4}{R^2} \right],$$

(4.23)

$$J_{os}(a, b; R, \boldsymbol{k}) = \frac{U_{y_c}^2 k_x^2}{4k_\perp^2 b (b + a^2 + k_\perp^2) R^2} \left[(3b + a^2 + k_\perp^2) R^2 + 16ab(3b + a^2 + k_\perp^2) R \right.$$
$$\left. + 4b \left(15b^3 + (a^2 + k_\perp^2)^3 + 9b^2(5a^2 + k_\perp^2) + 3b(a^2 + k_\perp^2)(5a^2 + k_\perp^2) \right) \right].$$

(4.24)

As before, the minima of these cost functions may be found by selecting the appropriate solution to the equations

$$\frac{\partial J_{sq}}{\partial a} = \frac{2U_{y_c}^2 k_x^2}{k_\perp^2 R^2} \left(6ab + 2a^3 + 2k_\perp^2 a + R \right) = 0$$

(4.25)

$$\frac{\partial J_{sq}}{\partial b} = \frac{U_{y_c}^2 k_x^2}{k_\perp^2} \left[-\frac{1}{4b^2} + \frac{2}{R^2} (3b + 3a^2 + k_\perp^2) \right] = 0$$

(4.26)

$$\frac{\partial J_{os}}{\partial a} = \frac{U_{y_c}^2 k_x^2}{k_\perp^2 (b + a^2 + k_\perp^2)^2} \left[1 + 4R^{-1} \left(ba^2 + 4k_\perp^2 b + (a^2 + k_\perp^2)^2 \right) \right.$$
$$\left. + 4R^{-2} a \left(15b^3 + 9b(a^2 + k_\perp^2)^2 + (a^2 + k_\perp^2)^3 + 3b^2(5a^2 + 9k_\perp^2) \right) \right] = 0$$

(4.27)

$$\frac{\partial J_{os}}{\partial b} = \frac{U_{y_c}^2 k_x^2}{k_\perp^2 (b + a^2 + k_\perp^2)^2} \left[-\frac{3}{4} + \frac{1}{2} b^{-1}(a^2 + k_\perp^2) + b^{-2}(a^2 + k_\perp^2)^2 + \frac{8}{R} a(a^2 + k_\perp^2) \right.$$
$$\left. + \frac{2}{R^2} \left(15a^3 + (a^2 + k_\perp^2)^2(7a^2 + k_\perp^2) + 9b^2(5a^2 + 3k_\perp^2) + 9b(5a^2 + k_\perp^2)(a^2 + k_\perp^2) \right) \right]$$
$$= 0.$$

(4.28)

Figure 11 compares the predicted shape parameters to those obtained from fitting these parameters to numerically-computed modes, which are computed for $Re = 1000$ and various values of k_x and k_z/k_x. We observe in subplots (a) and (c) that the Squire mode parameters are accurately predicted from solving equations 4.25 and 4.26. Subplots (b) and (d) show that solving equations 4.27 and 4.28 predicts the fitted parameters to the leading resolvent response mode of the Squire operator with Laplacian inner product. Furthermore, this prediction also accurately predicts the shape of the wall-normal vorticity component of leading response modes for the full Navier–Stokes system. Note that the scaling laws for small k_x are identical to those for small R observed in figure 10. The trends at high k_x differ from those in figure 10, due to the fact that here we keep k_z proportional to k_x (and thus $k_\perp \propto R$), whereas in figure 10 constant ω_c resulted in $k_\perp^2 \propto R$. These trends can again be inferred from studying the dominant
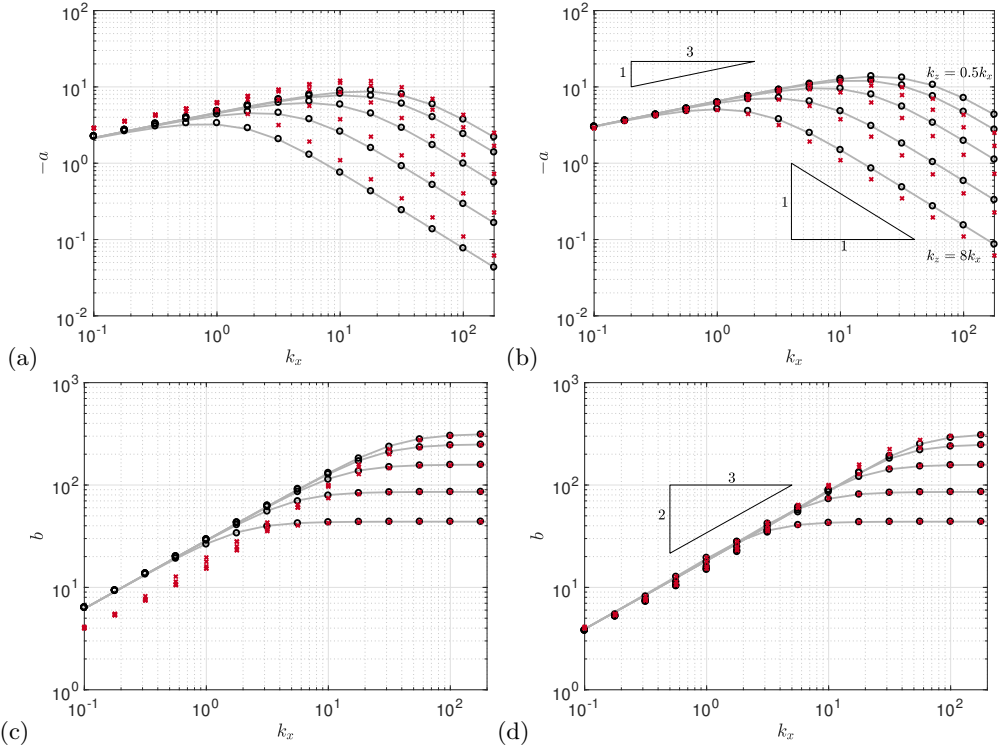
FIGURE 11. Comparison between predicted $(-)$ and fitted $(\circ)$ mode shape parameters a (subplots a,b) and b (c,d) for the Squire operator with a standard (a,c) and Laplacian (b,d) inner product, as a function of streamwise wavenumber k_x, for $Re = 1000$ and spatial aspect ratios $k_z/k_x \in \{0.5, 1, 2, 4, 8\}$. Also shown are fitted shape parameters for the η component of the full Navier–Stokes system ($\times$'s).

terms in the evolution equations for the governing parameters, which can be computed from considering the partial derivatives of J_{sq} and J_{os} with respect to a and b, which we omit for brevity.

For large k_x, the mode shapes for both operators converge, which may be explained by the fact that the Laplacian operator is dominated by the constant $k_\perp^2$ term in this regime. As a consequence, here analysis of the Squire operator gives accurate predictions of the behaviour of the full Navier–Stokes system, particularly for the mode width, which approaches a constant value with increasing k_x. There is some difference between the phase gradient parameter a for the full system and for the Squire system with both the standard and Laplacian inner product (with the value for the full system lying between those for the two simplified systems), though this difference decreases as k_x increases and the phase variation decays towards zero.

Figure 12 plots predicted and true mode amplitudes for several of the cases considered in figure 11. The predicted mode shapes for η closely match the computed modes for both the Squire and full Navier–Stokes system, with the modes for the latter being very close to those of the OS subsystem. The largest discrepancy arises in the $k_x = 1$ case, where the tails of the mode amplitudes are significantly heavier than those of a Gaussian distribution, and extend far from the critical layer towards the wall. This phenomenon is related to a wider distribution in the v-component of the mode (not plotted), and
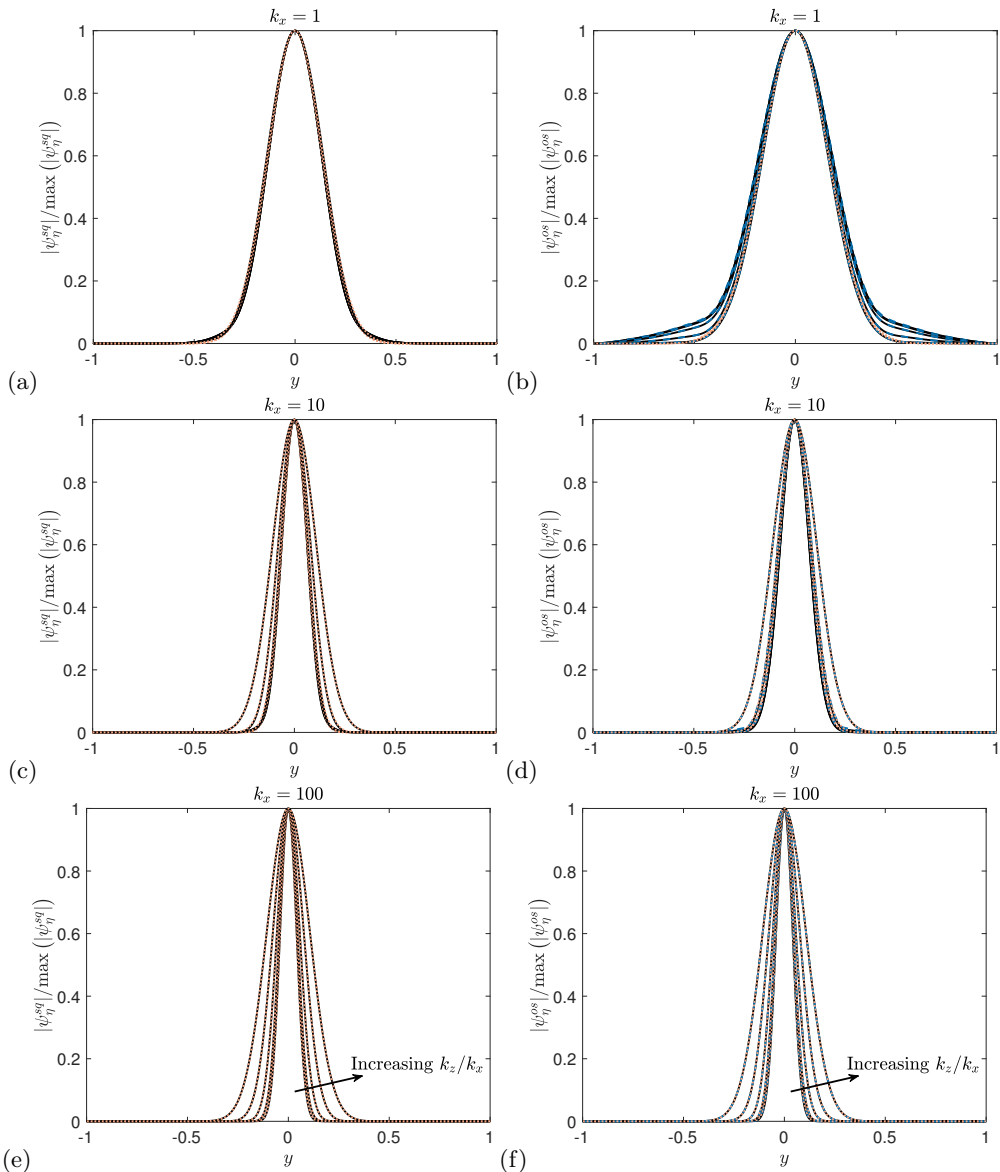
FIGURE 12. Comparison between true (numerically computed, solid lines) and predicted (dotted lines) mode amplitude for laminar Couette flow with $Re = 1000$ and $k_x = 1$ (a,b) 10 (c,d) and 100 (e,f), and aspect ratios $k_z/k_x \in \{0.5, 1, 2, 4, 8\}$. Subplots (a,c,e) show results for the Squire subsystem, while subplots (b,d,f) are for the Navier–Stokes operator. The dashed lines in subplots (b,d,f) also show (numerically computed) mode amplitudes for the Orr-Sommerfeld subsystem.

gives a larger variation in fitted b values for this k_x for the full Navier–Stokes system, as observed in figure 11.

Figure 13 compares the leading resolvent singular values for the Squire and Navier–Stokes systems to those estimated from the minima of the cost functions J_{sq} and J_{os}, for the same wavenumbers considered in figure 11. The cost functions are able to accurately predict the singular values of the scalar Squire operator with both the regular and Laplacian inner product, though this is only accurate for the full Navier–Stokes system
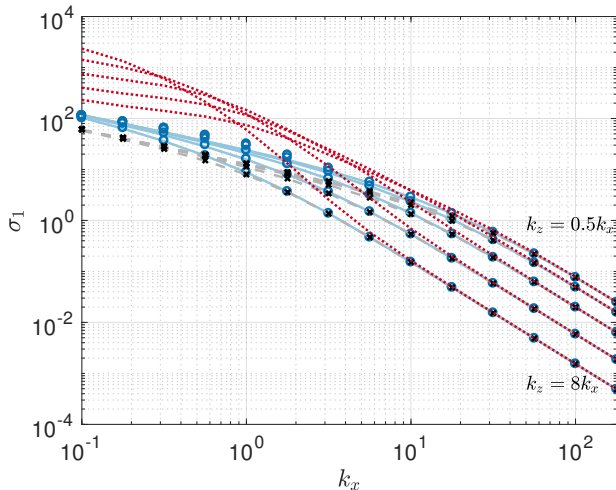
FIGURE 13. Comparison between predicted and computed leading singular values for the Squire subsystem with regular (predicted −−, computed ×), and Laplacian (predicted −, computed ∘) inner product, for $Re = 1000$ and spatial aspect ratios $k_z/k_x \in \{0.5, 1, 2, 4, 8\}$. Also shown are computed singular values for the full Navier–Stokes system (··).

for large k_x (and thus large $k_\perp^2$). In particular, these model operators are incapable of predicting the increase in singular value for high-aspect-ratio (i.e., large k_z/k_x) modes that is observed, though we have shown that they still accurately predict mode shapes in this regime.

4.4. Predicting mode shapes for a turbulent boundary layer

This section applies the methodology developed in sections 4.2 and 4.3 to a turbulent boundary layer. By linearizing the mean velocity profile about the critical layer, the equations for predicting mode shape parameters are the same as those developed in section 4.3 (i.e., equations 4.23-4.28), though now U_{y_c} and $R = k_x U_{y_c} Re$ are dependent on the critical layer location. Figure 14 shows the predicted and true response mode shapes for the Squire and Navier–Stokes resolvent operators for two pairs of spatial wavenumbers and various critical layer locations. Note that the case where $\{k_x, k_z, c\} = \{\pi/2, 2\pi, 0.8U_\infty\}$ as considered in figures 1-3 as representative of a typical large-scale motion, is included. The location typical of very large-scale motions ($c \approx 0.6U_\infty$) is also included, though these structures would correspond to slightly smaller streamwise wavenumbers than $k_x = \pi/2$. We observe that mode amplitude and phase variation (in the local region of high amplitude) is accurately estimated, provided the mode is not substantially affected by the presence of the wall. This shows in particular the validity of using a mean velocity profile linearised about the critical layer to estimate mode shapes.

Figure 15 compares predicted and fitted mode shape parameters as a function of k_x for various aspect ratios k_z/k_x, for a wavespeed $c = 0.8U_\infty$, with predicted and true modes shapes plotted in figure 16. We observe the same trends, and similar accuracy in prediction of parameters as for laminar Couette flow (figure 11).
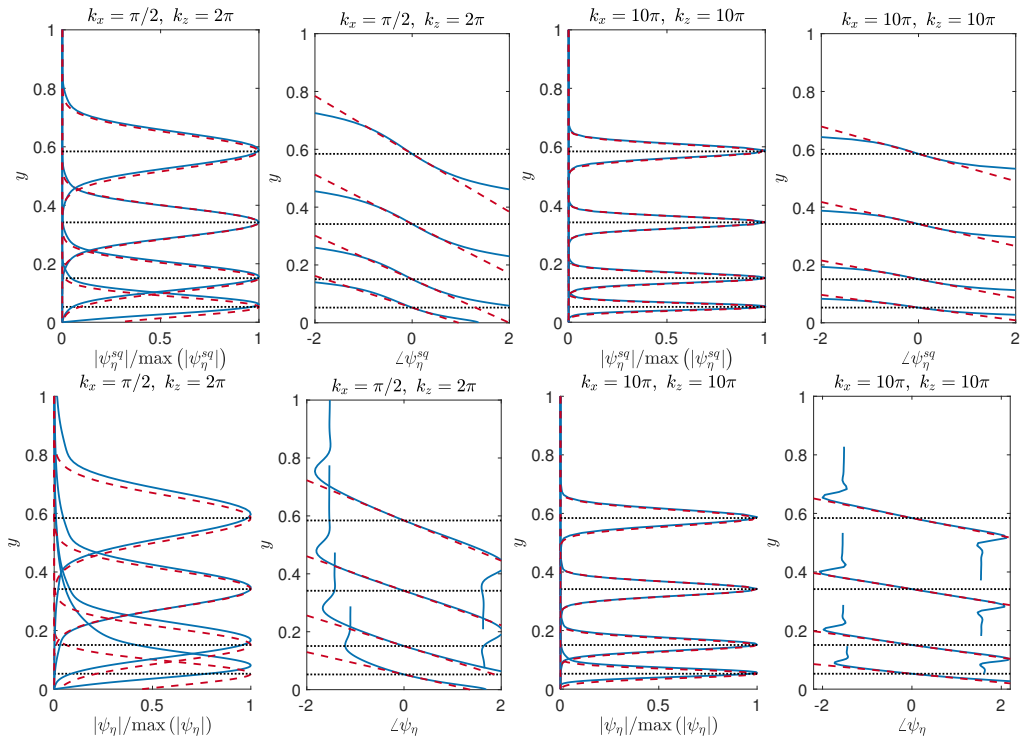
FIGURE 14. True (solid lines) and predicted (dashed) leading resolvent mode amplitudes and phases for the Squire system (top row) and wall-normal vorticity component of the Navier–Stokes system (bottom) for a turbulent boundary layer with $Re_\tau = 900$. Modes are shown for two wavenumber pairs, $(k_x, k_z) = (\pi/2, 2\pi)$ and $(10\pi, 10\pi)$, and temporal frequencies corresponding to wavespeeds of $0.6U_\infty$, $0.7U_\infty$, $0.8U_\infty$, $0.9U_\infty$, with critical layer locations indicated by dotted lines.

5. Discussion and conclusions

This work has presented a method for approximating leading resolvent response modes for quasi-parallel shear-driven flows. This method relies on the assumption that the true mode may be closely approximated by a simple template function, the general form of which can be reasoned from consideration of wavepacket pseudomode theory. In essence, the method reduces the space of possible mode shapes from an infinite-dimensional space (which in practice is approximated by a high dimensional space defined by the numerical discretisation) to a two-dimensional family of functions. Once this template function is identified, the optimal shape parameters (which govern the width and phase variation of the mode) may be found as the minimisers of a cost function, which is directly related to the resolvent norm of the underlying operator. In practice, this amounts to finding the roots of a pair of coupled equations, which may be arranged to be polynomials in the shape parameters. In addition, it is possible to derive differential equations in parameter space that govern the evolution of these optimal shape parameters. Importantly, this method precludes the need for the formulation and decomposition of discretised linear operators, leading to substantial reduction in computational cost. The extent of the reduction in computational cost is dependent on the size of the discretisation, and on the extent and resolution of the parameter space (e.g., wavenumbers and temporal frequencies) that one wishes to study. The method may be readily applied to a model operator, as considered in section 4.2, and in the analysis of the Squire operator in sections
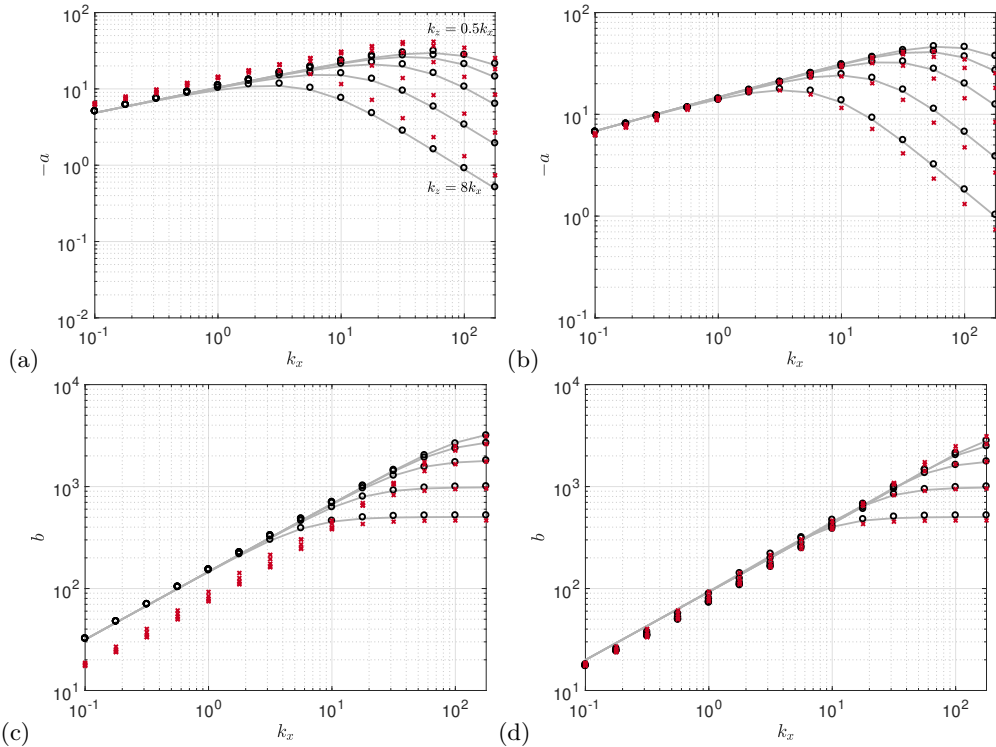
FIGURE 15. Comparison between predicted $(-)$ and fitted $(\circ)$ mode shape parameters a (subplots a,b) and b (c,d) for the Squire operator with a standard (a,c) and Laplacian (b,d) inner product, as a function of streamwise wavenumber k_x, for various mode aspect ratios for a turbulent boundary layer with $Re_\tau = 900$ and $c = 0.8U_\infty$. Also shown are fitted shape parameters for the η component of the full Navier–Stokes system ($\times$'S).

4.3-4.4. Application for the full Navier–Stokes system relies on additional simplifications to arrive at a scalar differential operator which has a leading response mode (left singular vector) which approximates the wall-normal vorticity component of the response mode of the Navier–Stokes resolvent operator, as detailed in section 3.2. This simplification is made in three steps. Firstly, the observation that the wall-normal vorticity response is dominated by the Orr-Sommerfeld component (equation 3.9). Secondly, that this operator is in turn dominated by the vorticity response to velocity forcing, governed by the scalar operator (equation 3.12). Finally, the leading left singular vector of this scalar operator may be approximated by that of the Squire operator furnished with the scalar Laplacian inner product (equation 3.6). This results in an operator which may be studied by applying the same techniques as those used for the model/Squire system. Note that, even without this analysis, study of the Squire operator (for which the associated cost function has a simpler form) typically gives the same qualitative behaviour observed for the full system. In particular, the Squire system obeys many of the same scaling laws of mode shape parameters with wavenumbers and Reynolds numbers. More detailed analysis of scaling and self-similarity properties of resolvent modes in wall-bounded flows are given in Moarref *et al.* (2013).

While the vorticity response mode shapes of the Squire and Orr-Sommerfeld resolvent operators are qualitatively similar, they represent quite different physical phenomena. The Squire resolvent operator describes amplification through forcing in the same component, with an upstream-leaning optimal forcing mode giving a downstream-leaning
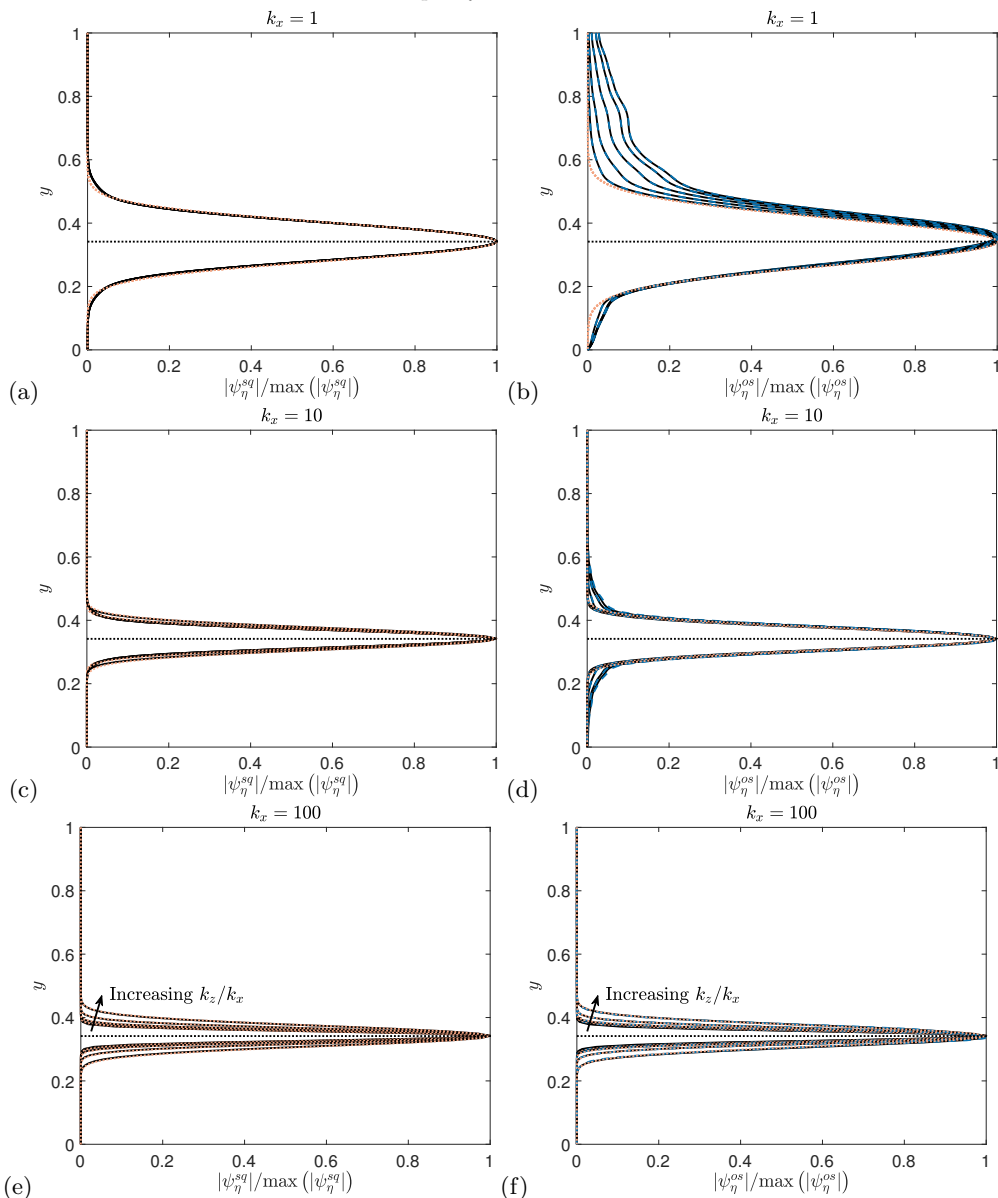
FIGURE 16. Comparison between true (numerically computed, solid lines) and predicted (dotted lines) mode amplitudes for various k_x, and aspect ratios $k_z/k_x \in \{0.5, 1, 2, 4, 8\}$, for a turbulent boundary layer with $Re_\tau = 900$ and $c = 0.8U_\infty$. The black horizontal dotted line indicates the critical layer location. Subplots (a,c,e) show results for the Squire subsystem, while subplots (b,d,f) are for the η-component of the Navier–Stokes operator. The dashed lines in subplots (b,d,f) also show (numerically computed) mode amplitudes for the Orr-Sommerfeld subsystem.

response mode. This is a manifestation of the classical Orr mechanism. Note in particular that the Squire forcing mode has the same amplitude profile as the response mode, but with an opposite phase variation. The Orr-Sommerfeld sub-operator on the other hand typically has a leading response mode that is dominated by the wall-normal vorticity component, but is forced primarily by wall-normal velocity, in a manner resembling the lift-up mechanism. Despite this phenomenological difference, we have shown that the

shape of the response may be accurately predicted from the Squire operator with a modified inner product.

This work has focused on characterising the shape of the (dominant) wall-normal vorticity component resolvent modes for parallel wall-bounded flows. It is possible that these methods could be extended for application to more complex geometries, and other mode components. For most of the cases considered in this work, the cost function had only one local minimum corresponding to a wavepacket mode (i.e., with $b > 0$), with the exception being for negative ω_c for the model operator considered in section 4.2, as seen in figure 8. More complex geometries might result in more complex cost functions, for which more care must be taken to select the true global optimum. Note that the operators considered here also typically have a large spectral gap between the first and second singular value. Future work could also seek to identify modes corresponding to additional singular values, which would be of particular interest for situations where the operator does not exhibit low-rank behaviour (i.e., there does not exist a large gap between the leading and second singular values). Similar methods could also be applied to study optimal forcing modes in more detail, and to compute nonlinear forcing terms induced from analytic approximations to wavepacket modes. This would provide an alternative route to study phenomena such as the self-similarity of the nonlinear forcing (Sharma *et al.* 2017).

In terms of the methodology itself, there are a number of possible refinements that could be investigated. For example, nonlinear terms in the expansion of the mean velocity profile about the critical layer could be retained, and additional terms in the template function (for example, a term could be added to allow for the phase variation to be cubic in $y - y_c$). The former modification might be particularly useful when dealing with mean velocity profiles that have stationary points, such as in channel flow. Such additions would lead to more complex cost functions, but the same techniques of analysis should be applicable. The accuracy of the assumed form of the modes relies on the mode being far enough away from the wall. Further extensions of the methodology could seek to explicitly model the effect of the wall.

REFERENCES

AUBRY, N., HOLMES, P., LUMLEY, J. L. & STONE, E. 1988 The dynamics of coherent structures in the wall region of a turbulent boundary layer. *Journal of Fluid Mechanics* **192**, 115–173.

BAMIEH, B. & DAHLEH, M. 2001 Energy amplification in channel flows with stochastic excitation. *Physics of Fluids* **13** (11), 3258–3269.

BERKOOZ, G., HOLMES, P. & LUMLEY, J. L. 1993 The proper orthogonal decomposition in the analysis of turbulent flows. *Annual Review of Fluid Mechanics* **25** (1), 539–575.

BÖBERG, L. & BRÖSA, U. 1988 Onset of turbulence in a pipe. *Zeitschrift für Naturforschung A* **43** (8-9), 697–726.

BUTLER, K. M. & FARRELL, B. F. 1992 Three-dimensional optimal perturbations in viscous shear flow. *Physics of Fluids A: Fluid Dynamics* **4** (8), 1637–1650.

CANTWELL, B. J. 1981 Organized motion in turbulent flow. *Annual Review of Fluid Mechanics* **13** (1), 457–515.

CHOMAZ, J. 2005 Global instabilities in spatially developing flows: Non-normality and nonlinearity. *Annual Review of Fluid Mechanics* **37**, 357–392.

COSSU, C., PUJALS, G. & DEPARDON, S. 2009 Optimal transient growth and very large–scale structures in turbulent boundary layers. *Journal of Fluid Mechanics* **619**, 79–94.

DAVIES, E. B. 1999*a* Pseudo–spectra, the harmonic oscillator and complex resonances. In *Proceedings of the Royal Society of London A: Mathematical, Physical and Engineering Sciences*, , vol. 455, pp. 585–599. The Royal Society.

DAVIES, E. B. 1999*b* Semi-classical states for non-self-adjoint Schrödinger operators. *Communications in Mathematical Physics* **200** (1), 35–41.

DEL ALAMO, J. C. & JIMENEZ, J. 2006 Linear energy amplification in turbulent channels. *Journal of Fluid Mechanics* **559**, 205–213.

DRAZIN, P. G. & REID, W. H. 2004 *Hydrodynamic stability*. Cambridge University Press.

FARRELL, B. & IOANNOU, J. 1993 Stochastic forcing of the linearized Navier–Stokes equations. *Phys. Fluids* **5** (11), 2600–2609.

GARNAUD, X., LESSHAFFT, L., SCHMID, P. & HUERRE, P. 2013 The preferred mode of incompressible jets: linear frequency response analysis. *Journal of Fluid Mechanics* **716**, 189–202.

GÓMEZ, F., BLACKBURN, H. M., RUDMAN, M., SHARMA, A. S. & MCKEON, B. J. 2016 A reduced-order model of three-dimensional unsteady flow in a cavity based on the resolvent operator. *Journal of Fluid Mechanics* **798**.

GUALA, M., HOMMEMA, S. E. & ADRIAN, R. J. 2006 Large-scale and very-large-scale motions in turbulent pipe flow. *Journal of Fluid Mechanics* **554**, 521–542.

GUSTAVSSON, L, H. 1986 Excitation of direct resonances in plane Poiseuille flow. *Studies in Applied Mathematics* **75** (3), 227–248.

HACK, M. J. P. & MOIN, P. 2017 Algebraic disturbance growth by interaction of Orr and lift-up mechanisms. *Journal of Fluid Mechanics* **829**, 112–126.

HEAD, M. R. & BANDYOPADHYAY, P. 1981 New aspects of turbulent boundary-layer structure. *Journal of Fluid Mechanics* **107**, 297–338.

HOLMES, P., LUMLEY, J. L., BERKOOZ, G. & ROWLEY, C. W. 2012 *Turbulence, coherent structures, dynamical systems and symmetry*. Cambridge University Press.

HUTCHINS, N. & MARUSIC, I. 2007 Evidence of very long meandering features in the logarithmic region of turbulent boundary layers. *Journal of Fluid Mechanics* **579**, 1–28.

HWANG, Y. & COSSU, C. 2010 Linear non-normal energy amplification of harmonic and stochastic forcing in the turbulent channel flow. *Journal of Fluid Mechanics* **664**, 51–73.

JEUN, J., NICHOLS, J. W. & JOVANOVIĆ, M. R. 2016 Input-output analysis of high-speed axisymmetric isothermal jet noise. *Phys. Fluids* **28** (4), 047101.

JIMÉNEZ, J. 2013 How linear is wall-bounded turbulence? *Physics of Fluids* **25** (11), 110814.

JIMÉNEZ, J. 2018 Coherent structures in wall-bounded turbulence. *Journal of Fluid Mechanics* **842**.

JOVANOVIĆ, M. R. & BAMIEH, B. 2005 Componentwise energy amplification in channel flows. *Journal of Fluid Mechanics* **534**, 145–183.

KIM, K. C. & ADRIAN, R. J. 1999 Very large-scale motion in the outer layer. *Physics of Fluids* **11** (2), 417–422.

KLINE, S. J., REYNOLDS, W. C., SCHRAUB, F. A. & RUNSTADLER, P. W. 1967 The structure of turbulent boundary layers. *Journal of Fluid Mechanics* **30** (4), 741–773.

KOVASZNAY, L. S. G., KIBENS, V. & BLACKWELDER, R. F. 1970 Large-scale motion in the intermittent region of a turbulent boundary layer. *Journal of Fluid Mechanics* **41** (2), 283–325.

LANDAHL, M. T. 1975 Wave breakdown and turbulence. *SIAM Journal on Applied Mathematics* **28** (4), 735–756.

LANDAHL, M. T. 1980 A note on an algebraic instability of inviscid parallel shear flows. *Journal of Fluid Mechanics* **98** (2), 243–251.

LEONARD, A. 2016 Approximate solutions to the linearized Navier–Stokes equations for incompressible channel flow. In *Proceedings of the 20th Australasian Fluid Mechanics Conference*.

LUMLEY, J. L. 1967 The structure of inhomogeneous turbulent flows. In *Proceedings of the International Colloquium on the Fine Scale Structure of the Atmosphere and its Influence on Radio Wave Propagation* (ed. A. M. Yaglam & V. I. Tatarsky). Doklady Akademii Nauk SSSR, Moscow, Nauka.

McKeon, B. J. 2017 The engine behind (wall) turbulence: perspectives on scale interactions. *Journal of Fluid Mechanics* **817**.

McKeon, B. J. & Sharma, A. S. 2010 A critical-layer framework for turbulent pipe flow. *Journal of Fluid Mechanics* **658**, 336–382.

Moarref, R., Sharma, A. S., Tropp, J. A. & McKeon, B. J. 2013 Model-based scaling of the streamwise energy density in high-Reynolds-number turbulent channels. *Journal of Fluid Mechanics* **734**, 275–316.

Monty, J. P., Hutchins, N., Ng, H. C. H., Marusic, I. & Chong, M. S. 2009 A comparison of turbulent pipe, channel and boundary layer flows. *Journal of Fluid Mechanics* **632**, 431–442.

Obrist, D. & Schmid, P. J. 2010 Algebraically decaying modes and wave packet pseudo-modes in swept Hiemenz flow. *Journal of Fluid Mechanics* **643**, 309–332.

Obrist, D. & Schmid, P. J. 2011 Algebraically diverging modes upstream of a swept bluff body. *Journal of Fluid Mechanics* **683**, 346–356.

Olver, F. W. J. 2014 *Asymptotics and special functions*. Academic press.

Orr, W. M'F. 1907 The stability or instability of the steady motions of a perfect liquid and of a viscous liquid. part ii: A viscous liquid. In *Proceedings of the Royal Irish Academy. Section A: Mathematical and Physical Sciences*, pp. 69–138. JSTOR.

Qadri, U. A. & Schmid, P. J. 2017 Frequency selection mechanisms in the flow of a laminar boundary layer over a shallow cavity. *Phys. Rev. Fluids* **2**, 013902.

Reddy, S. C. & Henningson, D. S. 1993 Energy growth in viscous channel flows. *Journal of Fluid Mechanics* **252**, 209–238.

Reddy, S. C., Schmid, P. J. & Henningson, D. S. 1993 Pseudospectra of the Orr–Sommerfeld operator. *SIAM Journal on Applied Mathematics* **53** (1), 15–47.

Reynolds, W. C. & Tiederman, W. G. 1967 Stability of turbulent channel flow, with application to Malkus's theory. *Journal of Fluid Mechanics* **27** (2), 253–272.

Robinson, S. K. 1991 Coherent motions in the turbulent boundary layer. *Annual Review of Fluid Mechanics* **23** (1), 601–639.

Rosenberg, K. & McKeon, B. J. 2018 Efficient representation of exact coherent states of the Navier–Stokes equations using resolvent analysis. *Fluid Dynamics Research* **51**, 011401.

Rowley, C. W. & Dawson, S. T. M. 2017 Model reduction for flow analysis and control. *Annual Review of Fluid Mechanics* **49** (1).

Rowley, C. W., Mezić, I., Bagheri, S., Schlatter, P. & Henningson, D. S. 2009 Spectral analysis of nonlinear flows. *Journal of Fluid Mechanics* **641** (1), 115–127.

Saxton-Fox, T. & McKeon, B. J. 2017 Coherent structures, uniform momentum zones and the streamwise energy spectrum in wall-bounded turbulent flows. *Journal of Fluid Mechanics* **826**.

Schmid, P. J. 2007 Nonmodal stability theory. *Annual Review of Fluid Mechanics* **39**, 129–62.

Schmid, P. J. 2010 Dynamic mode decomposition of numerical and experimental data. *Journal of Fluid Mechanics* **656**, 5–28.

Schmid, P. J. & Henningson, D. S. 1994 Optimal energy density growth in Hagen–Poiseuille flow. *Journal of Fluid Mechanics* **277**, 197–225.

Schmid, P. J. & Henningson, D. S. 2012 *Stability and transition in shear flows*. Springer Science & Business Media.

Schmid, P. J. & Sesterhenn, J. 2008 Dynamic mode decomposition of numerical and experimental data. In *61st Annual Meeting of the APS Division of Fluid Dynamics*. American Physical Society.

Schmidt, O. T., Towne, A., Rigas, G., Colonius, T. & Brès, G. A. 2018 Spectral analysis of jet turbulence. *Journal of Fluid Mechanics* **855**, 953–982.

Schoppa, W. & Hussain, F. 2002 Coherent structure generation in near-wall turbulence. *Journal of fluid Mechanics* **453**, 57–108.

Sharma, A. S., Mezić, I. & McKeon, B. J. 2016 Correspondence between Koopman mode decomposition, resolvent mode decomposition, and invariant solutions of the Navier–Stokes equations. *Phys. Rev. Fluids* **1**, 032402.

Sharma, A. S. & McKeon, B. J. 2013 On coherent structure in wall turbulence. *Journal of Fluid Mechanics* **728**, 196–238.

Sharma, A. S., Moarref, R. & McKeon, B. J. 2017 Scaling and interaction of self-similar

modes in models of high Reynolds number wall turbulence. *Phil. Trans. R. Soc. A* **375** (2089), 20160089.

SMITS, A. J., MCKEON, B. J. & MARUSIC, I. 2011 High–Reynolds number wall turbulence. *Annual Review of Fluid Mechanics* **43**.

SYMON, S., ROSENBERG, K., DAWSON, S. T. M. & MCKEON, B. J. 2018 Non-normality and classification of amplification mechanisms in stability and resolvent analysis. *Physical Review Fluids* **3** (5), 053902.

TAIRA, K., BRUNTON, S. L., DAWSON, S. T. M., ROWLEY, C. W., COLONIUS, T., MCKEON, B. J., SCHMIDT, O. T., GORDEYEV, S., THEOFILIS, V. & UKEILEY, L. S. 2017 Modal analysis of fluid flows: An overview. *AIAA Journal* pp. 1–29.

THEODORSEN, T. 1952 Mechanisms of turbulence. In *Proceedings of the 2nd Midwestern Conference on Fluid Mechanics, 1952*.

TOWNE, A., SCHMIDT, O. T. & COLONIUS, T. 2018 Spectral proper orthogonal decomposition and its relationship to dynamic mode decomposition and resolvent analysis. *Journal of Fluid Mechanics* **847**, 821–867.

TREFETHEN, L. N. 2005 Wave packet pseudomodes of variable coefficient differential operators. In *Proceedings of the Royal Society of London A: Mathematical, Physical and Engineering Sciences*, , vol. 461, pp. 3099–3122. The Royal Society.

TREFETHEN, L. N. & CHAPMAN, S. J. 2004 Wave packet pseudomodes of twisted Toeplitz matrices. *Communications on Pure and Applied Mathematics: A Journal Issued by the Courant Institute of Mathematical Sciences* **57** (9), 1233–1264.

TREFETHEN, L. N. & EMBREE, M. 2005 *Spectra and pseudospectra: the behavior of nonnormal matrices and operators*. Princeton University Press.

TREFETHEN, L. N., TREFETHEN, A. E., REDDY, S. C. & DRISCOLL, T. A. 1993 Hydrodynamic stability without eigenvalues. *Science* **261** (5121), 578–584.

VALLÉE, O. & SOARES, M. 2010 *Airy functions and applications to physics*. World Scientific Publishing Company.

WEIDEMAN, J. A. & REDDY, S. C. 2000 A Matlab differentiation matrix suite. *ACM Transactions on Mathematical Software (TOMS)* **26** (4), 465–519.

WU, X., MOIN, P., WALLACE, J. M., SKARDA, J., LOZANO-DURÁN, A. & HICKEY, J.-P. 2017 Transitional–turbulent spots and turbulent–turbulent spots in boundary layers. *Proceedings of the National Academy of Sciences* p. 201704671.

YEH, C.-A. & TAIRA, K. 2018 Resolvent-analysis-based design of airfoil separation control. *arXiv preprint arXiv:1805.02128* .

ZARE, A., JOVANOVIĆ, M. R. & GEORGIOU, T. T. 2017 Colour of turbulence. *Journal of Fluid Mechanics* **812**, 636–680.

ZHOU, J., ADRIAN, R. J., BALACHANDAR, S. & KENDALL, T. M. 1999 Mechanisms for generating coherent packets of hairpin vortices in channel flow. *Journal of Fluid Mechanics* **387**, 353–396.

Resolvent-based study of compressibility effects on supersonic turbulent boundary layers

H. Jane Bae[1]†, Scott T. M. Dawson[2] and Beverley J. McKeon[1]

[1]Graduate Aerospace Laboratories, California Institute of Technology, Pasadena, CA 91125, USA

[2]Mechanical, Materials and Aerospace Engineering Department, Illinois Institute of Technology, Chicago, IL 60616, USA

The resolvent formulation of McKeon & Sharma (2010) is extended to the compressible Navier-Stokes equations. Resolvent analysis is applied to the supersonic turbulent boundary layer in order to study the validity of Morkovin's hypothesis, which postulates that high-speed turbulence structure in zero pressure-gradient turbulent boundary layers remains largely the same as its incompressible counterpart. Supersonic turbulent boundary layers with adiabatic wall boundary conditions at Mach numbers ranging from 2 to 4 are considered. Resolvent analysis highlights two distinct regions of the supersonic turbulent boundary layer in the wave parameter space: the relatively supersonic region and the relatively subsonic region. In the relatively supersonic region, where the flow is supersonic relative to the freestream, resolvent modes display structures consistent with the eddy Mach wave radiation that are absent in the incompressible regime. In the relatively subsonic region, we show that the low-rank approximation of the resolvent operator is effective and that the model exhibits universal and geometrically self-similar behaviour via a transformation given by the semi-local scaling. Moreover, with semi-local scaling, we show that the resolvent modes follow the same scaling law as their incompressible counterparts in this region, which has implications for modelling and the prediction of turbulent high-speed wall-bounded flows. We also show that the thermodynamic variables exhibit similar mode shapes to the streamwise velocity modes, supporting the strong Reynolds analogy. Finally, we demonstrate that the principal resolvent modes can be used to predict the energy distribution between momentum and thermodynamic fluctuations.

1. Introduction

The prediction and modelling of turbulent high-speed wall-bounded flows remain an active field of study for their tremendous technological importance in the aerospace industry with respect to high-speed vehicles, where the turbulent boundary layers determine the aerodynamic drag and heat transfer. With respect to supersonic and hypersonic turbulent boundary layers, a major role has been historically played by experiments, with direct numerical simulations (DNS) becoming more and more common in the last decade.

Experimental investigations of supersonic and hypersonic turbulent boundary layers have been conducted historically with hot-wire anemometry (Kistler 1959; Laderman & Demetriades 1974; Owen *et al.* 1975; Spina & Smits 1987; Konrad & Smits 1998) (see also Roy & Blottner 2006, for a review), which suffer from uncertainties associated

† Email address for correspondence: hjbae@caltech.edu

with mixed-mode sensitivity (Kovasznay 1953) and were later shown to suffer from poor frequency response and spatial resolution (Williams *et al.* 2018). In addition to hot-wire anemometry, direct measurements of spatially varying velocity fields of high-speed turbulent boundary layers have been attempted using particle image velocimetry (Ekoto *et al.* 2008; Tichenor *et al.* 2013; Peltier *et al.* 2016; Williams *et al.* 2018), which range up to Mach number of 7.5 for a flat-plate turbulent boundary layer.

Complementary to experiments, DNS of high-speed turbulent boundary layers have been conducted to overcome the experimental difficulties and provide access to three-dimensional turbulence statistics. Several DNS have been conducted with emphasis on studying Morkovin's scaling in turbulent boundary layers with moderate freestream Mach numbers (Guarini *et al.* 2000; Maeder 2000; Pirozzoli *et al.* 2004; Martín 2007; Shahab *et al.* 2011; Bernardini & Pirozzoli 2011; Pirozzoli & Bernardini 2011; Hadjadj *et al.* 2015; Poggie *et al.* 2015; Trettel & Larsson 2016; Modesti & Pirozzoli 2016) for both adiabatic and isothermal wall boundary conditions. Higher Mach number hypersonic studies for turbulent boundary layers have also recently been available (Duan *et al.* 2010, 2011; Duan & Martin 2011; Lagha *et al.* 2011; Zhang *et al.* 2014, 2018) with data sets of up to Mach number of 20.

In spite of the recent developments in the numerical experiments, simulations of supersonic turbulent boundary layers still remain a daunting challenge. DNS in the incompressible regime (Simens *et al.* 2009) as well as earlier experiments (Erm & Joubert 1991) show that a fully developed state of the boundary layer requires the use of an extremely long computational domain, which makes accurate numerical simulations extremely computationally demanding. Simulations in the supersonic regime are further slowed down by the inherently larger computational effort and the possible occurrence of 'eddy shocklets'. This creates a critical demand for model-based approaches that describe and predict the behaviour of turbulent flows at technologically relevant high Reynolds numbers in the supersonic regime.

Resolvent analysis forms a rich tool to understand and predict flows using a low-rank approximation of the linear sub-system with the nonlinear interactions being considered a forcing term. Previous studies on incompressible flows show that resolvent analysis can capture a range of phenomena already observed in wall turbulence from near-wall streak and quasi-streamwise vortices (McKeon & Sharma 2010), hairpin vortices (Sharma & McKeon 2013) and the corresponding pressure signature (Luhar *et al.* 2014), very large scale motions (McKeon & Sharma 2010), to scaling of the statistics (Moarref *et al.* 2013). As such, it yields an efficient basis for the flow, which can be used to provide a low order representation of the key dynamical processes of turbulence. Several studies have investigated more sophisticated means of shaping the nonlinear forcing from data and analytical considerations (Moarref *et al.* 2014; Zare *et al.* 2017; Towne *et al.* 2019). For turbulent channel flows (and consequently for turbulent boundary layers), the resolvent has a universal scaling with Reynolds number, and in the overlap region of the mean velocity, it admits geometric self-similarity (Moarref *et al.* 2013, 2014). This observation has strong implications for modelling: resolvent modes throughout the entire region can be described in terms of modes assessed at one wall-normal plane. For example, under the correct scaling of the wall-parallel wavenumbers, the self-similar hierarchies of response modes give rise to self-similar families of vortical structures. However, there has been less work applying this operator based decomposition to fully-developed compressible flows, with the exception of the recent studies on compressible jet flows (Jeun *et al.* 2016; Towne *et al.* 2018; Schmidt *et al.* 2018) and subsonic aerofoils (Yeh & Taira 2019).

The main goal of this work is to extend the resolvent analysis framework to compressible flows and, in particular, to supersonic turbulent boundary layers. The resolvent

framework allows the decomposition of the governing equations in the wavenumber-frequency space, making a more in depth comparison of the underlying mechanisms possible. We utilise this tool to compare the mechanisms driving the incompressible and compressible boundary layer which will allows us to validate Morkovin's hypothesis (Morkovin 1962) on a mode-by-mode basis. Morkovin (1962) concluded from the analysis of supersonic boundary layer data available at the time that for moderate Mach numbers "the essential dynamics of these shear flows will follow the incompressible pattern." The hypothesis was used and reformulated by Bradshaw (1974) to indicate that high-speed boundary layers can be computed using the same model as at low speeds by assuming that the density fluctuations are weak. Another consequence of Morkovin's hypothesis is the analogy between the temperature and velocity fields that leads to velocity-temperature relations such as the classical Walz formula (Walz 1969) and the strong Reynolds analogy and its variants (Morkovin 1962; Gaviglio 1987; Huang *et al.* 1995; Zhang *et al.* 2014). It also motivates the so-called 'compressibility transformations' that transform the mean velocity and Reynolds stress profiles in a compressible boundary layer to equivalent incompressible profiles by accounting for mean property variations across the thickness of the boundary layer (Van Driest 1951; Brun *et al.* 2008; Zhang *et al.* 2012; Trettel & Larsson 2016; Yang & Lv 2018).

The paper is organised as follows. We first introduce the compressible Navier-Stokes equations and the resolvent operator in §2, where we discuss the relevant resolvent norm, boundary conditions and computational methods. In §3, we discuss the characteristics of the resolvent modes for the supersonic turbulent boundary layer and define the relatively supersonic and subsonic region. We show that the response modes in the relatively supersonic region display Mach waves. We also highlight the low-rank behaviour of the resolvent operator and discuss the necessary conditions for universality of the resolvent modes in the relatively subsonic region. In §4, we then provide the Reynolds and Mach number scaling for the principal resolvent modes and amplification factor for the inner, logarithmic and outer region of the boundary layer and demonstrate that the leading response mode is enough to predict the energy distribution between momentum and thermodynamic fluctuations. Finally, we conclude the paper in §5.

2. Resolvent formulation of compressible turbulent boundary layer

2.1. *Compressible Navier-Stokes equations*

The non-dimensional compressible Navier-Stokes equations for a perfect gas are given by

$$\rho \left(\frac{\partial u_i}{\partial t} + u_j \frac{\partial u_i}{\partial x_j} \right) = -\frac{1}{\gamma M^2} \frac{\partial p}{\partial x_i} + \frac{1}{Re} \frac{\partial}{\partial x_j} \left[\mu \left(\frac{\partial u_i}{\partial x_j} + \frac{\partial u_j}{\partial x_i} \right) + \lambda \frac{\partial u_k}{\partial x_k} \delta_{ij} \right], \quad (2.1)$$

$$\frac{\partial \rho}{\partial t} + u_j \frac{\partial \rho}{\partial x_j} = -\rho \frac{\partial u_i}{\partial x_i}, \quad (2.2)$$

$$\rho \left(\frac{\partial T}{\partial t} + u_j \frac{\partial T}{\partial x_j} \right) = -(\gamma - 1)p \frac{\partial u_i}{\partial x_i} + \frac{\gamma}{PrRe} \frac{\partial}{\partial x_j} \left(k \frac{\partial T}{\partial x_j} \right)$$

$$+ \gamma(\gamma - 1) \frac{M^2}{Re} \mu \left[\frac{\partial u_i}{\partial x_j} \frac{\partial u_i}{\partial x_j} + \frac{\partial u_i}{\partial x_j} \frac{\partial u_j}{\partial x_i} + \lambda \left(\frac{\partial u_k}{\partial x_k} \right)^2 \right], \quad (2.3)$$

where ρ, p, u_i, T are, respectively, density, pressure, velocity components, and temperature. Variables μ, λ are the coefficients of first and second viscosity, respectively, k is the coefficient of thermal conductivity, $\gamma = c_p/c_v$ is the ratio of specific heats, and δ_{ij} is

the Kronecker delta. We formulate the equations in nondimensionalised form using the Mach, Reynolds, and Prandtl numbers, given respectively by

$$M = \frac{u^*}{\sqrt{\gamma \mathcal{R} T^*}}, \quad Re = \frac{\rho^* u^* l^*}{\mu^*}, \quad Pr = \frac{\mu^* c_p}{k^*}, \tag{2.4}$$

where $(\cdot)^*$ denotes reference (dimensional) quantities, l is a length scale, and $\mathcal{R}$ is the gas constant. The system is closed with the equation of state, $p = \rho T$.

Here, we assume constant specific heat coefficients and constant Prandtl number, $Pr = 0.72$, and we set $\gamma = 1.4$ (diatomic gas). Furthermore, we assume that viscosity varies with temperature according to the Sutherland formula

$$\mu(T) = \frac{T^{3/2}(1+C)}{T+C} \tag{2.5}$$

with $C = S/T^*$, where $S = 110.4$K, and that the second coefficient of viscosity λ follows the Stokes' assumption $\lambda = -2/3\mu$.

2.2. *Resolvent operator*

Assuming a fully developed, locally parallel flow with the directions x_1, x_2 and x_3 signifying the streamwise, wall-normal, and spanwise directions, respectively, the state variable $\boldsymbol{q} = [q_1, q_2, q_3, q_4, q_5]^\dagger = [u_1, u_2, u_3, \rho, T]^\dagger$ is decomposed using the Fourier transform in homogeneous directions and time,

$$\boldsymbol{q}(x_1, x_2, x_3, t) = \iiint_{-\infty}^{\infty} \hat{\boldsymbol{q}}(x_2; \kappa_1, \kappa_3, \omega) e^{\mathrm{i}(\kappa_1 x_1 + \kappa_3 x_3 - \omega t)} \mathrm{d}\kappa_1 \mathrm{d}\kappa_3 \mathrm{d}\omega, \tag{2.6}$$

where $\hat{(\cdot)}$ denotes variables in the transformed domain, and the triplet $(\kappa_1, \kappa_3, \omega)$ identifies the streamwise and spanwise wavenumbers and the temporal frequency, respectively. Here, the superscript $\dagger$ denotes the transpose for real variables (vectors) and the conjugate transpose for complex values.

Note that the mean turbulent state, $\bar{\boldsymbol{q}}(x_2) = [\bar{u}_1(x_2), 0, 0, \bar{\rho}(x_2), \bar{T}(x_2)]^\dagger$, corresponds to $(\kappa_1, \kappa_3, \omega) = (0, 0, 0)$ and is assumed to be known. More generally, the shape of the mean profile acts as a constraint on the full nonlinear closure. Furthermore, with the parallel-flow assumption, which is reasonable as the base flow variations depend on the viscous time scale compared to the much faster convective times scale for fluctuations, the mean momentum equation (2.1) gives a constant $\bar{p}(x_2)$. In the remainder of the paper, we scale the pressure such that $\bar{p} = 1$ for simplicity. Note that the spatially-developing turbulent boundary layer can be studied using resolvent analysis, and the associated increase in computational effort is not prohibitive. However, the interpretation of the underlying physical mechanisms is significantly more straightforward for the quasi-parallel, one-dimensional mean.

Following a similar approach to McKeon & Sharma (2010), the governing equations

(2.1)–(2.3) can be rewritten in the Fourier domain for each $(\kappa_1, \kappa_3, \omega) \neq (0, 0, 0)$ as

$$
\begin{aligned}
-\mathrm{i}\omega\hat{u}_i + \bar{u}_1\partial_1\hat{u}_i + \hat{u}_2\partial_2\bar{u}_i = & -\frac{1}{\gamma M^2}\left(\partial_i\hat{T} + \partial_i\hat{\rho}\bar{T}^2 + \hat{\rho}\bar{T}\partial_i\bar{T}\right) \\
& + \frac{\bar{T}}{Re}\left[\bar{\mu}\partial_j\left(\partial_j\hat{u}_i + \partial_i\hat{u}_j\right) + \bar{\lambda}\partial_i\left(\partial_j\hat{u}_j\right) + \frac{\partial\bar{\mu}}{\partial T}\partial_j\hat{T}\left(\partial_j\bar{u}_i + \partial_i\bar{u}_j\right)\right] + \hat{f}_i \quad (2.7)
\end{aligned}
$$

$$
-\mathrm{i}\omega\hat{\rho} + \bar{u}_1\partial_1\hat{\rho} + \hat{u}_2\partial_2\bar{\rho} = -\bar{\rho}\partial_i\hat{u}_i + \hat{f}_4 \tag{2.8}
$$

$$
\begin{aligned}
-\mathrm{i}\omega\hat{T} + \bar{u}_1\partial_1\hat{T} + \hat{u}_2\partial_2\bar{T} = & -(\gamma - 1)\bar{T}\partial_i\hat{u}_i \\
& + \frac{\gamma\bar{T}}{PrRe}\left[\bar{\mu}\partial_j\partial_j\hat{T} + \frac{\partial^2\bar{\mu}}{\partial T^2}(\partial_2\bar{T})^2\hat{T} + 2\frac{\partial\bar{\mu}}{\partial T}\partial_2\bar{T}\partial_2\hat{T} + \frac{\partial\bar{\mu}}{\partial T}\partial_2^2\bar{T}\hat{T}\right] + \hat{f}_5, \quad (2.9)
\end{aligned}
$$

where $\hat{\boldsymbol{f}}$ contains the nonlinear terms and $(\partial_1, \partial_2, \partial_3) = (\mathrm{i}\kappa_1, \mathrm{d}/\mathrm{d}y, \mathrm{i}\kappa_3)$. This can be equivalently expressed as

$$
\hat{\boldsymbol{q}}(x_2; \kappa_1, \kappa_3, \omega) = [-\mathrm{i}\omega\boldsymbol{I} + \boldsymbol{L}(\kappa_1, \kappa_3, \omega)]^{-1}\,\hat{\boldsymbol{f}}(x_2; \kappa_1, \kappa_3, \omega), \tag{2.10}
$$

where $\boldsymbol{L}$ is the linearised operator of the governing equations around the supersonic turbulent mean profile (Mack 1984). The operator $\boldsymbol{H} = [-\mathrm{i}\omega\boldsymbol{I} + \boldsymbol{L}(\kappa_1, \kappa_3, \omega)]^{-1}$ is called the resolvent operator and exists if there are no eigenvalues of $\boldsymbol{L}$ with zero real part.

2.3. *Choice of resolvent norm*

From (2.10), we wish to find a decomposition of the resolvent that enables us to identify high gain input and output modes with respect to the linear operator. For the resolvent analysis, the decomposition is given by the Schmidt decomposition (called the singular value decomposition for the discrete case). However, this decomposition must be accompanied by a choice of inner product and the corresponding norm. In the case of the incompressible resolvent operator, the natural and physically meaningful norm is the kinetic energy norm, which is defined as

$$
2K = (\boldsymbol{q}, \boldsymbol{q})_K = \|\boldsymbol{q}\|_K^2 = \int_0^\infty \bar{\rho}u_i^\dagger u_i \, \mathrm{d}x_2. \tag{2.11}
$$

Unfortunately, there is no obvious choice for the compressible case and the standard incompressible kinetic energy norm becomes a seminorm on this space; however, Chu (1965) introduced a norm that eliminates pressure related energy transfer terms (compression work),

$$
2E = (\boldsymbol{q}, \boldsymbol{q})_E = \|\boldsymbol{q}\|_E^2 = \int_0^\infty \left(\bar{\rho}u_i^\dagger u_i + \frac{\bar{T}}{\gamma\bar{\rho}M^2}\rho^\dagger\rho + \frac{\bar{\rho}}{\gamma(\gamma - 1)\bar{T}M^2}T^\dagger T\right)\mathrm{d}x_2 \quad (2.12)
$$

which has been used in numerous other studies of compressible flows where the definition of an inner product is required (e.g., Hanifi *et al.* 1996; Malik *et al.* 2006; Özgen & Kırcalı 2008; Malik *et al.* 2008; de Pando *et al.* 2014; Bitter & Shepherd 2014; Dawson & McKeon 2019), and this norm will be used for the remainder of the paper. Discussion of other possible inner products and assumptions for compressible flows are given in Rowley *et al.* (2004). Preliminary study on the sensitivity of the resolvent modes with respect to the compressible inner product was studied in Dawson & McKeon (2019) for the compressible planar Couette flow, and the differences are attributed to both the change in mean profiles and the compressible fluctuation equations rather than the choice of the inner product.

We take the Schmidt decomposition of the resolvent, namely,

$$\boldsymbol{H} = \sum_{j=1}^{\infty} \boldsymbol{\psi}_j(\kappa_1, x_2, \kappa_3, \omega)\sigma_j(\kappa_1, \kappa_3, \omega)\boldsymbol{\phi}_j^{\dagger}(\kappa_1, x_2, \kappa_3, \omega), \quad (2.13)$$

with an orthogonality condition

$$(\boldsymbol{\psi}_i(\kappa_1, x_2, \kappa_3, \omega), \boldsymbol{\psi}_j(\kappa_1, x_2, \kappa_3, \omega))_E = \delta_{ij}, \quad (2.14)$$

$$(\boldsymbol{\phi}_i(\kappa_1, x_2, \kappa_3, \omega), \boldsymbol{\phi}_j(\kappa_1, x_2, \kappa_3, \omega))_E = \delta_{ij}, \quad (2.15)$$

$$(2.16)$$

and $\sigma_j \geqslant \sigma_{j+1} \geqslant 0$. The $\boldsymbol{\phi}_j$ and $\boldsymbol{\psi}_j$ form the right and left Schmidt bases (singular vectors) for the forcing and velocity fields, and the real σ_j are the singular values. This decomposition is unique up to a pre-multiplying unitary complex factor on both bases corresponding to a phase shift (Young 1988).

This basis pair can then be used to decompose arbitrary forcing and the resulting state vector at a particular Fourier component such that

$$\hat{\boldsymbol{f}}(x_2; \kappa_1, \kappa_3, \omega) = \sum_{j=1}^{\infty} \boldsymbol{\phi}_j(\kappa_1, x_2, \kappa_3, \omega)a_j(\kappa_1, \kappa_3, \omega) \quad (2.17)$$

$$\hat{\boldsymbol{q}}(x_2; \kappa_1, \kappa_3, \omega) = \sum_{j=1}^{\infty} \sigma_j(\kappa_1, \kappa_3, \omega)\boldsymbol{\psi}_j(\kappa_1, x_2, \kappa_3, \omega)a_j(\kappa_1, \kappa_3, \omega). \quad (2.18)$$

Clearly the forcing shape that gives the largest energy is given by $a_j = \delta_{1j}$. Moreover, we later show that the resolvent operator is low-rank, i.e. $\sigma_1 \gg \sigma_2$, where the flow is most energetic. Thus, in this paper, we focus on the principal Schmidt bases (singular vectors), i.e. the principal forcing mode $\boldsymbol{\phi}_1$ and the principal response mode $\boldsymbol{\psi}_1 = [(q_1)_1, (q_2)_1, (q_3)_1, (q_4)_1, (q_5)_1]^{\dagger} = [(u_1)_1, (u_2)_1, (u_3)_1, \rho_1, T_1]^{\dagger}$, and the principal singular value σ_1.

2.4. *Boundary conditions*

For the compressible boundary layer, the boundary conditions at the wall are given by

$$u_i(x_2 = 0) = 0, \quad T(x_2 = 0) = \bar{T}(x_2 = 0). \quad (2.19)$$

The boundary conditions on the velocity fluctuations are the usual no-slip conditions, and the boundary condition on the temperature fluctuation is consistent for a gas flowing over a solid wall.

The boundary conditions at the freestream are given by

$$u_i(x_2 \to \infty), \rho(x_2 \to \infty), T(x_2 \to \infty) < \infty, \quad (2.20)$$

which are less restrictive than requiring all fluctuations to be zero at infinity. However, in supersonic flow, waves may propagate to infinity and this boundary condition allows the waves with constant amplitude to be included.

2.5. *Computational methods*

Following the Schmidt decomposition in (2.13), there are an infinite number of singular values in principle. However, we solve the discrete equations using a spectral collocation methods with (N_2+1) points in the wall-normal direction, limiting the number of singular values to $5(N_2 + 1)$, the size of the state vector $\boldsymbol{q}$.

The discrete points in x_2 are given by a rational transformation of the Chebyshev collocation points. The Chebyshev collocation points are defined as

$$x'_2 = \cos \frac{\pi j}{N_2}, \quad j = 0, 1, \ldots, N_2 \tag{2.21}$$

in the domain $-1 \leqslant x'_2 \leqslant 1$. The rational transformation

$$x_2 = a \frac{1 + x'_2}{1 - x'_2} \tag{2.22}$$

maps x'_2 to the semi-infinite domain, where $a/\delta = 2$ is the wall-normal location containing $N_2/2$ points (Grosch & Orszag 1977; Christov 1982) and δ is the boundary layer thickness corresponding to the location where mean velocity reaches 99% of the freestream velocity. With this transformation, the value of a function $\chi(x_2)$ can be expressed as

$$\chi(x_2) = \sum_{n=0}^{N_2} b_n T_n \left(\frac{x_2 - a}{x_2 + a} \right) = \sum_{n=0}^{N_2} b_n T_n(x'_2), \tag{2.23}$$

where T_n is the nth order Chebyshev polynomial and b_n is the coefficient for the corresponding Chebyshev polynomial. Similarly, the derivative of the function $\chi(x_2)$ can be then expressed as

$$\frac{\partial}{\partial x_2} \chi(x_2) = \left(\frac{\partial x'_2}{\partial x_2} \right) \sum_{n=0}^{N_2} b_n \frac{\partial}{\partial x'_2} T_n(x'_2). \tag{2.24}$$

The rational transformation of the Chebyshev collocation points allows the use of spectral methods for the semi-infinite domain required for the turbulent boundary layer. The stretching of the collocation points such that the majority of the points lie within $x_2/\delta \leqslant 2$ is appropriate for most of the energy containing modes that are located within the boundary layer. However, in supersonic flows, waves may propagate to infinity and thus become under-resolved due to the fact the grid resolution $\Delta x_2 \to \infty$ as $x_2 \to \infty$. Nonetheless, the limitation stems from resolving a semi-infinite domain with a finite number of discrete points, and thus any choice of decomposition in the wall-normal direction suffers from this limitation. The resolvent modes considered for this paper are primarily located within the boundary layer, and thus we are not affected by this limitation.

The turbulent mean profiles for the supersonic case are obtained from direct numerical simulations of a spatially evolving zero-pressure-gradient supersonic turbulent boundary layer with the wall temperature set to its nominally adiabatic value (Bernardini & Pirozzoli 2011; Pirozzoli & Bernardini 2011), which are compared against a DNS of an incompressible turbulent boundary layer (Jiménez *et al.* 2010). The cases are chosen such that Re_τ is similar to the Reynolds number for the incompressible case ($Re_\tau \approx 450$). An additional case with $M_\infty = 2$ and $Re_\tau = 900$ was chosen to observe Reynolds number effects. The specific cases used are listed in table 1 along with their respective resolution in numerical computations, where N_2 is the number of collocation grid points in the x_2 direction, N_1 and N_3 are the number of spatial frequencies for κ_1 and κ_2, and N_c is the number of grid points for the wave speed $c = \omega/\kappa_1$.

M_∞	M_τ	Re_τ	Re_θ	N_1	N_2	N_3	N_c	$\log(\Delta\lambda_1/\delta)$	$\log(\Delta\lambda_3/\delta)$	$\Delta x_{2,\min}/\delta$
0	0	445.5	1100.0	81	400	81	25	0.05	0.05	3.08×10^{-5}
2	0.074	447.7	2081.6	81	400	81	25	0.05	0.05	3.08×10^{-5}
2	0.067	898.5	4747.1	81	400	81	25	0.05	0.05	3.08×10^{-5}
3	0.091	502.0	4342.9	81	400	81	25	0.05	0.05	3.08×10^{-5}
4	0.103	504.6	5914.9	81	400	81	25	0.05	0.05	3.08×10^{-5}

Table 1: The freestream Mach number M_∞, friction Mach number M_τ, friction Reynolds number Re_τ, Reynolds number based on momentum thickness Re_θ, and grid resolutions for the different cases. N_i is the number of grid points in the x_i direction and N_c is the number of grid points for the wave speed $c = \omega/\kappa_1$. $\Delta\lambda_i$ and Δx_2 are the grid resolutions in the wall-parallel and wall-normal directions, respectively.

3. Characteristics of resolvent modes for compressible turbulent boundary layer

We first examine the energy contained in the principal response mode. The energy contribution of $\boldsymbol{\psi}_k$ to the total response subject to broadband forcing in the wall-normal direction can be quantified by $\sigma_k^2/(\sum_j \sigma_j)$. Figure 1 shows the principal energy contribution from the principal response mode $\boldsymbol{\psi}_1$ for the incompressible case and the $M_\infty = 4$ case at two wall-normal locations $x_2^+ = 15$ and $x_2/\delta = 0.2$, where the superscript + denotes wall units defined in terms of $\bar{\rho}$ and μ at the wall and the friction velocity u_τ.

The results from the incompressible and compressible turbulent boundary layer show similarities in region where the principal energy contribution of the incompressible boundary layer is concentrated and thus low-rank approximation is valid for the incompressible regime. This region coincides with the most energetic wavenumbers from DNS of incompressible channel flows identified by the premultiplied energy spectra given by the contour lines in the figure.

The most notable difference between the incompressible and compressible results is the triangular region marked by freestream relative Mach number, $\overline{M}_\infty$, greater than unity (figure 1(b)). The relative Mach number, defined as

$$\overline{M}(x_2) = \frac{(\kappa_1 \bar{u}_1(x_2) - \omega)M_\infty}{(\kappa_1^2 + \kappa_3^2)^{1/2}\,\bar{T}(x_2)^{1/2}}, \tag{3.1}$$

can be understood as the local Mach number of the mean flow in the direction of the wavenumber vector, $[\kappa_1, \kappa_3]^\dagger$, relative to the wave speed at a given wall-normal location x_2. A three-dimensional depiction of the principal energy contribution as a function of streamwise and spanwise wavenumbers and wave speeds is given in figure 2 for the incompressible case and the compressible case at three different Mach numbers. It is clear that the region with $\overline{M}_\infty > 1$, i.e. the relatively supersonic region, increases with Mach number and grows from the wall towards the freestream. In linear stability theory, $\overline{M}$ has been used to classify disturbances as subsonic, sonic, or supersonic depending on its value at the boundary layer (Mack 1984; Schmid & Henningson 2000). Moreover, it has been shown that if $\overline{M} > 1$, a compressible boundary layer is unstable to inviscid waves regardless of any other feature of the velocity and temperature profiles (Mack 1984). Considering that the family of modes with $\overline{M} > 1$ does not have any counterpart in incompressible boundary layers, it is expected that the most deviation between the behaviour of the compressible and incompressible boundary layers occurs in this regime.
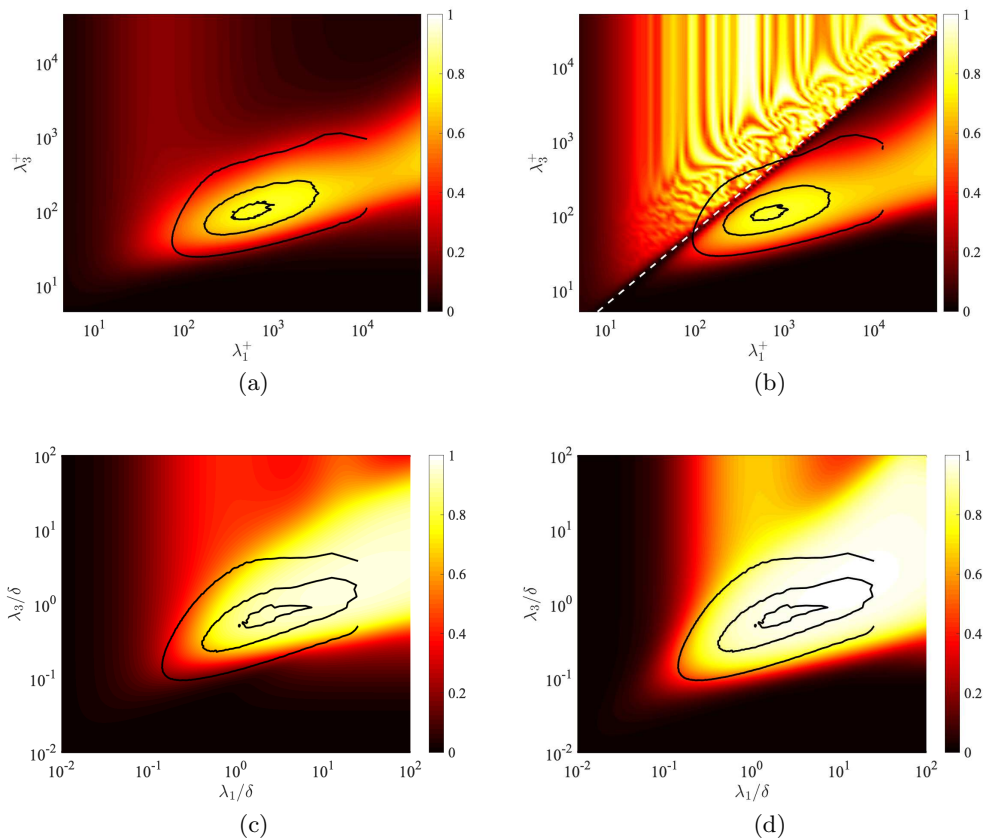
Figure 1: Energy contained in the principal response mode relative to the total response, $\sigma_1^2/(\sum_j \sigma_j^2)$, for different streamwise and spanwise wavelengths for the (a,c) incompressible and (b,d) compressible ($M_\infty = 4$) turbulent boundary layer at (a,b) $x_2^+ = 15$ and (c,d) $x_2/\delta = 0.2$. The contours are 10%, 50%, and 90% of the maximum energy of the premultiplied energy spectra for channel flow at $Re_\tau \approx 550$ (Del Alamo *et al.* 2004) at the corresponding wall-normal locations. The white dashed line indicates the relative Mach number of unity, $\overline{M}_\infty = 1$.

In particular, the irregular low-rank behaviour present in the relatively supersonic region in figure 1(b), marked by bright regions, is due to the discrete acoustic eigenmodes of the system approaching the wave speed c, thus giving resonant amplification of the resolvent operator (Dawson & McKeon 2019). For details, see Appendix A.

The second, and less significant, difference can be seen for the two spectra at $x_2/\delta = 0.2$, where the region of high energy contribution covers a much wider range of wall-parallel wavelengths for the $M_\infty = 4$ case, with the 'nose' of the spectra located at a smaller $(\lambda_1/\delta, \lambda_3/\delta)$.

The first observation regarding the relative Mach number of unity can be explained by the formation of Mach waves in the relatively supersonic region. The second can be comprehended in terms of the correct scaling required for the compressible boundary layer. The two main observations will be discussed in the remainder of this section.
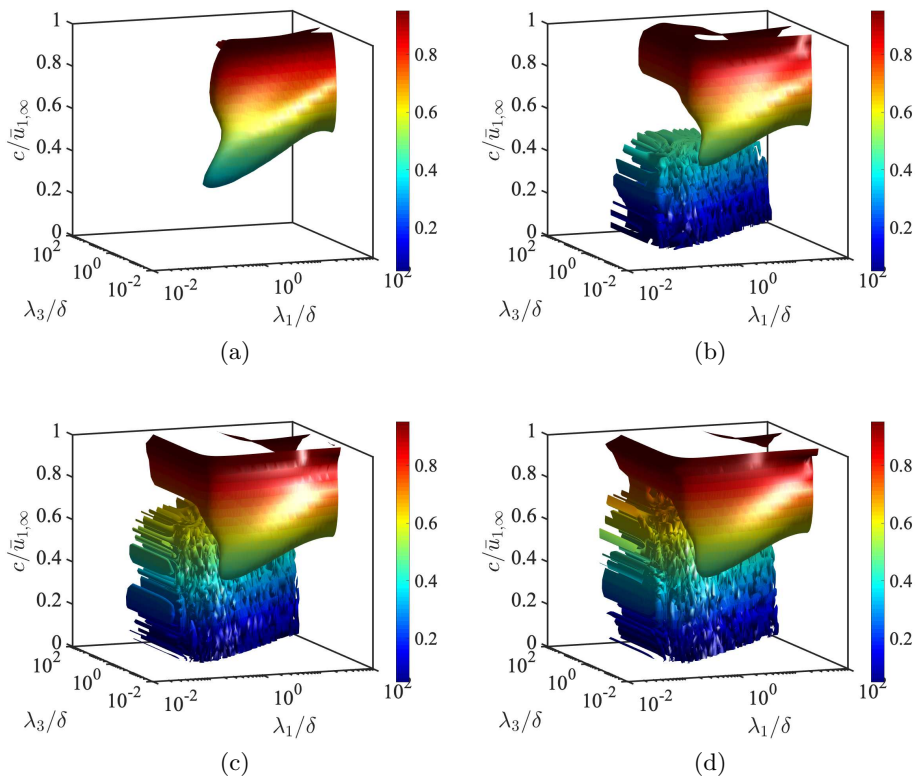
Figure 2: Energy contained in the principal response mode relative to the total response, $\sigma_1^2/(\sum_j \sigma_j^2)$, for different streamwise and spanwise wavelengths and wall-normal distance for the (a) incompressible, (b) $M_\infty = 2$, $Re_\tau = 450$, (c) $M_\infty = 3$ and (d) $M_\infty = 4$ cases. The contour surface is $\sigma_1^2/(\sum_j \sigma_j^2) = 0.75$ coloured by wall-normal distance from the wall.

3.1. *Relatively supersonic region and Mach waves*

As displayed by the energy contribution in figure 1, the resolvent operator is shown to be low-rank for the supersonic turbulent boundary layer as well. Moarref *et al.* (2013) showed that significant understanding of the scaling of wall turbulence can be obtained by using the simple rank-1 model. Here, we employ the same rank-1 model by only keeping the most energetic forcing and response directions corresponding to σ_1 and compute the premultiplied one-dimensional energy density of the principal response of $\boldsymbol{H}$ defined as

$$E_{qq}(x_2, \omega) = \sum_{i=1}^{5} \frac{\iint \kappa_1^2 \kappa_3 \left[\sigma_1(\kappa_1, \kappa_3, \omega) |(q_i)_1|(\kappa_1, x_2, \kappa_3, \omega) \right]^2 \mathrm{d}\log \kappa_1 \mathrm{d}\log \kappa_3}{\max \iint \kappa_1^2 \kappa_3 \sigma_1(\kappa_1, \kappa_3, \omega)^2 \mathrm{d}\log \kappa_1 \mathrm{d}\log \kappa_3}. \tag{3.2}$$

In figure 3(a) and (b), we plot the energy density as a function of wave speed c and x_2 for both the incompressible and supersonic ($M_\infty = 2$, $Re_\tau = 450$) turbulent boundary layers. Unlike the incompressible case, where the energy density is localised around the mean velocity profile (solid line), the compressible case shows a second region which is displaced from the mean velocity. The overlaid relative sonic line (dashed line), where the velocity profile corresponds to relative streamwise Mach number of unity at each
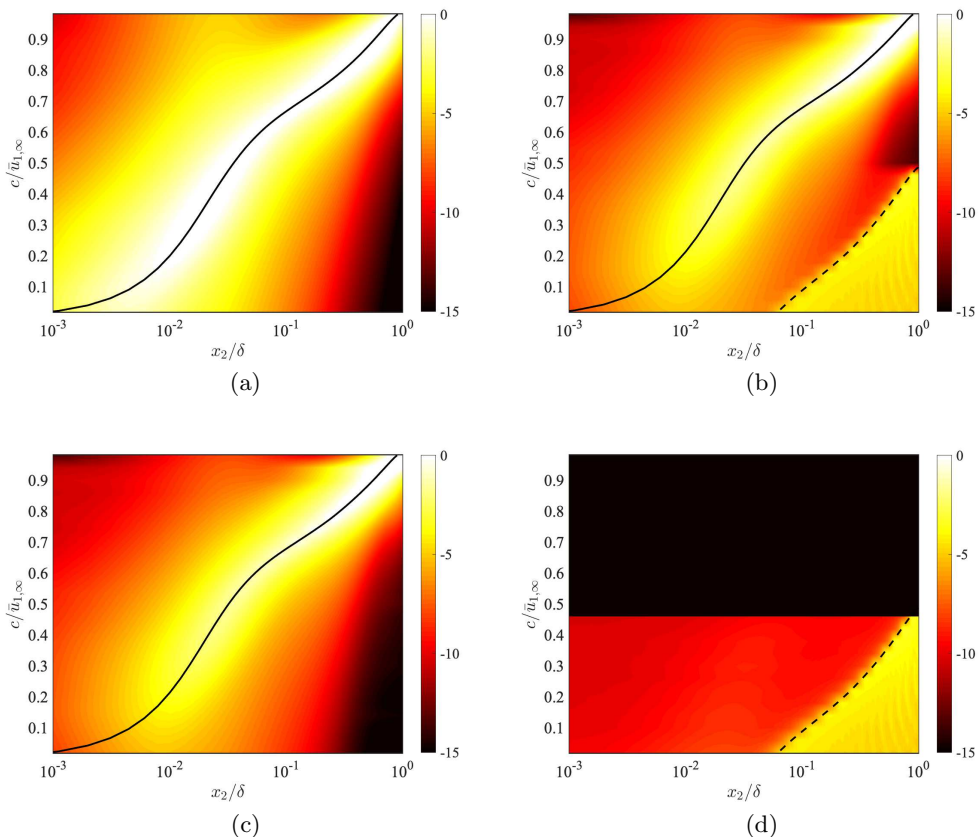
Figure 3: Premultiplied one-dimensional energy density E_{qq} for the (a) incompressible and (b) compressible ($M_\infty = 2$, $Re_\tau = 450$) cases, and the energy density for the compressible case conditionally sampled to (c) $\overline{M} < 1$ and (d) $\overline{M} > 1$. The turbulent mean velocity profile, $\bar{u}_1$ (——) and the relative sonic line $\bar{c}$ (- - -) are shown for reference.

wall-normal location, shows that the displacement of the areas of high energy density are indicative of Mach waves. The relative sonic line $\bar{c}$ is given by solving

$$\overline{M} = \frac{(\kappa_1 \bar{u}_1 - \kappa_1 \bar{c}) M_\infty}{\left(\kappa_1^2 + \kappa_3^2\right)^{1/2} \bar{T}^{1/2}} = 1 \tag{3.3}$$

at each x_2 for $\kappa_3 = 0$, i.e. $\bar{c} = \bar{u}_1 - \bar{T}^{1/2}/M_\infty$, and indicates the minimum streamwise velocity at each x_2 where a relatively supersonic region exists. By conditionally sampling the energy intensity for $\overline{M}_\infty < 1$ or $\overline{M}_\infty > 1$ (as shown in figure 3(c) and (d)), the two phenomenon can clearly be separated, and the region of high energy density resembling Mach waves are attributed entirely to the relatively supersonic region of $\overline{M}_\infty > 1$.

In figure 4, we plot a few of the principal streamwise velocity response modes $(u_1)_1$ for both the incompressible and compressible ($M_\infty = 2$, $Re_\tau = 450$) cases at $(\lambda_1/\delta, \lambda_3/\delta) = (0.01, 10)$, which lie within the region $\overline{M}_\infty > 1$ for the compressible case for a variety of wave speeds. Note that the modes under consideration are essentially two-dimensional, as we need $\lambda_1 \ll \lambda_3$ in order for the relatively supersonic region to exist for a wide range of wall-normal locations. This aspect ratio has not been studied in the past in
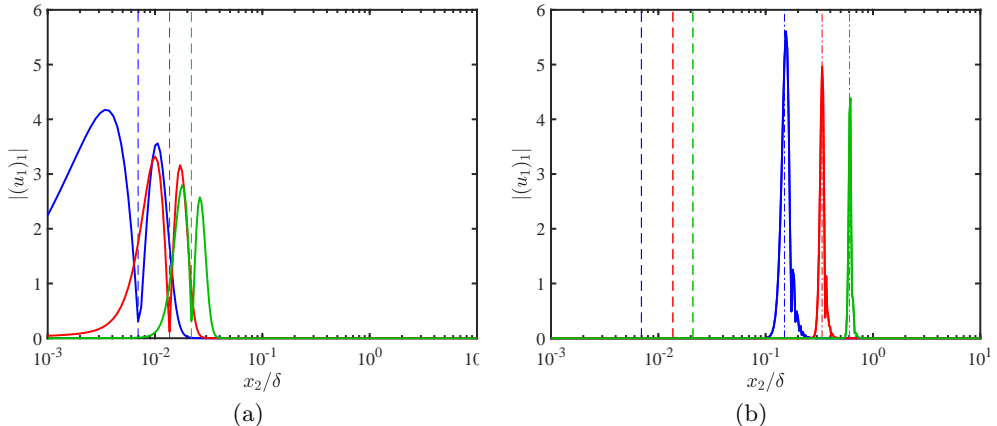
Figure 4: The response modes $(u_1)_1$ for the (a) incompressible and (b) supersonic ($M_\infty =$ 2, $Re_\tau = 450$) turbulent boundary layer with $\lambda_1/\delta = 0.01$, $\lambda_3/\delta = 10$, and $c = 0.14$ (blue), 0.26 (red), 0.38 (green). Reference lines are $x_2 = x_2^c$ (- - -) and $x_2 = x_2^s$ (-·-·).

the context of unforced turbulent boundary layers and the mode shapes that occur here are different from the nominal three-dimensional case. Examining the principal response modes, we see the the modes for the incompressible case (figure 4(a)) are centred at the critical layer x_2^c, where $\bar{u}_1(x_2^c) = c$, but the modes corresponding to $\overline{M}_\infty > 1$ for the compressible case (figure 4(b)) are centred at the sonic layer, x_2^s, where $\overline{M}(x_2^s) = 1$. These response modes are consistent with Mach waves that propagate towards the freestream and the idea of eddy shocklets (Phillips 1960; Ffowcs Williams & Maidanik 1965), where the instantaneous supersonic events cause local shock-like structures in the boundary layer. However, the formation of eddy shocklets from superimposed Mach waves require additional knowledge of phase for each wave parameter and is not dealt with here in regards to the linear analysis.

3.2. *Relatively subsonic region and universality of resolvent modes*

In order for the resolvent modes to exhibit universal behaviour for different Re_τ, the modes must have a narrow footprint in the wall-normal direction such that the resolvent modes are purely affected by a certain part of the mean velocity that scales uniquely with Reynolds number (Moarref *et al.* 2013). Moreover, the necessary condition for the existence of geometrically self-similar resolvent modes is the presence of a logarithmic region in the turbulent mean velocity profile.

In order for the resolvent modes to be universal for the supersonic boundary layer, not only do the modes have to be localised in x_2, but the mean velocity profile must have a scaling law similar to that of the incompressible case such that different regions of the mean profiles collapse for various M_∞ and Re_τ. In compressible flows, viscous heating causes non-uniform mean density and viscosity, which results in a mean velocity profile that no longer satisfies the scaling of its incompressible counterpart. Many attempts have been made to recover the scalings in this regime (Wilson 1950; Van Driest 1951; Coles 1964; Zhang *et al.* 2012; Trettel & Larsson 2016, among others), with particular emphasis on the logarithmic region. Most of these attempts have been made by seeking a transformation of $\bar{u}_1$ and x_2 such that the compressible velocity profile maps onto an equivalent incompressible profile. The most recent of these approaches given by Trettel
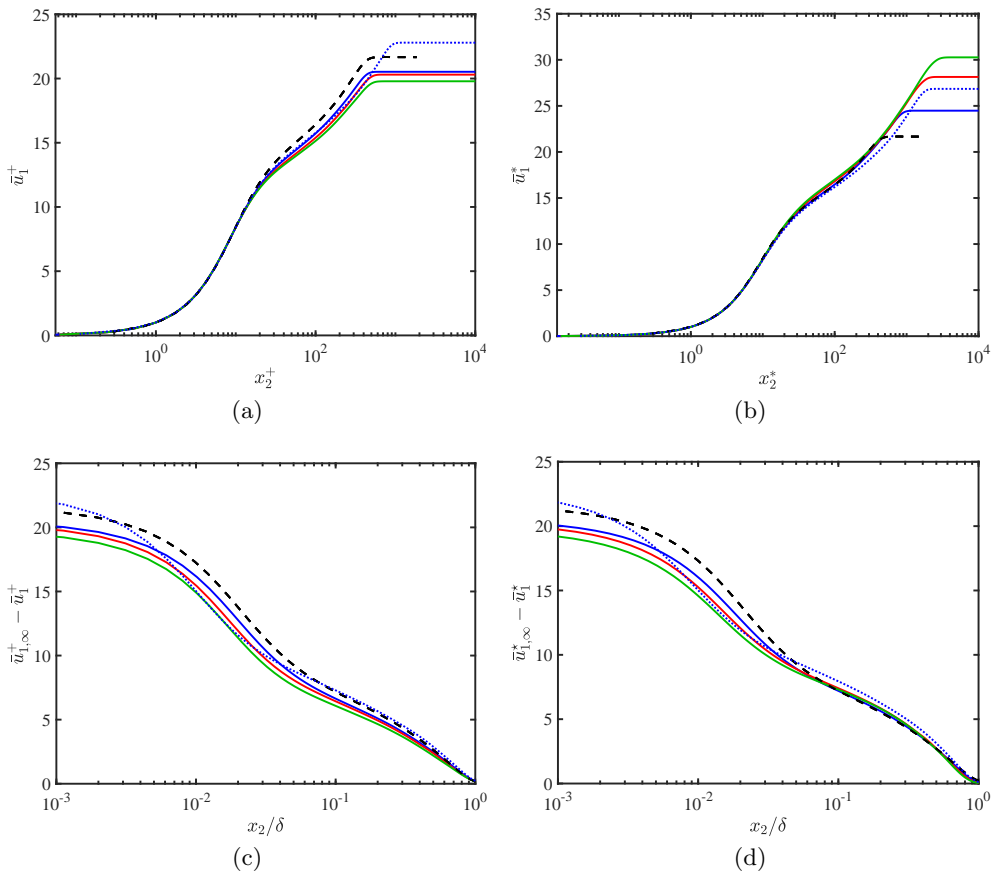
Figure 5: (a) Turbulent mean streamwise velocity profile $\bar{u}_1^+(x_2^+)$, (b) the transformed velocity profile $\bar{u}_1^*(x_2^*)$ given by (3.5), (c) the defect velocity $\bar{u}_{1,\infty}^+ - \bar{u}_1^+(x_2/\delta)$ with respect to the freestream, and (d) the transformed defect velocity $\bar{u}_{1,\infty}^\star - \bar{u}_1^\star(x_2/\delta)$ given by (3.7). Lines indicate $M_\infty = 0$ (- - -), $M_\infty = 2$, $Re_\tau = 450$ (——), $M_\infty = 2$, $Re_\tau = 900$ (⋯⋯), $M_\infty = 3$ (——), and $M_\infty = 4$ (——).

& Larsson (2016) utilises a semi-local scaling in x_2 and a integrated stress-balance condition, which assumes that the sum of viscous and Reynolds stresses in both the raw and transformed states must be equal, for the scaling of $\bar{u}_1$ such that

$$x_2^* = \frac{\bar{\rho}\,(\tau_w/\bar{\rho})^{1/2}\,x_2}{\bar{\mu}}, \tag{3.4}$$

$$\bar{u}_1^* = \int_0^{\bar{u}_1^+} \left(\frac{\bar{\rho}}{\bar{\rho}_w}\right)^{1/2} \left(1 + \frac{1}{2\bar{\rho}}\frac{\mathrm{d}\bar{\rho}}{\mathrm{d}x_2}x_2 - \frac{1}{\bar{\mu}}\frac{\mathrm{d}\bar{\mu}}{\mathrm{d}x_2}x_2\right)\mathrm{d}\bar{u}_1^+. \tag{3.5}$$

Here, the subscript w indicates quantities evaluated at the wall and τ_w is the wall shear stress. The results of this transformation are illustrated in figure 5(a) and (b), and an improved collapse of the mean velocity profile in the inner and logarithmic region for the various Mach numbers is achieved. The semi-local scaling x_2^* used here was introduced by Lobb *et al.* (1955), revisited by Huang *et al.* (1995) and Coleman *et al.* (1995) and generalised by Trettel & Larsson (2016). This scaling gives rise to a local Reynolds number

(Cebeci & Bradshaw 2012; Patel *et al.* 2015) at each wall-normal location

$$Re_\tau^*(x_2) = \frac{\bar{\rho}(\tau_w/\bar{\rho})^{1/2}\delta}{\bar{\mu}} \tag{3.6}$$

such that $x_2^* = (x_2/\delta)Re_\tau^*$. While the transformation proposed by Trettel & Larsson (2016) works well for the inner and logarithmic region, the collapse is not as good for the outer region. We find that best collapse is achieved with the transformation

$$\bar{u}_1^\star = \bar{u}_1^+ \left(\frac{\bar{\rho}}{\bar{\rho}_w}\right)^{1/2}, \tag{3.7}$$

which is equivalent to scaling the velocity with the semi-local $u_\tau^* = \sqrt{\tau_w/\bar{\rho}}$ instead of $u_\tau = \sqrt{\tau_w/\bar{\rho}_w}$, and the results are given in figure 5(c) and (d). A different transformation for the outer layer is expected, since the transformation given in (3.5) is based on the idea that the momentum conservation is equivalent to the stress balance condition, which only holds in the inner layer of nearly parallel shear flow at reasonable turbulence Mach numbers. Note that despite the better scaling in the outer region, the collapse is not perfect, which is a known issue for low Reynolds number boundary layer flows. Still, the inner, logarithmic and outer layer all utilise the semi-local scaling to achieve a universal mean velocity profile.

Given that the transformation of the turbulent supersonic mean velocity profile given in (3.4)–(3.7) produces a reasonable match to the incompressible profile in the inner, outer and logarithmic regions, the relatively subsonic ($\overline{M}_\infty < 1$) resolvent modes are expected to have a universal behaviour in both Reynolds and Mach number, as the one-dimensional energy density conditioned to $\overline{M}_\infty < 1$ in figure 3(c) show a localisation with respect to x_2. Moreover, the existence of a logarithmic region in the transformed mean streamwise velocity profile satisfies the necessary condition for the geometrically self-similar modes to be present. Due to the transformation in both $\bar{u}_1$ and x_2, the scaling of the resolvent modes should be with respect to the semi-local variables, x_2^* and Re_τ^*.

The semi-local scaling also provides explanation of the discrepancy between the principal energy contribution in the incompressible boundary layer (figure 1(c)) and the supersonic one (figure 1(d)). For the supersonic case of $M_\infty = 4$, the semi-local Reynolds number at $x_2/\delta = 0.2$ is $Re_\tau^* = 1020$, which is significantly larger than the Reynolds number of the incompressible case ($Re_\tau = 450$). In figure 6, we instead compare against the results from the incompressible turbulent boundary at $Re_\tau = 1040$ with the mean velocity profile from Schlatter & Örlü (2010) and the premultiplied energy spectra from turbulent channel flow at $Re_\tau = 950$ (Del Alamo *et al.* 2004), which show a better qualitative comparison between the two principal energy contribution spectra than the comparison given in figure 1.

4. Scaling of the principal singular value and resolvent modes

4.1. *Scaling of the principal response mode*

As observed in §3.2, the mean streamwise velocity profile with the semi-local scaling collapses to the incompressible boundary layer profile. This implies that the same scaling used in Moarref *et al.* (2013) for the incompressible channel flow can be extended to the compressible boundary layer by using the length-scale x_2^* and Reynolds number Re_τ^*. The proposed scaling of the resolvent analysis for the different classes of the the compressible boundary layer are given in table 2.

Note that the semi-local scaling already incorporates the Mach number (see figure 7).
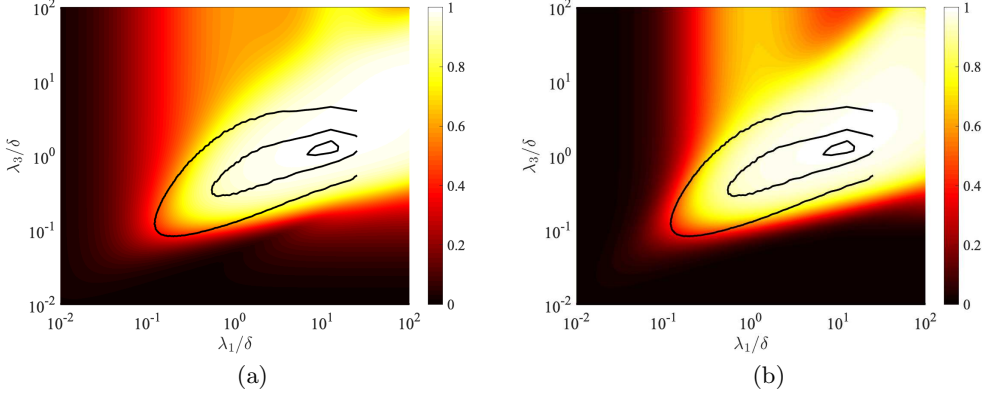
Figure 6: Energy contained in the principal response mode relative to the total response for different streamwise and spanwise wavelengths for the (a) incompressible ($Re_\tau = 1040$) and (b) compressible ($M_\infty = 4$, $Re_\tau^* = 1020$) turbulent boundary layer at $x_2/\delta = 0.2$. The contours are 10%, 50%, and 90% of the maximum energy of the premultiplied energy spectra for channel flow at $Re_\tau \approx 950$ (Del Alamo *et al.* 2004) at the corresponding wall-normal location.

For an adiabatic wall, the mean temperature profile is given by

$$\frac{\bar{T}}{T_\infty} = 1 + r\frac{\gamma - 1}{2}M_\infty^2 \left[1 - \left(\frac{\bar{u}_1}{\bar{u}_{1,\infty}}\right)^2\right], \tag{4.1}$$

where $r = Pr^{1/3}$ is the recovery factor (Walz 1969). Given the definition of the semi-local Reynolds number (3.6) and the mean equation of state $\bar{p} = \bar{\rho}\bar{T} = 1$, we have

$$Re_\tau^* = Re_\tau \frac{\bar{\mu}/\bar{\mu}_w}{\sqrt{\bar{\rho}/\bar{\rho}_w}} = Re_\tau \frac{(\bar{T}/\bar{T}_w)^{3/2} + C_w}{(\bar{T}/\bar{T}_w)^{3/2}(1 + C_w)}, \tag{4.2}$$

where $C_w = S/T_w$. When $x_2 = 0$, we have that $Re_\tau^* = Re_\tau$ as expected. In the limit $x_2 \to \infty$, $\bar{T}/\bar{T}_w = 1/\left(1 + r(\gamma - 1)M_\infty^2/2\right)$ and we have

$$Re_\tau^*(x_2 \to \infty) = Re_\tau \frac{1 + C_w\left(1 + r(\gamma - 1)M_\infty^2/2\right)^{3/2}}{1 + C_w} \tag{4.3}$$

giving approximately a M_∞^3 dependence for high Mach numbers.

In order for a fair comparison between the incompressible and compressible response modes, the compressible velocity modes must be normalised by the kinetic energy content in the response modes due to the orthonormality constraint of the singular vectors and the different norms used for the two cases. We define turbulent kinetic energy and turbulent thermodynamic energy as

$$E_K = (\boldsymbol{q}, \boldsymbol{q})_K = \int_0^\infty \bar{\rho}u_i^\dagger u_i \mathrm{d}x_2, \quad E_T = \int_0^\infty \frac{1}{\gamma M_\infty^2}\left(\frac{\rho^\dagger\rho}{\bar{\rho}^2} + \frac{T^\dagger T}{\bar{T}^2}\right)\mathrm{d}x_2, \tag{4.4}$$

respectively. We normalise the velocity and density and temperature modes such that

$$\widetilde{(u_i)}_1 = \frac{\bar{\rho}^{1/2}(u_i)_1}{\sqrt{E_K}}, \quad \widetilde{\rho}_1 = \frac{\rho_1/(\gamma M_\infty^2\bar{\rho}^2)^{1/2}}{\sqrt{E_T}}, \quad \widetilde{T}_1 = \frac{T_1/(\gamma M_\infty^2\bar{T}^2)^{1/2}}{\sqrt{E_T}}. \tag{4.5}$$

Class	κ_1-scale	κ_3-scale	x_2-scale	c-scale	$(u_1)_1, \rho_1, T_1$-scale
Inner	$\kappa_1^{\text{ref}} \dfrac{Re_\tau^*}{Re_\tau^{\text{ref}}}$	$\kappa_3^{\text{ref}} \dfrac{Re_\tau^*}{Re_\tau^{\text{ref}}}$	x_2^*	$\bar{u}_1\left(x_2^* = x_2^{\text{ref}*}\right)$	$\dfrac{1}{\sqrt{Re_\tau^*}}$
Outer	$\kappa_1^{\text{ref}} \dfrac{Re_\tau^{\text{ref}}}{Re_\tau^*}$	κ_3^{ref}	$\dfrac{x_2}{\delta}$	c^{ref}	1
Logarithmic	$\kappa_1^{\text{ref}} \dfrac{x_2^{\text{ref}} x_2^{\text{ref}*}}{x_2^c x_2^{c*}}$	$\kappa_3^{\text{ref}} \dfrac{x_2^{\text{ref}}}{x_2^c}$	$\dfrac{x_2}{x_2^{\text{ref}}}$	$-$	$\sqrt{\dfrac{x_2^c}{\delta}}$

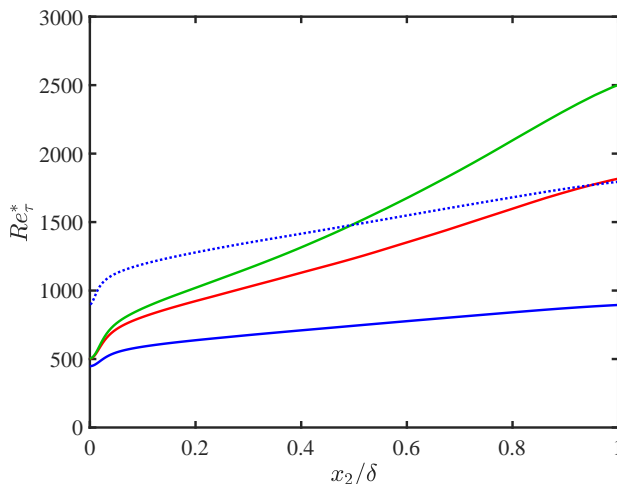Table 2: Expected length scales for the universal modes of the resolvent operator for the turbulent boundary layer.

Figure 7: Semi-local friction Reynolds number Re_τ^* as a function of x_2 for $M_\infty = 0$ (- - -), $M_\infty = 2$, $Re_\tau = 450$ (——), $M_\infty = 2$, $Re_\tau = 900$ (······), $M_\infty = 3$ (——), and $M_\infty = 4$ (——).

The relationship between E_K and E_T is later discussed in §4.2.

Because the difference between Re_τ and Re_τ^* grows as x_2 increases (see figure 7), the difference between the two scalings is expected to be most pronounced in the outer region, defined as $(\bar{u}_{1,\infty}^\star - \bar{u}_1^\star) \lesssim 6$ with $\kappa_3/\kappa_1 \gtrsim \epsilon Re_\tau^*/Re_{\tau,\min}^*$, $\epsilon \approx \sqrt{10}$ (see Appendix B and Moarref et al. 2013, for details). In this region, the x_2 dependent coefficients of $\boldsymbol{H}$ such as $\bar{u}_1 - c$ (and $\bar{T}$ and $\bar{\rho}$) are independent of Re_τ. And in the incompressible case, the balance between the viscous dissipation term and the mean advection term in the resolvent requires scaling of the spanwise coordinate in δ and the streamwise coordinate with δRe_τ (Moarref et al. 2013). Thus, the universal modes in the outer region for the incompressible case are given by the wave parameters

$$q_i^{\text{out},+} = q_i\left(\kappa_1 = \kappa_1^{\text{ref}} \frac{Re_\tau^{\text{ref}}}{Re_\tau}, \kappa_3 = \kappa_3^{\text{ref}}, c = c^{\text{ref}}\right) \tag{4.6}$$

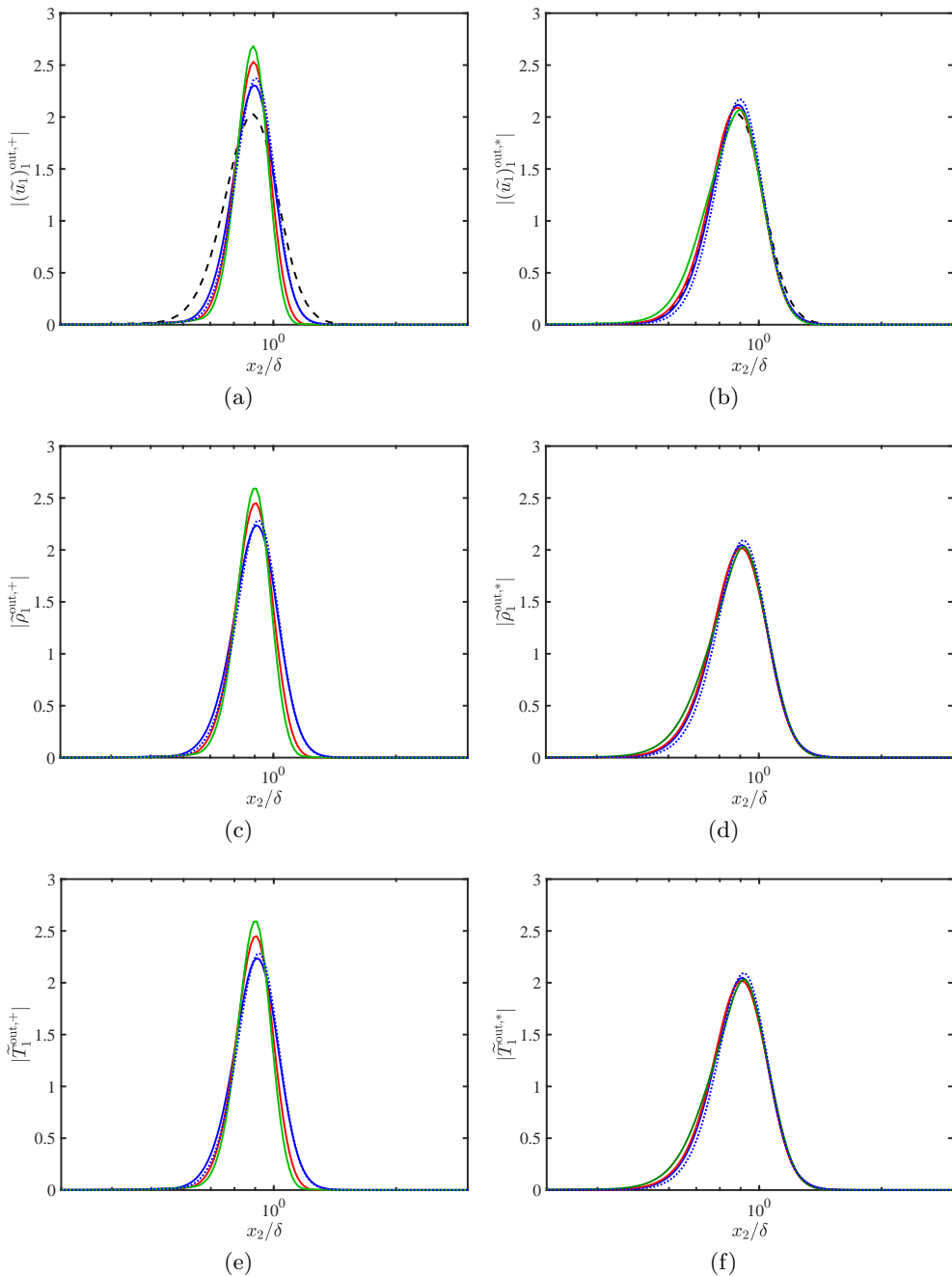in wall units. Using semi-local variables, we expect the wave parameters for the com-

Figure 8: Normalised and scaled response modes in the outer region for streamwise velocity (a) $\widetilde{(u_1)}_1^{\text{out},+}$ and (b) $\widetilde{(u_1)}_1^{\text{out},*}$, density (c) $\widetilde{\rho}_1^{\text{out},+}$ and (d) $\widetilde{\rho}_1^{\text{out},*}$ and temperature (e) $\widetilde{T}_1^{\text{out},+}$ and (f) $\widetilde{T}_1^{\text{out},*}$. Lines indicate $M_\infty = 0$ (- - -), $M_\infty = 2$, $Re_\tau = 450$ (——), $M_\infty = 2$, $Re_\tau = 900$ (······), $M_\infty = 3$ (——), and $M_\infty = 4$ (——).

pressible case to be

$$q_i^{\mathrm{out},*} = q_i \left(\kappa_1 = \kappa_1^{\mathrm{ref}} \frac{Re_\tau^{\mathrm{ref}}}{Re_\tau^*}, \kappa_3 = \kappa_3^{\mathrm{ref}}, c = c^{\mathrm{ref}} \right). \tag{4.7}$$

Due to the scaling of the wall-normal distance in outer units as well as the orthonormality condition for the velocity and thermodynamic quantities, the response mode height is expected to scale in outer units. In figure 8, we plot the normalised and scaled principal streamwise velocity, density and temperature response modes, with the reference parameters $Re_\tau = 445.5$, $\kappa_1^{\mathrm{ref}} = 1$, $\kappa_3^{\mathrm{ref}} = 10$ and $c^{\mathrm{ref}}/\bar{u}_{1,\infty} = 0.98$. The collapse among different Mach numbers is excellent for the semi-local scaling, and the streamwise velocity modes for the supersonic cases are indistinguishable from the incompressible response modes. Although not shown, the wall-normal response modes exhibit a similar collapse when scaled with Re_τ^* as opposed to Re_τ, as proposed in Sharma *et al.* (2017) for the incompressible case. The collapse is not as good for the spanwise response modes, although the mode shape is still very similar among different Mach numbers. Furthermore, the mode shapes are similar for the streamwise velocity, density and temperature. The similarity in density and temperature response modes can be explained by fact that from the equation of state, the two are linked with the pressure fluctuations. Moreover, the similarity between the streamwise velocity and thermal modes reinforce the strong Reynolds analogy, which links the transport of momentum and heat transfer and concludes that the velocity and temperature profiles are correlated.

In the case of the inner region, the deviation of Re_τ and Re_τ^* is not as significant, leading to a similar result for both the wall-unit scaling and the semi-local scaling. For the universal modes in the inner region, where the streamwise and spanwise coordinates are given in wall units, we expect the universal wave parameters to be

$$q_i^{\mathrm{in},*} = q_i \left(\kappa_1 = \kappa_1^{\mathrm{ref}} \frac{Re_\tau^*}{Re_\tau^{\mathrm{ref}}}, \kappa_3 = \kappa_3^{\mathrm{ref}} \frac{Re_\tau^*}{Re_\tau^{\mathrm{ref}}}, c = \bar{u}_1(x_2^* = x_2^{\mathrm{ref}*}) \right) \tag{4.8}$$

for $x_2^{\mathrm{ref}*} < 30$ and $\kappa_3/\kappa_1 \gtrsim \epsilon$, and analogously defined for $q_i^{\mathrm{in},+}$. In figure 9, we plot the normalised and scaled principal streamwise velocity, density and temperature response modes for reference Reynolds number, $Re_\tau^{\mathrm{ref}} = 445.5$ and wave parameters $\kappa_1^{\mathrm{ref}} = 1$, $\kappa_3^{\mathrm{ref}} = 10$ and $x_2^{\mathrm{ref}+/*} = 10$. Here, the scaling of the wall-normal distance is in semi-local (or wall) units. Thus, the orthonormality condition for the velocity and thermodynamic quantities concludes that the response mode height is expected to scale as $1/\sqrt{Re_\tau^*}$ (or $1/\sqrt{Re_\tau}$). Again, the collapse of the response modes among different Mach numbers are good for both cases, and the streamwise velocity modes also collapse with the incompressible case. The wall-normal and spanwise velocity modes also collapse for the various Mach numbers to the incompressible case but are not shown for brevity. The mode shapes for density and temperature are almost identical for the same reason discussed above. The temperature and density modes scaled in wall units are not shown, but they are almost identical to the ones given in semi-local units.

Finally, while the Re_τ for the cases under consideration is too small for a clearly defined logarithmic region, we consider the self-similar response modes. The wave parameters in this region are given by

$$q_i^{\mathrm{log},*} = q_i \left(\kappa_1 = \kappa_1^{\mathrm{ref}} \frac{x_2^{\mathrm{ref}} x_2^{\mathrm{ref}*}}{x_2^c x_2^{c*}}, \kappa_3 = \kappa_3^{\mathrm{ref}} \frac{x_2^{\mathrm{ref}}}{x_2^c}, c \right) \tag{4.9}$$

for wave speeds c in the logarithmic region ($30/Re_\tau^* < x_2/\delta < 0.15$), where x_2^{ref} denotes the critical layer for c^{ref}. The wave parameters in wall units are given analogously for
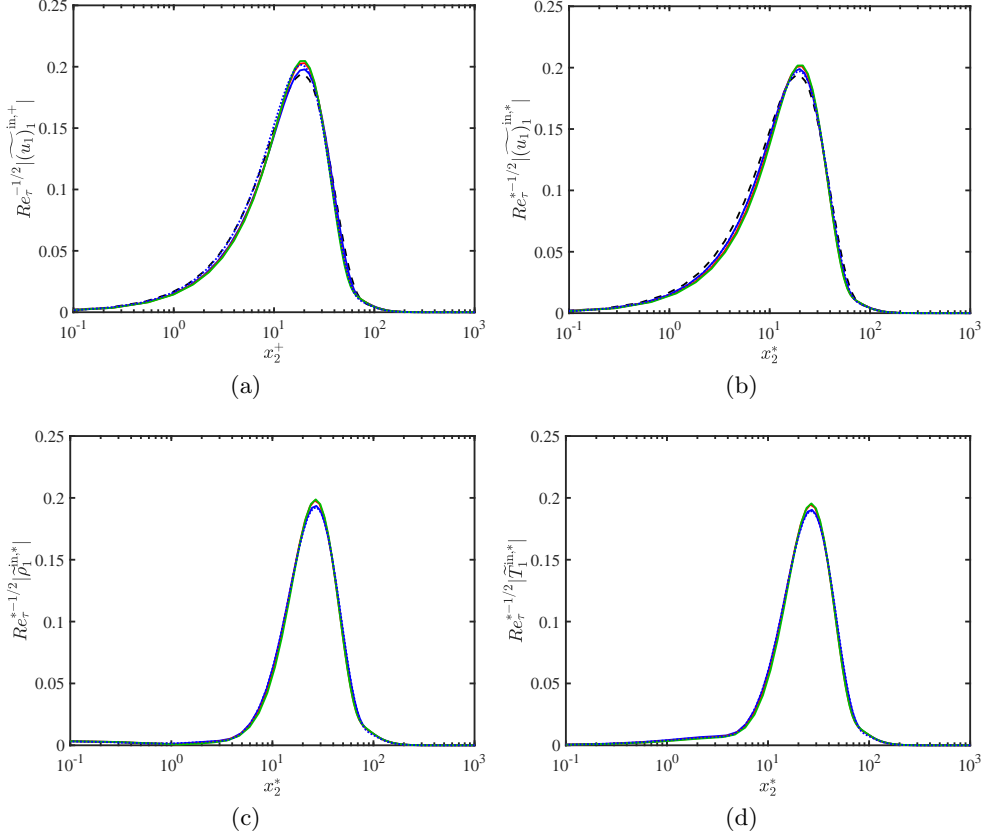
Figure 9: Normalised and scaled response modes in the inner region for streamwise velocity (a) $\widetilde{(u_1)}_1^{\mathrm{in},+}$ and (b) $\widetilde{(u_1)}_1^{\mathrm{in},*}$, (c) density, $\widetilde{\rho}_1^{\mathrm{in},*}$ and (d) temperature $\widetilde{T}_1^{\mathrm{in},*}$ scaled by either $Re_\tau^{-1/2}$ (a) or $Re_\tau^{*-1/2}$ (b,c,d) for reference parameters $Re_\tau^{\mathrm{ref}} = 445.5$, $\kappa_1^{\mathrm{ref}} = 1$, $\kappa_3^{\mathrm{ref}} = 10$ and $x_2^{*/+,\mathrm{ref}} = 10$. Lines indicate $M_\infty = 0$ (- - -), $M_\infty = 2$, $Re_\tau = 450$ (——), $M_\infty = 2$, $Re_\tau = 900$ (······), $M_\infty = 3$ (——), and $M_\infty = 4$ (——).

$q_i^{\log,+}$. In figure 10, we plot the normalised and scaled principal streamwise velocity, density and temperature response modes for reference Reynolds number, $Re_\tau^{\mathrm{ref}} = 445.5$, and reference wave parameters $\kappa_1^{\mathrm{ref}} = 1$, $\kappa_3^{\mathrm{ref}} = 10$, and $c^{\mathrm{ref}}/\bar{u}_{1,\infty} = 0.5$. The orthonormality condition for the velocity and thermodynamic quantities give the response mode height scaling of $\sqrt{x_2^c/\delta}$. Similar to the outer region, the semi-local scaling gives a better collapse among the supersonic response modes for various Mach numbers. While the agreement with the incompressible case is not perfect, some improvement is made from the use of the semi-local scale. As mentioned earlier, the Re_τ for cases under consideration is too low for an actual logarithmic layer and a better collapse is expected for higher Reynolds numbers. Additionally, as in the case of the inner and outer region, the temperature and density modes are identical and are similar to the streamwise velocity mode shape as well.

In addition to the universality and self-similarity of the response modes, the scaling of the principal singular values is also investigated. The expected scaling of the singular values for the incompressible case are given by $1/Re_\tau$ in the inner region, $x_2^{+2}x_2/\delta$ in the
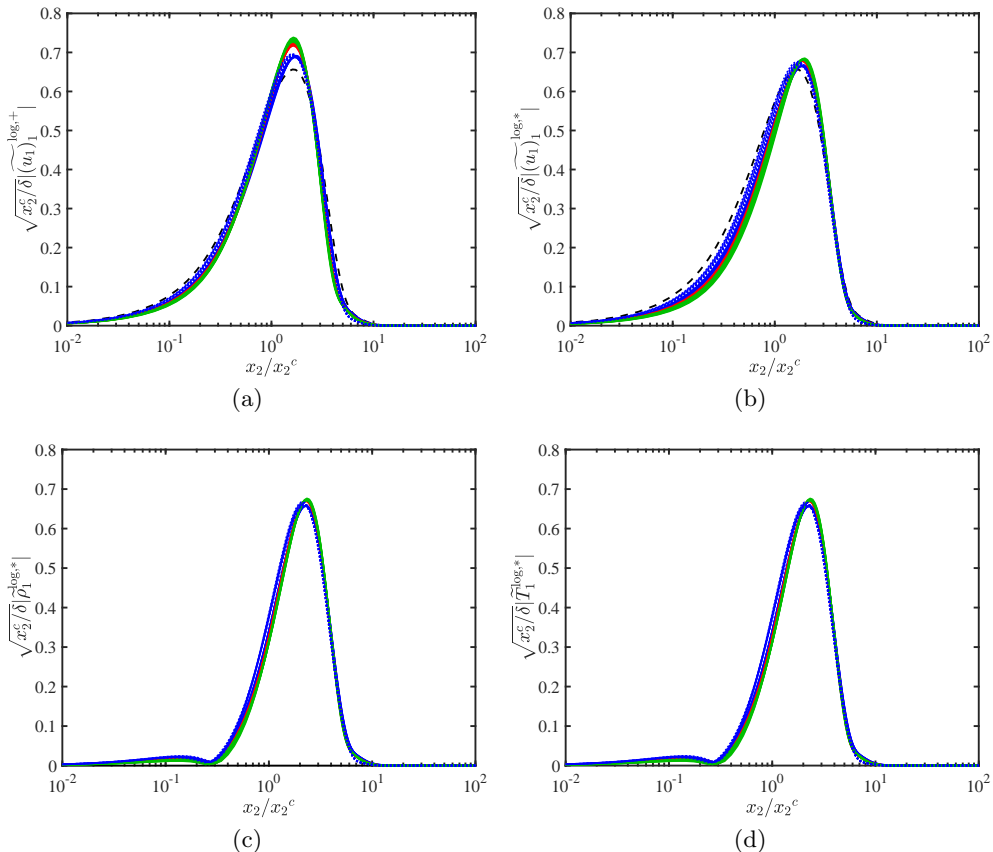
Figure 10: Normalised and scaled response modes in the logarithmic region for streamwise velocity (a) $\widetilde{(u_1)}_1^{\log,+}$ and (b) $\widetilde{(u_1)}_1^{\log,*}$, (c) density $\widetilde{\rho}_1^{\log,*}$ and (d) temperature $\widetilde{T}_1^{\log,*}$ scaled by $\sqrt{x_2^c}$ for reference parameters $Re_\tau^{\mathrm{ref}} = 445.5$, $\kappa_1^{\mathrm{ref}} = 1$, $\kappa_3^{\mathrm{ref}} = 10$ and $c^{\mathrm{ref}} = 0.5$. Lines indicate $M_\infty = 0$ (- - -), $M_\infty = 2$, $Re_\tau = 450$ (——), $M_\infty = 2$, $Re_\tau = 900$ (······), $M_\infty = 3$ (——), and $M_\infty = 4$ (——).

logarithmic region and Re_τ^2 in the outer region (Moarref *et al.* 2013; Sharma *et al.* 2017). The scaling of the principal singular values with the corresponding semi-local scaling is plotted in figure 11(a), (b), and (c). However a better approximation can be given by performing a scaling analysis on the resolvent operator **H** (see Appendix B for details). The elements of the resolvent operator matrix, and thus the leading singular value, can be shown to follow $1/\sqrt{Re_\tau^* Re_\tau^\star}$ in the inner region, $x_2^\star x_2^\star x_2/\delta$ in the logarithmic region, and $Re_\tau^* Re_\tau^\star$ in the outer region, where $Re_\tau^\star = \bar{\rho} u_\tau \delta/\bar{\mu}$ and $x_2^\star = Re_\tau^\star x_2/\delta$. This is due to the presence of the factor $\bar{T}\bar{\mu}/Re$ (or equivalently $\bar{\mu}/(Re\bar{\rho})$) in the governing equations combined with the semi-local scaling of the κ_1, κ_3 and x_2. The new proposed scaling for the principal singular values are given in figure 11(d) for the outer region. Notice the better collapse, especially in the innermost and outermost contour lines. The modified scaling for the inner and logarithmic region are not shown as $Re_\tau^* \approx Re_\tau^\star$ in this region and no visible changes are detected.
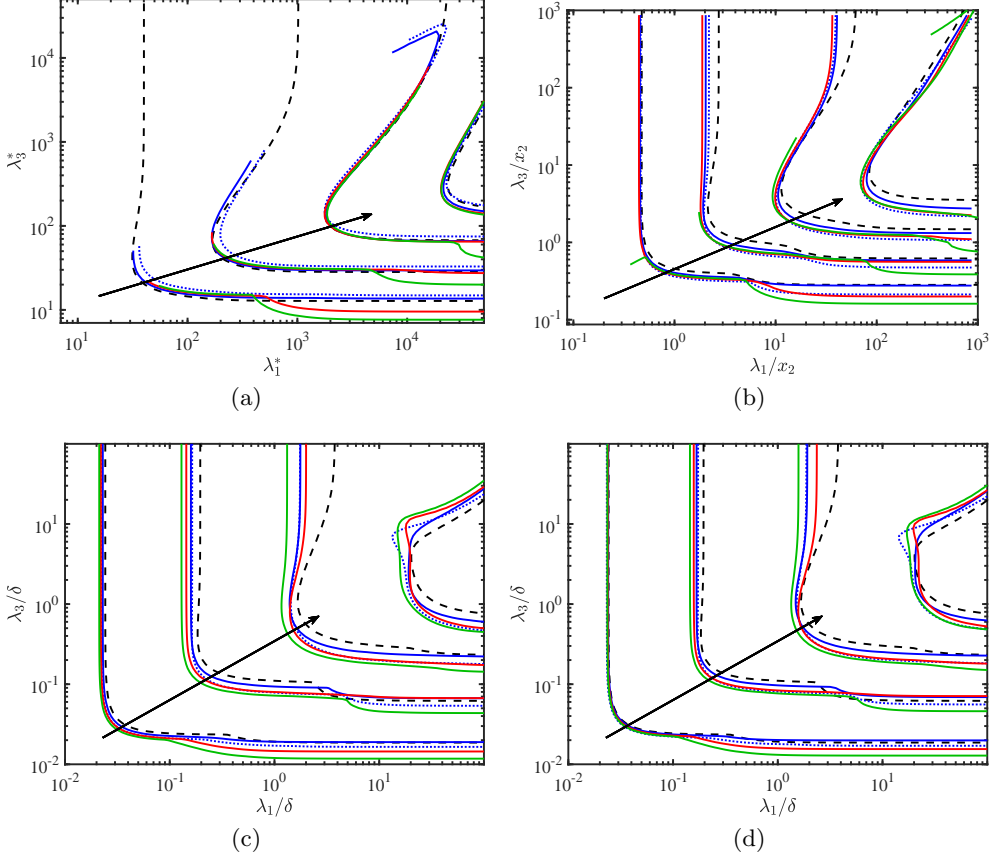
Figure 11: Principal singular value in the relatively subsonic region for (a) $c = \bar{u}_{1,\infty}(x_2^* = 10)$ for the inner layer, (b) $c/\bar{u}_{1,\infty} = 0.7$ for the logarithmic layer, and (c,d) $c/\bar{u}_{1,\infty} = 0.88$ for the outer layer. Contour lines are (a) $(10^2, 10^4, 10^6, 10^8)/Re_\tau^*$, (b) $(10^{-3}, 10^{-1}, 10^1, 10^3) \times x_2^{*2} x_2/\delta$, (c) $(10^{-7}, 10^{-5}, 10^{-3}, 10^{-1}, 10^1) \times Re_\tau^{*2}$, and (d) $(10^{-7}, 10^{-4}, 10^{-1}, 10^2) \times Re_\tau^\star Re_\tau^*$. Lines indicate $M_\infty = 0$ (‑ ‑ ‑), $M_\infty = 2$, $Re_\tau = 450$ (——), $M_\infty = 2$, $Re_\tau = 900$ (·····), $M_\infty = 3$ (——), and $M_\infty = 4$ (——). Arrows indicate direction of increasing σ_1.

4.2. *Scaling of the kinetic and thermodynamic energy ratio*

Due to the orthonormality constraint of the resolvent modes, the comparison between the compressible and incompressible resolvent modes in the previous section was for normalised response modes $\widetilde{(q_i)}_1$. However, it is equally important to assess the distribution of energy among the kinetic and thermodynamic variables for the supersonic cases.

In figure 12(a), (b) and (c), we plot the spectra of the ratio of thermodynamic energy and kinetic energy E_T/E_K for the resolvent modes for $M_\infty = 2$ and $Re_\tau = 450$ for two different wall normal heights. For the incompressible case, this ratio would be uniformly zero. Close to the wall, where relatively supersonic region is present, the thermodynamic energy clearly dominates in the relatively supersonic region as expected. Further away from the wall at $x_2/\delta = 0.2$ and $x_2/\delta = 0.5$, the thermodynamic energy still dominates in a smaller region with $\lambda_3 > \lambda_1$ with the strongest amplification centred around $\kappa_1 \approx 0.5$. This may be explained by the observation from Pirozzoli & Bernardini (2011) that in
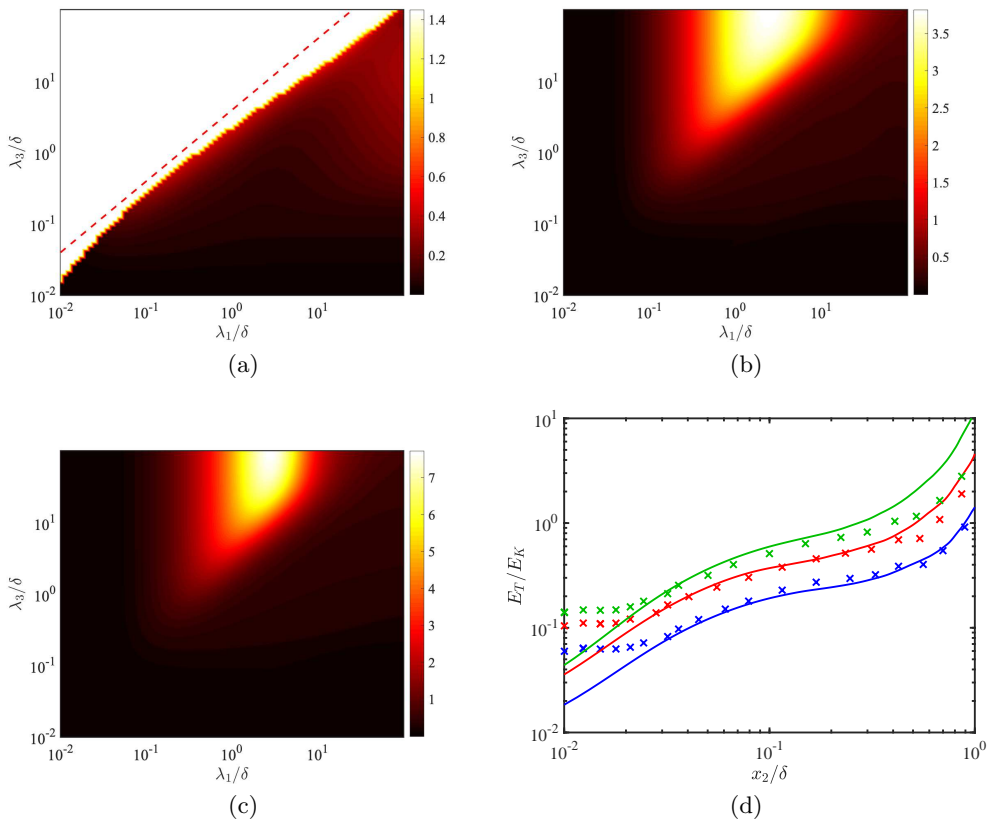
Figure 12: The spectra of the ratio of turbulent thermodynamic and kinetic energy, E_T/E_K computed from the principal resolvent modes at (a) $x_2^s = 15$, (b) $x_2/\delta = 0.2$ and (c) $x_2/\delta = 0.5$ for the $M_\infty = 2$, $Re_\tau = 450$ case. The relative sonic line $\bar{c}$ (- - -) is shown for reference. (d) The values of E_T/E_K at the most energetic wave parameters as defined in (4.11) for the principal resolvent modes ($\times$) and DNS (——) for $M_\infty = 2$, $Re_\tau = 450$ (blue), $M_\infty = 3$ (red), and $M_\infty = 4$ (green).

this region, the thermal streaks spread significantly in the spanwise direction compared to the velocity streaks. It is also consistent with the observation that large-scale pressure-carrying eddies or wavepackets, which are correlated with thermodynamic fluctuations, are more coherent in the spanwise direction for both incompressible (Sillero *et al.* 2014) and hypersonic (Duan *et al.* 2016) boundary layers.

We also plot the ratio of turbulent kinetic energy to the sum of the mean-square density and temperature fluctuations obtained from DNS (Bernardini & Pirozzoli 2011; Pirozzoli & Bernardini 2011) as a function of x_2 in figure 12(d). In particular, we plot

$$\left(\frac{E_T}{E_K}\right)^{\mathrm{DNS}} = \gamma M_\infty^2 \frac{\bar{\rho} u_{i,rms} u_{i,rms}}{\rho_{rms}^2/\bar{\rho}^2 + T_{rms}^2/\bar{T}^2}, \qquad (4.10)$$

where rms denotes the root-mean-squared fluctuations from DNS. For all wall-normal locations, the the ratio increases with Mach number. Moreover, the ratio increases as a function of x_2 for a fixed Mach number. In order to compare the results from the resolvent

modes to DNS, we define the energy ratio of the most energetic mode as

$$\left(\frac{E_T}{E_K}\right)^{\text{res}} = \frac{E_T}{E_K}\left(\arg\max_{\kappa_1,\kappa_3} \Phi_{u_1 u_1}(\kappa_1, \kappa_3)\right), \qquad (4.11)$$

where $\Phi_{u_1 u_1}$ is the premultiplied streamwise energy spectra for the channel flow at $Re_\tau = 550$ obtained *a priori* from Del Alamo *et al.* (2004). The $(E_T/E_K)^{\text{res}}$ given by these wave parameters is plotted in figure 12(c). The agreement between the ratio of kinetic and thermodynamic energy given by the most energetic principal response mode of the resolvent analysis and the DNS is excellent in the logarithmic region. The discrepancy in the outer region, especially for the higher Mach numbers, may be due to the larger value of Re_τ^* compared to the Re_τ of the premultiplied spectra used to choose the wave parameters for the most energetic modes. In the inner region, the estimated energy ratio plateaus, deviating from the DNS profile. This could be due to the increased contributions from relatively supersonic region, which is more prevalent in the near-wall region (see figures 1 and 2). Additionally, it is shown in LeHew *et al.* (2011) that the energetic contribution of structures with convection velocities less than $10u_\tau$ is negligible in real turbulent flows, which corresponds to the region where the mismatch is pronounced.

The observation that the correct energy distribution between E_T and E_K can be obtained by considering the most energetic principal response modes in a wide range of wall normal locations is a useful tool in terms of modelling and flow prediction.

5. Conclusions

We have extended the resolvent analysis to the compressible Navier-Stokes equations and have applied it to supersonic zero-pressure-gradient turbulent boundary layer. From the low-rank approximation formulated for individual wall-parallel wavenumbers and frequencies, we have identified two distinct regions in the wave parameter space: the relatively supersonic region and the relatively subsonic region.

In the relatively supersonic region, marked by relative Mach number greater than unity, we show that the resolvent modes are centred around the relative sonic line rather than the critical layer and that the majority of the energy is carried by the thermodynamic fluctuations. These response modes are consistent with acoustic Mach waves propagating towards the freestream and the idea of eddy shocklets, where the instantaneous supersonic events cause local shock-like structures in the boundary layer. Additionally, the modes in this region are also shown to follow a modal amplification mechanism. The range of wave parameters corresponding to the relatively supersonic region, where the compressibility effects are concentrated, grows with Mach number, which might be an indicator of why the Morkovin's hypothesis fails for high Mach numbers.

In the relatively subsonic region, we show that the principal response modes are localised around the critical layer corresponding to the mean velocity profile. Furthermore, with the semi-local scaling proposed by Trettel & Larsson (2016), the mean velocity profiles can collapse for various Reynolds and Mach numbers. This provides the necessary condition for the resolvent modes to exhibit universality and geometrically self-similarity when scaled with the semi-local Reynolds number and wall-normal distance. We show that the principal response modes are indeed universal and self-similar and that they follow the same scaling laws as the incompressible boundary layer when normalised by the fluctuating kinetic energy. This validates the notion of Morkovin's hypothesis for the relatively subsonic region on a mode-by-mode basis. Moreover, the velocity modes and the temperature and density modes are qualitatively similar, consistent with the

strong Reynolds analogy. We also provide scaling laws for the amplification factor of the principal response mode.

Finally we show that the energy distribution between the velocity fluctuations and the thermodynamic fluctuations can be predicted from the energy distribution of the most energetic response mode. Coupled with the universality and self-similarity of the resolvent modes in the relatively subsonic region, this has implications in modelling and prediction of high-speed turbulence. As in the incompressible case, the self-similar resolvent modes facilitate analytical developments in the logarithmic region of the boundary layer. Additionally, this allows prediction tools developed for resolvent analysis of incompressible fluids to be applied to supersonic boundary layers.

The results show that the main difference between the compressible Navier-Stokes equations and the incompressible equations are due to density variations in the wall-normal direction and the acoustic contribution in the relatively supersonic region. The full nonlinear closure then propagates the deviation through triadic interactions, which results in the variation in the mean velocity profile. Future efforts will be focused on studying the effect of the feedback loop by incorporating limited self-interactions to estimate the forcing term as in Rosenberg *et al.* (2019) for the incompressible Navier-Stokes equations. Also, further efforts are necessary to study the effects of higher Mach numbers and different wall boundary conditions such as cooled walls.

Appendix A. Modal amplification mechanism in the relatively supersonic region

The spectrum of the linear operator $\boldsymbol{L}$ is obtained from solving the eigenvalue problem $\boldsymbol{L}\boldsymbol{q} = i\omega\boldsymbol{q}$. Here, we plot the results for the $M_\infty = 4$ case in terms of the complex wave speed $c = \Re(c) + i\Im(c)$ in figure 13. The spectrum for $(\kappa_1, \kappa_3) = (0.2, 2)$ shown in figure 13(a) consists of viscous modes that is typical for both incompressible and compressible boundary layers flows. Note that the freestream velocity projected onto $[\kappa_1, \kappa_3]^\dagger$, $\overline{M}_\infty = 0.39$ is subsonic, and thus relatively supersonic modes are absent in this case. However, the spectrum for $(\kappa_1, \kappa_3) = (1, 2)$ (figure 13(b), where relatively supersonic regions are present, show an additional feature indicative of "acoustic" eigenmodes along $\Im(c) = 0$. In the relatively supersonic region, the resolvent norm shows peaks in both the leading singular value and the energy contained in the principal resolvent mode due to spectral amplification of these acoustic eigenmodes near their defined wave speeds.

For a given wave speed c, we can plot the distance d_Λ from $\omega = c\kappa_1$ to the closest acoustic eigenvalue as a function of wavenumbers κ_1 and κ_3. In figure 14, the inverse of the minimum eigenvalue distance is shown to correlate well with the leading singular value, which leads to correlation with the principal energy contribution $\sigma_1/(\sum_j \sigma_j)$. As mentioned before, this is due to the resonant amplification of the resolvent operator through modal amplification mechanisms. The change in discrete location of the acoustic eigenvalues as a function of κ_1 and κ_3 explains the irregular patterns in figure 1(b) in the relatively supersonic region.
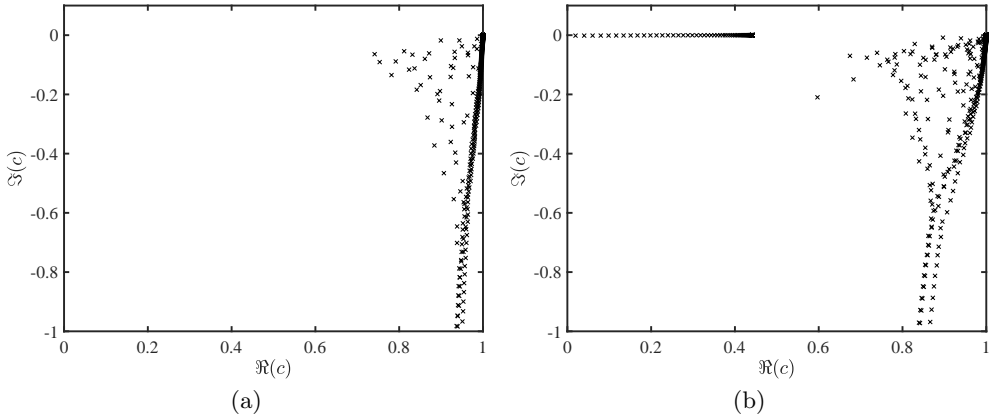
Figure 13: Eigenvalues for the linearised operator $\boldsymbol{L}$ for the compressible ($M_\infty = 4$) turbulent boundary layer for wave parameters (a) $(\kappa_1, \kappa_3) = (0.2, 2)$ and (b) $(\kappa_1, \kappa_3) = (1, 2)$.
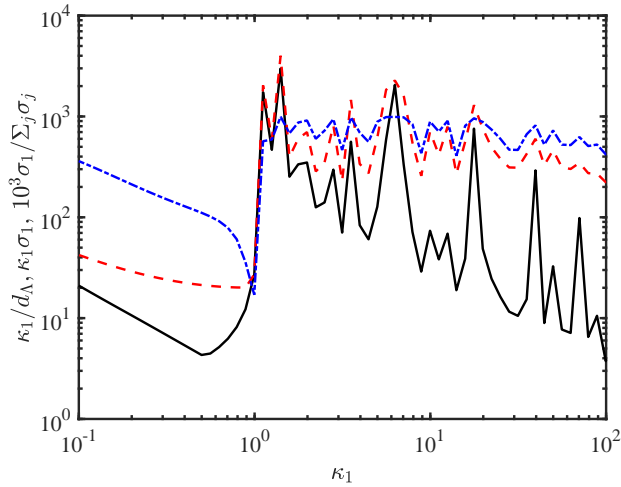

Figure 14: Inverse of the distance of the wave speed to the closest acoustic eigenvalue with $\Im(c) = 0$, κ_1/d_Λ (——), compared with the premultiplied principal singular value $\kappa_1 \sigma_1$ (- - -) and energy contribution from the leading singular value $\sigma_1/(\sum_j \sigma_j)$ (-·-·) for $\kappa_3 = 2$.

Appendix B. Reynolds number scaling of the principal singular value

In inner region where the collapse of the mean velocity profile is achieved through the semi-local scaling, the coordinates scale as

$$\kappa_1 \sim Re_\tau^*, \quad \kappa_3 \sim Re_\tau^*, \quad \mathrm{d}/\mathrm{d}x_2 \sim Re_\tau^*. \tag{B 1}$$

We then analyse the scaling of the linear operator $\boldsymbol{H}$ by assessing the Reynolds number dependency of the terms in the linearised operator $\boldsymbol{L}$. In this process, we assume that the Mach number plays a secondary role, since we know Re_τ^* (or $Re_\tau^\star$) reflects the Mach number dependency as seen in §4.1. Doing so, the linear operator $\boldsymbol{L}$ approximately scales

as

$$
\boldsymbol{L} \sim
\begin{bmatrix}
Re_\tau^* + \frac{Re_\tau^{*2}}{Re_\tau^\star} & Re_\tau^* + \frac{Re_\tau^{*2}}{Re_\tau^\star} & Re_\tau^* + \frac{Re_\tau^{*2}}{Re_\tau^\star} & Re_\tau^* & Re_\tau^* + \frac{Re_\tau^{*2}}{Re_\tau^\star} \\
\frac{Re_\tau^{*2}}{Re_\tau^\star} & Re_\tau^* + \frac{Re_\tau^{*2}}{Re_\tau^\star} & \frac{Re_\tau^{*2}}{Re_\tau^\star} & Re_\tau^* & Re_\tau^* + \frac{Re_\tau^{*2}}{Re_\tau^\star} \\
\frac{Re_\tau^{*2}}{Re_\tau^\star} & \frac{Re_\tau^{*2}}{Re_\tau^\star} & Re_\tau^* + \frac{Re_\tau^{*2}}{Re_\tau^\star} & Re_\tau^* & Re_\tau^* \\
Re_\tau^* & Re_\tau^* & Re_\tau^* & Re_\tau^* & 0 \\
Re_\tau^* + \frac{Re_\tau^{*2}}{Re_\tau^\star} & Re_\tau^* + \frac{Re_\tau^{*2}}{Re_\tau^\star} & Re_\tau^* & 0 & Re_\tau^* + \frac{Re_\tau^{*2}}{Re_\tau^\star}
\end{bmatrix}.
\tag{B 2}
$$

As $Re_\tau^* \approx Re_\tau^\star$ in this region, the scaling can be seen as $\boldsymbol{L} \sim \sqrt{Re_\tau^* Re_\tau^\star}$, giving $\boldsymbol{H} = (\mathrm{i}\omega \boldsymbol{I} + \boldsymbol{L})^{-1} \sim 1/\sqrt{Re_\tau^* Re_\tau^\star}$. Thus, the leading singular value is expected to be proportional to $1/\sqrt{Re_\tau^* Re_\tau^\star}$.

In the outer region, the coordinates scale as

$$
\kappa_1 \sim 1/Re_\tau^*, \quad \kappa_3 \sim 1, \quad \mathrm{d}/\mathrm{d}x_2 \sim 1.
\tag{B 3}
$$

Additionally, if we assume that κ_3^2 dominates κ_1^2 for all values of Re_τ^*, such that for the streamwise wavenumber in the outer coordinate given by $\kappa_1^- = Re_\tau^* \kappa_1$ we have $\kappa_3/\kappa_1^- > \epsilon/Re_\tau^*$, the linear operator $\boldsymbol{L}$ scales as

$$
\boldsymbol{L} \sim
\begin{bmatrix}
\frac{1}{Re_\tau^*} + \frac{1}{Re_\tau^\star} & \frac{1}{Re_\tau^* Re_\tau^\star} & \frac{1}{Re_\tau^* Re_\tau^\star} & \frac{1}{Re_\tau^*} & \frac{1}{Re_\tau^*} + \frac{1}{Re_\tau^\star} \\
\frac{1}{Re_\tau^* Re_\tau^\star} & \frac{1}{Re_\tau^*} + \frac{1}{Re_\tau^\star} & \frac{1}{Re_\tau^*} & 1 & \frac{1}{Re_\tau^* Re_\tau^\star} \\
\frac{1}{Re_\tau^* Re_\tau^\star} & \frac{1}{Re_\tau^*} & \frac{1}{Re_\tau^*} + \frac{1}{Re_\tau^\star} & 1 & 1 \\
\frac{1}{Re_\tau^*} & 1 & 1 & \frac{1}{Re_\tau^*} & 0 \\
\frac{1}{Re_\tau^*} + \frac{1}{Re_\tau^\star} & \frac{1}{Re_\tau^* Re_\tau^\star} & 1 & 0 & \frac{1}{Re_\tau^*} + \frac{1}{Re_\tau^\star}
\end{bmatrix}.
\tag{B 4}
$$

The resolvent $\boldsymbol{H}$ then scales as $Re_\tau^* Re_\tau^\star$, which gives the scaling for the leading singular value σ_1.

Finally, for the logarithmic region, the differential operators are scaled as

$$
\kappa_1 \sim 1/(x_2^{c*} x_2^c), \quad \kappa_3 \sim 1/x_2^c, \quad \mathrm{d}/\mathrm{d}x_2 \sim 1/x_2^c.
\tag{B 5}
$$

We also assume that the spanwise coordinate dominates the spanwise coordinate, i.e. $(\kappa_3/\kappa_1) > \epsilon$ with a conservative estimation of $\epsilon \approx \sqrt{10}$, and arrive at

$$
\boldsymbol{L} \sim
\begin{bmatrix}
\frac{1}{x_2^{c*} x_2^c} + \frac{1}{x_2^{c*} x_2^c} & \frac{1}{x_2^{c*} x_2^c} & \frac{1}{x_2^{c*} x_2^{c*}} & \frac{1}{x_2^{c*} x_2^c} & \frac{1}{x_2^{c*} x_2^c} + \frac{1}{x_2^{c*} x_2^c} \\
\frac{1}{x_2^{c*} x_2^{c*}} & \frac{1}{x_2^{c*} x_2^c} + \frac{1}{x_2^{c*} x_2^c} & \frac{1}{x_2^{c*} x_2^c} & \frac{1}{x_2^c} & \frac{1}{x_2^{c*} x_2^{c*} x_2^c} \\
\frac{1}{x_2^{c*} x_2^{c*} x_2^c} & \frac{1}{x_2^{c*} x_2^c} & \frac{1}{x_2^{c*} x_2^c} + \frac{1}{x_2^{c*} x_2^c} & \frac{1}{x_2^c} & \frac{1}{x_2^c} \\
\frac{1}{x_2^{c*} x_2^c} & \frac{1}{x_2^c} & \frac{1}{x_2^c} & \frac{1}{x_2^{c*} x_2^c} & 0 \\
\frac{1}{x_2^{c*} x_2^c} + \frac{1}{x_2^{c*} x_2^c} & \frac{1}{x_2^{c*} x_2^{c*} x_2^c} & \frac{1}{x_2^c} & 0 & \frac{1}{x_2^{c*} x_2^c} + \frac{1}{x_2^{c*} x_2^c}
\end{bmatrix}.
\tag{B 6}
$$

And a similar analysis as the inner and outer regions reveals that the singular values scale with $x_2^* x_2^\star x_2$.

REFERENCES

BERNARDINI, M. & PIROZZOLI, S. 2011 Wall pressure fluctuations beneath supersonic turbulent boundary layers. *Phys. Fluids* **23** (8), 085102.

BITTER, N. & SHEPHERD, J. 2014 Transient growth in hypersonic boundary layers. In *7th AIAA Theoretical Fluid Mechanics Conference*, p. 2497.

BRADSHAW, P. 1974 The effect of mean compression or dilatation on the turbulence structure of supersonic boundary layers. *J. Fluid Mech.* **63** (3), 449–464.

BRUN, C., BOIARCIUC, M. P., HABERKORN, M. & COMTE, P. 2008 Large eddy simulation of compressible channel flow. *Theor. Comp. Fluid Dyn.* **22** (3-4), 189–212.

CEBECI, T. & BRADSHAW, P. 2012 *Physical and computational aspects of convective heat transfer*. Springer Science & Business Media.

CHRISTOV, C. I. 1982 A complete orthonormal system of functions in $L^2(-\infty, \infty)$ space. *SIAM J. Appl. Math.* **42** (6), 1337–1344.

CHU, B.-T. 1965 On the energy transfer to small disturbances in fluid flow (Part I). *Acta Mech.* **1** (3), 215–234.

COLEMAN, G. N., KIM, J. & MOSER, R. D. 1995 A numerical study of turbulent supersonic isothermal-wall channel flow. *J. Fluid Mech.* **305**, 159–183.

COLES, D. 1964 The turbulent boundary layer in a compressible fluid. *Phys. Fluids* **7** (9), 1403–1423.

DAWSON, S. T. M. & MCKEON, B. J. 2019 Studying the effects of compressibility in planar Couette flow using resolvent analysis. In *AIAA SciTech*, p. 2139.

DEL ALAMO, J. C., JIMÉNEZ, J., ZANDONADE, P. & MOSER, R. D. 2004 Scaling of the energy spectra of turbulent channels. *J. Fluid Mech.* **500**, 135–144.

DUAN, L., BEEKMAN, I. & MARTIN, M. P. 2010 Direct numerical simulation of hypersonic turbulent boundary layers. Part 2. Effect of wall temperature. *J. Fluid Mech.* **655**, 419–445.

DUAN, L., BEEKMAN, I. & MARTIN, M. P. 2011 Direct numerical simulation of hypersonic turbulent boundary layers. Part 3. Effect of Mach number. *J. Fluid Mech.* **672**, 245–267.

DUAN, L., CHOUDHARI, M. M. & ZHANG, C. 2016 Pressure fluctuations induced by a hypersonic turbulent boundary layer. *J. Fluid Mech.* **804**, 578–607.

DUAN, L. & MARTIN, M. P. 2011 Direct numerical simulation of hypersonic turbulent boundary layers. Part 4. Effect of high enthalpy. *J. Fluid Mech.* **684**, 25–59.

EKOTO, I. W., BOWERSOX, R. D. W., BEUTNER, T. & GOSS, L. P. 2008 Supersonic boundary layers with periodic surface roughness. *AIAA J.* **46** (2), 486–497.

ERM, L. P. & JOUBERT, P. N. 1991 Low-Reynolds-number turbulent boundary layers. *J. Fluid Mech.* **230**, 1–44.

FFOWCS WILLIAMS, J. E. & MAIDANIK, G. 1965 The Mach wave field radiated by supersonic turbulent shear flows. *J. Fluid Mech.* **21** (4), 641–657.

GAVIGLIO, J. 1987 Reynolds analogies and experimental study of heat transfer in the supersonic boundary layer. *Int. J. Heat Mass Transf.* **30** (5), 911–926.

GROSCH, C. E. & ORSZAG, S. A. 1977 Numerical solution of problems in unbounded regions: coordinate transforms. *J. Comput. Phys.* **25** (3), 273–295.

GUARINI, S. E., MOSER, R. D., SHARIFF, K. & WRAY, A. 2000 Direct numerical simulation of a supersonic turbulent boundary layer at Mach 2.5. *J. Fluid Mech.* **414**, 1–33.

HADJADJ, A., BEN-NASR, O., SHADLOO, M. S. & CHAUDHURI, A. 2015 Effect of wall temperature in supersonic turbulent boundary layers: A numerical study. *Int. J. Heat Mass Transf.* **81**, 426–438.

HANIFI, A., SCHMID, P. J. & HENNINGSON, D. S. 1996 Transient growth in compressible boundary layer flow. *Phys. Fluids* **8** (3), 826–837.

HUANG, P. G., COLEMAN, G. N. & BRADSHAW, P. 1995 Compressible turbulent channel flows: DNS results and modelling. *J. Fluid Mech.* **305**, 185–218.

JEUN, J., NICHOLS, J. W. & JOVANOVIĆ, M. R. 2016 Input-output analysis of high-speed axisymmetric isothermal jet noise. *Phys. Fluids* **28** (4), 047101.

JIMÉNEZ, J., HOYAS, S., SIMENS, M. P. & MIZUNO, Y. 2010 Turbulent boundary layers and channels at moderate Reynolds numbers. *J. Fluid Mech.* **657**, 335–360.

KISTLER, A. L. 1959 Fluctuation measurements in a supersonic turbulent boundary layer. *Phys. Fluids* **2** (3), 290–296.

KONRAD, W. & SMITS, A. J. 1998 Turbulence measurements in a three-dimensional boundary layer in supersonic flow. *J. Fluid Mech.* **372**, 1–23.

KOVASZNAY, L. S. G. 1953 Turbulence in supersonic flow. *J. Aeronaut. Sci.* **20** (10), 657–674.

LADERMAN, A. J. & DEMETRIADES, A. 1974 Mean and fluctuating flow measurements in the hypersonic boundary layer over a cooled wall. *J. Fluid Mech.* **63** (1), 121–144.

LAGHA, M., KIM, J., ELDREDGE, J. D. & ZHONG, X. 2011 A numerical study of compressible turbulent boundary layers. *Phys. Fluids* **23** (1), 015106.

LeHew, J., Guala, M. & McKeon, B. J. 2011 A study of the three-dimensional spectral energy distribution in a zero pressure gradient turbulent boundary layer. *Exp. Fluids* **51** (4), 997–1012.

Lobb, R. K., Winkler, E. M. & Persh, J. 1955 NOL hypersonic tunnel No. 4, results 7: experimental investigation of turbulent boundary layers in hypersonic flow. *Tech. Rep.*. Naval Ordnance Lab, White Oak, MD.

Luhar, M., Sharma, A. S. & McKeon, B. J. 2014 On the structure and origin of pressure fluctuations in wall turbulence: predictions based on the resolvent analysis. *J. Fluid Mech.* **751**, 38–70.

Mack, L. M. 1984 Boundary-layer linear stability theory. AGARD Report No. 709, Part 3. NASA Jet Propulsion Laboratory.

Maeder, T. 2000 *Numerical investigation of supersonic turbulent boundary layers*, , vol. 394. ETH Zurich.

Malik, M., Alam, M. & Dey, J. 2006 Nonmodal energy growth and optimal perturbations in compressible plane Couette flow. *Phys. Fluids* **18** (3), 034103.

Malik, M., Dey, J. & Alam, M. 2008 Linear stability, transient energy growth, and the role of viscosity stratification in compressible plane Couette flow. *Phys. Rev. E* **77** (3), 036322.

Martín, M. P. 2007 Direct numerical simulation of hypersonic turbulent boundary layers. Part 1. Initialization and comparison with experiments. *J. Fluid Mech.* **570**, 347–364.

McKeon, B. J. & Sharma, A. S. 2010 A critical-layer framework for turbulent pipe flow. *J. Fluid Mech.* **658**, 336–382.

Moarref, R., Jovanović, M. R., Tropp, J. A., Sharma, A. S. & McKeon, B. J. 2014 A low-order decomposition of turbulent channel flow via resolvent analysis and convex optimization. *Phys. Fluids* **26** (5), 051701.

Moarref, R., Sharma, A. S., Tropp, J. A. & McKeon, B. J. 2013 Model-based scaling of the streamwise energy density in high-Reynolds-number turbulent channels. *J. Fluid Mech.* **734**, 275–316.

Modesti, D. & Pirozzoli, S. 2016 Reynolds and Mach number effects in compressible turbulent channel flow. *Int. J. Heat Fluid Fl.* **59**, 33–49.

Morkovin, M. V. 1962 Effects of compressibility on turbulent flows. In *Mécanique de la Turbulence* (ed. A. Favre), pp. 367–380. CNRS, Paris.

Owen, F. K., Horstman, C. C. & Kussoy, M. I. 1975 Mean and fluctuating flow measurements of a fully-developed, non-adiabatic, hypersonic boundary layer. *J. Fluid Mech.* **70** (2), 393–413.

Özgen, S. & Kircali, S. A. 2008 Linear stability analysis in compressible, flat-plate boundary-layers. *Theor. Comp. Fluid Dyn.* **22** (1), 1–20.

de Pando, M. F., Schmid, P. J. & Sipp, D. 2014 A global analysis of tonal noise in flows around aerofoils. *J. Fluid Mech.* **754**, 5–38.

Patel, A., Peeters, J. W. R., Boersma, B. J. & Pecnik, R. 2015 Semi-local scaling and turbulence modulation in variable property turbulent channel flows. *Phys. Fluids* **27** (9), 095101.

Peltier, S. J., Humble, R. A. & Bowersox, R. D. W. 2016 Crosshatch roughness distortions on a hypersonic turbulent boundary layer. *Phys. Fluids* **28** (4), 045105.

Phillips, O. M. 1960 On the generation of sound by supersonic turbulent shear layers. *J. Fluid Mech.* **9** (1), 1–28.

Pirozzoli, S. & Bernardini, M. 2011 Turbulence in supersonic boundary layers at moderate Reynolds number. *J. Fluid Mech.* **688**, 120–168.

Pirozzoli, S., Grasso, F. & Gatski, T. B. 2004 Direct numerical simulation and analysis of a spatially evolving supersonic turbulent boundary layer at $M = 2.25$. *Phys. Fluids* **16** (3), 530–545.

Poggie, J., Bisek, N. J. & Gosse, R. 2015 Resolution effects in compressible, turbulent boundary layer simulations. *Comput. Fluids* **120**, 57–69.

Rosenberg, K., Symon, S. & McKeon, B. J. 2019 The role of parasitic modes in nonlinear closure via the resolvent feedback loop. *Phys. Rev. Fluids* **4**, 052601(R).

Rowley, C. W., Colonius, T. & Murray, R. M. 2004 Model reduction for compressible flows using POD and Galerkin projection. *Physica D* **189** (1-2), 115–129.

Roy, C. J. & Blottner, F. G. 2006 Review and assessment of turbulence models for hypersonic flows. *Prog. Aerosp. Sci.* **42** (7-8), 469–530.

Schlatter, P. & Örlü, R. 2010 Assessment of direct numerical simulation data of turbulent boundary layers. *J. Fluid Mech.* **659**, 116–126.

Schmid, P. J. & Henningson, D. S. 2000 *Stability and transition in shear flows*, *Applied Mathematical Sciences*, vol. 142. Springer Science & Business Media.

Schmidt, O. T., Towne, A., Rigas, G., Colonius, T. & Brès, G. A. 2018 Spectral analysis of jet turbulence. *J. Fluid Mech.* **855**, 953–982.

Shahab, M. F., Lehnasch, G., Gatski, T. B. & Comte, P. 2011 Statistical characteristics of an isothermal, supersonic developing boundary layer flow from DNS data. *Flow Turbul. Combust.* **86** (3-4), 369–397.

Sharma, A. S. & McKeon, B. J. 2013 On coherent structure in wall turbulence. *J. Fluid Mech.* **728**, 196–238.

Sharma, A. S., Moarref, R. & McKeon, B. J. 2017 Scaling and interaction of self-similar modes in models of high Reynolds number wall turbulence. *Philos. Trans. Royal Soc. A* **375** (2089), 20160089.

Sillero, J. A., Jiménez, J. & Moser, R. D. 2014 Two-point statistics for turbulent boundary layers and channels at Reynolds numbers up to $\delta^+ \approx 2000$. *Phys. Fluids* **26** (10), 105109.

Simens, M. P., Jiménez, J., Hoyas, S. & Mizuno, Y. 2009 A high-resolution code for turbulent boundary layers. *J. Comput. Phys.* **228** (11), 4218–4231.

Spina, E. F. & Smits, A. J. 1987 Organized structures in a compressible, turbulent boundary layer. *J. Fluid Mech.* **182**, 85–109.

Tichenor, N. R., Humble, R. A. & Bowersox, R. D. W. 2013 Response of a hypersonic turbulent boundary layer to favourable pressure gradients. *J. Fluid Mech.* **722**, 187–213.

Towne, A., Lozano-Durán, A. & Yang, X. I. A. 2019 Resolvent-based estimation of space-time flow statistics. *J. Fluid Mech.* p. under review.

Towne, A., Schmidt, O. T. & Colonius, T. 2018 Spectral proper orthogonal decomposition and its relationship to dynamic mode decomposition and resolvent analysis. *J. Fluid Mech.* **847**, 821–867.

Trettel, A. & Larsson, J. 2016 Mean velocity scaling for compressible wall turbulence with heat transfer. *Phys. Fluids* **28** (2), 026102.

Van Driest, E. R. 1951 Turbulent boundary layer in compressible fluids. *J. Aeronaut. Sci.* **18** (3), 145–160.

Walz, A. 1969 *Boundary layers of flow and temperature*. MIT press.

Williams, O. J. H., Sahoo, D., Baumgartner, M. L. & Smits, A. J. 2018 Experiments on the structure and scaling of hypersonic turbulent boundary layers. *J. Fluid Mech.* **834**, 237–270.

Wilson, R. E. 1950 Turbulent boundary-layer characteristics at supersonic speeds-theory and experiment. *J. Aeronaut. Sci.* **17** (9), 585–594.

Yang, X. I. A. & Lv, Y. 2018 A semi-locally scaled eddy viscosity formulation for LES wall models and flows at high speeds. *Theor. Comp. Fluid Dyn.* **32** (5), 617–627.

Yeh, C.-A. & Taira, K. 2019 Resolvent-analysis-based design of airfoil separation control. *J. Fluid Mech.* **867**, 572–610.

Young, N. 1988 *An introduction to Hilbert space*. Cambridge University Press.

Zare, A., Jovanović, M. R. & Georgiou, T. T. 2017 Colour of turbulence. *J. Fluid Mech.* **812**, 636–680.

Zhang, C., Duan, L. & Choudhari, M. M. 2018 Direct numerical simulation database for supersonic and hypersonic turbulent boundary layers. *AIAA J.* **56** (11), 4297–4311.

Zhang, Y.-S., Bi, W.-T., Hussain, F., Li, X.-L. & She, Z.-S. 2012 Mach-number-invariant mean-velocity profile of compressible turbulent boundary layers. *Phys. Rev. Lett.* **109** (5), 054502.

Zhang, Y.-S., Bi, W.-T., Hussain, F. & She, Z.-S. 2014 A generalized Reynolds analogy for compressible wall-bounded turbulent flows. *J. Fluid Mech.* **739**, 392–420.

Modeling Passive Scalar Dynamics in Wall-Bounded Turbulence using Resolvent Analysis

Scott T. M. Dawson[*] and Beverley J. McKeon[†]
California Institute of Technology, Pasadena, CA, 91125

Theresa Saxton-Fox[‡]
Princeton University, Princeton, NJ, 08544

This work develops a framework for studying the behavior of a passive scalar field in incompressible wall-bounded turbulence using the resolvent operator. This approach expresses the state of the system as the result of applying a linear (resolvent) operator to the nonlinear terms in the governing Navier-Stokes equations. By augmenting the system with a passive scalar equation, this formulation is used to study the relationship between velocity and scalar fluctuations. Additional insight into the mechanisms responsible for driving scalar fluctuations is attained by considering the resolvent form of the passive scalar equation in isolation from the momentum equations. We demonstrate that the passive scalar resolvent operator admits rescaling properties that relates the behavior of scalar fields with different diffusivities, and investigate the ability of this modeling framework to predict statistical properties of the fluctuating scalar field.

I. Introduction

The behavior of a passive scalar field (e.g. density or temperature) within turbulent flows is of importance both for understanding turbulent mixing and heat transfer, and also to provide context and interpretation for experimental techniques that measure such fields (e.g., [1]). Many aspects of passive scalar behavior in wall-bounded turbulence remain active areas of investigation, including scalar scaling laws and statistics [2–4], modulation of scalar fields by emergent structures in transitional flow [5, 6], and correlations between the scalar and momentum fields [7] and various functions and derivatives thereof [8, 9]. See [10] for a review of many other aspects of passive scalar behavior in turbulence. Of particular interest is the extent to which, and contexts in which, the strong Reynolds analogy applies for predicting and understanding the behavior of scalar fields (e.g. [11, 12]). Note also that the utility of developing an understanding of passive scalar dynamics extends to the compressible regime if one assumes Morkovin's hypothesis [13] that the dominant effects of (mild) compressibility are accounted for by changes in the relevant mean profiles.

The resolvent of a given linear operator gives information about its pseudospectral properties [14, 15], which is of particular relevance for highly nonnormal operators [16], such as those that arise in shear flows. Indeed, considering the leading singular vectors of the resolvent operator obtained from linearizing about the turbulent mean has been found to give a useful reduced-order representation of wall-bounded turbulent flows [17–20]. This approach has shown promise and success for the prediction of numerous pertinent features of wall-boulder turbulence, including structures [19] and statistics [21] in wall-bounded turbulence, as well as showing promise for use as a reduced order modeling framework for control [22]. Note that this and similar approaches has also been applied to a range of other fluids systems, such as turbulent jet [23–25] and cavity flows [26, 27].

The present work explores the potential for studying passive scalar dynamics in wall-bounded shear flows using the resolvent framework. The incorporation of a passive scalar field into resolvent analysis is presented in section II, before results from applying this analysis to turbulent boundary layer profiles, using both experimental and numerical mean flow data, are given in section III

---

[*]Postdoctoral Scholar, Graduate Aerospace Laboratories, AIAA member
[†]Theodore von Karman Professor of Aeronautics, Graduate Aerospace Laboratories, AIAA Associate Fellow
[‡]Postdoctoral Scholar, Department of Mechanical and Aerospace Engineering

II. Resolvent formulation with a passive scalar field

Upon taking a temporal Fourier transform, the incompressible Navier-Stokes equations may be written as

$$\begin{pmatrix} -i\omega + (\nabla \boldsymbol{u}_0) \cdot + \boldsymbol{u}_0 \cdot \nabla - Re^{-1}\Delta & \nabla \\ \nabla^T & 0 \end{pmatrix} \begin{pmatrix} \boldsymbol{u}_\omega \\ p_\omega \end{pmatrix} = \begin{pmatrix} \boldsymbol{f}_\omega \\ 0 \end{pmatrix}$$

where p is the pressure, $\boldsymbol{u}_0$ is the mean velocity, and $\boldsymbol{u}_\omega$ and $\boldsymbol{f}_\omega$ represent the mean-subtracted velocity, and nonlinear (forcing) term respectively. We consider wall-bounded flow with a mean velocity component in the streamwise direction only, which is assumed to not vary in the streamwise or spanwise directions. In this case we may take a spatial Fourier transform in the streamwise and spanwise directions, giving

$$\begin{pmatrix} -i\omega + ik_xU - Re^{-1}\Delta & D_yU & 0 & ik_x \\ 0 & -i\omega + ik_xU - Re^{-1}\Delta & 0 & D_y \\ 0 & 0 & -i\omega + ik_xU - Re^{-1}\Delta & ik_z \\ ik_x & D_y & ik_z & 0 \end{pmatrix} \begin{pmatrix} u \\ v \\ w \\ p \end{pmatrix} = \boldsymbol{f}, \tag{1}$$

where U is the mean streamwise velocity (i.e., $\boldsymbol{u}_0 = (U(y),0,0)$), k_x and k_z are the streamwise and spanwise wave numbers, D_y is the partial derivative operator in the wall-normal direction, and $\Delta = D_{yy} - k_x^2 - k_z^2$. Here u and P represent mean-subtracted quantities (as do v and w, though they are assumed to have zero mean component), and for clarity we have dropped the ω subscripts. We wish to incorporate an additional equation governing the transport of a passive scalar in the system, denoted by $T_{TOT} = T_0 + T$, with T_0 being the mean field. We will use terminology as if this is a temperature field, but note that the findings hold for any scalar. The scalar satisfies the advection-diffusion equation (after temporal Fourier transform)

$$-i\omega T + \boldsymbol{u} \cdot \nabla T - (RePr)^{-1}\Delta T = 0, \tag{2}$$

where Pr is the Prandtl number, which represents the ratio between viscous and thermal diffusion. Decomposing this into mean (which we again assume only varies in the wall-normal direction) and fluctuating components, and subtracting off the mean equation, we have

$$-i\omega T + Uik_xT + vD_yT_0 - (RePr)^{-1}\Delta T = -(uk_x + vD_y + wk_z)T = f_T. \tag{3}$$

We may insert this as an additional equation into Eq. 1, to obtain

$$\begin{pmatrix} -i\omega + ik_xU - Re^{-1}\Delta & D_yU & 0 & ik_x & 0 \\ 0 & -i\omega + ik_xU - Re^{-1}\Delta & 0 & D_y & 0 \\ 0 & 0 & -i\omega + ik_xU - Re^{-1}\Delta & ik_z & 0 \\ ik_x & D_y & ik_z & 0 & 0 \\ 0 & D_yT_0 & 0 & 0 & -i\omega + ik_xU - (RePr)^{-1}\Delta \end{pmatrix} \begin{pmatrix} u \\ v \\ w \\ p \\ T \end{pmatrix} = \begin{pmatrix} f \\ 0 \\ f_T \end{pmatrix}, \tag{4}$$

where we have dropped the primes from elements of the state vector. Note in particular that there is forcing in the temperature equation, but not the linear continuity equation. Eq. 4 may be rearranged and expressed compactly as

$$\mathbf{q} = \mathcal{H}_\omega \boldsymbol{f}_\mathbf{q}, \tag{5}$$

where $\mathbf{q} = [u \ v \ w \ p \ T]^T$, $\boldsymbol{f}_\mathbf{q} = [f_u \ f_v \ f_w \ 0 \ f_T]^T$ and $\mathcal{H}_\omega$ is the inverse of the operator on the left side of Eq. 4. Resolvent analysis proceeds by considering the leading singular vectors of the singular value decomposition (SVD) of $\mathcal{H}_\omega$ (or equivalently, the singular vectors corresponding to the smallest singular values of the operator in Eq. 4). The leading resolvent response and forcing modes are the leading left and right singular vectors of $\mathcal{H}_\omega$, respectively.

Note also that if we keep the inner product as the (turbulent kinetic) energy norm, then the velocity forcing and response modes will be both unaffected by the additional equation in the system. However, we may propagate the forcing mode through the resolvent operator to determine the response of the scalar. Note that this is similar to the approach taken in [28], for example, to compute pressure response modes. Viewing our underlying vector space as that
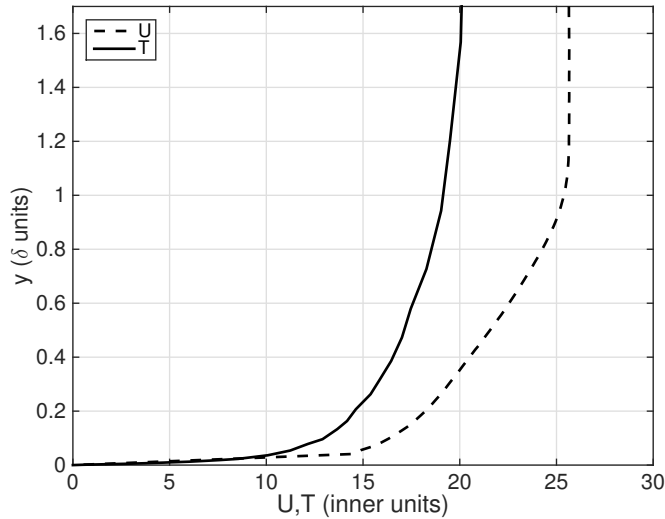
2

Fig. 1 Mean streamwise velocity and pressure profiles for a turbulent boundary layer at $Re_\tau = 910$. Temperature data obtained from [30].

containing all values of the state $\mathbf{q}$, the energy norm for incompressible fluids is really a seminorm, as it does not satisfy the uniqueness property that $\|\mathbf{q}\| = 0$ implies $\mathbf{q} = 0$. This means that there are, mathematically speaking, multiple solutions to the SVD problem when using the energy seminorm as defined. However, the velocity field is fixed for the family of solutions to the SVD, and the pressure and temperature fields may be determined such that they satisfy the governing equations. In the case of pressure, this means that the pressure field is that which enforces incompressibility of the resolvent modes (which may be computed either from the resolvent operator, or through Green's functions [28]).

III. Results and analysis

We now apply the formulation presented in Section II to a turbulent boundary layer with no external pressure gradient. The majority of the results presented in this section will use mean streamwise velocity and scalar (temperature) profiles obtained from wind tunnel experiments at $Re_\tau = 910$, shown in Fig. 1. The temperature gradient is obtained by heating the boundary upstream of the measurement plane, where here and henceforth we flip the sign of the scalar field (i.e., we consider as a variable the temperature deficit from the wall temperature), which results in the gradient of the mean scalar field having the same sign as that for the velocity. The heating elements were heated to a temperature 22 K above than the freestream air temperature. Comparison to statistics for an unheated boundary layer confirmed that the temperature field could be considered as a passive scalar field for this configuration. The Prandtl number is assumed to be 0.7 throughout. Refer to [29–32] for further details about the experimental setup. As is typical, the thermal boundary later extends further from the wall than the velocity boundary layer. We assume that variations in the streamwise direction are sufficiently small that we can perform a local (one dimensional) analysis as described in Section II.

Resolvent analysis is performed using a Chebyshev pseudospectral method, with a domain extending 10δ in the wall-normal direction, where δ is the boundary layer thickness corresponding to the location where the mean velocity is 99% of the freestream. We show in Figs. 2 and 3 typical results (in the form of amplitude of leading forcing and response modes) from carrying out the analysis as described in section II, for a given set of spatial wavenumbers, and temporal frequencies corresponding to wave speeds of $c^+ = \omega/k_x = 10$ and 20. Shown are the amplitude of the forcing and response mode components in the velocity and temperature field, as well as the response shapes for each component in a two dimensional cross-section at a fixed spanwise location. The kinetic energy norm is used, so the inner product is not weighted, and consequently the forcing modes do not have any scalar component. In both cases the modes are

3

typically localized near the critical layer, with those in Fig. 2 "attached" to the wall, and those in Fig. 3 detached, owing to the critical layer being further from the wall. We make the preliminary observation that, for this set of wavenumbers the temperature response mode amplitude looks similar to that of the streamwise velocity for both cases.

This is explored further in Fig. 4, where the (scaled) amplitude and phase of the streamwise velocity and temperature response mode components are plotted together for three wave speeds. We find that the temperature response does indeed closely match the response in streamwise velocity, with the largest discrepancy occurring when the critical layer is closest to the wall.

To understand the behavior of the scalar field in more detail, we will now turn our attention back to the governing equations to study the expected behavior for this system under a variety of conditions. By rearranging Eq. 3, we have

$$(-i\omega + Uik_x - (RePr)^{-1}\Delta)T = f_T - vD_yT_0. \tag{6}$$

If T is not included in the norm, then f_T may be set to zero (note that this is non-physical, as there would still be a fluctuations due to the forcing in the velocity). Since the velocity response mode is determined without considering this equation, we may consider v as known. This means that the T component of the response mode may be computed using

$$T = (-i\omega + Uik_x - (RePr)^{-1}\Delta)^{-1}(-vD_yT_0). \tag{7}$$

Rather than explicitly using Eq. 4, this allows us to compute the response mode(s) of the scalar after computing the regular resolvent operator, which reduces the maximum sizes of the matrices that we need to assemble, and also allows for passive scalar modes to be computed after-the-fact when velocity response modes are known. We emphasize that this may only be done when the inner product does not give any weight to the passive scalar (though later we will demonstrate that the choice of inner product generally has negligible effect on the shapes of each component of a given mode). The formulation given in Eq. 7 also suggests that the behavior of the scalar response can be studied without explicit knowledge of the velocity response. This idea is explored in Section A.

A. Passive scalar analysis without momentum equations

Considering Eq. 7, we may draw an analogy with the resolvent formulation of the Navier-Stokes equations. That is, we have an input, or forcing, which is acted on by the operator

$$Q_\omega = (-i\omega + Uik_x - (RePr)^{-1}\Delta)^{-1} \tag{8}$$

to obtain the scalar response for a given velocity response. It is natural, then, to wonder how much the scalar response depends on the particular forcing, as opposed to the properties of the operator Q_ω itself. To analyze this, we consider the optimal forcing and response modes for Q_ω (obtained as usual through an SVD) in Fig. 5. We observe that the "uncoupled" response modes, obtained from Q_ω, have a similar shape to the coupled (i.e., with "forcing" of Q_ω as defined in Eq. 7) mode. The similarity between the streamwise velocity and scalar response modes further suggest that streamwise velocity response mode shapes can also be approximated using a scalar operator similar to that defined in Eq. 8. While the forcing for the coupled case $(-vD_yT_0)$, and the right singular vectors of Q_ω in the uncoupled case) are typically supported in a similar wall-normal location (with the former typically being supported on a larger region), the phase variation between the two is quite different. In particular, the coupled forcing modes $(-vD_yT_0)$ have very little phase variation with wall-normal height, while the decoupled scalar forcing is inclined upstream. The fact that similar responses are observed for different forcing inputs suggests that the scalar operator Q_ω is acting as a highly directional amplifier, and amplifying the component of the forcing in the direction of its optimal forcing, but providing little amplification to the remaining component. This is the same general principle that can allow resolvent analysis to make predictions about turbulent flows without specific knowledge of the forcing: so long as the forcing has some component in the direction of optimal forcing, that component will excite the optimal response.

This observation that the uncoupled scalar equations predict features observed in the full system is broadly consistent with the conclusions of other methods of analysis for passive scalar dynamics [33]. These findings also mean that, at least in some regimes, the scalar response is relatively insensitive to the precise shape of the mean scalar field, since
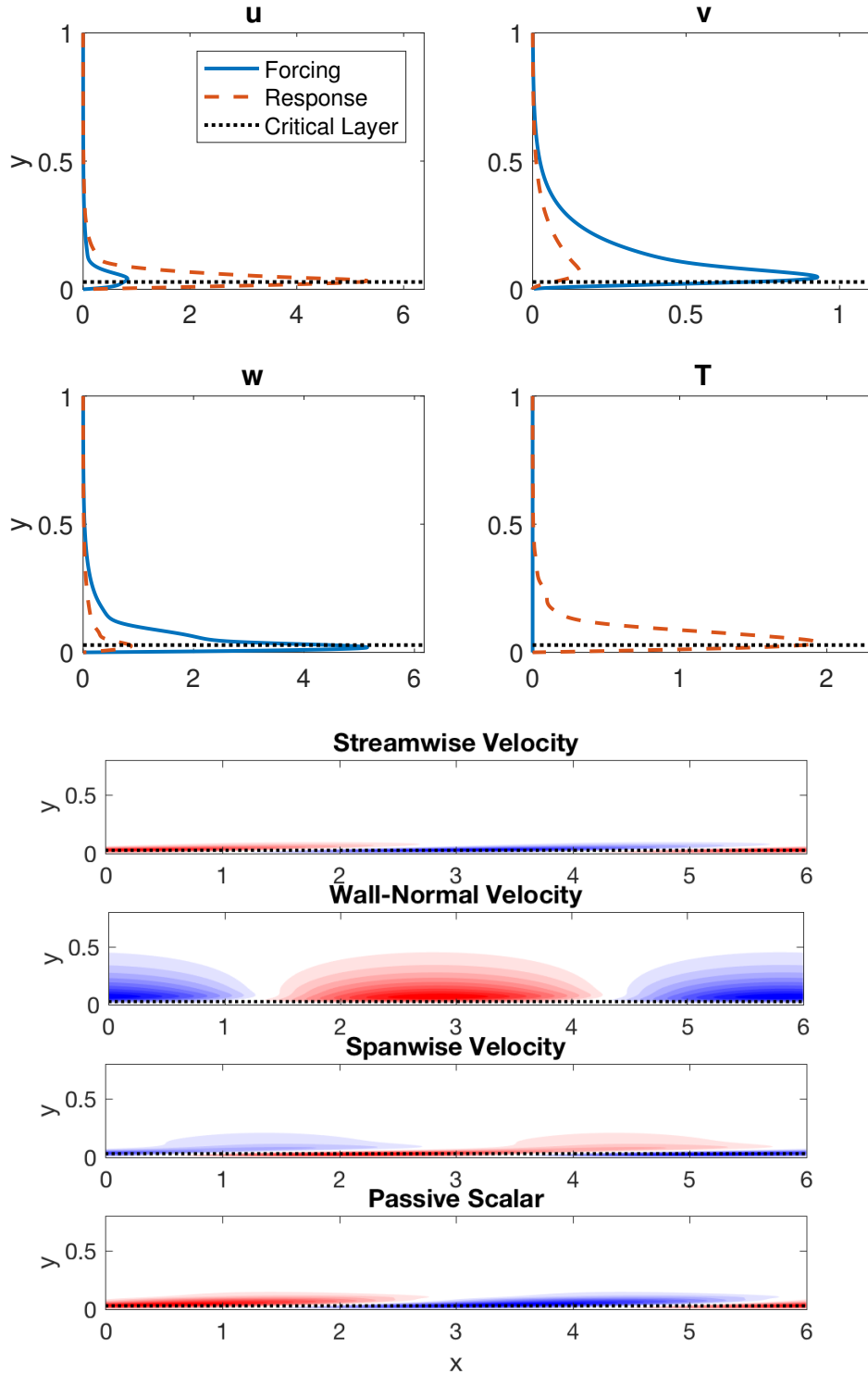
4

Fig. 2 **Resolvent modes (forcing and response) with the inclusion of a passive temperature field, with** $Pr = 0.7$, $k_x = \pi/3$, $k_z = 2\pi$, **and** $c^+ = \omega/k_x = 10$. **The top four subplots show the amplitudes of each component of the forcing and response modes (each having unit norm), while the lower subplots show response mode shapes in a two dimensional cross-section at a fixed spanwise location. Red and blue contours represent positive and negative fluctuations, respectively, with contour levels for each field scaled by the maximum of each mode component. Also shown is the location of the critical layer, where** $c^+ = U$.

5
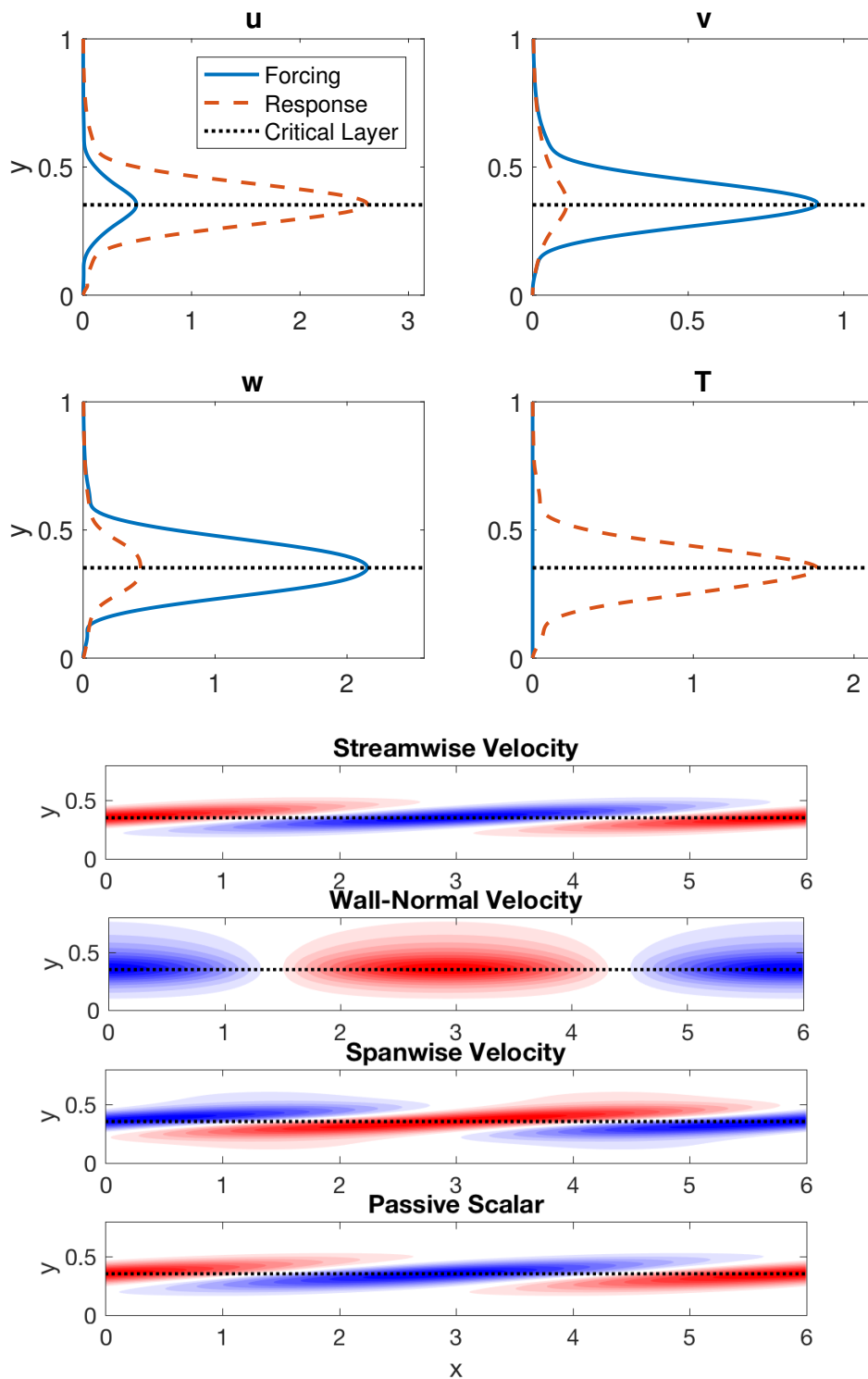
Fig. 3 As for Fig. 2, but with $c^+ = 20$.
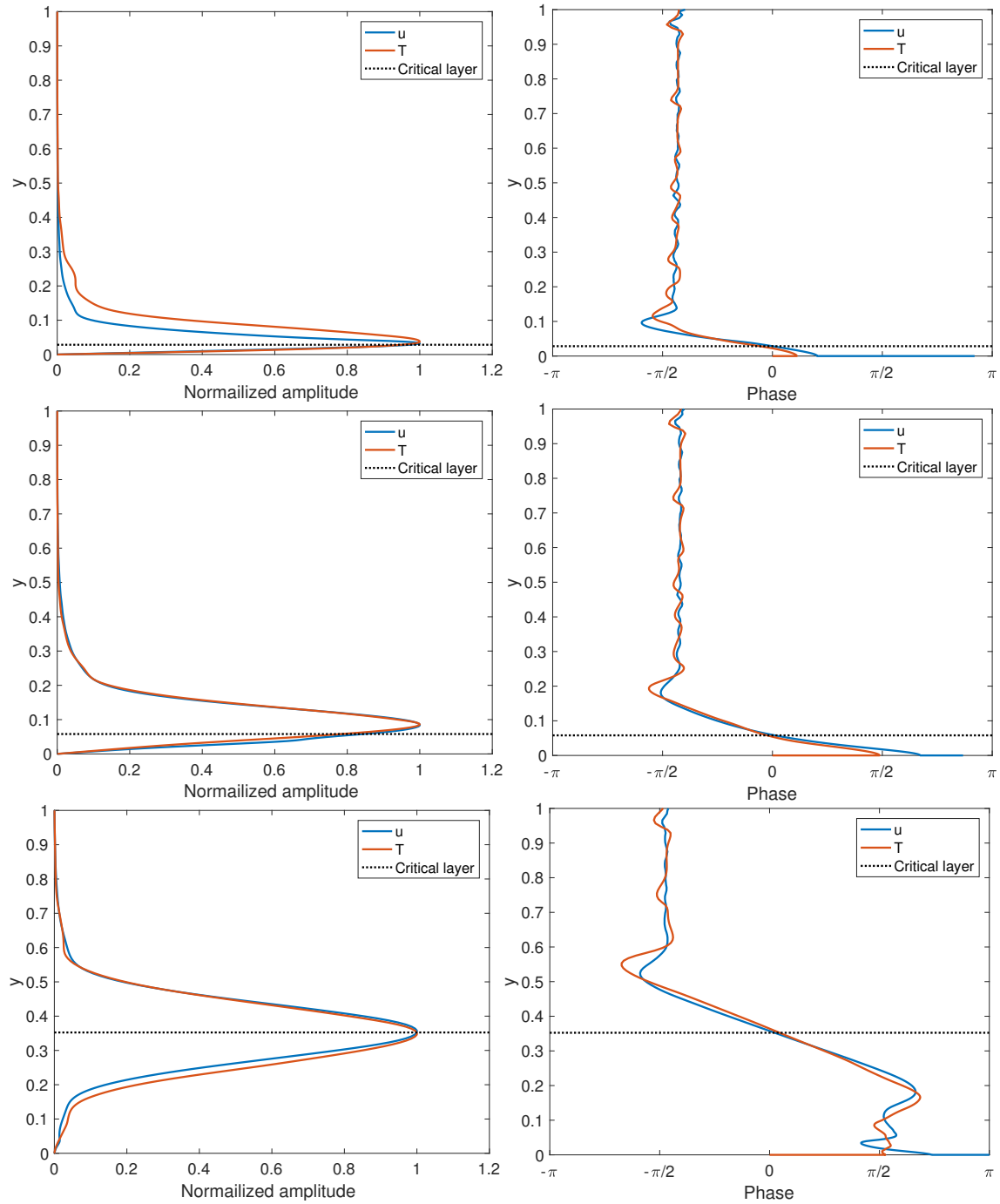
Fig. 4 Amplitude (left) and phase (right) of streamwise velocity and passive scalar components of resolvent response modes with $k_x = \pi/3$, $k_z = 2\pi$, and $c^+ = 10$ (top row), 15 (center), and 20 (bottom).
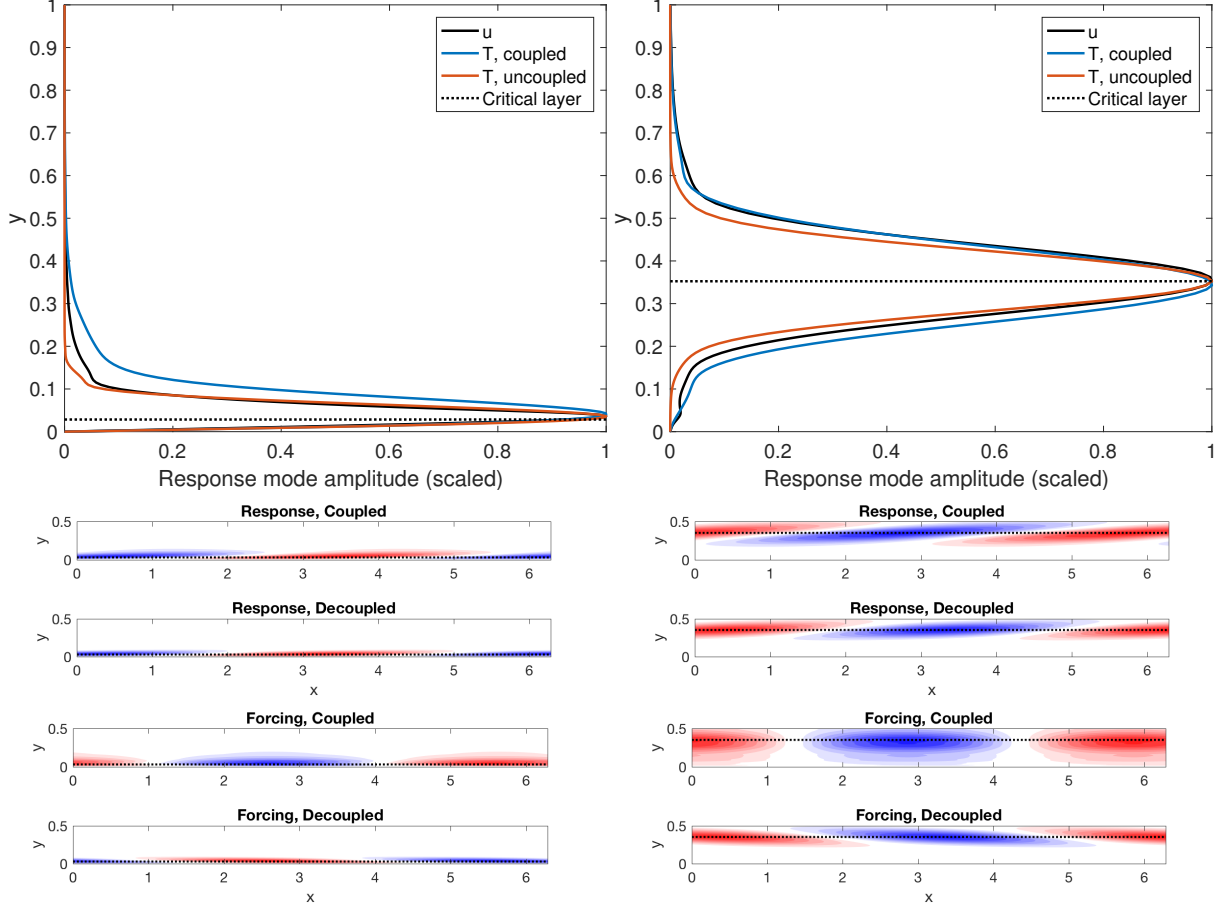
7

Fig. 5 Scalar forcing and response modes identified both from the computed velocity modes (coupled), and from taking an SVD of Q_ω (decoupled), with $k_x = \pi/3$, $k_z = 2\pi$, and $c^+ = 10$ (left subplots) and 20 (right). The top row of plots show the scaled response amplitudes of the coupled and decoupled scalar modes in comparison to the streamwise velocity component, while the lower subplots show forcing and response modes in a two dimensional cross-section at a fixed spanwise location.

the analysis of the scalar operator does not account for the mean scalar profile (though note that, while it is not done here, one could use the gradient of the mean scalar field to weight the norm used in the study of the scalar operator). This suggests that it is reasonable to investigate the dynamics of scalar fields with different properties, even without the availability of modified mean scalar field data. This is investigated in Section B.

B. Effect of scalar diffusivity and boundary conditions

We show in Figs. 6 and 7 the effect of the Prandtl number (i.e. scalar diffusivity) on the passive scalar component of the resolvent response mode. As discussed at the end of Section A, this is done without changing the mean scalar field. We observe that larger Pr typically corresponds to a larger response, which is more concentrated on the critical layer. We can understand this behavior by considering the limits of small and large scalar diffusivity.
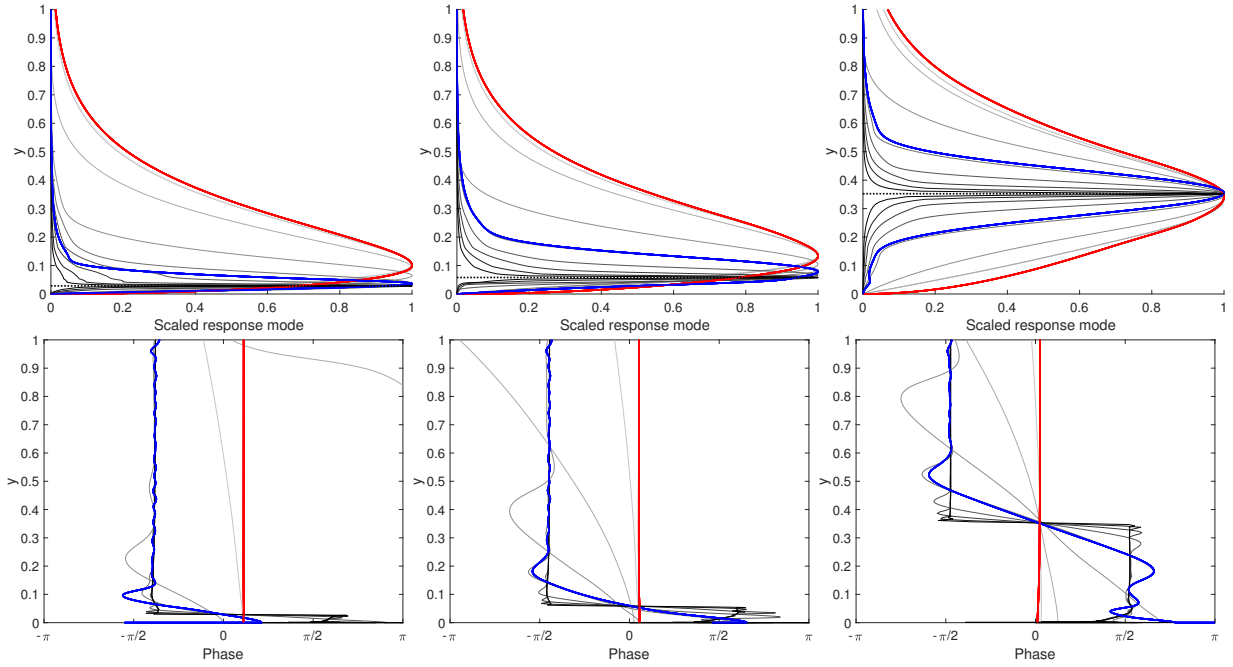
8

Fig. 6 **Passive scalar resolvent response modes, for** Pr **ranging from 0.00001 (lightest gray) to 10000 (black). Also shown in blue are the streamwise velocity component of the modes, and in red are the Green's function approximations where the non-diffusive terms are neglected. All plots are for** $k_x = \pi/3$ **and** $k_z = 2\pi$**, with** $c^+ = 10$ **(left) 15 (center) and 20 (right).**
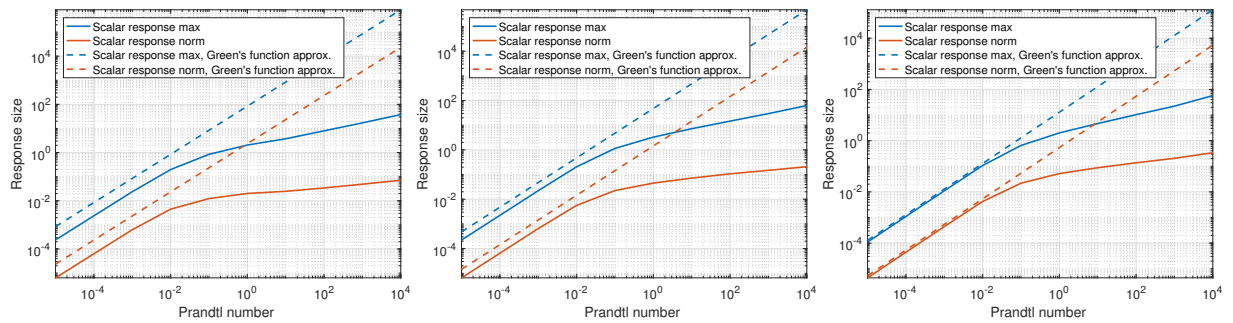

Fig. 7 **Comparison between true and low** Pr **approximations of the magnitude of the leading passive scalar resolvent response mode as a function of Prandtl number, for** $k_x = \pi/3$**,** $k_z = 2\pi$**, and** $c^+ = 10$ **(left) 15 (center) and 20 (right).**

9

As $Pr \to \infty$, the diffusion term becomes negligible. This means that

$$T \to (-i\omega + Uik_x)^{-1}vD_yT_0 = i(Uk_x - \omega)^{-1}vD_yT_0,$$

$$= ik_x(U - c^+)^{-1}vD_yT_0.$$

$$= \begin{cases} \frac{-ik_x}{\|U-c^+\|}vD_yT_0, & y < y_{crit} \\ \frac{ik_x}{\|U-c^+\|}vD_yT_0, & y > y_{crit} \end{cases}$$

which has a singularity when $Uk_x = \omega$ (i.e., on the critical layer), so long as vD_yT_0 is nonzero at this location. We thus expect for the amplitude of the scalar mode to approach a delta function at the critical layer, with the phase jumping by π across the critical layer (when $-i\omega + Uik_x$ changes sign). Aside from this, we also expect for the phase to match v, offset by $\pi/2$, as this is the only complex term in the equation. If T_0 is an increasing function, then D_yT_0 will be negative. This means that we expect the scalar response to have a phase offset from v of $+\pi/2$ below the critical layer, and $-\pi/2$ above it.

In this case of negligibly small Prandtl number, the diffusive term will dominate. We observe in Figs. 6 and 7 that the magnitude of the response becomes wider, with a peak amplitude further from the wall than the other modes for $c^+ = 10$ and 15. The phase also becomes approximately constant and locked to the phase of the streamwise velocity response at the critical layer. This is the location of the peak for low scalar diffusion, so for fast diffusion it makes sense that the scalar will quickly dissipate throughout the domain at this phase.

If we ignore the non-diffusion terms from the right hand side of Eq. 6, we obtain

$$\Delta T = \left(-(k_x^2 + k_z^2) + D_{yy}\right)T = -(RePr)vD_yT_0. \tag{9}$$

The Pr term on the right hand side of this equation explains the observation in Fig. 7 that the size of the temperature response is proportional to Pr for small Pr. Eq. 9 (which is now self-adjoint, and allowing for the application of Sturm-Liouville theory) can be solved directly using Green's functions. In particular, when using Dirichlet boundary conditions at the wall and in the far field, we have the Green's function

$$G(y,\xi) = \begin{cases} \frac{1}{2k}\left[e^{k_\perp(y-\xi)} + e^{-k_\perp(y+\xi)}\right] & y \le \xi \\ \frac{1}{2k}\left[e^{k_\perp(\xi-y)} + e^{-k_\perp(y+\xi)}\right] & y > \xi \end{cases}, \tag{10}$$

where $k_\perp = \sqrt{k_x^2 + k_z^2}$. The fluctuating scalar field response can then be computed through

$$T(y) = -RePr \int_0^\infty G(y,\xi)v(\xi) \left.\frac{\partial T_0}{\partial y}\right|_{y=\xi} d\xi. \tag{11}$$

Figs. 6 and 7 show that this approximation is indeed accurate for small Pr. Note also that while we only consider one set of spatiotemporal wavenumbers here, the range of Prandtl numbers at which these asymptotic approximations are accurate will be wavenumber-dependent.

So far, we have assumed Dirichlet boundary conditions on T, which corresponds to a constant temperature wall. We compare these results to those assuming an adiabatic wall (Neumann boundary conditions) in Figs. 8 and 9. We observe, as might be expected, that the resulting modes differ the most for smaller wave speeds, where the critical layer, and the location of the response mode, are closer to the wall. In particular, adiabatic boundary conditions allow for larger scalar response amplitudes closer to the wall.

C. Scaling relationships of passive scalar diffusivity

The analysis in Section A suggests that the scalar response can, in many cases, be attributed to the properties of the operator $\mathcal{Q}_\omega$, rather than the nature in which it is forced. To study such ideas further, we seek a transformation in spatio-temporal wavenumber space that accounts for the effect of different Prandtl numbers. Note first that we have

$$\mathcal{Q}_\omega = Pr\left[-i(\omega Pr + Uk_xPr) - (Re)^{-1}(D_{yy} - k_x^2 - k_z^2)\right]^{-1}. \tag{12}$$
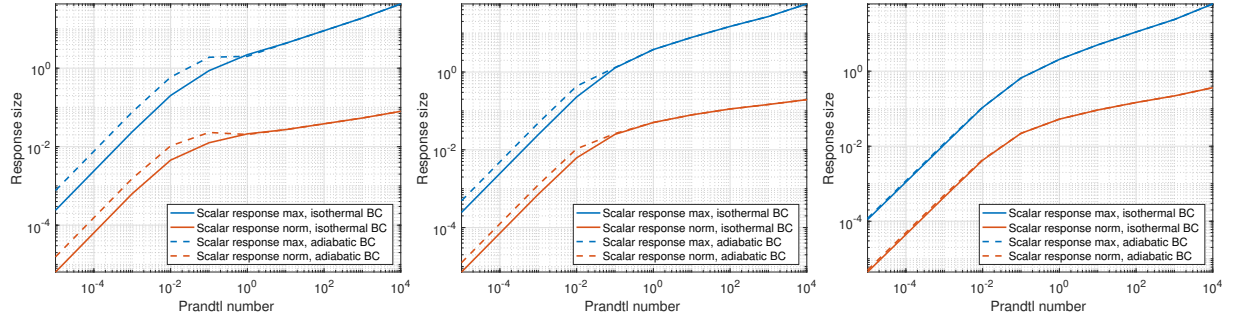
10

Fig. 8 Comparison between the magnitude of the leading passive scalar resolvent response mode as a function of Prandtl number for an isothermal (solid lines) and adiabatic (dashed) wall, for $c^+ = 10$ (left) 15 (center) and 20 (right), with $k_x = \pi/3$ and $k_z = 2\pi$ throughout.
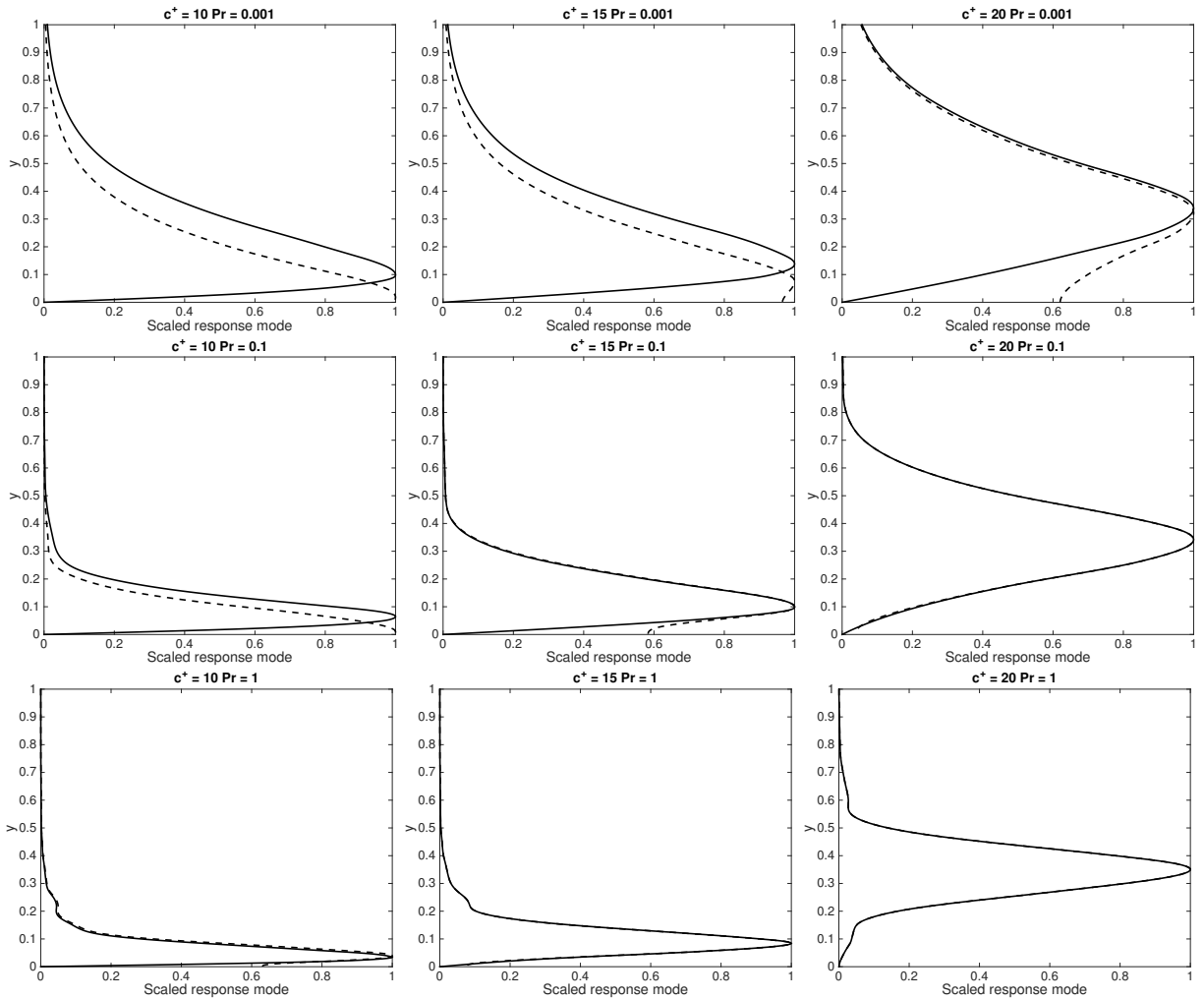

Fig. 9 Comparison between scalar response for an isothermal (solid) and adiabatic (dashed) wall, for various wave speeds and Prandtl numbers. The spatial wavenumbers are fixed, with $k_x = \pi/3$ and $k_z = 2\pi$.

11

It is then evident that k_x and k_z may be adjusted as Pr varies such that Q_ω is only changed by a scalar factor (Pr). In particular, suppose that $Q_{0,\omega}$ corresponds to ω_0, k_{x0}, k_{z0}, and Pr_0. Then if we let

$$\omega_1 Pr_1 = \omega_0 Pr_0, \quad k_{x1} Pr_1 = k_{x0} Pr_0, \quad k_{x1}^2 + k_{z1}^2 = k_{x0}^2 + k_{z0}^2, \tag{13}$$

we find that

$$\frac{Q_{1,\omega}}{Pr_1} = \frac{Q_{0,\omega}}{Pr_0}. \tag{14}$$

To test how well the temperature response collapses under these rescalings, we show in Fig. 10 the results from applying the relations defined in Eq. 13, for a given set of ω_0, k_{x0}, k_{z0}, and Pr_0. Note that in order to ensure real wave numbers, we require that

$$Pr_1^2 > \frac{Pr_0^2 k_{x0}^2}{k_{x0}^2 + k_{z0}^2}.$$

We observe that the passive scalar response shapes collapse well, except for higher Prandtl numbers and low wave speeds. In these cases, the most prominent discrepancy is the emergence of a secondary response peak located further from the wall. This corresponds to cases where the wall-normal velocity response reaches a peak further from the wall than the peak responses of the streamwise velocity and the passive scalar. This is consistent with our previous analysis: the component of the response due to the amplifying properties of Q_ω match, but those due to the nature of the forcing do not, which is most apparent when the forcing peak (i.e., the wall-normal velocity response) is at a different location to the peak response of Q_ω. Note once more that Q_ω is independent of the mean scalar profile, so it is possible to analyze it for varying Prandtl number without having to account for differences in the mean scalar gradient that would come with changing Prandtl numbers.

D. Effect of norm

The SVD computes optimal forcing and response modes of the resolvent operator with respect to a specified (semi)norm. Up to this point, we have chosen a norm corresponding to the kinetic energy of the flow. We now investigate more general norms of the form

$$E = \frac{1}{2} \int_\Omega \left(\boldsymbol{u}^2 + \alpha T^2 \right) dV, \tag{15}$$

for a variety of values of α (the previous results have implicitly used $\alpha = 0$). We show in Fig. 11 that the shape of the forcing and response modes is largely unaffected by different values of α. This suggests that the outcomes of analysis are insensitive to the choice of norm. It further suggests that, even for nonzero α, it should be possible to compute the scalar mode after the velocity mode has been computed. The phase variation of the modes are not shown, but collapse similarly for each α. Note that we could also choose different norms for forcing and response, which is not considered here. We postulate that this could be a consequence of both a large spectral gap between the leading and subdominant singular values, and that the optimal scalar response arises from forcing in a similar wall-normal location to the the wall-normal velocity of the optimal streamwise velocity response, as discussed in Section A. Further studies (not presented here) indicate that the almost identical mode shapes do not always extend to suboptimal modes, though they seem to do so for smaller Pr, for example. In addition, this lack of sensitivity of the optimal mode shapes does not seem to be universal across all wavenumbers. For example, large k_z gives rise to much larger variation in optimal modes.

E. Prediction of turbulent statistics

One of the main goals of seeking a reduced order modeling framework for turbulent flows is the ability to make predictions about quantities of interest, which could otherwise only be evaluated from high fidelity simulations or experiments. In this section, we explore the ability of the resolvent framework to model single point statistics. In [21], the resolvent framework is used to model energy spectra and densities of streamwise velocity in turbulent channel flow.
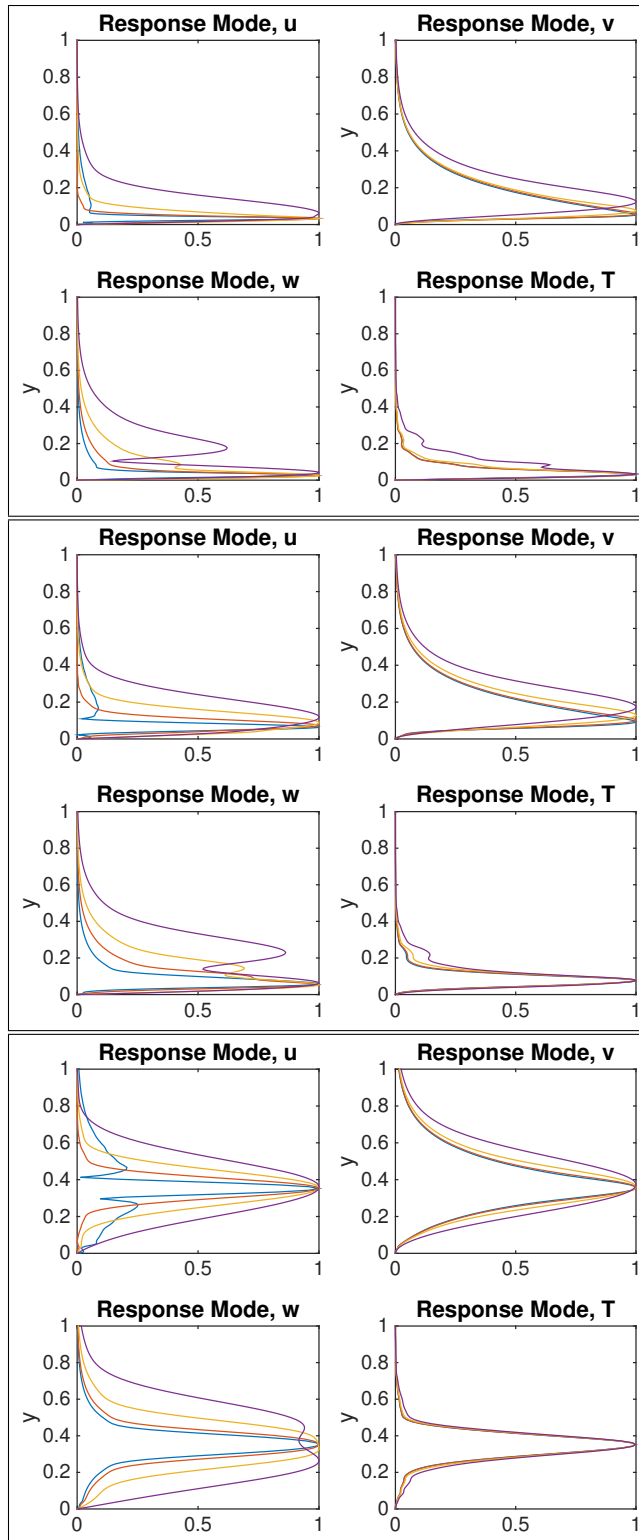
12

Fig. 10 **Normalized response modes for Prandtl numbers 0.5 (blue curves), 1 (red), 5 (yellow), and 25 (purple)** where ω, k_x and k_z have been adjusted such that $Pr\,k_x = \pi/6$, $k_x^2 + k_z^2 = (1+4)\pi^2$, with $c^+ = 10$ (top), 15 (center) and 20 (bottom).
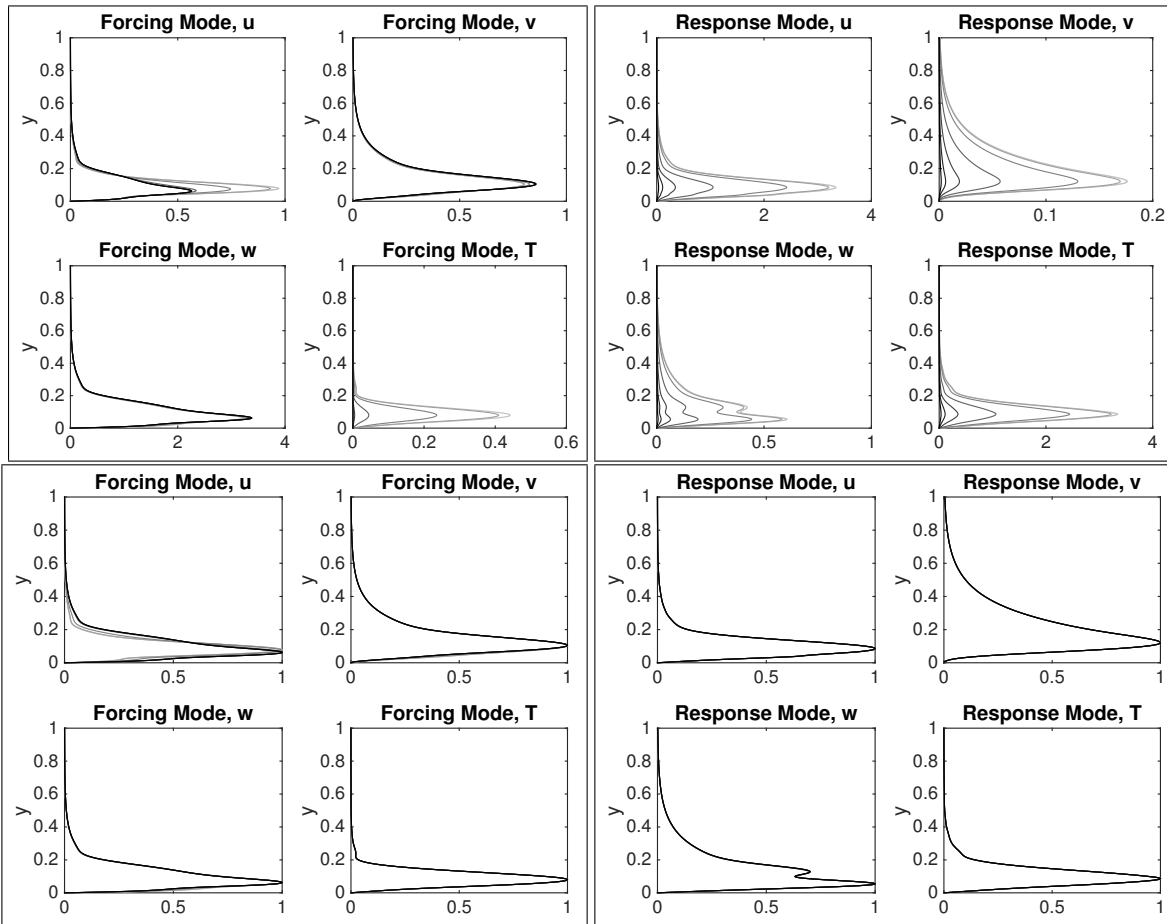
13

Fig. 11 Forcing and response modes (absolute value) for norms with α ranging from 0 (lightest shading) to 10000 (black), with $k_x = \pi/3$, $k_z = 2\pi$, and $c^+ = 15$. The lower 8 subplots show the same modes as the upper 8, but where the mode components have been normalized such that they have maximum of 1.

14

In this section, we explore how this approach can be extended to model passive scalar statistics in a turbulent boundary layer.

Whereas the previous results presented in this work have use experimentally measured velocity and temperature profiles, for this section we use direct numerical simulation data of a zero-pressure-gradient turbulent boundary layer. The DNS data was obtained from the simulations described in [34] and [6]. The mean profiles and turbulent statistics are computed from data collected at a constant streamwise location, corresponding to a friction Reynolds number of approximately 900. The scalar field has unit Prandtl number, and the dimensionless scalar field has a value of unit at the wall, and zero in the far field. In contrast to the experimental data, here we keep the mean scalar field with an opposite gradient to the mean streamwise velocity.

Following [21], we define the premulitiplied streamwise energy density of the resolvent model by

$$E_{uu}(y; k_x, k_z, c) = k_x^2 k_z \left[\sigma_1(k_x, k_z, c) |u_1(y; k_x, k_z, c)| \right]^2, \tag{16}$$

where σ_1 is the leading singular value, and u_1 is the streamwise component of the leading response mode, and the associated integrated energy density as a function of wall-normal location:

$$E_{uu}(y) = \iiint_{k_x, k_z, c} E_{uu}(y; k_x, k_z, c) d\log(k_x) d\log(k_z) dc. \tag{17}$$

Note that the exponent of 2 on the k_x term in Eq. 16 arises due to the fact that we integrate over c rather than ω in Eq. 17. We may similarly define the equivalent quantities for the fluctuating temperature field:

$$E_{TT}(y; k_x, k_z, c) = k_x^2 k_z \left[\sigma_1(k_x, k_z, c) |T_1(y; k_x, k_z, c)| \right]^2 \tag{18}$$

$$E_{TT}(y) = \iiint_{k_x, k_z, c} E_{TT}(y; k_x, k_z, c) d\log(k_x) d\log(k_z) dc, \tag{19}$$

where T_1 is the temperature component of the leading resolvent response mode. We can further consider the cross-correlation between streamwise velocity and temperature:

$$E_{uT}(y; k_x, k_z, c) = k_x^2 k_z \sigma_1(k_x, k_z, c) u_1^*(y; k_x, k_z, c) T_1(y; k_x, k_z, c) \tag{20}$$

$$E_{uT}(y) = \iiint_{k_x, k_z, c} E_{UT}(y; k_x, k_z, c) d\log(k_x) d\log(k_z) dc. \tag{21}$$

It was demonstrated in [21] that introducing an empirical weighting function into the integral in Eq. 17 can give a quantitatively accurate fit to the equivalent directly measured quantities in numerical simulations. For example, we may introduce a weight function W_{uu} into the integral in Eq. 17 to give the weighted energy intensity

$$E_{uu,W}(y) = \iiint_{k_x, k_z, c} W_{uu}(c) E_{uu}(y; k_x, k_z, c) d\log(k_x) d\log(k_z) dc. \tag{22}$$

W_{uu} may be computed using a regularized least-squares optimization, as described in [21]. Figure 12 shows W_{uu}, as well as a comparison between the fitted energy density and that computed from DNS data. Also shown for comparison is the energy density computed with a constant weight function. This shows that the unweighted resolvent prediction is able to approximately capture the peak in energy density, and that the primary effect of W_{uu} is to suppress the predicted energy content towards the upper edge of the boundary layer (as well as slightly shifting the inner energy density peak).

In Fig. 13, we apply the same methods to predict the scalar fluctuation energy, as well as the covariance between u and T. Not only can an accurate prediction be made when directly fitting the corresponding (and similarly defined) weight functions W_{TT} and W_{uT}, but it is further observed that using only W_{uu} also gives estimated statistics that match the main features of the scalar statistics of the DNS data. Note that the amplitude of the predicted scalar energy density will also be affected by the choice of norm used for resolvent analysis. As with the majority of results presented here, these results are based on a kinetic energy seminorm that does not weight the scalar field.
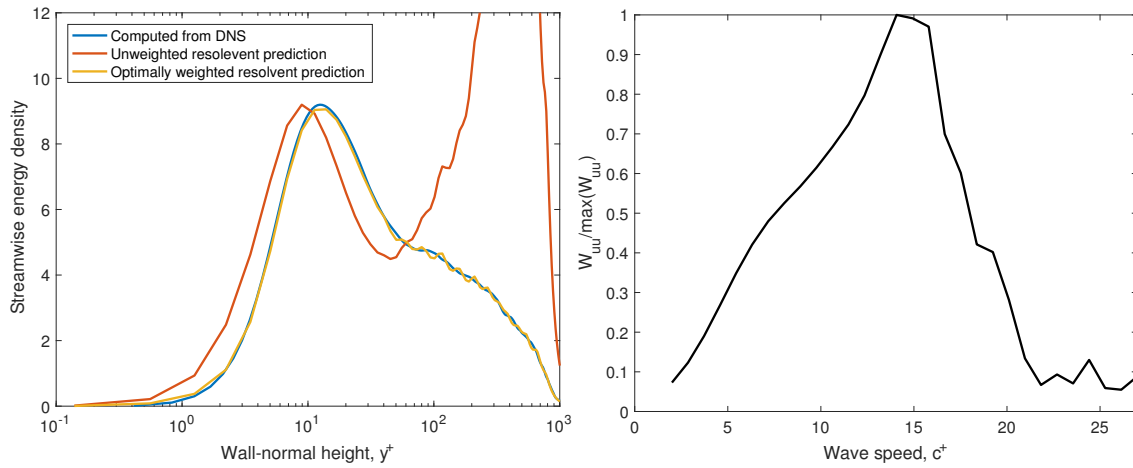
15

Fig. 12 **(left) Measured and predicted/fitted streamwise energy density, integrated over all wavelengths at each wall-normal location, (right) optimal weight function** $W_{uu}(c)$
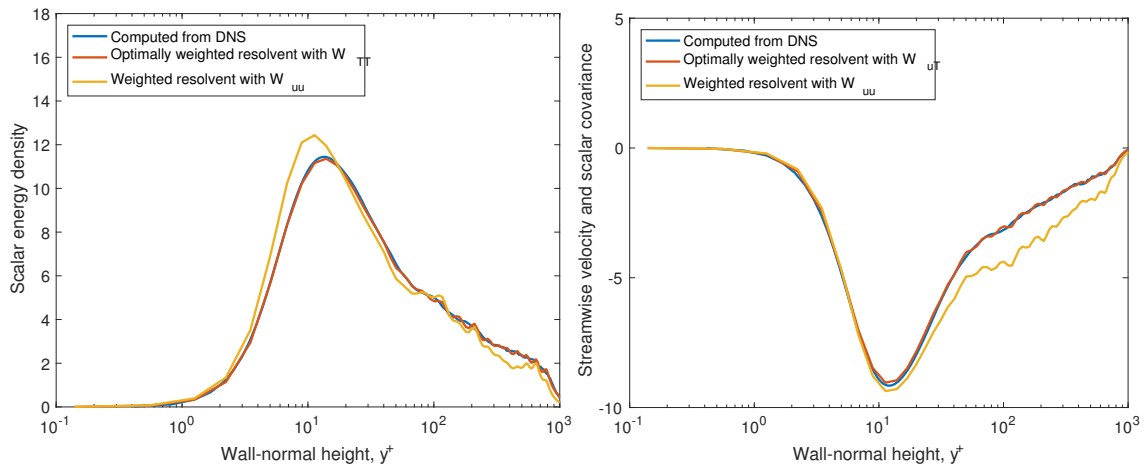

Fig. 13 **Measured and predicted/fitted scalar energy density (left), and streamwise velocity-scalar covariance (right)**

16

The fact that the streamwise velocity is typically the dominant component in leading resolvent response modes seems to be part of the underlying reason as to why statistics in this component are easiest to predict using resolvent analysis [21]. A modification that decomposes the underlying operators into Orr-Sommerfeld and Squire components is given in [35], which shows promise for improved capabilities for modeling non-streamwise velocity components. The similarity between the streamwise velocity and scalar components of response modes, as has been discussed previously in this work, along with the strong statistical correlation between these fluctuating quantities in turbulent shear flows (e.g. [7]), suggests the utility of the resolvent framework for modeling scalar fluctuations. The results of this section appear to indicate that this inference is well-founded.

IV. Conclusions

This work has extended resolvent analysis of incompressible wall-bounded turbulence to include a passive scalar field. This gives a framework for studying and predicting structures and statistics of scalar fluctuations at specified length and timescales, and in particular their correspondence with fluctuations in the velocity field. Similar observations (in terms of mode shapes) for the passive scalar field are observed when considering the passive scalar operator independently from the velocity field. This suggests that, in certain regimes, passive scalar structures are largely a result of the most amplified modes of the passive scalar operator itself, which can be predicted independently of the velocity field. This allowed for the analysis of the effect of scalar diffusivity, where mode shapes in the limits of small and large diffusivity were presented, and a scaling relationship was derived that allows for the identification of families of spatial wavenumbers and scalar diffusivities that are predicted to share similar scalar response mode shapes. The similarity between passive scalar and streamwise velocity modes (as might be expected from invoking the strong Reynolds analogy) also suggests that a similar decoupled scalar operator can also be used to analyze the streamwise velocity component of resolvent response modes. This scalar operator is more conducive to analytic treatment than the full Navier-Stokes system, and further analysis in this direction is the subject of ongoing work.

Acknowledgments

References

[1] Chen, C.-H. P., and Blackwelder, R. F., "Large-scale motion in a turbulent boundary layer: a study using temperature contamination," *Journal of Fluid Mechanics*, Vol. 89, No. 1, 1978, pp. 1–31.

[2] Li, Q., Schlatter, P., Brandt, L., and Henningson, D. S., "DNS of a spatially developing turbulent boundary layer with passive scalar transport," *International Journal of Heat and Fluid Flow*, Vol. 30, No. 5, 2009, pp. 916–929.

[3] Saha, S., Klewicki, J., Ooi, A., Blackburn, H., and Wei, T., "Scaling properties of the equation for passive scalar transport in wall-bounded turbulent flows," *International Journal of Heat and Mass Transfer*, Vol. 70, 2014, pp. 779–792.

[4] Pirozzoli, S., Bernardini, M., and Orlandi, P., "Passive scalars in turbulent channel flow at high Reynolds number," *Journal of Fluid Mechanics*, Vol. 788, 2016, pp. 614–639.

[5] Wu, X., Moin, P., Adrian, R. J., and Baltzer, J. R., "Osborne Reynolds pipe flow: Direct simulation from laminar through gradual transition to fully developed turbulence," *Proceedings of the National Academy of Sciences*, Vol. 112, No. 26, 2015, pp. 7920–7924.

[6] Wu, X., Moin, P., Wallace, J. M., Skarda, J., Lozano-Durán, A., and Hickey, J.-P., "Transitional–turbulent spots and turbulent–turbulent spots in boundary layers," *Proceedings of the National Academy of Sciences*, 2017, p. 201704671.

[7] Kim, J., and Moin, P., "Transport of passive scalars in a turbulent channel flow," *Turbulent Shear Flows 6*, Springer, 1989, pp. 85–96.

[8] Abe, H., Antonia, R. A., and Kawamura, H., "Correlation between small-scale velocity and scalar fluctuations in a turbulent channel flow," *Journal of Fluid Mechanics*, Vol. 627, 2009, pp. 1–32.

[9] Antonia, R. A., Abe, H., and Kawamura, H., "Analogy between velocity and scalar fields in a turbulent channel flow," *Journal of Fluid Mechanics*, Vol. 628, 2009, pp. 241–268.

[10] Warhaft, Z., "Passive scalars in turbulent flows," *Annual Review of Fluid Mechanics*, Vol. 32, No. 1, 2000, pp. 203–240.

[11] Huang, P., Coleman, G., and Bradshaw, P., "Compressible turbulent channel flows: DNS results and modelling," *Journal of Fluid Mechanics*, Vol. 305, 1995, pp. 185–218.

[12] Zhang, Y.-S., Bi, W.-T., Hussain, F., and She, Z.-S., "A generalized Reynolds analogy for compressible wall-bounded turbulent flows," *Journal of Fluid Mechanics*, Vol. 739, 2014, pp. 392–420.

[13] Morkovin, M. V., "Effects of compressibility on turbulent flows," *Mécanique de la Turbulence*, Vol. 367, 1962, p. 380.

[14] Kato, T., *Perturbation theory for linear operators*, Vol. 132, Springer Science & Business Media, 2013.

[15] Schmid, P. J., and Henningson, D. S., *Stability and transition in shear flows*, Vol. 142, Springer Science & Business Media, 2012.

[16] Trefethen, L. N., Trefethen, A. E., Reddy, S. C., and Driscoll, T. A., "Hydrodynamic stability without eigenvalues," *Science*, Vol. 261, No. 5121, 1993, pp. 578–584.

[17] McKeon, B. J., and Sharma, A. S., "A critical-layer framework for turbulent pipe flow," *Journal of Fluid Mechanics*, Vol. 658, 2010, pp. 336–382.

[18] Hwang, Y., and Cossu, C., "Linear non-normal energy amplification of harmonic and stochastic forcing in the turbulent channel flow," *Journal of Fluid Mechanics*, Vol. 664, 2010, pp. 51–73.

[19] Sharma, A. S., and McKeon, B. J., "On coherent structure in wall turbulence," *Journal of Fluid Mechanics*, Vol. 728, 2013, pp. 196–238.

[20] McKeon, B., "The engine behind (wall) turbulence: perspectives on scale interactions," *Journal of Fluid Mechanics*, Vol. 817, 2017.

[21] Moarref, R., Sharma, A. S., Tropp, J. A., and McKeon, B. J., "Model-based scaling of the streamwise energy density in high-Reynolds-number turbulent channels," *Journal of Fluid Mechanics*, Vol. 734, 2013, pp. 275–316.

[22] Luhar, M., Sharma, A. S., and McKeon, B. J., "Opposition control within the resolvent analysis framework," *Journal of Fluid Mechanics*, Vol. 749, 2014, pp. 597–626.

[23] Garnaud, X., Lesshafft, L., Schmid, P., and Huerre, P., "The preferred mode of incompressible jets: linear frequency response analysis," *J. Fluid Mech.*, Vol. 716, 2013, pp. 189–202.

[24] Jeun, J., Nichols, J. W., and Jovanović, M. R., "Input-output analysis of high-speed axisymmetric isothermal jet noise," *Physics of Fluids (1994-present)*, Vol. 28, No. 4, 2016, p. 047101.

[25] Towne, A., Schmidt, O. T., and Colonius, T., "Spectral proper orthogonal decomposition and its relationship to dynamic mode decomposition and resolvent analysis," *arXiv preprint arXiv:1708.04393*, 2017.

[26] Gómez, F., Blackburn, H. M., Rudman, M., Sharma, A. S., and McKeon, B. J., "A reduced-order model of three-dimensional unsteady flow in a cavity based on the resolvent operator," *Journal of Fluid Mechanics*, Vol. 798, 2016. doi:10.1017/jfm.2016.339.

[27] Qadri, U. A., and Schmid, P. J., "Frequency selection mechanisms in the flow of a laminar boundary layer over a shallow cavity," *Phys. Rev. Fluids*, Vol. 2, 2017, p. 013902.

[28] Luhar, M., Sharma, A., and McKeon, B., "On the structure and origin of pressure fluctuations in wall turbulence: predictions based on the resolvent analysis," *Journal of Fluid Mechanics*, Vol. 751, 2014, pp. 38–70.

[29] Jacobi, I., and McKeon, B., "New perspectives on the impulsive roughness-perturbation of a turbulent boundary layer," *Journal of Fluid Mechanics*, Vol. 677, 2011, pp. 179–203.

[30] Rought, R., "Identification of thermally-tagged coherent structures in the zero pressure gradient turbulent boundary layer," Master's thesis, California Institute of Technology, 2013.

18

[31] Saxton-Fox, T., and McKeon, B. J., "Modeling momentum and scalar transport in a wall-bounded turbulent flow," *10th International Symposium on Turbulence and Shear Flow Phenomena*, 2017.

[32] Saxton-Fox, T., "Coherent Structures, their Interactions, and their Effects on Passive Scalar Transport and Aero-optic Distortion in a Turbulent Boundary Layer," Ph.D. thesis, California Institute of Technology, 2018.

[33] Shraiman, B. I., and Siggia, E. D., "Scalar turbulence," *Nature*, Vol. 405, No. 6787, 2000, pp. 639–646.

[34] Wu, X., Moin, P., and Hickey, J.-P., "Boundary layer bypass transition," *Physics of Fluids*, Vol. 26, No. 9, 2014, p. 091104.

[35] Rosenberg, K., and McKeon, B., "Efficient representation of exact coherent states of the Navier-Stokes equations using resolvent analysis," *Fluid Dynamics Research*, 2018.

Studying the Effects of Compressibility in Planar Couette Flow using Resolvent Analysis

Scott T. M. Dawson[*] and Beverley J. McKeon[†]

California Institute of Technology, Pasadena, CA, 91125

Analysis of the resolvent operator is used to study the properties of compressible planar Couette flow. In particular, we study how changing the Mach number affects the shape and amplitude of responses to optimal disturbances across a range of spatial and temporal frequencies. We consider Mach numbers up to 5, and show that the dependence of the resolvent norm (leading singular value) on streamwise and spanwise wavenumbers follows similar trends to the incompressible case, with the amplitude of the resolvent norm typically decreasing with increasing Mach number. An exception to this occurs when acoustic eigenmodes (which are not present in the incompressible regime) have eigenvalues sufficiently close to the temporal frequency ω such that modal resonance with this mode is the dominant contributor to the resolvent gain. This occurs, for example, for streamwise-constant disturbances for sufficiently low spanwise wavenumber. In addition, the resolvent formulation of the governing equations allows us to study independently the effects due to an altered mean/equilibrium profile due to compressibility, and the effects due to the changing linearized Navier-Stokes equations. This approach provides a framework for the study of compressible turbulent wall-bounded flows.

I. Nomenclature

$\tilde{\boldsymbol{u}}$	=	Total velocity
$\boldsymbol{u}_0$	=	Mean velocity
U_0	=	Mean streamwise velocity
$\boldsymbol{u}$	=	Mean-subtracted velocity
$\tilde{\rho}$	=	Total density
ρ_0	=	Mean density
ρ	=	Mean-subtracted density
$\tilde{T}$	=	Total temperature
T_0	=	Mean temperature
T	=	Mean-subtracted temperature
$\tilde{\mu}$	=	Total viscosity
μ_0	=	Mean viscosity
μ	=	Mean-subtracted viscosity
$\tilde{\lambda}$	=	Total second coefficient of viscosity
λ_0	=	Mean second coefficient of viscosity
λ	=	Mean-subtracted second coefficient of viscosity
$\tilde{\mathbf{q}}$	=	Total state vector $(\tilde{\boldsymbol{u}}, \tilde{\rho}, \tilde{T})$.
$\mathbf{q}_0$	=	Mean state vector $(\boldsymbol{u}_0, \rho_0, T_0)$.
$\mathbf{q}$	=	Mean-subtracted state vector $(\boldsymbol{u}, \rho, T)$.
M	=	Mach number
Re	=	Reynolds number
Pr	=	Prandtl number

---

[*]Postdoctoral Scholar, Graduate Aerospace Laboratories, AIAA member
[†]Theodore von Karman Professor of Aeronautics, Graduate Aerospace Laboratories, AIAA Associate Fellow

c_p	=	Specific heat at constant pressure
c_v	=	Specific heat at constant volume
γ	=	Ratio of specific heats, c_p/c_v
$\mathcal{R}$	=	Universal gas constant, $c_p - c_v$
U^*	=	Dimensional reference velocity
T^*	=	Dimensional reference temperature
ρ^*	=	Dimensional reference density
H^*	=	Dimensional reference distance
μ^*	=	Dimensional reference viscosity
κ^*	=	Dimensional reference thermal conductivity
ω	=	Temporal frequency
c	=	Wavespeed, ω/k_x
L	=	Linearized compressible Navier-Stokes operator
f	=	Nonlinear terms in the compressible Navier-Stokes equations
D_y	=	First derivative operator in wall-normal direction
D_{yy}	=	Second derivative operator in wall-normal direction
∇	=	Spatial derivative operator
k_x	=	Streamwise wavenumber
k_z	=	Spanwise wavenumber
$X_{0,y}$	=	First derivative of quantity X_0 with respect to the wall-normal coordinate
$X_{0,y}$	=	First derivative of quantity X_0 with respect to the wall-normal coordinate
$X_{0,T}$	=	First derivative of quantity X_0 with respect to the mean temperature
$X_{0,TT}$	=	Second derivative of quantity X_0 with respect to the mean temperature
$\mathcal{H}_\omega$	=	Resolvent operator for temporal frequency ω
W	=	Inner product weighting operator

II. Introduction

Studies over the past decade have demonstrated that the properties of the mean-linearized resolvent operator provides a framework with which to understand and predict the properties of incompressible wall-bounded turbulence [1–4]. The utility of this approach is enhanced by the fact that it requires no assumptions about the size of the nonlinear "forcing" term in the governing equations, and that it can account for both spectral and non-normal sources of amplification (e.g., [5, 6]). Note that while compressible resolvent analysis has been applied to a number of flows, most notably in the study of jets [7–10], there has been little work extending findings of resolvent analysis of wall-bounded turbulent flows to the compressible regime.

The present work, while motivated by turbulent flows, will develop, validate, and apply these resolvent analysis methods to compressible, laminar Couette flow. While not studied as comprehensively as its incompressible counterpart, there is a substantial body of work studying the properties of the linearized Navier-Stokes operator for this system, characterizing both the spectral [11–16] and transient growth [14, 15, 17] characteristics. In particular, note that unlike its incompressible counterpart, compressible laminar Couette flow can be asymptotically unstable [11, 12]. On the other hand, the maximum transient growth of perturbations over a finite time horizon typically decreases with increasing Mach number [17], though the opposite is true when only considering two-dimensional perturbations [14]. Note that there also exists a sizable body of work on the modal and nonmodal stability properties of compressible boundary layers [18–24]. That said, there has been little work looking at the compressible Couette system with the type of frequency-specific analysis that comes from the resolvent operator. Therefore, as well as developing methods of analysis that will ultimately be applied to turbulent flows, we believe that the findings of the present work will be of independent interest.

Generally speaking, we are motivated by questions relating to what properties of wall-bounded turbulence extend to the compressible regime. Such questions have been well-studied previously, with perhaps the most prominent specific examples being Morkovin's hypothesis [25] that the changing mean profile drives the majority of the changing dynamics with Mach number, and the Van Driest transformation [26] and its extensions and variants (e.g., [27]). It is hoped that

2

the approach outlined in this work will ultimately complement recent experimental and numerical data for compressible wall-bounded flows (e.g., [28–31]).

Sect. III describes the resolvent formulation of the compressible Navier-Stokes equations, while Sect. IV shows results from applying this formulation to compressible planar Couette flow.

III. The compressible Navier-Stokes equations

We consider compressible flow of a fluid that has the properties of a perfect gas with constant specific heat coefficients, and constant Prandtl number. The formulation and assumptions are relatively standard for previous works that have considered modal and nonmodal stability analysis of compressible flows, e.g., [15, 17, 22].

The velocity, density, and temperature are decomposed into mean and fluctuating components as follows, with a $\tilde{\ }$ denoting the total field:

$$\tilde{\boldsymbol{u}} = \boldsymbol{u}_0 + \boldsymbol{u}, \quad \tilde{\rho} = \rho_0 + \rho, \quad \tilde{T} = T_0 + T, \tag{1}$$

with other variables (e.g., viscosity) decomposed similarly. Let the state of the system be given by $\tilde{\mathbf{q}} = \mathbf{q}_0 + \mathbf{q}$, where $\mathbf{q} = (u, v, w, \rho, T)$ representing the mean-subtracted state. We formulate the Navier-Stokes equations in nondimensionalized form using the Mach, Reynolds, and Prandtl numbers, given respectively by

$$M = \frac{U^*}{\sqrt{\gamma \mathcal{R} T^*}}, \tag{2}$$

$$Re = \frac{\rho^* U^* H^*}{\mu^*}, \tag{3}$$

$$Pr = \frac{\mu^* c_p}{\kappa^*}, \tag{4}$$

where the asterisk superscript denotes a reference (dimensional) quantity. The compressible Navier-Stokes equations are then given by

$$\tilde{\rho} \frac{D\tilde{u}_j}{Dt} = -\frac{1}{\gamma M^2} \nabla \tilde{p} + \frac{1}{Re} \left[\tilde{\mu} \nabla^2 \tilde{u}_j + \frac{\partial}{\partial x_j} (\tilde{\lambda} \nabla \cdot \tilde{\boldsymbol{u}}) + \tilde{\mu} \frac{\partial}{\partial x_j} (\nabla \cdot \tilde{\boldsymbol{u}}) + (\nabla \tilde{\mu}) \cdot (\nabla \tilde{u}_j) + (\nabla \tilde{\mu}) \cdot \frac{\partial \tilde{\boldsymbol{u}}}{\partial x_j} \right] \tag{5}$$

$$\frac{\partial \tilde{\rho}}{\partial t} = -\nabla \cdot (\tilde{\rho} \tilde{\boldsymbol{u}}) \tag{6}$$

$$\tilde{\rho} \frac{D\tilde{T}}{Dt} = (1 - \gamma) \tilde{p} \nabla \cdot \tilde{\boldsymbol{u}} + \frac{\gamma}{Re} \nabla \cdot \left(\frac{\tilde{\mu}}{Pr} \nabla \tilde{T} \right) + \tilde{\lambda} (\nabla \cdot \tilde{\boldsymbol{u}})^2 + \frac{\tilde{\mu}}{2} \left(\nabla \tilde{\boldsymbol{u}} + (\nabla \tilde{\boldsymbol{u}})^T \right)^2, \tag{7}$$

where $\frac{D}{Dt} = \frac{\partial}{\partial t} + \tilde{\boldsymbol{u}} \cdot \nabla$.

We assume that the viscosity varies with temperature according to the Sutherland formula

$$\tilde{\mu}(\tilde{T}) = \frac{\tilde{T}^{3/2}(1 + C)}{\tilde{T} + C}, \tag{8}$$

where the constant $C = 0.5$. The second coefficient of viscosity λ is assumed to follow Stokes' assumption, $\tilde{\lambda} = -2/3\tilde{\mu}$.

Upon using the decomposition in Eq. 1, eliminating pressure using the equation of state $\tilde{p} = \tilde{\rho}\tilde{T}$, and assuming that $\boldsymbol{u}_0 = (U_0, 0, 0)$, we find from the momentum equation that p_0 is constant in y, and we scale pressure such that this constant is 1. This leads to the following equations describing the variation of the mean state $\mathbf{q}_0 = (U_0, 0, 0, \rho_0, T_0)$ in the y-direction:

$$\frac{d}{dy} \left(\mu_0 \frac{dU_0}{dy} \right) = 0, \tag{9}$$

$$\frac{d}{dy} \left(\frac{\mu_0}{Pr} \frac{dT_0}{dy} \right) + (\gamma - 1) M^2 \mu_0 \left(\frac{dU_0}{dy} \right) = 0, \tag{10}$$

$$\rho_0 T_0 = 1. \tag{11}$$

3

The governing equations for the fluctuating component of the state $\mathbf{q} = (u, v, w, \rho, T)$, upon temporal Fourier transform, may written as

$$(-i\omega I + L)\mathbf{q} = \boldsymbol{f}, \tag{12}$$

where L is the linearization of Eqs. 5-7, and $\boldsymbol{f}$ contains all of the remaining nonlinear terms. After also taking spatial Fourier transforms in the streamwise and spanwise directions, the sub-operators of L are given by

$$L_{11} = ik_x U_0 + Re^{-1}T_0 \left(2k_x^2\mu_0 + k_z^2\mu_0 + k_x^2\lambda_0 - \mu_0 D_{yy} - \mu_{0,y}D_y\right)$$

$$L_{12} = U_{0,y} - ik_x Re^{-1}T_0 \left(\lambda_0 D_y + \mu_0 D_y + \mu_{0,y}\right)$$

$$L_{13} = k_x k_z Re^{-1}T_0(\lambda_0 + \mu_0)$$

$$L_{14} = ik_x \left(\gamma M^2\right)^{-1} T_0^2$$

$$L_{15} = ik_x \left(\gamma M^2\right)^{-1} - Re^{-1}T_0 \left(U_{0,yy}\mu_{0,T} + U_{0,y}T_{0,y}\mu_{0,TT} + U_{0,y}\mu_{0,T}D_y\right)$$

$$L_{21} = -ik_x Re^{-1}T_0(\lambda_{0,y} + (\lambda_0 + \mu_0)D_y)$$

$$L_{22} = ik_x U_0 + Re^{-1}T_0 \left(\mu_0(k_x^2 + k_z^2) - (2\mu_0 + \lambda_0)D_{yy} - \lambda_{0,y}D_y - 2\mu_{0,y}D_y\right)$$

$$L_{23} = -ik_z Re^{-1}T_0 \left(\lambda_{0,y} + (\lambda_0 + \mu_0)D_y\right)$$

$$L_{24} = \left(\gamma M^2\right)^{-1} T_0(T_{0,y} + T_0 D_y)$$

$$L_{25} = \left(\gamma M^2\right)^{-1} (T_0\rho_{0,y} + D_y) - ik_x Re^{-1}T_0 U_{0,y}\mu_{0,T}$$

$$L_{31} = k_x k_z Re^{-1}T_0(\mu_0 + \lambda_0)$$

$$L_{32} = -ik_z Re^{-1}T_0 \left((\mu_0 + \lambda_0)D_y + \mu_{0,y}\right)$$

$$L_{33} = ik_x U_0 + Re^{-1}T_0 \left(\mu_0(k_x^2 + k_z^2) - \mu_0 D_{yy} + k_z^2(\mu_0 + \lambda_0) - \mu_{0,y}D_y\right)$$

$$L_{34} = ik_z \left(\gamma M^2\right)^{-1} T_0^2$$

$$L_{35} = ik_z \left(\gamma M^2\right)^{-1}$$

$$L_{41} = ik_z\rho_0$$

$$L_{42} = \rho_{0,y} + \rho_0 D_y$$

$$L_{43} = ik_z\rho_0$$

$$L_{44} = ik_x U_0$$

$$L_{45} = 0$$

$$L_{51} = ik_x(\gamma - 1)T_0 - 2\gamma(\gamma - 1)M^2 Re^{-1}T_0\mu_0 U_{0,y}D_y$$

$$L_{52} = T_{0,y} + (\gamma - 1)T_0 D_y - 2ik_x\gamma(\gamma - 1)M^2 Re^{-1}T_0\mu_0 U_{0,y}$$

$$L_{53} = ik_z(\gamma - 1)T_0$$

$$L_{54} = 0$$

$$L_{55} = ik_x U_0 - \gamma Re^{-1}\left(Pr^{-1}T_0\left(2T_{0,y}\mu_{0,T}D_y + (T_{0,y})^2\mu_{0,TT} + T_{0,yy}\mu_{0,T} - \mu_0(k_x^2 + k_z^2) + \mu_0 D_{yy}\right) - (\gamma - 1)M^2 T_0\mu_{0,T}(U_{0,y})^2\right),$$

where subscripts y and T following commas denote derivatives with respect to wall-normal position and mean temperature, respectively. Resolvent analysis considers the leading singular vectors and values of the operator

$$\mathcal{H}_\omega = (-i\omega I + L)^{-1},$$

which requires the definition of an inner product on the space in which the state $\mathbf{q}$ resides. We are particularly interested in the (spectral) norm of this operator, which is equal to the leading singular value. We take an inner product which enforces that there is no pressure-related work, given by

$$\langle \mathbf{q}_1, \mathbf{q}_2 \rangle = \int_\Omega \bar{\mathbf{q}}_2 W \mathbf{q}_1 d\boldsymbol{x}, \tag{13}$$

4

where the overbar denotes the complex conjugate, and the weighting operator W is given by

$$W = \text{diag}\left(\rho_0, \rho_0, \rho_0, \frac{T_0}{\gamma \rho_0 M^2}, \frac{\rho_0}{\gamma(\gamma-1)T_0 M^2}\right). \tag{14}$$

This norm seems to originate with the work of Chu [32], but is also attributed to Mack [33], where it was first used in the context of modal analysis. This norm (or equivalent/similar norms using different thermodynamic variables) have been used in numerous other studies of compressible flows where the definition of an inner product is required (e.g., [15, 17, 22, 34, 35]). Discussion of other possible inner products and assumptions for compressible flows are given in [36]. The standard incompressible kinetic energy norm (which is a pseudonorm on this space, and which we will use for purposes of comparison) is proportional to

$$W_K = \text{diag}\left(\rho_0, \rho_0, \rho_0, 0, 0\right). \tag{15}$$

IV. Resolvent analysis of compressible laminar Couette flow

We consider flow between two parallel plates with no external pressure gradient, with the top plate moving at a constant velocity, and the bottom plate stationary. With reference to Eqs. 2-4, let the characteristic velocity, temperature, density, and viscosity be those of the upper surface, with the lower surface stationary and adiabatic. The characteristic length is the distance between the upper and lower surfaces. We assume a fixed Prandtl number of 0.72. The resolvent operator for this system is then parametrized by Re, Ma, k_x, k_z, and $c = \omega/k_x$. We will not be able to comprehensively explore the full parameter space, but will present results abstained from varying one or more parameters that highlight certain typical features of this system. The governing equations are discretized using a Chebyshev collocation method, which is implemented using the toolbox given in [37]. The code is validated by comparing the eigenvalues of the linearized compressible Navier-Stokes operator to those reported in the literature (e.g., [12]).

A. Mean profiles

Eqs. 9-10 may be solved numerically on the domain $y \in [0, 1]$ given the (non dimensional) boundary conditions for the mean profiles

$$U_0(0) = 0, \quad U_0(1) = 1, \quad T_0(0) = T_L, \quad T_0(1) = 1,$$

where T_L is the mean temperature of the lower wall. The following procedure is similar to that given in [12, 17], for example. Defining the recovery temperature T_r and recovery factor r

$$T_r = 1 + \frac{(\gamma-1)PrM^2}{2}, \tag{16}$$

$$r = \frac{T_L}{T_r}, \tag{17}$$

it can be shown from Eq. 10 that the mean temperature is a quadratic function of the mean velocity, given by

$$T_0(y) = T_r\left[r + (1-r)U_0(y) - \left(1 - T_r^{-1}U_0(y)^2\right)\right]. \tag{18}$$

In this work we will focus on the case where the lower wall is adiabatic, for which we have $r = 1$. Using Eqs. 8 and 18, Eq. 9 may then be solved numerically to obtain $U_0(y)$. Note that this is easiest to do by assuming that U_0 is monotone in y, and solving for y as a function of U_0. Figure 1 shows mean velocity, temperature, density, and viscosity profiles for various Mach numbers. Note that these mean profiles are independent of Reynolds number.

B. Code validation and sample results

Fig. 2 shows the resolvent norm and spectrum of the linear operator for $k_x = k_z = 0.1$, $M = 2$, and $Re = 2 \times 10^5$, which match parameters considered in [17], for example. For comparison, we also plot the resolvent norm for the
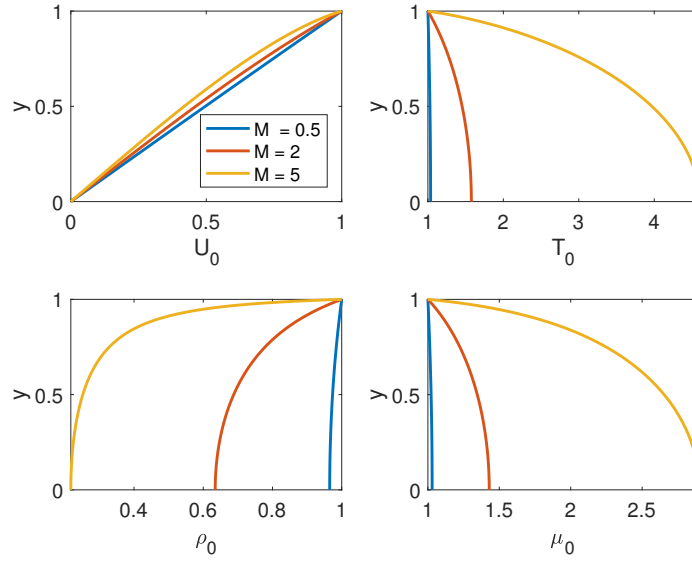
5

Fig. 1 Mean streamwise velocity, temperature, density, and viscosity for compressible planar Couette flow at various Mach numbers.
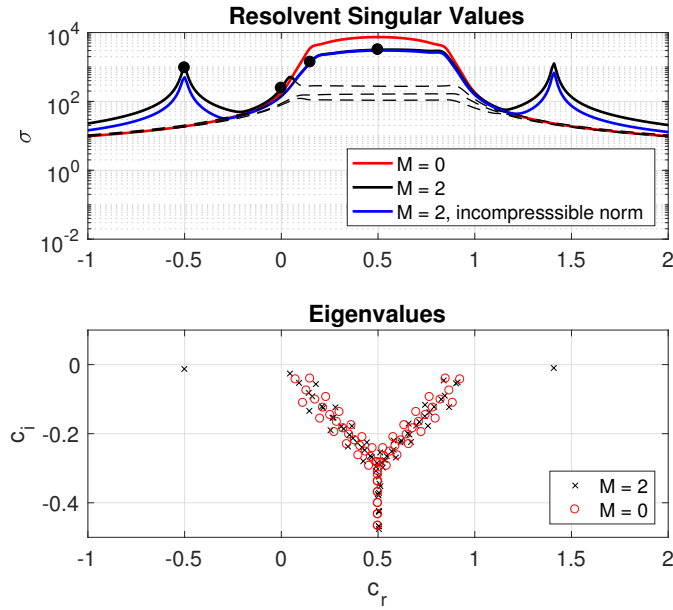

Fig. 2 (Upper subplot) The leading four resolvent singular values for a range of wavespeeds $c = c_r$ (top), and eigenvalues of the system for $k_x = k_z = 0.1$, $M = 2$, and $Re = 2 \times 10^5$. Also plotted is the leading singular value for the incompressible ($M = 0$) case, and for the $M = 2$ case where an incompressible norm is used. The circles represent wavespeeds that have resolvent response modes plotted in Fig. 3. (Lower subplot) Eigenvalues for the system with these parameters for the compressible ($M = 2$) and incompressible ($M = 0$) cases.

6

incompressible case, as well as the compressible case with an incompressible (kinetic energy) inner product. The spectrum is obtained from solving the eigenvalue problem $L\mathbf{q} = i\omega\mathbf{q}$, and we plot results in terms of the complex wavespeed $c = c_r + ic_i = \omega/k_x$. The spectrum consists of viscous modes that make a "Y" shape that is typical for both incompressible and compressible Couette flows [12], as well as a set of "acoustic" eigenmodes that extend to large positive and negative wavepeeds for the compressible case, only two of which are included in the domain shown in Fig. 2. The resolvent norm shows peaks due to spectral amplification of these acoustic eigenmodes near their defined wavespeeds. In this region, the second singular value matches the leading singular value for the incompressible case. There is also a large region of high amplification for wavespeeds within the range of the mean velocity profile (i.e., between 0 and 1) for both the compressible and incompressible cases. This non-modal amplification is a consequence of the nonnormality of the system, and particularly the extreme sensitivity of modes near the intersection of branches in the "Y" [38]. In this region, the leading singular value for the compressible case appears to be insensitive to the choice of inner product, which reflects the the modes in this region are dominated by the momentum variables.

Fig. 3 plots sample resolvent response modes for selected wavespeeds for this system, which correspond to (compressible) singular values indicated by circles in Fig. 2. The compressible resolvent response mode at $c = -0.5$ closely resembles the neighboring acoustic eigenmode, which spans across the entire domain with very little phase variation in the wall-normal direction. At $c = 0$, the leading compressible resolvent response mode is dominated by the density and temperature fields, which have fluctuations localized near the lower wall. At these two wavespeeds, the incompressible resolvent response mode is qualitatively different from the compressible case.

For wavespeeds slightly larger than 0, the leading mode for the compressible case swaps to a mode that is dominated by streamwise and spanwise velocity components (as well as temperature), as shown for $c = 0.15$. This type of mode persists across all other wavespeeds giving a critical layer within the physical domain (that is, a location where the wavespeed matches the local mean velocity). The relatively constant leading resolvent singular value for $0.2 \le c \le 0.8$ may be explained by the fact that the leading resolvent modes are mostly "detached" from the boundaries within this region for these wavenumbers, and thus have properties that are somewhat independent of the critical layer location (though they will be influenced to some extent by changing mean properties at different locations). The decrease in singular value close to either wall may then be explained by the boundary conditions imposing a constraint that impedes the amplification mechanism giving rise to this mode shape. For this range of wavespeeds, the compressible and incompressible modes share similar features. Connections with incompressible case, and the affect of Mach number variation, will be further explored in Sect. C. While this section only considered one sample case, many of the observations are at least qualitatively typical of those observed across a range of parameter values.

C. Effect of Mach number on resolvent gains

This section will focus on studying the variation of resolvent norm (i.e., the leading singular value of the resolvent operator) with k_x, k_z, and M. We will consider two Reynolds numbers: $Re = 2 \times 10^5$ as considered in Sect. B, and a substantially lower value of $Re = 10^3$. By varying the spatial wavenumbers k_x and k_z, we may identify the size and shape of structures that are most amplified by the resolvent operator. Fig. 4 shows the resolvent norm (leading singular value) for various Mach numbers, with the wavespeed fixed at $c = 0.5$ (similar results are obtained at other wavespeeds). The $M = 0$ case uses the incompressible Navier-Stokes equations and kinetic energy norm. In all cases, there is a local maximum for $k_x \to 0$ and $k_z \approx 2$ (with substantially higher amplification for the higher Reynolds number case), which is typical for incompressible flows (e.g., [39]). Note that this peak is also similar to that observed for maximum transient growth for compressible Couette flows [17]. As M increases, we also observe for the low Re case the growth of a region of high amplification for small k_x and k_z. It may be shown that this peak arises due to the presence of an (acoustically dominated) eigenvalue near $c_r = 0.5$, which moves closer to the marginally stability axis with increasing Mach number.

Fig. 4 shows high resolvent norm for both Reynolds numbers as k_x approaches 0. To study this limit in more detail, we show in Fig. 5 the resolvent norm for $k_x = 0$ for both Reynolds numbers and all Mach numbers considered. We observe the local maximum at $k_z \approx 2$ for all cases except for when $Re = 10^3$ and $M = 5$. This peak reduces in amplitude with increasing M, and the value of k_z at this maximum shows little dependence with either Re or M. We also observe an increase in σ_1 for low values of k_z for both Reynolds numbers, and all nonzero Mach numbers. This
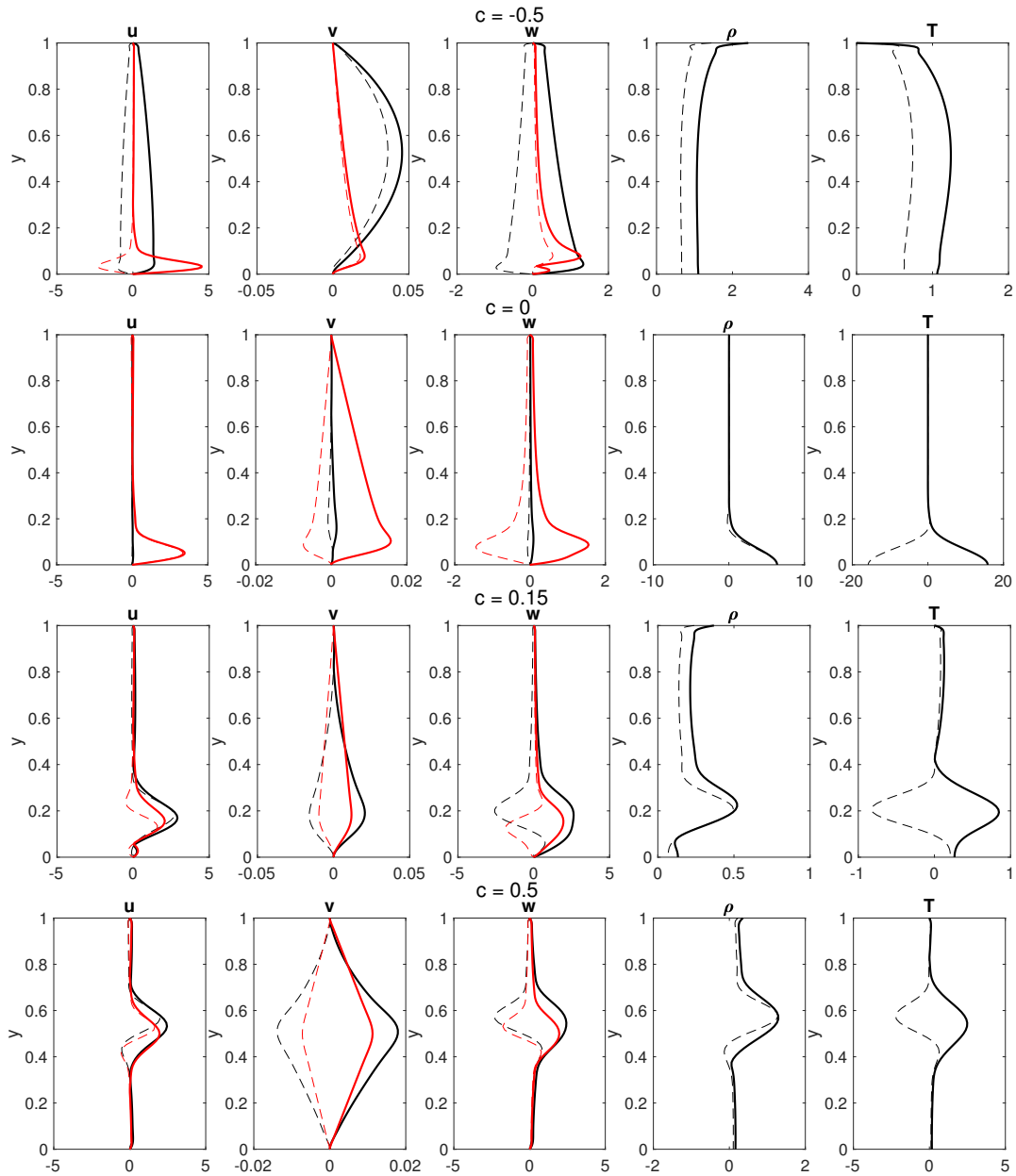
7

Fig. 3 Absolute value (solid lines) and real component (dashed lines) of resolvent response modes for selected wavespeeds, with $M = 2$ (black lines) and $M = 0$ (red lines). Parameters are identical to Fig. 2, which also indicates corresponding singular values.
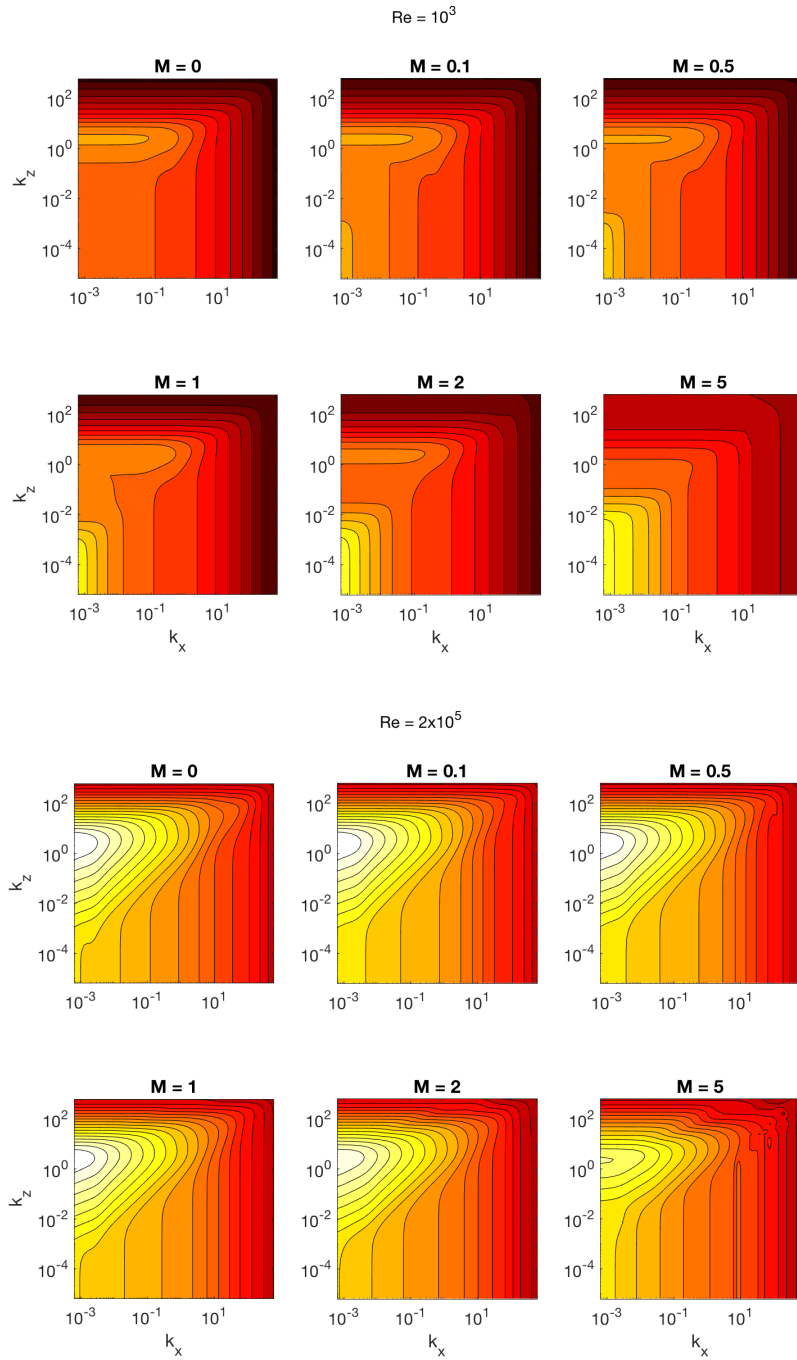
8

Fig. 4   Resolvent gain (σ_1) as a function of k_x, k_z and M for $Re = 10^3$ (top two rows) and 2×10^5 (bottom two rows), $c = 0.5$. Contours are logarithmically spaces at values 10^{-8}, 10^{-7}, ... 10^{16}.

9
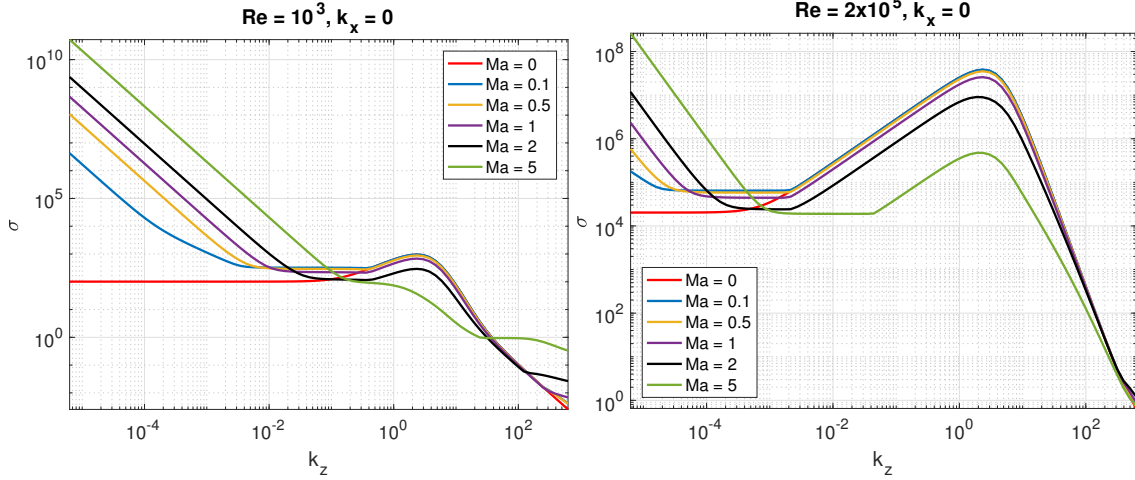
Fig. 5 **Resolvent gain (σ_1) as a function of k_z for $k_x = 0$, $\omega = 0$, and $Re = 10^3$ (left) and 2×10^5 (right).**

behavior was apparent from the $Re = 10^3$ case in Fig. 4, but was not apparent for the $Re = 2 \times 10^5$ case due to the range of k_x plotted. This increase in σ_1 as $k_z \to 0$ has a constant slope of -2 (on the log-log plot) across all Mach and both Reynolds numbers, with the onset of this scaling occurring at larger k_z for larger Mach and smaller Reynolds numbers. As mentioned previously, this low k_z behavior for the compressible system is due to an acoustic eigenmode approaching the origin, thus giving resonant amplification of the resolvent operator. To show this directly, we demonstrate in Fig. 6 that the resolvent norm in the low k_z limit matches the inverse of the distance of the closest eigenvalue from $\omega = 0$. This represents a lower bound on the resolvent norm, which is achieved for purely modal amplification mechanisms. For further discussion of such acoustic modes may be found in past modal analyses of this system [12, 13]. In contrast, we observe the peak at $k_z \approx 2$ must occur from nonmodal amplification (as has been observed previously in the contest of finite-time optimal transient growth analysis (e.g., [14, 17]).

To study this peak in more detail, in Fig. 7 we now fix k_z to a constant value of 2.332, and study how the resolvent norm σ_1 (as well as the premultiplied resolvent norm $k_x \sigma_1$) varies with k_x. As before, we observe qualitatively similar behavior across all Reynolds and Mach numbers, with the maximum σ_1 occurring in the low Reynolds number limit. Additionally, while σ_1 approaches its maximum value as $k_x \to 0$, the premultiplied plots show clear peaks for k_x values that increase with M and decrease with Re. The oscillations that occur for large k_x in the $M = 5$ case appear to be caused by the appearance of acoustic modes at this wavespeed for certain k_x values.

D. Effect of compressible inner product and mean on mode shape

In this section, we present sample results comparing typical resolvent response mode shapes for compressible and incompressible flow. All modes in this section are computed with $Re = 1000$, $k_x = 5\pi/3$, $k_z = 10\pi/3$, and $c = \omega/k_x = 0.5$. Figs. 8 (incompressible), 9 (compressible, with a Mach number of 2) and 10 (as for Fig. 9, but with a kinetic energy pseudo-norm as described in Eq. 15) show resolvent response mode shapes for these parameters. For the incompressible case, we augment the standard incompressible Navier-Stokes equations with a passive scalar field, which is not weighted in the (standard incompressible) inner product. Further details of this formulation are given in [40].

For these parameters, compressibility has a noticeable effect on the mode shapes, particularly for the wall-normal component of velocity. However, Fig. 10, which considers compressible flow but with a (pseudo)-norm based on kinetic
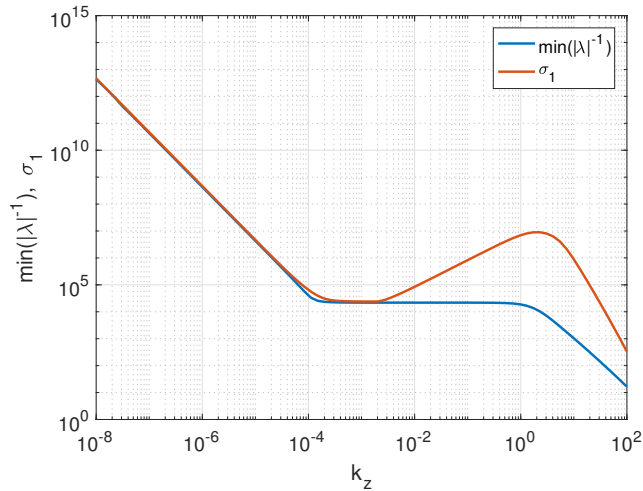
10

Fig. 6   Comparison between resolvent gain (σ_1) and inverse distance from closest eigenvalue to $\omega = 0$ as a function of k_z for $k_x = 0$ and $Re = 2 \times 10^5$.

energy only (as used in incompressible analysis), shows that some of variation is due to the choice of inner product used. This dependency on inner product weighting is in contrast to the incompressible case with a passive scalar, where previous work ([41]) suggests that changing the inner product to weight the scalar field had negligible effect on the mode shapes. The changes when compressibility is introduced are due to both the change in mean profiles, and due to the compressible fluctuation equations. The resolvent framework is amenable to the study of each of these individual effects in isolation. Fig. 11 shows sample results exploring this matter, where compressible and incompressible equations for fluctuations are used with means from both compressible and incompressible Couette flow. Note in particular that the velocity response amplitude functions for the compressible fluctuation equations when using an incompressible mean and pseudo-norm are almost identical to those for the fully incompressible case.

V. Conclusions

This work has analyzed properties of the resolvent operator for compressible laminar Couette flow. We have presented sample results showing how the gain associated with the response to optimal disturbances changes for nonzero Mach number. In the cases where the leading response mode has the majority of its energy associated with the momentum (rather than thermodynamic) variables, there are typically qualitative similarities between the compressible and incompressible cases. An increasing Mach number typically reduces the amplification associated with such modes, which is consistent with previous findings for transient growth analysis [17].The presence of acoustic modes, however, can lead to qualitative changes in the leading resolvent response modes, due to resonant amplification from this mode. While we have only considered the case where a single acoustic mode affects the resolvent norm, note that the tuned synchronization of multiple acoustic modes [16] could have an even greater influence. Both sources of amplification appear to follow relatively simple scaling relationships with respect to the governing parameters, which could be utilized for the efficient characterization of this system (and could be identified from either physical/mathematical insights, or empirically from numerically computed data). Further work could also study componentwise amplification [39] of the compressible operator, which could provide further insight into the linear amplification mechanism present in the system. While this work has only considered laminar Couette flow, the properties of turbulent-mean-linearized operators for compressible wall-bounded flows share similar properties. This suggests that this approach could be utilized to study the properties of structures within compressible turbulent flows, in a manner akin to the approaches that have been successfully applied in the incompressible regime (e.g., [4]).
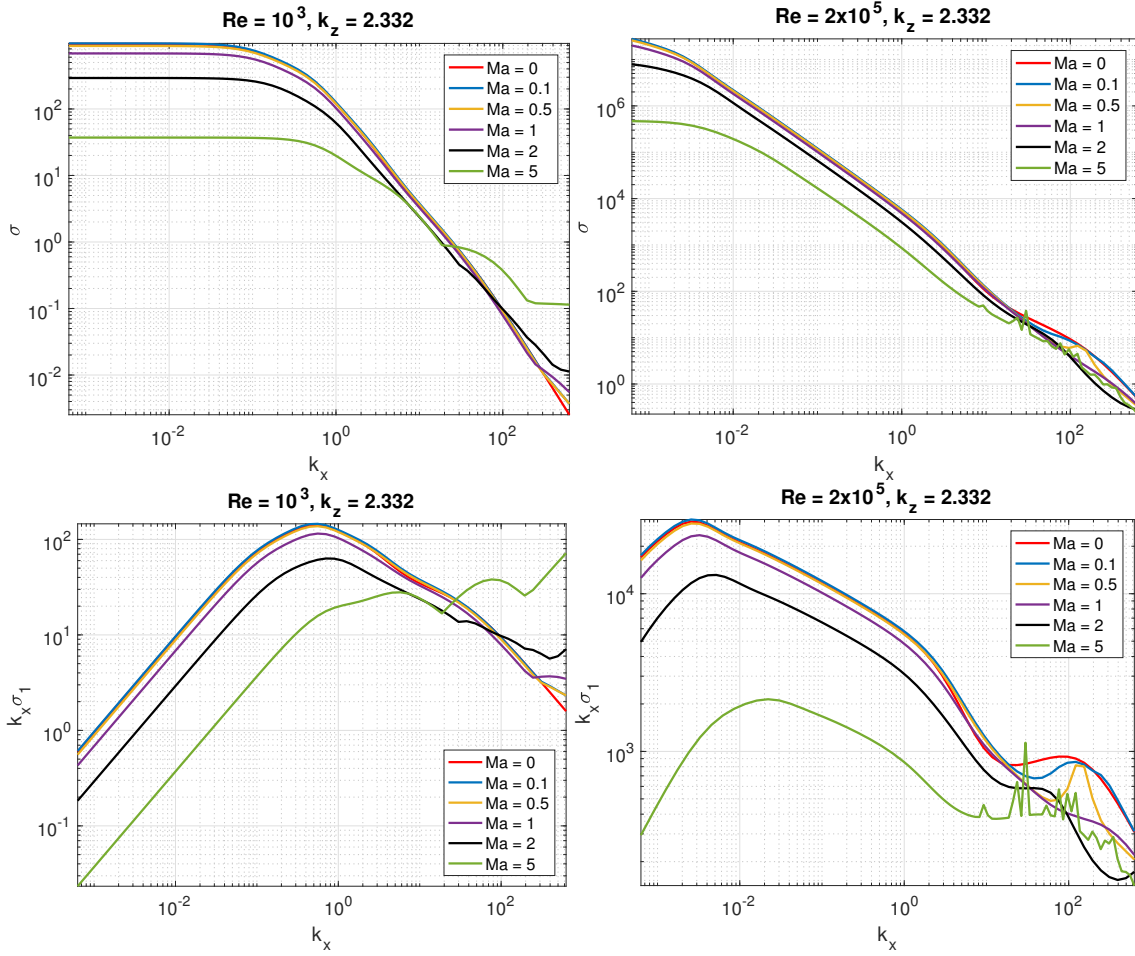
11

Fig. 7 **Resolvent norm (σ_1, upper subplots) and premultiplied resolvent norm ($k_x\sigma_1$, lower subplots) as a function of k_x for $k_z = 2.332$, $c = 0.5$, and $Re = 10^3$ (left) and 2×10^5 (right).**
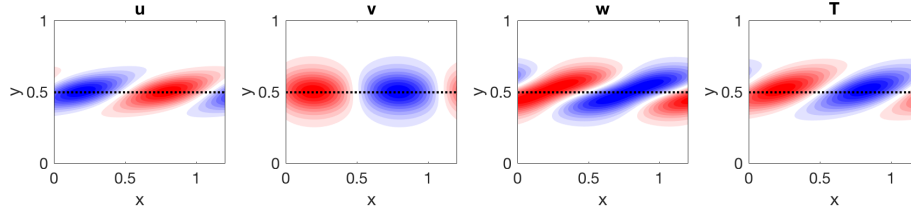
12

Fig. 8   Leading resolvent modes for incompressible, laminar Couette flow, with $Re = 1000$**,** $k_x = 5\pi/3$**,** $k_z = 10\pi/3$**, and** $c = \omega/k_x = 0.5$**. Red and blue contours represent positive and negative values respectively of the mean-subtracted variables**
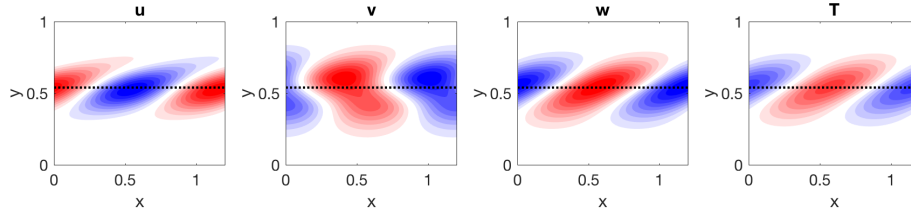

Fig. 9   Leading resolvent modes for compressible, laminar Couette flow, with $M = 2$**,** $Re = 1000$**,** $k_x = 5\pi/3$**,** $k_z = 10\pi/3$**, and** $c = \omega/k_x = 0.5$**, using an inner product as defined in eq. 14. Red and blue contours represent positive and negative values respectively of the mean-subtracted variables**
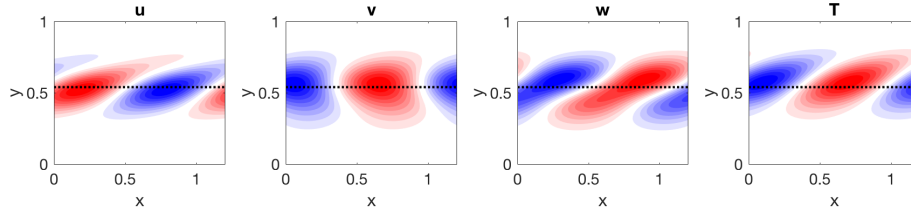

Fig. 10   Leading resolvent modes for compressible, laminar Couette flow, with $M = 2$**,** $Re = 1000$**,** $k_x = 5\pi/3$**,** $k_z = 10\pi/3$**, and** $c = \omega/k_x = 0.5$**, using a kinetic energy pseudo-norm. Red and blue contours represent positive and negative values respectively of the mean-subtracted variables**

Acknowledgments

References

[1] McKeon, B. J., and Sharma, A. S., "A critical-layer framework for turbulent pipe flow," *Journal of Fluid Mechanics*, Vol. 658, 2010, pp. 336–382.

[2] Hwang, Y., and Cossu, C., "Linear non-normal energy amplification of harmonic and stochastic forcing in the turbulent channel flow," *Journal of Fluid Mechanics*, Vol. 664, 2010, pp. 51–73.

[3] Sharma, A. S., and McKeon, B. J., "On coherent structure in wall turbulence," *Journal of Fluid Mechanics*, Vol. 728, 2013, pp. 196–238.

[4] McKeon, B., "The engine behind (wall) turbulence: perspectives on scale interactions," *Journal of Fluid Mechanics*, Vol. 817, 2017.
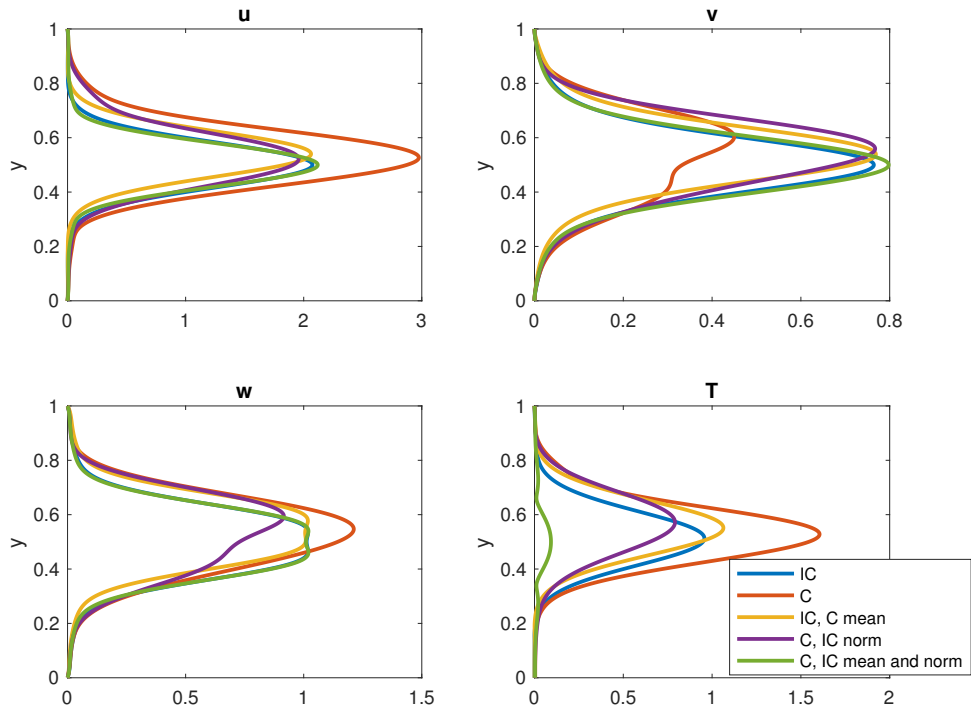
13

Fig. 11 Leading resolvent mode amplitudes for incompressible (IC in the figure legend), compressible (C, with $M = 2$) incompressible with a compressible mean, compressible with an incompressible (kinetic energy) pseudo-norm, and compressible with an incompressible mean and pseudo-norm, with $Re = 1000$, $k_x = 5\pi/3$, $k_z = 10\pi/3$, and $c = \omega/k_x = 0.5$.

[5] Schmid, P. J., "Nonmodal Stability Theory," *Annual Review of Fluid Mechanics*, Vol. 39, 2007, pp. 129–62. doi:10.1146/annurev.fluid.38.050304.092139.

[6] Symon, S., Rosenberg, K., Dawson, S. T., and McKeon, B. J., "Non-normality and classification of amplification mechanisms in stability and resolvent analysis," *Physical Review Fluids*, Vol. 3, No. 5, 2018, p. 053902.

[7] Garnaud, X., Lesshafft, L., Schmid, P., and Huerre, P., "The preferred mode of incompressible jets: linear frequency response analysis," *Journal of Fluid Mechanics*, Vol. 716, 2013, pp. 189–202.

[8] Jeun, J., Nichols, J. W., and Jovanović, M. R., "Input-output analysis of high-speed axisymmetric isothermal jet noise," *Physics of Fluids (1994-present)*, Vol. 28, No. 4, 2016, p. 047101.

[9] Towne, A., Schmidt, O. T., and Colonius, T., "Spectral proper orthogonal decomposition and its relationship to dynamic mode decomposition and resolvent analysis," *Journal of Fluid Mechanics*, Vol. 847, 2018, pp. 821–867.

[10] Rigas, G., Schmidt, O. T., Colonius, T., and Bres, G. A., "One Way Navier-Stokes and resolvent analysis for modeling coherent structures in a supersonic turbulent jet," *23rd AIAA/CEAS Aeroacoustics Conference*, 2017, p. 4046.

[11] Glatzel, W., "The linear stability of viscous compressible plane Couette flow," *Journal of Fluid Mechanics*, Vol. 202, 1989, pp. 515–541.

[12] Duck, P. W., Erlebacher, G., and Hussaini, M. Y., "On the linear stability of compressible plane Couette flow," *Journal of Fluid Mechanics*, Vol. 258, 1994, pp. 131–165.

[13] Hu, S., and Zhong, X., "Linear stability of viscous supersonic plane Couette flow," *Physics of Fluids*, Vol. 10, No. 3, 1998, pp. 709–729.

[14] Farrell, B., and Ioannou, P., "Transient and asymptotic growth of two-dimensional perturbations in viscous compressible shear flow," *Physics of Fluids*, Vol. 12, No. 11, 2000, pp. 3021–3028.

[15] Malik, M., Dey, J., and Alam, M., "Linear stability, transient energy growth, and the role of viscosity stratification in compressible plane Couette flow," *Physical Review E*, Vol. 77, No. 3, 2008, p. 036322.

[16] Ramachandran, A., Saikia, B., Sinha, K., and Govindarajan, R., "Effect of Prandtl number on the linear stability of compressible Couette flow," *International Journal of Heat and Fluid Flow*, Vol. 61, 2016, pp. 553–561.

[17] Malik, M., Alam, M., and Dey, J., "Nonmodal energy growth and optimal perturbations in compressible plane Couette flow," *Physics of Fluids*, Vol. 18, No. 3, 2006, p. 034103.

[18] Lees, L., and Lin, C. C., "Investigation of the stability of the laminar boundary layer," Tech. Rep. 1115, NACA, 1946.

[19] Lees, L., and Reshotko, E., "Stability of the compressible laminar boundary layer," *Journal of Fluid Mechanics*, Vol. 12, No. 4, 1962, pp. 555–590.

[20] Malik, M. R., "Numerical methods for hypersonic boundary layer stability," *Journal of Computational Physics*, Vol. 86, No. 2, 1990, pp. 376–413.

[21] Chang, C.-L., Malik, M., Erlebacher, G., and Hussaini, M., "Compressible stability of growing boundary layers using parabolized stability equations," *22nd AIAA Fluid Dynamics, Plasma Dynamics and Lasers Conference*, 1991, p. 1636.

[22] Hanifi, A., Schmid, P. J., and Henningson, D. S., "Transient growth in compressible boundary layer flow," *Physics of Fluids*, Vol. 8, No. 3, 1996, pp. 826–837.

[23] Özgen, S., and Kırcalı, S. A., "Linear stability analysis in compressible, flat-plate boundary-layers," *Theoretical and Computational Fluid Dynamics*, Vol. 22, No. 1, 2008, pp. 1–20.

[24] Bitter, N., and Shepherd, J., "Stability of highly cooled hypervelocity boundary layers," *Journal of Fluid Mechanics*, Vol. 778, 2015, pp. 586–620.

[25] Morkovin, M. V., "Effects of compressibility on turbulent flows," *Mécanique de la Turbulence*, Vol. 367, 1962, p. 380.

[26] Van Driest, E. R., "Turbulent boundary layer in compressible fluids," *Journal of the Aeronautical Sciences*, Vol. 18, No. 3, 1951, pp. 145–160.

15

[27] Zhang, Y.-S., Bi, W.-T., Hussain, F., Li, X.-L., and She, Z.-S., "Mach-number-invariant mean-velocity profile of compressible turbulent boundary layers," *Physical Review Letters*, Vol. 109, No. 5, 2012, p. 054502.

[28] Pirozzoli, S., and Bernardini, M., "Turbulence in supersonic boundary layers at moderate Reynolds number," *Journal of Fluid Mechanics*, Vol. 688, 2011, pp. 120–168.

[29] Martín, M. P., "Direct numerical simulation of hypersonic turbulent boundary layers. Part 1. Initialization and comparison with experiments," *Journal of Fluid Mechanics*, Vol. 570, 2007, pp. 347–364.

[30] Ringuette, M. J., Wu, M., and Martín, M. P., "Coherent structures in direct numerical simulation of turbulent boundary layers at Mach 3," *Journal of Fluid Mechanics*, Vol. 594, 2008, pp. 59–69.

[31] Duan, L., Beekman, I., and Martín, M. P., "Direct numerical simulation of hypersonic turbulent boundary layers. Part 3. Effect of Mach number," *Journal of Fluid Mechanics*, Vol. 672, 2011, pp. 245–267.

[32] Chu, B.-T., "On the energy transfer to small disturbances in fluid flow (Part I)," *Acta Mechanica*, Vol. 1, No. 3, 1965, pp. 215–234.

[33] Mack, L. M., "Boundary-layer linear stability theory," Tech. Rep. 709, AGARD, 1984.

[34] de Pando, M. F., Schmid, P. J., and Sipp, D., "A global analysis of tonal noise in flows around aerofoils," *Journal of Fluid Mechanics*, Vol. 754, 2014, pp. 5–38.

[35] Bitter, N., and Shepherd, J., "Transient growth in hypersonic boundary layers," *7th AIAA Theoretical Fluid Mechanics Conference*, 2014, p. 2497.

[36] Rowley, C. W., Colonius, T., and Murray, R. M., "Model reduction for compressible flows using POD and Galerkin projection," *Physica D: Nonlinear Phenomena*, Vol. 189, No. 1, 2004, pp. 115–129.

[37] Weideman, J. A., and Reddy, S. C., "A MATLAB differentiation matrix suite," *ACM Transactions on Mathematical Software (TOMS)*, Vol. 26, No. 4, 2000, pp. 465–519.

[38] Reddy, S. C., Schmid, P. J., and Henningson, D. S., "Pseudospectra of the Orr–Sommerfeld operator," *SIAM Journal on Applied Mathematics*, Vol. 53, No. 1, 1993, pp. 15–47.

[39] Jovanović, M. R., and Bamieh, B., "Componentwise energy amplification in channel flows," *Journal of Fluid Mechanics*, Vol. 534, 2005, pp. 145–183.

[40] Dawson, S. T. M., Saxton-Fox, T., and McKeon, B. J., "Modeling Passive Scalar Dynamics in Wall-Bounded Turbulence using Resolvent Analysis," *2018 AIAA Fluid Dynamics Conference*, 2018, p. 4042.

[41] Dawson, S. T. M., Saxton-Fox, T., and McKeon, B. J., "Modeling Passive Scalar Dynamics in Wall-Bounded Turbulence using Resolvent Analysis," *2018 Fluid Dynamics Conference*, 2018, p. 4042.